VILNIUS UNIVERSITY
CENTER FOR PHYSICAL SCIENCES AND TECHNOLOGY

Armandas
BALČYTIS

Fabrication of subwavelength functional components by means of lithographic methods

DOCTORAL DISSERTATION

Technological sciences,
Materials engineering 08T

VILNIUS 2018

Dissertation was prepared during the 2013 – 2018 yearspan at the Department of Laser Technologies of the Center for Physical Sciences and Technology.

Scientific supervisor:
dr. Raimondas Petruškevičius Department of Laser Technologies, Center for Physical Sciences and Technology, Technological Sciences, Materials Engineering – 08T.

Scientific consultant:
prof. Saulius Juodkazis Centre for Micro-Photonics, Swinburne University of Technology.

VILNIAUS UNIVERSITETAS
FIZINIŲ IR TECHNOLOGIJOS MOKSLŲ CENTRAS

Armandas
BALČYTIS

Subbanginių funkcinių komponentų gamyba litografijos metodais

DAKTARO DISERTACIJA

Technologijos mokslai,
Medžiagų inžinerija 08T

VILNIUS 2018

Disertacija rengta 2013– 2018 metais valstybinio mokslinių tyrimų instituto Fizinių ir technologijos mokslų centre, Lazerinių technologijų skyriuje.

Mokslinis vadovas:
dr. Raimondas Petruškevičius Fizinių ir technologijos mokslų centras, Lazerinių technologijų skyrius, technologijos mokslai, medžiagų inžinerija - 08T

Mokslinis konsultantas:
prof. Saulius Juodkazis Centre for Micro-Photonics, Swinburne University of Technology

Contents

List of Abbreviations 7

PREFACE **9**
Purpose and novelty of this work 10
Contribution statement 12
Outline of the thesis 14

1 LITHOGRAPHY METHODS **17**
1.1 Electron beam lithography 18
1.1.1 EBL instrumentation 19
1.1.2 Electron beams and their interaction with matter . . . 25
1.1.3 Outline of an EBL process 31
1.2 Focused ion beam milling 34
1.2.1 FIB instrumentation 35
1.2.2 Ion beams and their interaction with matter 41
1.2.3 FIB lithography procedures 42

2 MICRO-RING PHOTONIC SENSORS **51**
2.1 Fundamentals of micro-cavity resonators 51
2.1.1 Coupling and spectral characteristics 53
2.1.2 Silicon micro-ring loss mechanisms 58
2.1.3 Micro-ring resonators in sensing 60
2.2 Fabrication of SOI waveguide structures 63
2.2.1 Comparison of EBL and UV lithography 65
2.2.2 EBL patterning of photonic devices 67
2.2.3 Optimization for low propagation loss 71
2.3 Micro-ring sensor mode engineering 76
2.3.1 Gradient index micro-ring structures 77
2.3.2 Dispersion-tuned resonators 82

3 FOCUSED ION BEAM FABRICATION **89**
3.1 Rescalable solid-state nanopores 90
3.1.1 Ion beam perforation of membranes 91
3.1.2 Electron beam sculpting 96
3.2 FIB milling of optical polarizer structures 98
3.2.1 Fabrication of nanoscale-period concentric Au gratings 99
3.2.2 Mid-IR characterization of orientationally anisotropic systems 101
3.3 Curved micro-optical spiral zone plates 106
3.3.1 Beam shaping by spiral zone plates 107

3.3.2 Fabrication of 3D SZP structures 110
3.3.3 Characterization of focused topological beams 113

4 LAYERED METAL FUNCTIONAL DEVICES 119
4.1 Micro-thermocouple on a nano-membrane 120
4.1.1 Fabrication of thermocouples on membrane chips . . . 120
4.1.2 Micro-thermocouple response to beam-induced heating 123
4.2 Hydrogen sensing using modified Pd films 128
4.2.1 Deposition of Pd/Au composite films 129
4.2.2 Optical transmittance response of thin-films to hydrogen 132
4.2.3 Hydrogen sensing using Pd infrared wavelength plasmonics 136
4.3 Plasmonic absorber metasurfaces at mid-IR 141
4.3.1 Lithographic patterning of plasmonic metasurfaces . . 142
4.3.2 Spectroscopic characterization of mid-IR absorbance . 144
4.3.3 FDTD simulation of insulator and morphology effects 147
4.4 Magnetic lattices for atom trapping 152
4.4.1 EBL fabrication of submicron magnetic lattices 154
4.4.2 Atom trapping in a submicron-period 2D lattice 159

CONCLUSIONS 165
ABSTRACT 169

REFERENCES 170
ACKNOWLEDGMENT 191

LIST OF PUBLICATIONS 193

List of Abbreviations

CMOS	Complimentary Metal-Oxide-Semiconductor
CVD	Chemical Vapor Deposition
DUV	Deep Ultraviolet
EBL	Electron Beam Lithography
ER	Extinction Maximum
EUV	Extreme Ultraviolet
FDE	Finite Difference Eigenmode
FDTD	Finite-Difference Time-Domain
FET	Field-Effect Transistor
FIB	Focused Ion Beam
FSR	Free Spectral Range
FWHM	Full-Width at Half-Maximum
HSQ	Hydrogen Silsesquioxane
ICP	Inductively Coupled Plasma
IPA	Isopropyl Alcohol
IR	Infrared
LED	Light-Emitting Diode
LMIS	Liquid-Metal Ion Source
LSPR	Localized Surface Plasmon Resonance
MFM	Magnetic Force Microscopy
MHA	Metal Hole Array
MIBK	Methyl Isobutyl Ketone
NDA	Nanodisk Array
OAM	Orbital Angular Momentum

PHB	Poly-Hydroxybutyrate
PLLA	Poly-L-Lactic Acid
PMMA	Poly(methyl Methacrylate)
PVD	Physical Vapor Deposition
RI	Refractive Index
RIE	Reactive Ion Etching
RT	Room Temperature
SEM	Scanning Electron Microscopy
SIMOX	Separation by Implantation of Oxygen
SOI	Silicon on Insulator
SZP	Spiral Zone Plate
TE	Transverse Electric
TEM	Transmission Electron Microscopy
TM	Transverse Magnetic
UV	Ultraviolet
WGM	Whispering Gallery Mode
XRD	X-ray Diffraction

PREFACE

Application of submicron lithography methods

Miniaturization of devices or their constituent functional components has been one of the most rewarding routes for technological development throughout the recent decades. The benefits of scaling down are many and often manifest in a multiplicative fashion. The most evident of such examples relate to the massive gains in manufacturing yield that increasing the density of electronic or photonic components can deliver, which has been instrumental in simultaneously expanding the capacity and decreasing the cost of computer memory devices [1]. In addition, miniaturization can be used to enhance key performance parameters, such as the energy efficiency and response rate, best exemplified by the Moore's law driven 10^4-fold increase in the clock rates of ever shrinking field-effect transistor-based microprocessors [2].

Conversely, entirely new functional behavior can be observed when structural features of a given device span over a scale that is conducive to either individual or collective interaction with a particular physical phenomenon. A notable case-in-point is the periodic arrangement of optical wavelength-scale components that, through scattering, diffraction and interference, allow for control over propagation and confinement of light at the nanoscale in photonic crystal structures [3]. Another clear example is given by metamaterials – artificial periodic or quasiperiodic arrays of metallic structural components that collectively become endowed with properties like negative refraction that are wholly absent in the natural world [4].

Creation of the aforementioned structures in the 1 μm to 1 nm size span is enabled by a range of techniques jointly referred to using the blanket term of nanolithography. Nanofabrication methods can be either parallel, such as the wide range of self-assembly driven approches [5] or master pattern replication by way of mask photolithography [6] and nanoimprint lithography [7], or serial processing based, as exemplified by laser [8], scanning probe [9], electron [10] and ion beam [11] direct-write techniques. The former set of approaches are particularly affordable and rapid, the most stand-out example being the immersion deep UV lithography used for the production of complementary metal–oxide–semiconductor (CMOS) integrated circuits, omnipresent in digital logic devices. Still, while through continuous development this type of lithography was shown to be capable of reproducing structures down to 10 nm in size, as evidenced by recent advances in finFET semiconductor manufacturing technology [12], one of its main disadvantages is a large up-front cost of photolithography masks. Serial patterning techniques, in contrast, struggle with limited scalability, however, offer unmatched flexibility for various niche

applications, such as the creation of aforementioned photo-masks, editing of integrated circuits, or for rapid prototyping of novel devices in both scientific and industrial research.

Purpose and novelty of this work

This thesis describes the fabrication of various structures, mostly photonic with some digressions into thermometric, nanopore molecular sensor or atom trapping realizations, that rely on structural components which are submicron in at least one of their dimensions. To this end primarily two state-of-the-art nanoscale precision charged particle beam EBL and FIB lithographic fabrication techniques, as well as physical vapor deposition (PVD) or reactive ion etching (RIE) pattern transfer methods, were leveraged.

The aims of this work are:

1. Develop electron beam lithography fabrication processes for the creation of telecommunication wavelength micro-ring resonator sensors on the silicon-on-insulator platform.
2. Develop ion beam lithography fabrication processes for the creation of advanced micro-optical elements for optical manipulation using polarized and structured light.
3. Employ PVD and RIE bolstered lithography methods for creation of layered metal-based functional planar devices for optical sensing, thermometry and ultracold atom trapping.

The thesis statements of this work are:

1. Electron beam lithography patterning of silicon-on-insulator micro-ring resonator devices with an up to $\sim$ 10 nm pattern fidelity is sufficient to create subwavelength photonic structures that allow for spatial and spectral control over supported resonant modes.
2. Combining the additive three-dimensional structuring capability of laser polymerization and the subtractive subwavelength resolution patterning of focused ion beam lithography allows for the creation of hybrid (dielectric/metallic) micro-optical elements that combine both refractive and diffractive optical functionalities.
3. Au-Ni micro-thermocouple junctions electron beam lithography fabricated on a 30-nm-thick Si_3N_4 membrane exhibited responsiveness to thermal effects modulated at up to 10 kHz frequencies, which is up to five times higher than for equivalent structures fashioned on bulk substrates.
4. Electron beam lithography is capable of exposing 1 mm^2 sized areas with 10 nm pattern fidelity, that allows for the creation of 700 nm period 2D lattice magnetic gratings in which ultracold ^{87}Rb atoms can be captured in permanent submicron scale traps.

The main findings pertaining to this work are:

1. Micro-ring resonators with controlled fill-factor annular Bragg gratings were fabricated and indicate dispersion-derived Q-factor enhancement for a specific resonance, as well as the suppression of all modes that are at odds with the diffraction condition, which led to an increase in the dynamic range of such a device.
2. Gradient effective refractive index micro-ring resonators, designed to achieve optical field delocalization for probing extended sensing volumes, despite having an increased surface area were shown to have $Q \simeq 15000$ quality factor, a threefold improvement over a standard micro-ring.
3. Sub-10 nm diameter nanopores were milled into Si frame suspended $10-30$ nm thickness Si_3N_4 membranes, whereby the ultimate hole diameter and shape was shown to be controllable *via* exposure dose and intensity distribution of the focused ion beam, and gradual closure of the nanopore can be realized through raster scan exposure to an electron beam.
4. FIB milling enabled the creation of 200 nm period 0.5 duty cycle Au polarizer gratings, that exhibited an extinction ratio upwards of $T_{\max}/T_{\min} \approx 150$, and enabled the verification of the four polarization mid-IR microspectroscopy method for determining the molecular alignment in complex anisotropic materials.
5. The large depth of focus in FIB systems allowed for nanoscale processing of complex non-planar surface topology structures, such as those polymerized through 3D laser exposure, and was leveraged for creating of hybrid refractive/diffractive micro-optical elements that deliver a well-defined topological shaping of light exemplified by $NA \approx 0.7$ numerical aperture focused optical vortices.
6. A sensitive rapid-response rate Au-Ni micro-thermocouple with only 2.5-µm-wide electrodes on a 30-nm-thick Si_3N_4 membrane was fabricated using a low-resolution electron beam lithography and lift off procedure, and the device was shown to be sensitive to heat generated by laser as well as an electron beam, and temperature changes at the rate of 2×10^5 Ks^{-1} could be measured.
7. Sub-100 nm thickness Au and Pd alloy films made by magnetron co-sputtering can decrease the response time during H_2 uptake and release stages as observed by near-IR radiation transmittance at $\lambda = 1.3$ µm wavelength, whereas alternating sputter-deposited layered films have a higher sensitivity to hydrogen compared to co-sputtered samples.
8. Metal-insulator-metal nanodisk array based plasmonic absorber metasurfaces, prepared by means of reduction projection photolithography,

attain plasmonic resonances with around 50% extinction at a predefined narrowband mid-IR wavelength range, particularly when Au and Ag noble metals in conjunction with Si insulating dielectrics are used.

9. Electron beam lithography was employed to create 2D lattice magnetic gratings, that were used for trapping of ^{87}Rb atoms at distances of about 100 nm from the chip surface for the first time, and supported trap frequencies as high as 800 kHz, which establishes hitherto unexplored new possibilities for trapping ultracold atoms.

Approbation is evidenced by the fact that over the course of this PhD project a total of 43 peer reviewed publications have been published, and 13 of them are directly related to this thesis. Also, including co-authorships, a total of 17 contributions to conferences were made, 8 of them were presented personally by the author, and out of this number respectively 9 and 5 directly reflect on the work included in the present thesis. All published and presented work is summarized in the Appendix "Publications during this PhD project".

Contribution statement

Work described here is the result of several collaborative research initiatives and research projects, varying in both complexity and the number of participating research groups. In every case, collaborators on any given project are acknowledged in the introductory part of the relevant section. Similarly, data and figures obtained from colleagues without direct involvement of the author are denoted as such in every respective caption.

The author of this thesis has performed all of the nanofabrication as well as the numerical photonic simulation work described here. Most noteworthy contributions include:

- EBL process development and patterning of subwavelength scale functional components, in particular, integrated SOI waveguide-coupled micro-resonator sensor devices, membrane-suspended micro-thermocouple junctions, and submicron magnetic atom trapping latices.
- FIB lithography process development and fabrication of solid-state nanopore molecular translocation sensors, as well as nanoscale resolution wire grid polarizer and spiral zone plate micro-optical elements.
- Performing requisite lithographic pattern transfer steps, including subtractive inductively coupled plasma RIE as well as additive sputtering or thermal evaporation PVD methods.
- Development and execution of protocols for PVD deposition of different Pd, Au, Ag, Cu, Ti, Si, SiO_2 and ZnO alloy and layered composite thin films, as well as performing lift-off procedures where applicable.
- Setting up and conducting FDTD photonic simulations on SOI micro-ring resonators, spiral zone plates, as well as plasmonic absorber metasurfaces.
- Characterization of the fabricated structures using SEM, optical profilom-

etry, atomic force microscopy, lock-in thermovoltage measurements, as well as mid-IR micro-spectroscopy at the Australian synchrotron.

The co-authors and colleagues were heavily relied upon to perform experimental characterization work and frequently dictated the requirements a given structure or device had to fulfill, most notably:

- SOI micro-ring resonator devices detailed in Section 2.3 were devised at the Center for Physical Sciences and Technology by the group under the supervision of Dr. Raimondas Petruškevičius, where waveguide transmittance was characterized by Konstantinas Vaškevičius.
- Solid-state nanopores introduced in Section 3.1 were characterized using TEM and electrochemical conductivity measurement setups operated by engineers at the company "Nanopore Solutions Lda" based in Portugal.
- The four polarization method for visualizing orientationally selective absorption, invoked in Section 3.2, was developed and applied to experimental data jointly measured at the Australian synchrotron by the research group headed by Prof. Junko Morikawa at Tokyo Institute of Technology.
- Non-planar dielectric pedestals, supporting the the curved micro-optical spiral zone plates described in Section 3.3, were laser polymerized by the team of researchers headed by Dr. Mangirdas Malinauskas at Vilnius University, and the beam shaping properties of resultant FIB milled structures were investigated by the group supervised by Prof. Etienne Brasselet at University of Bordeaux.
- The idea for creating a micro-thermocouple device on an ultrathin membrane, detailed in Section 4.1, was brought forward by Prof. Saulius Juodkazis, whereas its creation and characterization was facilitated by the experience and capabilities of the research group headed by Prof. Junko Morikawa at Tokyo Institute of Technology.
- Hydrogen uptake optical characterization of the palladium-based thin films and micro-structures, described in Section 4.2, was performed by the research group headed by Assoc. Prof. Yoshiaki Nishijima at Yokohama National University, using their in-house developed gas flow chamber optical transmittance measurement setup.
- Mid-IR spectroscopy characterization of the nanodisk array plasmonic absorber metasurfaces, described in Section 4.3, was likewise executed by the team under supervision of Assoc. Prof. Yoshiaki Nishijima at Yokohama National University.
- Magnetic multilayer films used for EBL fabrication of lattices presented in Section 4.4 were prepared at University of Augsburg under the supervision of Prof. Manfred Albrecht, whereas atom trapping experiments were performed by the group led by Prof. Peter Hannaford at Swinburne University of Technology.

The overarching structure of this thesis is summarized in Figure A. It starts with a general overview of the most important fabrication methods employed in this work, and is followed by individual chapters that describe the research performed along three main directions. Detailed descriptions of structure-specific manufacturing, experimental characterization and numerical simulation techniques are given as needed in the relevant sections, so that writeup of each disparate contribution remains relatively self-contained.

The contents of the thesis can be briefly summarized as follows:

- **Chapter 1 – Lithography methods** describes the apparatus, operation principles and general application considerations of resist-based EBL and direct material modification capable FIB nanofabrication approaches. The major advantages and shortcomings of these techniques are summarized and generic fabrication process outlines are also provided.
- **Chapter 2 – Micro-ring photonic sensors** focuses on high-precision EBL fabrication of planar silicon-on-insulator waveguide label-free sensor structures, that are modified with subwavelength scale deterministic structural features geared towards inducing either mode delocalization *via* a gradient effective refractive index distribution, or increasing the free spectral range of a resonator by means of dispersion engineering. Fabrication fidelity is verified by the close correspondence of numerical simulation predictions to experimental characterization results.

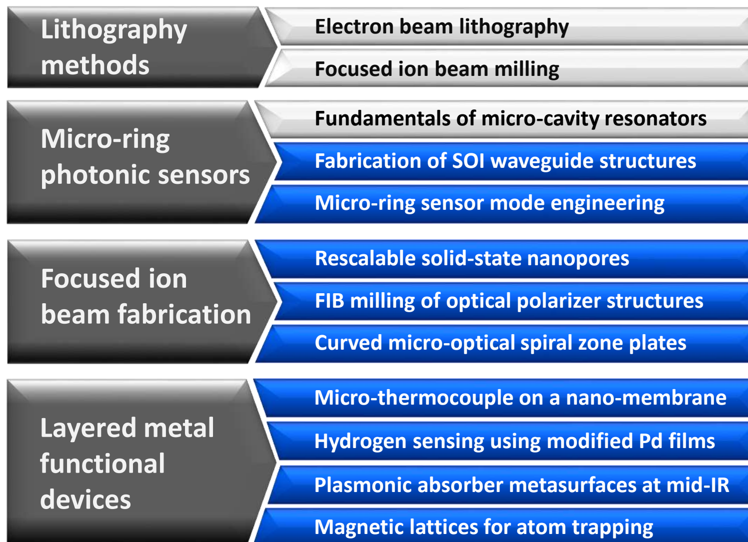

Figure A: Schematic outline of this thesis. Sections detailing original research contributions are highlighted in blue.

- **Chapter 3 – Focused ion beam fabrication** outlines the application of the unique properties of focused ion beam lithography for creation of various structures through direct modification of materials. It begins with the description of solid-state nanopore sensor fabrication, which simultaneously reveals much of the physics behind FIB milling. This is followed by examples of more complex processing of polarized and structured light generating micro-optical elements.
- **Chapter 4 – Layered metal functional devices** shows how, in addition to the 2D patterning enabled by lithography, layered physical vapor deposition of disparate metal films provides a way to exert control over the third fabrication dimension as well. This principle is illustrated by examples of lithographically defined micro-thermocouple devices as well as 2D magnetic lattices for the trapping of ultra-cold atoms. Use of palladium films and plasmonic structures for optical gas sensing is also described in some detail.

1 LITHOGRAPHY METHODS

Most work on contemporary photonics and cutting-edge integrated electronics hinges on reliable methods of producing strictly defined nanometer length-scale structures. Furthermore, to keep pace with ever broadening demands, said methods need to be able to process materials ranging from insulating to metallic, crystalline to glassy, and hard to soft. Over the years, mainstream photolithographic nanofabrication techniques have reached extreme sophistication, so that, with predictive simulations and iterative improvement that compensate for many of their fundamental limitations, precision that inches toward the 10 nm range has been demonstrated. However, while mask-based parallel patterning possesses extraordinary commercial viability, more free-form direct serial writing techniques remain indispensable for rapid prototyping of devices in research settings as well as for creating of the mask templates themselves.

Among all maskless direct-write lithography methods the two realizations where tightly focused charged particle beams are scanned over a surface and used to induce material modification, namely electron beam lithography (EBL) and focused ion beam (FIB) milling, exhibit the highest versatility and can offer patterning fidelity on the order of 10 nm and below. In EBL the small mass of electrons renders their energy transfer to atoms largely inefficient. Therefore, patterning has to proceed by first inducing chemical changes in a specially selected resist film, just as is the case for photolithography. As a result shaping of functional structural components must be performed during subsequent resist pattern transfer steps, the most widely used among which are the subtractive reactive ion etching (RIE) and the additive physical vapor deposition (PVD). In FIB based processes, on the other hand, given sufficient exposure the massive ions can directly sputter away atoms of any material at a sub-10 nm resolution [13]. Hence, this technique can perform grayscale patterning without any intermediary processing steps, albeit at a lower rate than other lithography methods.

This chapter focuses on describing the general properties and principles of the nanofabrication methods employed throughout this work. It begins with a description of electron beam lithography – its apparatus, the way electron beams interact with matter, as well as a general outline of a typical process. Its second part deals with tools and processes involved in realization of FIB milling, and provides some examples of its unique versatility – including direct-write lithography, surface modification as well as beam-induced etching and deposition.

Electron beam lithography was developed in the 1960s as an offshoot of the now ubiquitous scanning electron microscopy technique. This was in large part facilitated by the discovery of the electron beam sensitivity of poly(methyl methacrylate) (PMMA) polymer films [14], which continue to be widely used as a positive tone EBL resists to this day. PMMA molecules in resist areas that are exposed to energetic electrons undergo chain scission, thereby altering the solubility of the polymer in organic solvents. Almost immediately after its inception, EBL was capable of patterning components as small as 60 nm across [15], a feat that optical lithography was able to replicate only in the last decade. Fundamentally, the ultimate resolution of any lithography approach is limited by the smallest dimensions the energy of a given exposure method can be confined to. Mass-endowed charged particles are characterized by de Broglie wavelengths in the picometer range, therefore, diffraction limitations are much less restrictive than those in place for photons, to the point of being largely irrelevant. Contemporary EBL systems can focus their charged particle fluxes down to spot sizes below 10 nm, and patterning fidelity is mainly limited by the mutual scattering of electrons in the beam and nanoscale roughness of the developed resist layer.

Furthermore, EBL is a direct write method, meaning that patterns are generated by scanning of an electron beam along numerically defined trajectories that can be shaped into planar patterns with arbitrary geometry. As a result of this flexibility and the massive advantage in resolution EBL became the premier technique not only for small-scale fabrication of functional components with features from 10 to 100 nm in size, but also for enabling industrial-scale DUV and EUV optical as well as nanoimprint lithography by creating high resolution master templates essential for these pattern replication methods.

However, despite its numerous advantages EBL is severely hampered by its low throughput, hence, is not a commercially viable approach for large-scale manufacturing of integrated devices. The serial scanning of a single nanoscale diameter beam spot over an extended area simply cannot compete with mask-based parallel projection optical lithography that can on average expose 60 wafers per hour. To attain a similar throughput an EBL system would be required to scan a 50 nm diameter electron beam spot at a 20 kmh^{-1} speed and dwelling at each pixel for only 2.5 ps [16]. Of course it is unreasonable to expect such scanning rates for a single-beam system, and no known resist even approaches the required sensitivity. While there has been much progress in devising parallel electron or ion beam projection lithography realizations, they are hampered by mask degradation due to energetic charged particle bombardment. An alternative approach for increasing EBL throughput pursued the realization of multi-beam systems, where the electron flux from a field emission source is split into hundreds of exposure spots [13], however, none of

these systems have reached the maturity required for commercialization.

This section provides a brief overview of EBL, starting with the operational principles of a typical tool and its constituent components. Next, the interactions between an electron beam that pertain to EBL are described, This leads into a discussion on the different types of resists used for charged particle-based lithography. Lastly, some general observations regarding a typical EBL fabrication process are given.

1.1.1 EBL instrumentation

The first realizations of EBL functionality were simply scanning electron microscopes which had their electron beam deflector coils connected to a digital-analog converter, otherwise called a pattern generator, and equipped with a beam blanking module, which can rapidly deflect the electron flux from passing through an aperture, thereby allowing for intermittent pauses in exposure. Hence, it is unsurprising that construction of an EBL apparatus closely mirrors that of an SEM tool. However, an important difference is that the goal of electron beam lithography is to modify resist materials, not merely to image them, so exposure energies have to be increased considerably. For that reason EBL tends to employ substantially larger electron currents and acceleration voltages in the 30 kV to 100 kV range. In response to these demands contemporary dedicated high performance EBL realizations diverged specifically towards the use of high brightness electron sources and ever higher acceleration voltages. Furthermore, in order to perform patterning over extended wafer areas, precise movement of a substrate relative to the beam axis becomes a necessity so that substrate regions out of the sub-millimeter scale reach of the beam deflector can be exposed. This is typically achieved using interferometrically controlled nanometer-precision piezoelectric sample stages. The main components of an EBL system are outlined in Figure 1.1.

Electron source represents the origin point of charged particles in an EBL system. A key principle of any imaging system, equally applicable to the focusing of electrons, is that the beam spot focused on the sample surface can, at best, be an image of the radiation source. Hence, a small and bright region of electron emission is necessary for realization of tight beam focusing. Furthermore, while not critical for SEM, source stability is a major concern in EBL for attaining consistent fabrication outcomes.

The first EBL systems were equipped with thermionic tungsten cathodes which were sharpened down to a $10-50$ µm tip diameter needle-like active mission region. This shape serves to facilitate charge accumulation and decreases the electron work function by way of the lightning rod effect. When the electrode is heated by a large current flowing through it, the thermal energy is dissipated by the emission of thermal radiation and liberation of electrons. These charge carriers are accelerated using electrostatic fields and filtered out into a primary beam by way of an aperture. The electron current density j_c

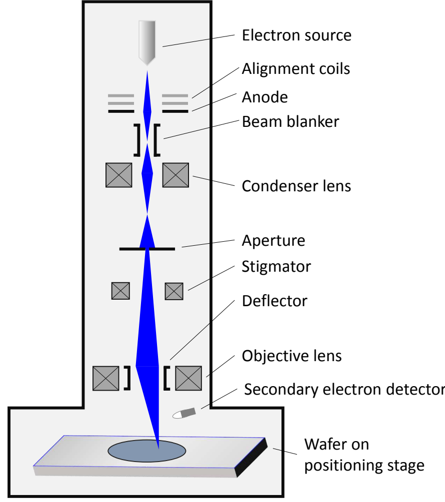

Figure 1.1: A simplified schematic diagram illustrating the main components of a typical EBL system. The shaded region represents a high vacuum environment.

generated by a typical thermionic source is described by Richardson's law [17]:

$$j_c = AT_c^2 e^{-\frac{\phi_w}{kT_c}}, \tag{1.1}$$

where A is a cathode material dependent constant, T_c is the temperature of an emitting tip, ϕ_w is the cathode electron work function, and k represents the Boltzmann's constant. This type of charged particle emission results in an approximately Gaussian radial beam intensity profile distribution:

$$j(r) = j_0 e^{-\left(\frac{r}{r_0}\right)^2}, \tag{1.2}$$

where r_0 is the radius of the emission region. However, while thermionic filament sources are affordable and are still used in some EBL systems, due to the fairly large size of the emission area their performance is less than optimal when small beam spot sizes have to be achieved. This can be partially mitigated by using strong magnetic lenses to establish a cross-over point close to the emitter thereby creating a much smaller virtual electron source. Yet, even this technique is somewhat limited by electron-electron scattering interactions in this region.

Most of these shortcomings can be avoided when field emission sources are used, which were likewise borrowed from scanning electron microscopy. Their operation does not necessitate heating, and instead relies on strong electric

fields ($> 10^8$ Vm^{-1}), established between a cathode tip and concentric anode electrodes, that, by way of the Schottky effect, enable electrons to tunnel out of a material. Since electrons are liberated only from regions where the electric field exceeds a threshold value, the emission site can be exceedingly small and well defined. A typical realization of a field emission source employs a sharp (100) lattice plane-terminated crystalline tungsten cathode, which is usually coated by a thin ZrO film that serves to decrease the work function from 4.5 eV to 2.5 eV. The first major difference between field emission implementation in SEM and EBL systems is that for lithographic purposes sources have to be heated up to a $\sim$ 1800 K temperature in order to avoid adsorption of gas molecules that alter the current density and cause instability and drift of exposure conditions. Despite its numerous advantages, field emission systems can only operate at high vacuum conditions of approximately 10^{-8} Torr, which notably increases the cost of such a tool.

Lastly, it is important to mention that only a small portion of electrons emitted from the cathodes ultimately reach the sample surface. The vast majority of charge carriers do not propagate along the direction along which the beam is being shaped, and hence are stopped by means of an aperture. Therefore, the intensity of an electron beam depends not only on the source brightness, but is also determined by the diameter of this spatial filter. So there exists a trade-off between beam intensity, which is highest when a large area aperture is used, and tight focusing, best realized for small apertures.

Electron optics for directing a charged particle beam and focusing it down to a < 5 nm spot are reliant on either electric or magnetic fields. Despite being fundamentally different from traditional optics, charged particle beam shaping systems nevertheless can be adequately described using equivalent parameters such as focal length or refractive index. Similarly, beam optics strive to minimize the usual chromatic and spherical aberrations as well as astigmatism. Charged particle systems, unlike the optics that control the propagation of bosonic photons, have to account for a unique set of issues related to their mutual repulsion scattering, which manifests as an energy dispersion of the beam and is the ultimate factor limiting the resolution of EBL and FIB systems.

Beam shaping is performed downstream from the particle source and is realized by a cascade of, in the case of electron beam systems, mostly magnetic lenses as well as apertures. A schematic view of a cylindrical magnetic lens of a type frequently employed in an electron column is given in Figure 1.2. A tipical electron beam column, sketched in Figure 1.1, will, at the very least, possess a condenser lens for controlling the current strength and the beam diameter, a stigmator lens for eliminating astigmatism and ensuring a circular beam spot, as well as an objective lens that focuses the beam onto the sample surface. A further important prerequisite for EBL is the ability to rapidly switch the electron flux on or off as needed during pattern definition. This function is performed by a beam blanking system comprised of an electrostatic lens

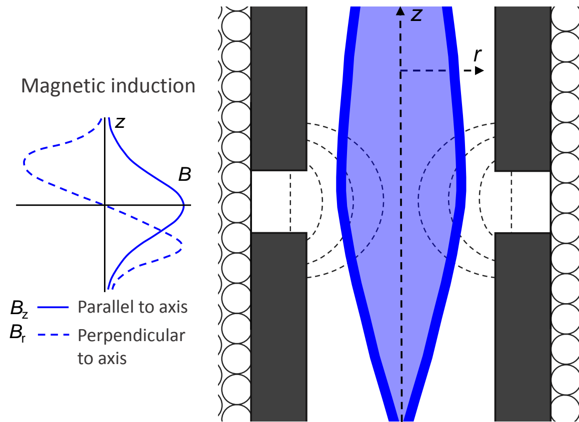

Figure 1.2: A side cross-section schematic view of a cylindrical magentic lens frequently used in various SEM or EBL systems [17]. The electron beam, shown with blue shading, is deflected by a Lorentz force acting on it during propagation through the magnetic induction line-denoted regions and gets directed along a helical trajectory bending towards the column axis. Plots on the left approximately correspond to radial and longitudinal components of the magnetic induction in the column.

that, on command, deflects the electron flux out of the transmittance region of the aperture. Lastly, an electrostatic deflector lens is used for controlling the trajectory that the beam traces during resist exposure. Both the beam blanker and the deflector are connected to a beam controller, which in essence is a rapid, *i.e.* at least 30 kHz frequency, digital-analog converter that serves to interpret the pattern design data into voltage signals used for beam steering.

Imaging and positioning is crucial for performing the necessary pre-exposure adjustments of the lenses to achieve the smallest possible beam spot with minimal aberrations. Furthermore, beam deflection distances should be calibrated to the movements of the precision stage so that the position of the beam spot remains accurately mapped to the the substrate surface even during exposures of large areas. Also, often patterns have to be defined with nanometer-scale precision at specific positions, usually set by markers created over the course of previous exposures, that need to be both discoverable and visible.

As EBL systems share most of their composition with SEM tools, it is hardly surprising that imaging is realized by employing solutions devised for scanning electron microscopy. In most cases visual feedback in EBL is established by using back-scattered electron detectors, situated inside the beam column and comprised of a negatively biased wire-mesh filter that rejects low-energy secondary electrons so that only elastically scattered carriers can reach the scintillator. This component, in turn, through cathodoluminescence converts the

Figure 1.3: Examples of the different classes of EBL tools manufactured by Raith GmbH. (a) ELPHY Plus EBL attachment to an existing analytical SEM tool. (b) eLINE Plus modular 30 kV EBL system. (c) EBPG5200 100 kV dedicated high performance EBL tool.

kinetic energy of electrons into photons that are readily detected and amplified by way of photo-multiplication. This signal is interpreted as the pixel value at the present beam position. In principle, one could also use secondary electron detectors for imaging, however, their low sensitivity to chemical and charge accumulation contrast renders their output less informative for observing beam-induced changes in a resist. On the other hand, in back-scattered SEM images these changes manifest as bright areas and are usually exploited to perform beam adjustment by exposing single-pixel dots and optimizing lens settings until a small aberration-free round spot of electron incidence is attained.

The write-field over which deflector coils can deflect an electron beam is limited to a span below 1 mm for high performance EBL machines, and to an even more modest 50 – 200 µm range in commonly encountered realizations. In addition, the size of a write field is inversely tied to the attainable resolution, as it represents the span over which the output levels of the pattern generator, usually realized by two 12 bit digital-to-analog converters, one for each of the two axes, have to be distributed over. Hence, for higher fidelity patterning write-fields as small as 5 µm can sometimes become unavoidable. Therefore, EBL exposure is conducted not only pixel-by-pixel, but also sequentially over surface segments. For this reason accuracy of stage movements has to be close to that of the electron beam patterning resolution, and such nanoscale precission can be assured only by costly piezoelectric motors with interferometric control schemes.

Typical EBL tool realizations can be found in settings ranging from small scientific research laboratories all the way to the device prototyping and process development departments of large foundries. While EBL has not yet been able to perform as an industrial-scale technique, recent development was notably successful in increasing its throughput. On the other hand, in basic research patterning rate is often not the primary concern and simple realizations that only minimally diverge from their SEM-based origins remain perfectly adequate. Hence, commercially available electron beam lithography tools come in a range

of classes that cater to the needs and resources of a given user, as highlighted in Figure 1.3 by solutions provided by a particular company.

- *Pattern processor attachment*, displayed in Figure 1.3 (a), is an affordable way to upgrade a pre-existing SEM tool with the capability of lithographic pattern exposure, and is thus the most popular entry level solution. It is comprised of a 16 bit digital-to-analog converter, which connects to the SEM deflector coils that move the beam spot in the sample x-y plane, as well as a computer with a specialized software package, that processes patterning design files and provides a user interface. Despite their simplicity such systems can be capable of creating uniquely fine structures, since most SEM tools operate on a low electron current that can be focused down to a 1 nm spot with relative ease. However, SEM columns are not optimized for rapid EBL exposure, which causes a whole slew of problems. For instance, beams can experience excessive aberrations when deflected too far of the column axis, which limits the attainable write-fields to roughly 50 µm and below. Next, the deflector coils in SEM tools do not allow for rapid scanning as they tend to have too many turns, hence to high of an inductivity. Furthermore, electron sources in SEM systems do not tend to emphasize stability, which is crucial for reproducible EBL work. Lastly, positioning systems in SEM systems in most cases are straightforward step motors, which do not possess the requisite precision for lithographic use and are also susceptible to strong drift that can distort patterns during prolonged exposure.
- *Modular EBL system*, illustrated in Figure 1.3 (a) is geared toward users that require all the main capabilities of a nanoscale resolution patterning system at an intermediate upfront and upkeep cost. In essence such a tool is an extensively modified SEM system, with electron columns that are optimized for lithographic exposure and operate at up to 30 kV acceleration voltages while maintaining a reasonably small $\sim$ 1.5 nm diameter exposure spot size. Furthermore, it relies on a interferometrically controlled piezoelectric stage that can accurately track its own position so that software can use its output to alter beam deflection to compensate for any drift. The main advantage of a modular EBL system is its remarkable flexibility - SEM functions are kept in place in addition to the availability numerous optional attachments such as nanoprobes, nanomanipulators as well as gas injection systems for electron beam induced etching or deposition purposes. Main shortcomings are the somewhat low currents that make exposures over areas in excess of 100×100 µm^2 hours long, as well as the presence of write-field stitching errors. However, these issues are not particularly severe for research oriented applications where such tools are most common.
- *Dedicated EBL system*, unlike both of the aforementioned cases, is built from the ground up exclusively for lithography. Here the electron column

employs a high brightness field emission source and 50 – 100 kV acceleration voltages. Furthermore, electron optics tend to be more complex and can contain auxiliary lenses for automatic real-time adjustments over the course of an exposure. Such systems use large electron currents for faster exposure, however, this means that beam scanning electronics have to be equally rapid, *i.e.* at least 50 kHz, to keep pace and to not overexpose the resist. High-currents generated by field emission systems can be difficult to focus to a fine spot below 3 nm in diameter, however, beams possess remarkable temporal stability and remain mostly aberration-free even at 500 μm off-axis beam deflection. This, in turn, enables patterning over write fields spanning up to 1 mm without stage movement, which minimizes the amount of stitching related defects and cuts down on process duration. In the system shown in Figure 1.3 (c) this is realized by using a two stage deflection system, where a comparatively slow digital-analog converter steers the beam between different 4 μm span sub-write-fields, which are patterned sequentially by a more rapid 12 bit controller. Lastly, dedicated EBL systems are industry oriented, hence, posses a high degree of automation that allows all beam spot and stage calibration adjustments to be done without user input. However, such a specialized system is exceedingly costly, therefore, affordable only to foundries or large research institutions.

1.1.2 Electron beams and their interaction with matter

As mentioned previously, spot sizes of focused electron beams employed in EBL systems, unlike their optical counterparts, are not limited by diffraction. Indeed, electrons, much like any other quantum particle, possess a corresponding mass and energy dependent wavelength λ, defined as [18]:

$$\lambda = \frac{h}{\sqrt{2m_0 eU}} \cdot \frac{1}{\sqrt{1 + eU/2m_0c^2}}, \tag{1.3}$$

where h is the Planck's constant, m_0 and e respectively are the particle mass and charge values, c is the speed of light, and U is the acceleration potential. Therefore, according to this expression, when electrons are accelerated by a 100 kV potential used in high-resolution EBL implementations, their de Broglie wavelengths are around 4 pm - orders of magnitude below the dimensions of any lithographically defined structures. Still, mutual Coulombic interactions do limit the attainable resolutions, where higher beam currents result in larger beam spots. The primary mechanism responsible for limiting electron beam patterning fidelity is chromatic aberrations that arise due to electron energy dispersion, however, electron beams can nevertheless be focused onto a resist layer to spots with diameters not larger than 5 nm.

Resist exposure proceeds when the incident electron flux initiates certain chemical modifications in the molecular structure of the film. Depending on

whether electron irradiation increases or decreases the solubility of exposed areas, the resist is referred to as either a positive or negative tone, respectively. Positive tone resists are usually organic polymers or resins, where inelastic collisions with incident energetic particles result in breakage of the macromolecular bonds, giving rise to increased solubility of reaction products. Conversely, negative tone resists are constituted out of inorganic oligomeric compounds, that cross-link by way of electron-initiated polymerization reactions and become largely insoluble. Regardless of what type of resist is chosen, the electron beam spot gets scanned over its surface and imprints a latent lithographic pattern that subsequently is developed in a specially selected solvent. How the developed 2D pattern gets turned into 3D functional components depends on the properties of the resist itself and the deposition or etching process requirements.

The most important properties of a resist material pertaining to electron beam exposure are its sensitivity S and contrast γ. The definitions of these figures of merit are most evident when the sensitivity curves, displayed in Figure 1.4 for hypothetical positive and negative tone resists, are considered. In the positive resist case its sensitivity is defined as an electron exposure dose which, upon development, results in its complete local removal from the substrate surface. Conversely, for negative tone resists sensitivity is understood as the dose that results in half of the initial film thickness remaining on the patterned regions after development. High sensitivity resists have an obvious advantage of allowing for more rapid patterning.

In addition to the general sensitivity to electron beam exposure it is also important for a resist to possess a maximally nonlinear dose response. To this end, contrast γ represents how abrupt the transition threshold between neighboring irradiated and unirradiated regions is, and can be quantified as:

$$\gamma = \frac{1}{\lg D_1 - \lg D_0}, \tag{1.4}$$

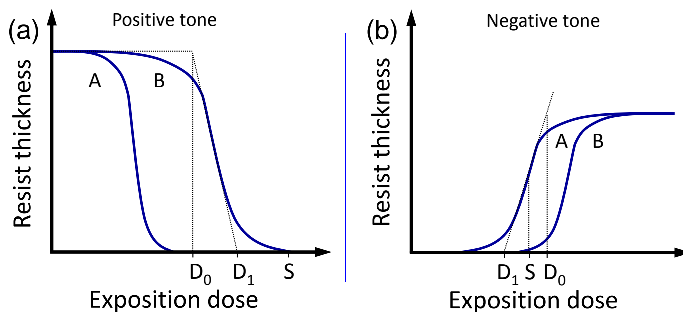

Figure 1.4: Hypothetical examples of sensitivity characteristics of (a) positive tone and (b) negative tone resists. In both cases resist A would be considered to have a higher sensitivity than resist B.

where dose values D_0 ir D_1 are defined from sensitivity curves, as denoted in Figure 1.4 (a) and (b) for positive and negative resists, respectively. In more direct terms, contrast can be defined as the slope of a sensitivity curve at 50% of resist height. A higher contrast is always preferable, as it defines the steepness of the side-walls of a developed resist pattern. It has to be noted that the resist sensitivity and contrast values given in the literature are only approximate, as they can differ based on the EBL acceleration voltage, film thickness, development conditions and similar considerations particular to each individual fabrication process. While the full list of electron beam resists is long, a select few stand out as particularly popular or interesting:

- *PMMA* (poly(methyl methacrylate)), despite being among the oldest known positive tone electron beam resists, remains in extensive use to this day. This is in large part due to it exhibiting one of the highest attainable resolutions of ~ 10 nm as well as due to a very competitive cost. It is commercially available in numerous molecular weight variants (*e.g.* 495 kDa and 950 kDa) and in different solvent solutions. PMMA contrast values are also reasonably high, ranging from $\gamma = 6$ to $\gamma = 9$. On the other hand, this resist has only a mediocre sensitivity and a fairly low etch selectivity.
- *ZEP-520* (1:1 methyl styrene and chloromethyl acrylate copolymer) is likewise a high < 20 nm resolution positive tone EBL resist resin. Its main advantages when compared to PMMA is its 3 times higher dose sensitivity as well as a factor of two higher etch selectivity in most Cl and F based reactive ion etching plasma chemistries. The main shortcomings of ZEP520 is its fairly high cost as well as its high sensitivity sometimes becoming a limiting factor when defining dense nanoscale structure arrays.
- *HSQ* (hydrogen silsesquioxane) is a type of inorganic polymer compound with the chemical formula $[HSO_{3/2}]_n$ that is a liquid equivalent of silica glass. It has been commercialized by the Dow Corning Corporation under the trade name "Fox-12", short for flowable oxide, as a spin-on dielectric. While this material was never intended as an EBL resit, it turned out to exhibit an outstanding negative tone performance. HSQ has an extraordinarily high contrast and routinely allows to achieve resolutions on the order of several nanometers. Furthermore, polymerized HSQ patterns are very resilient to etching. However, this resist has notable issues, first of which is its exorbitant cost, a notably low sensitivity that is 4 times below that of PMMA, frequent process inconsistencies due to its rapid aging and susceptibility to variations in ambient conditions. Furthermore, after development residual HSQ can be removed from the substrate only by performing etching in HF.
- *Bioresists*, such as the aqueous solutions of fibroin protein extracted from silk fibers, are an important new branch of EBL patterning materials [19].

Their most noteworthy feature is an inherent biocompatibility as well as a water and ethanol based chemistry that completely avoids the use of toxic compounds at any stage of the patterinig process. Depending on preparation, silk can act as both a positive tone resist that is approximately 5 times less sensitive than PMMA, or even as a negative tone resist when doses are impractically large. While, with respect to its dose response properties, silk is inferior to most other commercial resists, it is unique in that it can be functionalized with various organic biomolecules in a way that preserves their biomedically relevant properties in EBL patterned devices [20].

In summary, incident charged particles interact with resist material and expend their energy on breaking of molecular bonds, as a key prerequisite for electron beam patterning. However, the energetic particle beam does not stop at the resist layer, and its exposure occurs not solely due to electrons directly incident from the focused beam.

Electron scattering provides another important yet mostly deleterious contribution to lithographic pattern exposure. Due to the massive disparity between the masses of atoms and electrons almost all their collisions are elastic, hence result in a change of incident electron trajectory but not its energy. On the other hand, electron-electron collisions are inelastic and provide the pathway for gradual kinetic energy dissipation by transferring it to the resist or the underlying substrate. In general, electrons undergo numerous elastic scattering events by colliding with atoms that chaotically change their propagation direction. Between any two such events a number of dissipative inelastic electron-electron collisions can occur. However, the rate of energy loss is quite slow, and as a result electrons can penetrate all the way through a thin-film resist and notably far into the substrate material before loosing most of their kinetic energy. Hence, the volume of a substrate that gets irradiated over the course of an EBL exposure is far larger than the nanoscale area of a focused beam spot.

Elastic electron collisions with atoms in a particular material can be interpreted as Rutherford scattering, and its cross-section σ with respect to a solid angle Ω can be calculated according to the well known expression:

$$\frac{\mathrm{d}\sigma}{\mathrm{d}\Omega} = \frac{Z^2 e^4}{4E^2}\left(1 - \cos\theta + 2\mu\right), \tag{1.5}$$

where Z is the atomic number, e and E are the charge and energy of an electron respectively, the scattering angle is denoted as θ, and μ is a screening parameter usually considered to be a constant [21]. Here it should be noted that the mean free path is inversely related to the scattering cross-section, and, by extension, increases quadratically with either increasing electron kinetic energy or decreasing atomic number of irradiated material. The latter dependence means that electrons cross the resist film almost without changing their propagation direction, whereas in the denser substrate materials they undergo much stronger

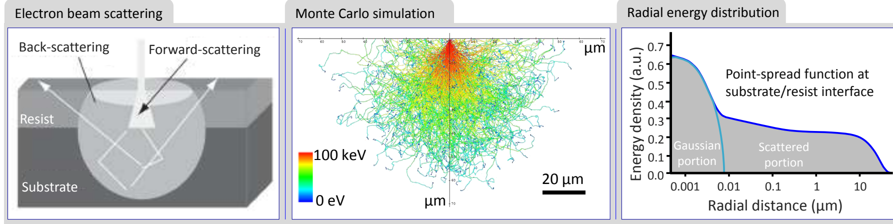

Figure 1.5: (a) Schematic illustration of close-range forward-scattering and long-range back-scattering contributions that underlie the proximity effect. (b) Monte Carlo simulated trajectories of 10^2 100 kV electrons incident onto an PMMA coated Si wafer. (c) Point spread function of energy transferred from the Gaussian electron beam into a thin resist film, accounting for both directly incident and scattered particle contributions.

scattering [22]. Electron-electron interactions represent the second of the two scattering mechanisms and is described by the Bethe continuous-slowing-down approximation [21]:

$$\frac{\mathrm{d}E}{\mathrm{d}s} = -\left(\frac{2\pi e^2 N_A \rho Z}{A}\right)\frac{\ln(\gamma E/J)}{E}, \tag{1.6}$$

where N_{A} is the Avogadro's constant, ρ is the material density, s is the mean free path of an electron, $\gamma = 1.1658$ is a constant, and J is the mean ionization energy. With respect to EBL it is important to point out that loss of electron kinetic energy over a unit propagation distance is proportional to the density of a material and inversely dependent on particle energy. Therefore, in low density materials like resists electron energy transfer proceeds at a much lower rate than in an underlying, say, silicon-based substrate. Furthermore, as particles decelerate the probability of them undergoing inelastic scattering notably rises. For example, when acceleration voltage used in an electron column is decreased from 100 kV to 50 kV, the rate of energy transfer from the particle beam to a material is doubled. This is the reason behind the disparity between exposure doses for the same resist using different EBL tools. For instance, PMMA requires an approximately 500 µC/cm^2 exposure dose at 100 kV, around 200 µC/cm^2 at 50 kV, and only 40 µC/cm^2 for a 10 kV voltage accelerated beam.

The scattering of an electron beam during EBL exposition can be visualized as depicted in Figure 1.5 (a). The particles impinging onto the 100 – 500 nm thickness resist experience only a limited amount of deflection by way of small-angle forward-scattering, which causes the focused beam to spread out slightly. As an example, when a 100 kV acceleration voltage is used only approximately 0.5% of the primary incident electrons end up interacting with a 250 nm thickness PMMA layer and generating secondary electrons. These particles in particular, while not numerous, are notably slower, hence, more

strongly interacting with the resist and therefore are responsible for up to 80% of the overall exposure. However, the vast majority of electrons end up penetrating far into the underlying substrate, as shown by the Monte Carlo simulation visualized in Figure 1.5 (b), and can reach depths of up to $5-50$ μm depending on material density and initial kinetic energy, where most of the elastic and inelastic scattering takes place. Over the course of a cascade of interactions some electrons can end up being scattered towards angles in excess of 90° with respect to their initial incidence direction and return back into the resist film. These back-scattered electrons mildly expose a microscale area around the nanoscale spot of initial beam incidence and are the underlying cause of the proximity effect.

The proximity effect is a major impediment for successfully performing electron beam nanofabrication of densely-packed structures. While back-scattered electron irradiation is too small to notably affect the exposure of a small isolated feature, it can readily accumulate when extended areas have to be patterned. Figure 1.5 (c) shows the radial distribution of incident electron energy outward from the incidence region of a Gaussian beam spot – the so called point spread function. Since full exposure of an adequate resist requires the local dose to be above a certain threshold, the comparatively small number of back-scattered electrons, even when the tail end of the point spread function is accumulated over its full peripheral area, is not sufficient to generate structures of its own. Instead, this extra energy serves to distort the dimensions of directly patterned elements by pushing the doses at their periphery to be above the sensitivity threshold.

The most direct method of avoiding the proximity effect involves fabrication on thin membrane substrates, however, this severely complicates the process and is only rarely compatible with device functionality. A more broadly used method of minimizing such distortion leverages the key feature of EBL, namely its serial pixel-by-pixel patterning, to correct for any potential distortions. To this end, first, the spread of electron energy around the incident primary beam spot is simulated by way of Monte Carlo simulations, where the scattering of a large number of electrons is treated as a stochastic value problem, which yield trajectory plots as given in Figure 1.5 (b). Next, the total energy imparted from all electrons to the resist is integrated and quantified as the aforementioned point spread function in Figure 1.5 (c). Lastly, when the full effect of a beam spot is known, one can iteratively simulate what dose needs to be assigned to each pixel so that, even when accounting for the influence of back-scattering from all nearby pixels, the overall exposure of all patterned features would remain constant. Manifestations of the proximity effect will be discussed with specific examples in subsequent chapters.

1.1.3 Outline of an EBL process

The main purpose of EBL is to generate 2D patterns of certain pre-defined shape in a planar resist film with the highest possible resolution, throughput and reproducibility. These considerations are often mutually exclusive, hence, some compromise particular to every situation has to be made. The main determinants of attainable result adequacy are the quality of the available electron optics, the choice of substrate, resist and developer, as well as the process conditions, which include but are not limited to: electron energy, exposure dose, development duration and temperature. Similarly, the main complicating factors are the proximity effect that arises due to particle scattering, the collapse of nanoscale resist features during development due to capillary forces, and stochastic fluctuations of feature sizes due to resist side-wall roughness.

Despite all of these variables and factors the vast majority of EBL fabrications, including the ones described in this work, tend to proceed in a similar way. A typical EBL process for creating planar functional structures can be briefly summarized as follows:

- *Cleaning* of the substrate surface upon which patterning is to be performed is critical for subsequent formation of a uniform resist layer and helps avoid issues at later stages of fabrication. Standard cleaning of Si wafers is generally performed by way of several sonication steps in different organic solvents – first in acetone, then isopropanol and, lastly, in methanol. Then substrates are blow-dried using N_2 gas and heated on a ~ 180 °C temperature hot-plate to evaporate any residual solvent molecules. As a final step it is often worthwhile to treat the substrate in oxygen plasma. In special cases when the substrate material is sufficiently resilient, strong acids, such as the piranha solution, are also used.
- *Spin-coating resist* represents the most widely used method of creating an electron beam sensitive material layer. The thickness of this film is controlled through the spin rate, acceleration and duration based on the resist solution-particular calibration curve. After spin-coating residual resist solvent is evaporated by again heating the substrate on a ~ 180 °C temperature hot-plate. The choice of resist layer thickness is largely dictated by what the smallest dimension of the patterned structures is. As an approximate rule of thumb, typically a 3:1 ratio between resist height and feature size is sought. On the other hand, it is always preferable to have a thicker resist film, as this makes it easier to perform pattern transfer into functional materials by way of subsequent etching or deposition and lift-off. Therefore, the final resist thickness represents a compromise between patterning resolution and robustness. However, for high acceleration voltage electron beams the influence of resist thickness becomes minimal.
- *Exposure* represents the stage at which patterning inside the high vacuum

chamber of an EBL tool, according to the geometry set by a design file, is conducted. For best results the sample should be stored inside the vacuum chamber for at least 1 to 2 hours before exposure, so that any thermal drift can run its course prior to patterning so as not to distort it. Furthermore, care must be taken to properly ground the sample so that electrons incident from the beam do not accumulate in the resist and warp the pattern by way of coulombic repulsion. For conductive substrates merely using a metal clip or tape at the periphery of the sample might be sufficient for charge removal, whereas insulating materials require deposition of a few nanometers of metal or spin-coating of a conductive polymer over the entire area of the resist-coated substrate.

- *Development* is when the latent image imprinted in the resist by selective electron irradiation is converted into a binary mask pattern. To this end the substrate is treated in appropriately chosen solvents. For positive tone resists the solvents remove the electron exposed areas with abundant bond breakdown, whereas the inverse is true for negative tone layers, where the polymerized and cross-linked beam-scanned sites are more resistant to solvation. In the case of certain negative tone resists it may be beneficial to do a post-exposure heating step to accelerate polymerization at a slight cost to the attainable contrast.
- *Pattern transfer* involves the imprinting of the resist pattern into layers of functional materials required for the operation of the device being created. Subsequent steps are the stage where different fabrication processes tend to diverge most strongly based on specific requirements:
  - *Etching* is used to transfer a pattern directly into the substrate material. Wet chemical etching is generally rapid, isotropic and low fidelity, whereas reactive ion plasma treatments are more flexible as they can also produce anisotropic removal of material that creates steep side walls. However, care must be taken to ensure that resists have sufficient thickness and chemical resilience to withstand the full etching duration.
  - *Lift-off process* is done when samples have to be coated with materials different than the substrate, for instance when metal patterns or electrodes have to be defined. Deposition is usually performed using PVD, particularly using thermal evaporation due to its directionality that avoids covering the side walls and eases subsequent resist removal. The lift-off method is also used when creating inverted hard masks that may be needed to withstand aggressive etching processes.
- *Mask stripping* comes at the final stage of the process when the electron beam-defined pattern no longer has any use. This is typically done chemically with either special organic solvents or corrosive liquids.

After all of these steps lithography can either be considered concluded or

repeated all over again to create the next functional layer by what is called overlay exposure. However, such multi-step lithography necessitates forethought and the creation of marker structures at precisely known positions that can be imaged through a resist layer. All subsequent exposures then have to perform stage calibration and pattern alignment against these reference points to ensure adequate positioning precision.

Ion beams can be understood by invoking similar principles to those applied previously when describing EBL systems, and can be used to attain similar fabrication results. In both cases the charged particle beam is generated and accelerated using equivalent methods of field emission. Furthermore, ions and electrons share most of the conceptual basics of beam shaping and control *via* a sequence of electrostatic or magnetic lenses as well as apertures. Lastly, either of these particles can be used for sample imaging, resist exposure and to perform gas induced etching or deposition.

As for differences, unlike electrons, ions can carry either a negative or a positive charge. However, the key disparity between electron and ion beams is the several orders of magnitude larger mass of the latter particles, which underlies most of the differences in the realizations of their respective beam focusing columns and applications. Since ions carry a large momentum and posses a substantive cross-section they, in contrast to electrons, can readily displace the atoms of any material they irradiate, implant themselves into the host lattice and cause local heat buildup. As ions are far more destructive than electrons they are most often used for direct substrate surface ablation. Consequently, FIB milling, unlike its electron-based counterpart, does not necessitate the use of resists or any subsequent pattern transfer methods, such as etching. Given sufficient time virtually any material can be milled without special preparation steps, which makes FIB patterning extraordinarily flexible. In addition, ion implantation allows for precise local modification of surface conductivity.

On the other hand, FIB milling gives rise to numerous secondary effects, *e.g.* redeposition of sputtered atoms, formation of material defects or its outright amorphization, as well as emission of secondary electrons or photons, that can severely hamper a fabrication process. Furthermore, ion bombardment is known to cause thermal inter-diffusion of substrate materials, phase transitions, induce roughening, cratering, or porosity in the surface, all of which detrimentally affect the performance of a finished device [17]. Therefore, FIB milling is a much more versatile, however, much less predictable approach to nanoscale lithography than the straightforward resist patterning enabled by EBL.

Ion beam lithography, which much like EBL is based on scanning a focused particle flux over a predefined geometrical pattern on a planar surface, first came into use in an industry-oriented setting for selective editing of large-scale integrated microelectronic circuits. Here its main advantage was that FIB could both directly ablate away undesired features, or, with the help of gaseous precursors, be used to deposit metals to reconstruct missing details. Another major application of FIB tools is in fundamental research, where the well controlled 3D removal of material is put to use for preparing nanoscale thickness TEM lamellas. Overall, however, due to its very low processing

rate and high cost, FIB milling is an even more niche technique than EBL and is mostly relegated to the creation of one of a kind prototype devices for research purposes. Yet for such intents FIB is a uniquely useful complement to other nanofabrication methods, as it can be harnessed to both deposit and remove materials with extremely high precision to create complex 3D surface topologies.

This section provides a brief overview of FIB milling in a way that largely mirrors the previous discussion on EBL. Much of the information provided here is in comparative reference to the electron beam lithography case and begins with the operational principles of a typical FIB tool and its constituent components. This leads into the discussion of the interactions between ion beams and materials, with particular emphasis given to both fairly general resist exposure and beam-induced etching or deposition, as well as the unique applications enabled by FIB, like direct implantation of an etch mask.

1.2.1 FIB instrumentation

In the most general therms an FIB lithography tool generates and directs a flux of relatively large atomic weight ions into a nanoscale spot on a substrate placed in a high 10^{-8} Torr vacuum chamber. Incident charged particles not only displace substrate atoms from their lattice sites, but also generate secondary electrons, which are picked up by detectors that allow for imaging and visual feedback. Therefore, the main components comprising an FIB lithography system are fully analogous to those in an EBL system, and arranged as depicted in Figure 1.1, although the exact technical realization of each individual element might be quite different. The vacuum systems used for FIB systems are largely identical to those of mid-range EBL tools, as they are beholden to similar requirements set by the field emission process. Likewise, sample positioning systems also have to be equivalent and based on interferometric feedback controlled piezoelectric motors. The first difference is that in dedicated FIB systems imaging is performed based exclusively on the secondary electron signal. However, it is the ion source and optic components that depart most drastically from their EBL counterparts.

Ion sources in their earliest realizations were based on gas field-ionization and had too wide of a spatial distribution that prevented tight beam focusing required for nanoscale fabrication. As a result such systems were mainly used for ion implantation and general low resolution sputtering of surfaces. This all changed around the year 1978 with the development of high brightness liquid-metal ion sources [23] that underlie virtually all of the contemporary FIB lithography realizations. As a curious side-note, LMIS were first investigated for the purpose of devising spaceship propulsion engines based on the emission of small electrically charged metal droplets [23]. However, it was soon determined that liquid metals, due to their high surface tension, in a strong electric field emit ions instead of droplets.

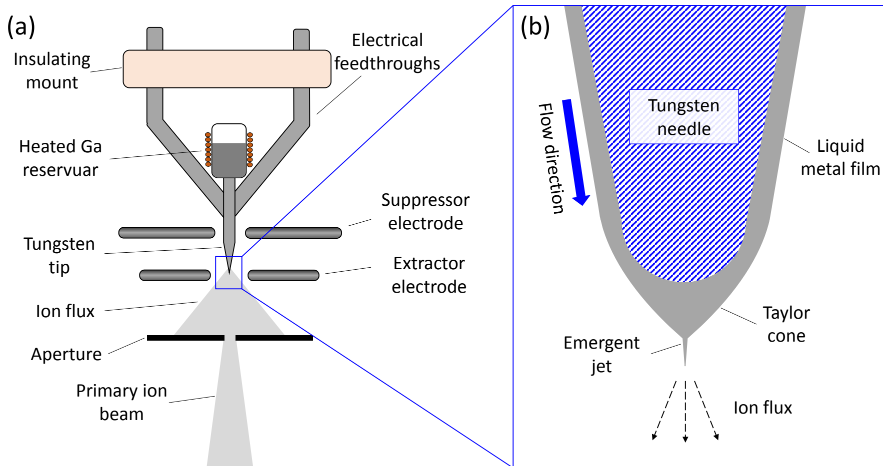

Figure 1.6: (a) Schematic illustration of a liquid metal ion source used in the majority of high performance FIB lithography systems. (b) A close-up view of a liquid metal wetted LMIS tungstein needle tip. Figure was adapted from the literature [17]

A schematic depiction of a typical LMIS realization is provided in Figure 1.6 (a). It is comprised of a heated reservoir containing some kind of reasonably heavy metal, in most cases gallium, which is connected to a heat resistant tungsten needle sharpened down to a $2-5$ µm diameter tip. When the metal is brought to a temperature close to evaporation it begins wetting and covering the needle surface all the way to its very tip, as shown in Figure 1.6 (b). The liquid is then subjected to a strong electric field of around 10^8 Vm^{-1} that is established between the needle and a concentric extractor electrode and sufficient to generate ions by pulling them out of the metal. More precisely, the interplay between electrostatic and surface tension forces shapes the liquid metal into a so called Taylor cone shape, terminated by an emergent jet with a tip as small as 5 nm in diameter that is, in fact, the actual field evaporated ion source.

Gallium, as a result of its low melting temperature and a negligible degree of inter-diffusion with tungsten comprising the needle, is the most widely used metal for LMIS purposes. Furthermore, Ga is not particularly volatile, hence its reservoir needs to be refilled fairly infrequently. Next, the mass of Ga^+ strikes a good balance between being large enough to enable efficient sputtering of even the heaviest elements, however, is not excessive in a way that would lead to the destruction of small structures. Lastly, the low vapor pressure of Ga enables it to be used in its pure form instead of an alloy. This notably simplifies and reduces the cost of a Ga ion beam system, as it is not required to be equipped with costly E–B mass separator components. While gallium is by

far not the only viable candidate for LMIS realization, not every metal can be intrinsically supported. For instance, a metal has to wet a needle – this renders Ag and Cu incompatible with tungsten; it must not alloy with the needle – Al is incompatible with tungsten as a result; not sublimate too easily when heated in a vacuum – Mg and Zn are thus unsuitable; and also have a sufficiently low melting point. Despite these issues presently at least 39 different elements, namely Ag, Al, As, Au, B, Be, Bi, Ce, Co, Cr, Cs, Cu, Dy, Er, Ga, Ge, Hg, In, K, Li, Mg, Mn, Na, Nb, Nd, Ni, P, Pb, Pd, Pr, Pt, Rb, Sb, Si, Sm, Sn, U, Y, and Zn, were demonstrated to operate in a LMIS configuration. Most these metals become compatible when used in an eutectic alloy mixture with other elements [24], and the appropriate ions are selected by means of an E–B mass separator.

In order to attain a high beam stability and a low ion kinetic energy dispersion that are both required for lithography applications, LMIS sources are typically operated in the low emission regime where currents are in the $1-3$ μA range. Higher emission currents are associated with the generally undesirable formation of ionized dimers, trimers or even droplets. The ion flux propagating out of a source is called the extraction current, and its strength is regulated by the extractor and suppressor electrode tandem, which respectively correspond to coarse and fine control regimes. The main function of a suppressor is to compensate for current drift that occurs over the course of source aging without inducing instabilities in the Taylor cone associated with strong nonlinear jumps in current. The liberated ions are then spatially filtered through an aperture and passed along for further beam shaping in the ion column.

Ion optics is another field where the large disparity between the masses of electrons and ions imposes specific requirements on component design. As mentioned previously, the fast-moving low mass electrons are focused almost exclusively using magnetic fields. The main advantage of magnetic lenses is that it is relatively straightforward to ensure spatial uniformity and that magnetic fields do not alter the kinetic energy of charged particles. However, while the velocity of Ga^{+} ions amounts to only 0.0028 of the speed of electrons in an equivalent system, their momentum is 370 times larger and requires much stronger fields for beam shaping. Magnetic lenses would have to be impractically large to exert the requisite refractive power. Electrostatic lenses, on the other hand, can be extraordinarily powerful for their size, and, therefore, form the basis of any ion optics realization. Furthermore, electrostatic lenses have very short response times and, for that reason, are used to perform beam blanking and deflection for pattern scanning in both electron and ion beam lithography systems.

A schematic of a three-electrode electrostatic lens commonly used in FIB systems is provided in Figure 1.7. Positive charge-carrying ions propagate from left to right and first cross a strong electric field established between the first two electrodes. Here, particles move along the field lines and are accelerated and

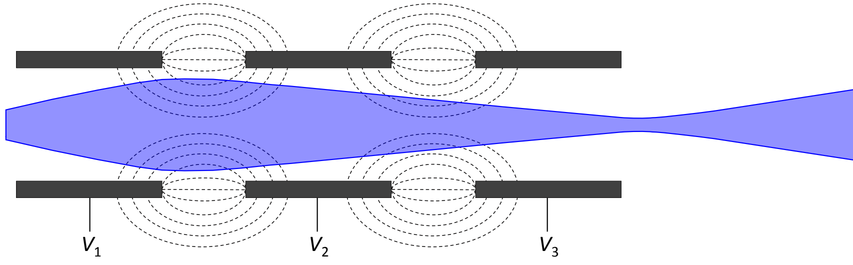

Figure 1.7: A schematic view of a three-electrode electrostatic lens comonly used in various FIB systems [17]. Dashed lines represent the electric fields generated by electrodes with voltages applied to them. The probable ion trajectories are shaded in blue.

deflected towards the beam axis. As the ions move past the second electrode they would be spread out again, however, as they now are closer to the axis the force acting upon them is lessened. The two final electrodes are biased oppositely, hence, while the beam gets deflected towards the central axis again, the ions are being decelerated to a speed close to its original value. In aggregate, the ion beam exits the lens converging towards a focal point. This type of focusing is exactly opposite to the diverging lenses used in TEM systems.

Both ion and electron beam focusing systems are susceptible to spherical and chromatic aberrations as well as astigmatism. Chromatic aberration in particular is the key factor impeding the attainable resolution of all focused beam lithography approaches, and options for its compensation are severely limited due to it arising from emission characteristics of the source. Ions generated in LMIS systems vary in kinetic energy by approximately $\Delta E = 5$ eV, which is notably more than the $\Delta E = 0.3$ eV energy typical for field emission electron sources. The diameter of a charged particle beam can be expressed as [13]:

$$d_p^2 = Md_0^2 + (\Delta f_A \alpha)^2 + \left(0.5 C_s \alpha^3\right)^2 + \left(C_c \frac{\Delta E}{E} \alpha\right)^2, \tag{1.7}$$

where M represents the magnification factor, α is the beam convergence angle, Δf_A is the difference between focal distances in the tangential and sagittal planes, C_s and C_c respectively are the spherical and chromatic aberration coefficients, and, lastly, d_0 is the diameter of a virtual charged particle source. For FIB systems a finite particle source diameter and chromatic aberration, which are given by terms 1 and 4 on the right side of Equation 1.7, are the most detrimental, whereas astigmatism and spherical aberrations represented by therms 2 and 3 are pronounced notably less than in the electron case.

The final important difference between electron and ion optics is in the role apertures play in each of the two systems. In EBL apertures represent mainly

Figure 1.8: Examples of FIB tools capable of lithographic patterining. (a) FEI Helios NanoLab 460F1 with dual ion and electron beam columns, geared towards the preparation of TEM lamellas. (b) Raith ionLINE Plus ion beam lithography setup with interferometric sample stage control and the option to pattern using either Si, Ge and Au ions. (c) Zeiss ORION NanoFab ultra-high resolution FIB tool which employs He and Ne gas ions, and can optionally also be equipped with a Ga LMIS.

a way to minimize aberrations, since the effect of electron irradiation on the substrate is minimal, hence, control over current strength does not have to go beyond merely precisely knowing its value. Conversely, ion beams can be quite destructive to microscale features on any surface, hence, apertures installed in FIB columns, in addition to spatially filtering out stray ions, fulfill an important ion current limiting function.

Apart from these differences, ion beam shaping proceeds in a fashion described for EBL – acceleration voltages are typically in the 5-50 kV range, and the same types of condenser, stigmator and objective lenses are used. Contemporary FIB milling systems are capable of focusing the most common Ga^+ ion beams down to a 5 nm diameter spot, whereas highest resolution gas field-ionization source equipped tools produce He^+ spots as small as 1 nm. Such beams can be used not only for direct processing of materials, but also for resist exposure, and deposition *via* dissociation of gaseous precursors. Taken together, all of these capabilities make FIB milling systems extremely versatile.

Typical FIB tool realizations that are commercially available generally cater to various needs in scientific research as well as for fabrication of prototype electronic or photonic devices. Two main exceptions from the broader industrial domain are the limited utilization of FIB systems for editing and repairing of integrated circuits in major foundries [25], as well as some final process steps in fashioning magnetic writing heads for hard disk drive manufacturing [26]. The different FIB milling tools described here are geared towards more general research uses, however.

Dual beam systems combine FIB milling with scanning electron microscopy and, arguably, are the most widely used ion beam tool variants at the present time. This type of machine, illustrated in Figure 1.8 (a), has a vertically aligned electron column and an ion beam column mounted at an $\sim 50-55^\circ$ angle to the

sample plane, so that both of their axes converge onto the same spot. Therefore, such a configuration allows non-destructive SEM imaging of the sample and to conduct real-time monitoring of FIB processes. While many such dual beam tools are employed for semiconductor device inspection, the vast majority is used for preparing nanoscale < 100 nm thickness lamellas necessary for TEM imaging. For this reason dual beam systems are heavily specialized for that role – have Pt precursor syringes to perform local protective ion-induced metal sputtering over the sample surface, and are equipped with nanomanipulators for lamella extraction. The users for these FIB realizations prioritize system stability and a high level of automation, even at the expense of resolution and versatility, hence, exclusively Ga ion sources are used. Similarly, dual beam setups require the use of a 5 axis sample stage, which, even when piezoelectrically driven, does not have the requisite precision to scan over patterns larger than one write-field. Lastly, the equipment and software necessary for patterning in accordance to more complex design structures usually has to be acquired separately.

Dedicated FIB lithography systems, in essence, are the ion beam equivalent of an EBL machine, where tool design is largely the same apart form the charged particle column used. These are usually "single beam" realizations with a vertically mounted ion column and an interferometrically controlled 3 axis high precision piezoelectric stage. Taken together these features help to avoid various deleterious artifacts related to positional drift. Furthermore, the characteristics of all the electronic components are around one order of magnitude superior to those typically installed in SEM/FIB devices, which helps to further improve stability during extended exposures. Here, likewise, Ga ion sources are the most common, although recent developments have moved towards the wider acceptance of LMIS that support multiple ion species. It is well understood that implantation of metallic Ga can adversely affect the dielectric properties of devices fashioned by ion beams. The FIB lithography system depicted in Figure 1.8 (b) has an ion source that can select between Si, Ge and Au elements, where the fairly light Si is used for imaging and minimally destructive processing of silicon wafer based structures, heavy Ge is capable of rapid milling, whereas Au can enable surface functionalization. The main disadvantage of such a tool is its cost, as well as the generally destructive ion imaging. However, side-mounted SEM attachments are available for an additional cost even in dedicated FIB tools.

Gas field ionization source systems are the most expensive and technologically demanding realizations of ion beam lithography. Figure 1.8 (c) depicts the Zeiss ORION NanoFab system that uses He and Ne gas ion beams. The He ion beam exhibits some extraordinary properties – first of all it acts as a scanning microscope with subnanometer resolution and a depth of focus 5 to 10 times larger than that of a field emission SEM. Furthermore, as this ion microscope operates on positively charged ions, any charge accumulation effects can be

easily mitigated by using an electron flood gun. From a fabrication oriented point of view, He ion beams can be focused down to < 1 nm diameter spots, hence, single nanometer precision can be attained with relative ease [27]. Of course, all this comes at a high financial and functionality cost. Due to the small atomic mass of He, milling rates are extremely low, a drawback that can be somewhat mitigated by switching the system over to use a beam of heavier Ne ions, or by bringing to bear an auxiliary Ga LMIS column that can be installed as an option. Furthermore, implementation of gas field ionization sources for such high precision applications is very complex and fragile, as it relies on a ionization needle tip that is comprised of three and only three atoms arranged in a plane. When this atomic configuration spontaneously changes the system has to undergo long regeneration cycles, rendering it unusable for the duration. This tool is also based around a microscopy platform, hence, it does not possess a lithographic precision sample stage and is unable to perform adequate write-field alignment. Overall, the high complexity of such a system substantially lowers its reliability.

1.2.2 Ion beams and their interaction with matter

The substantial mass carried by ions greatly expands the range of effects that they can induce when irradiating a material. The most notable differences between electron and ion beam interactions with matter is that heavy particles are scattered and deflected much less and lose their energy through inelastic collisions much more rapidly, which, in conjunction, leads to a low ion penetration depth. For example, the penetration depth of 30 kV Ga^+ ions into a Si crystal is approximately 100 times lower than for electrons carrying the same

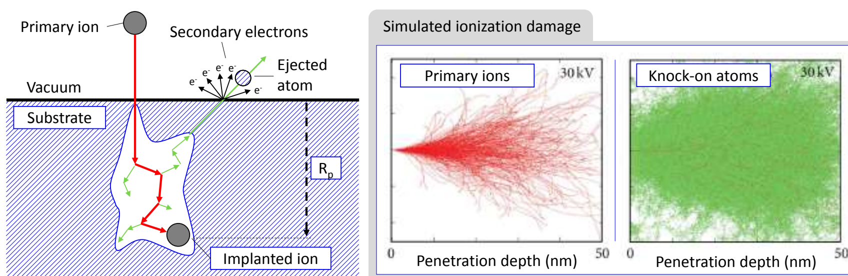

Figure 1.9: Left panel gives a simplified schematic illustration of the interactions between energetic ions and a substrate material. Thick red lines represent the trajectory of a primary ion, whereas thinner green ones correspond to trajectories of knock-on secondary atoms. The two pannels on the right show Monte Carlo simulated trajectories of 500 30 kV Ga^+ ions penetrating into bulk Si as well as those of knock-on Si atoms displaced from their lattice sites. Figure was adapted from the literature [11]

kinetic energy, *i.e.* $R_\mathrm{p}^\mathrm{i} = 50$ nm and $R_\mathrm{p}^\mathrm{e} = 5$ µm respectively. Furthermore, the amount of energy transferred from ions to atoms in the irradiated material is approximately three orders of magnitude larger than from electrons under equivalent conditions. Another important aspect is that ion beams are not subject to much back-scattering, hence, ion beam lithography does not exhibit a direct counterpart to the proximity effect in EBL.

The left side of Figure 1.9 depicts a simplified schematic summarizing the processes taking place when energetic ions bombard a solid state material surface. Quite unlike the low rate of energy loss occurring during electron irradiation, ion interactions with matter quite rapidly result in dissipation of kinetic energy over the course of numerous elastic collisions. When an energetic ion impacts a stationary atom it can, with relative ease, overcome its binding energy and cause its displacement from a lattice site. Furthermore, these knock-on atoms obtain sufficient kinetic energy to act as secondary projectiles that can start a displacement cascade, as shown in the right panels of Figure 1.9 which provide the Monte Carlo simulated trajectory comparisons of incident ions and the atoms that ended up being liberated as part of the chain reaction. It is evident that the surface layers of energetic ion irradiated materials are severely disrupted, eroded or amorphized mostly due to knock-on cascade effects [11]. More importantly, a fraction of the knock-on atoms can reach the material surface with enough kinetic energy to be ejected into the surrounding vacuum, which underlies FIB milling. Ion bombardment can also cause various inelastic processes, like the generation of secondary electrons that are used for imaging and real-time process feedback, as well as photon, X-ray or Cherenkov radiation emission, and even generation of plasmons. Lastly, if the ion does not get ejected out of the material in some way, it will remain implanted in the host lattice at some stochastically defined penetration depth R_p as either a defect or a dopant.

1.2.3 FIB lithography procedures

The wealth of phenomena that occur as a result of ion-matter interaction makes FIB rife with options that EBL lacks, however, their complexity does not allow for a concise summary from first principles. Here, to stay on-point, focused ion beam induced effects will be described purely from an application oriented view. In particular, most important uses of FIB for (i) resist exposure, (ii) direct milling, (iii) ion-induced etching and deposition, and (iv) local implantation and amorpization for direct mask writing will be described. Processes (i) and (iii) can also be performed using electron beams, however (ii) and (iv) are ion beam exclusive.

Resist exposure is the FIB lithography mode most akin to EBL, described in Section 1.1. However, the key difference between the masses of different charged particles makes patterning of beam-sensitive layers by FIB and EBL somewhat different. First of all, chemical changes in a resist film, be they

of bond dissociation or polymerization nature respectively for positive and negative resists, are not primarily induced by incident ions, but instead by secondary electrons generated during a collision cascade. Indeed, a single 5-50 kV ion and the knock-on atoms it displaced can on average generate around 200 secondary electrons, whereas a single electron can produce only 2. Hence, electron beam resists, such as PMMA, can likewise be patterned using ion beams. The high yield of ion-induced secondary electrons means that FIB patterning proceeds at around 100 times lower doses than for EBL, therefore, even low sensitivity resists like HSQ can be processed relatively rapidly. Also, for FIB resist patterning proximity effect related pattern distortions are generally less severe and not as far reaching as is the case in EBL, since ion-generated secondary electrons have insufficient available kinetic energy to propagate over microscale distances. Taken together the aforementioned features would put FIB among the highest resolution methods for resist layer patterning. For example, using the common PMMA resist and applying it by means of EBL identical substrate preparation steps, definition of features as small as 8 nm could be accomplished [28].

However, resist exposure using FIB is subject to several limitations that have hampered its wider adoption. First and foremost, the low penetration depth of ions prevents the use of resist films notably thicker than 50 nm, which is a severe restriction when performing either etching or lift-off mask transfer steps. Next, the enormous amounts of secondary electrons generated by massive ions results in the acceptable process dose range being quite narrow, and exceeding it even by a small margin results in rapid resist cross-linking and difficulties during its subsequent removal. Lastly, sample contamination by implanted ions in exposed regions can also turn out to be detrimental to device performance and is not always possible to eliminate. Many of these shortcomings can be addressed and mitigated through the use of more complex multilayer resist stacks, however, such additional complexity, and a lack of more substantial advantages with respect to EBL, has made resist pattering by FIB a largely neglected approach.

FIB milling is, by far, the most important and widely used ion beam lithography technique, both in this work and overall in the field of nanofabrication. The large amount of kinetic energy that massive ions can impart to atoms in a material during their elastic collisions is the critical feature of FIB that electron beams are unable to replicate. Therefore, direct nano/microscale engraving of various substrates is the primary niche that ion beam lithography solutions are specialized for. It is for this reason that most FIB columns support $5-50$ kV acceleration voltages, as this range provides ions with sufficient kinetic energy for the initiation of atom displacement cascades while ensuring a reasonably shallow affected depth that stays within ~ 10 nm of the surface. At higher acceleration voltages the effect of incident ions is not as well localized and is more suitable for implantation rather than sputtering applications.

As was touched upon in Section 1.2.2, FIB milling is predicated on the kinetic energy transfer from incident ions to lattice atoms during their elastic collisions. If the energy that an atom is imparted with exceeds a certain threshold it becomes displaced from its position in the lattice and an interstitial atom/vacancy pair is generated. Furthermore, if a knock-on atom has sufficient energy to displace its counterparts from other lattice sites, where bonding energies are usually in the 5-20 eV range, the process can continue as a chain reaction. While the energy of an incident atom is very high, only a tiny fraction of displaced atoms are able to reach the surface with sufficient energy to overcome the interfacial forces and sublimate into the surrounding vacuum. Regardless, the aggregate effect of a large flux of incident ions is to gradually erode any material it irradiates.

FIB milling allows for the routine direct engraving of complex patterns into a material surface with a 20 nm precision, and when He^+ is employed single nanometer precision similarly becomes routine. Furthermore, milling depth can be precisely controlled by simply changing the ion dose, which allows for the straightforward creation of complex grayscale surface patterns. One further advantage of FIB processing is that it is purely physical, hence, is not particularly selective with regards to the materials it can mill, nor does it require much in the way of surface preparation apart from grounding to minimize surface charging. Furthermore, ion beams have a large depth of focus, thus enabling milling of uneven surfaces with minimal distortion. All of these advantages make FIB systems popular for preparation of TEM lamellas, generating metamaterial patterns and plasmonic structures, as well as engraving of thin membranes.

On the other hand, FIB milling is subject to severe limitations as well, chief among them being its very low rate. As was mentioned previously, only a small subset of ion-displaced atoms are able to leave the substrate. The ratio of ejected substrate material atoms and incident ions is called the sputtering yield Y, and depends on the mass and energy of incoming charged particles, target material, as well as on the ion beam angle of incidence. For example, a single 30 keV Ga^+ ion on average removes 2.4 atoms of crystalline Si, however, under similar conditions the yield for Au can be up to 27 as gold is among the most easily milled materials [29]. Still the average yield factor among all materials when Ga^+ ions are used is close to $Y \approx 2$ [30]. The sensitivity of a material to ion beam milling is quantified as the volume sputtered by a unit charge $S[\mu m^3 nC^{-1}]$ [30]:

$$S = \frac{YM}{\rho N_A e}, \tag{1.8}$$

where Y is the aforementioned sputtering yield, M and ρ respectively correspond to atomic mass and density of the irradiated material, e is the electron charge, and N_A is Avogadro's number. Therefore, it becomes evident that, when

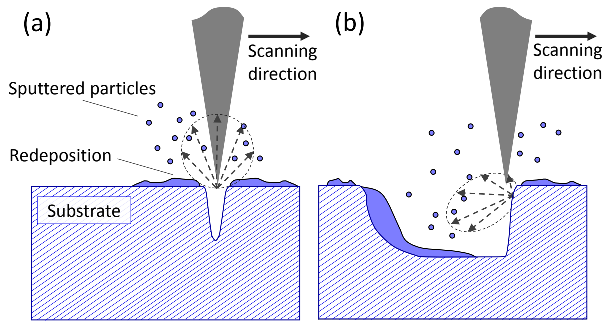

Figure 1.10: Schematic illustration of focused ion beam milling. (a) Symmetric case which represents either the initial stage of a more complex milling process or when a single hole is being drilled. It corresponds to a cosine-type exected atom flux angular distribution. (b) The effect of redeposition during prolonged milling of extended substrate areas. When the ion beam is incident at oblique angles to the surface normal sputtered atom flux angular distribution becomes asymmetric.

using presently practically feasible ion fluxes, FIB sputtering can, at best, only proceed at rates on the order of a few cubic microns per minute.

Further difficulties arise as a result of charge accumulation in the substrate over the course of ion bombardment, which can give rise to a multitude of drift effects as well as result in distortion of inscribed patterns. These issues can be eliminated or, at the very least, mitigated by grounding the substrate, using lower ion currents or, if all else fails, by coating the surface with a thin conductive layer (say, 5 – 10 nm of Au) or by using UV illumination [31]. Another more severe and largely unavoidable problem are ion-induced defects that can completely undermine the performance of functional materials, such as that of III-V semiconductor quantum wells or 2D electron gasses.

In order to give an adequate description of the principal limitations in the quality of structures attainable by way of FIB milling, special consideration must be given to the redeposition phenomenon. When ion beam incidence is normal to the surface plane of a substrate, propagation of sputtered atoms exhibits a cosine angular distribution illustrated in Figure 1.10 (a). In plain terms, this means that most sputtered atom trajectories are pointed backwards towards the ion source, whereas barely any particles are directed along the surface plane. In the simplest possible case of a single-pixel dot drilling FIB milling is a self limiting process, in which the deeper a beam penetrates into a material the larger the fraction of sputtered atoms that are redeposited onto the side walls of a hole. Hence, the rate of hole drilling gradually decreases along with its depth, until the point where redeposition and milling rates equalize, and terminates in a "V" shaped profile. For this reason, despite the microscale

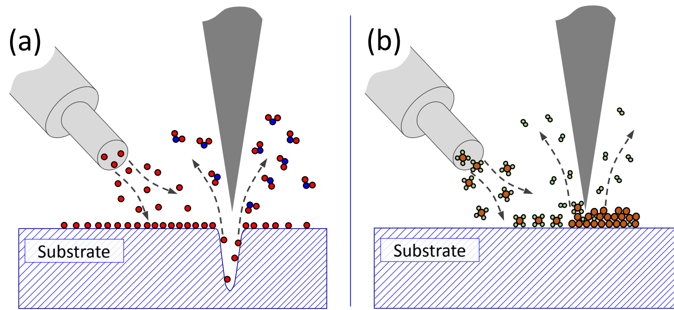

Figure 1.11: Schematic representations of gas assisted ion beam processing. (a) Chemically enhanced FIB milling. Gas molecules are adsorbed onto the substrate surface and react with displaced atoms thus forming volatile compounds. This increases the rate of milling and minimizes redeposition at the cost of decreased resolution. (b) Ion beam induced deposition. A gaseous precursor is dissociated by the secondary electrons generated during ion beam interaction with solid matter.

FIB depth of focus, in practice it is quite difficult to mill structures with depth-to-width aspect ratios notably higher than unity. Furthermore, redeposition can be detrimental not only when milling holes or narrow grooves, but even in the opposite case when defining extended area structures. The situation is schematically illustrated in Figure 1.10 (b), and represents the case when an ion beam is incident onto a surface at oblique angles, which is always the case when milling against a side-wall. Here, the angular distribution of liberated atoms is distorted from its previously mentioned cosine shape, and its maximum is no longer colinear to the ion beam. An evident result of such a shift is the redeposition of sputtered material onto previously milled areas. To combat this effect, ion beam patterning, unlike the single-pass exposures performed in EBL, is conducted over hundreds or thousands of incremental milling cycles over the same scanning area, whilst minimizing dwell time at any single point. However, the most effective way of minimizing redeposition involves the use of reactive gases that, when exposed to charged particle beams, react with the atoms of the target material to form volatile compounds.

Beam-induced etching and deposition adds a chemical aspect to the aforementioned physical kinetic energy transfer driven FIB sputtering, and leads to quantitatively or even qualitatively different process results. For instance, the redeposition effect occurs in large part due to the relatively small amount of kinetic energy, that ejected atoms posses, being insufficient to prevent it settling down close to the milled region. Thus, a reactive ion etching component was introduced to both increase the efficiency of material removal under FIB irradiation and to minimize redeposition [32]. It must be noted that etching and deposition can also be induced by electron beams, as the relevant chemical

reactions are mainly initiated by secondary electrons. Regardless of the incident charged particles, this process can be realized under high vacuum conditions by injecting process gasses through a capillary that is positioned close to where the beam impacts the sample surface by means of a micromanipulator, as illustrated in Figure 1.11 (a). For FIB in particular, a portion of these gaseous molecules are adsorbed onto the substrate and strongly react with sputtered atoms by forming volatile compounds. These products can then be rapidly removed by the vacuum system of the lithography tool, hence, are not likely to be redeposited. When reactive gasses with special affinity to the material of the surface and appropriate exposure conditions are selected, milling rate improvements of up to 10-100 and, furthermore, notably higher structure aspect ratios can be attained.

Of further note is that reactive gasses add selectivity to FIB milling. For instance, XeF_2 increases the removal rate of SiO_2 by approximately a factor of nine, however, does not change the milling rate of Al. For this reason, in addition to the overall increase in process rate, ion beam induced etching is quite popular for editing of microelectronic integrated circuits. However, injecting gasses into the ion beam path causes certain problems, such as implantation of reactive components into the substrate surface which may make materials incompatible with fabrication of certain devices. Furthermore, scattering of the ion beam by gas molecules tends to expand the attainable beam spot, thus reducing the attainable resolution.

Ion beam-induced deposition of materials relies on the same technical solutions as those used for ion beam-induced etching, namely the injection of certain precursor gasses through a capillary. However, in this case chemical

Table 1.1: Reactive etching gasses and deposition precursors used in the gas injection systems of commercially available FIB and EBL tools, as reported in the literature [33].

Etchant or precursor	Function
Water	carbon, resist etching
Xenon difluoride	silicon, silica etching
Chlorine	aluminum, silicon etching
Nitryl chloride	aluminum, silicon etching
Bromine	copper, titanium etching
Iodine	silicon, metal etching
Pentacene	carbon deposition
Tungsten carbonyl	tungsten deposition
Methylcyclopentadienyl-(trimethyl)Pt	platinum deposition
Dimethyl(acetylacetonate)gold	gold deposition
Tetramethoxysilane	silica deposition

reactions proceed in the opposite direction – gas molecules are dissociated by secondary electrons generated as a result of ion beam interaction with the sample material and the non-volatile reaction products are deposited onto the substrate, as sketched in Figure 1.11 (b). The precursor gasses have to exhibit strong adsorption to the substrate surface and, furthermore, have to undergo dissociation more rapidly than the FIB milling of the deposited products.

As a result, when performing ion beam-induced deposition care must be taken that the beam spot dwell time at each pixel is high enough to decompose all adsorbates, yet not sufficient to sputter away too much of the reaction product. Similarly, deposition of appreciable material volumes can only be obtained over numerous pattern scanning repetitions, separated by pauses that allow for replenishment of the adsorbed precursor molecule layer. Ion beam-induced deposition can generate both conductive (platinum, tungsten, carbon) as well as insulating (silica) materials. However, materials deposited in this way suffer from limited purity, as they tend to contain a notable fraction of beam ion and adventitious carbon contaminants. For instance, ion beam-deposited tungsten is made up of only $\sim 75\%$ W atoms, whereas platinum is comprised of an even more modest $\sim 42\%$ Pt. Contamination also results in a lower conductance of beam-deposited metals, still, regardless of said shortcomings, ion beam-induced deposition is quite useful for high-precission local re-welding of integrated circuits and provides FIB lithography with a lot of flexibility.

Surface modification is another FIB process feature that, for better or worse, cannot be replicated by electron beam systems. While in most situations ion implantation and material amorphization that occurs in the top ~ 10 nm layer of milled areas is considered to be a detrimental source of defects, there are a few applications where localized material modification can be quite useful. At the earliest stages of FIB technology development substantial efforts were dedicated into devising methods for fabricating complex integrated circuits by performing direct write localized doping of semiconductors. An exemplary realization of this principle was scanning ion beam implantation performed *in situ* inside a molecular beam epitaxy chamber, which allowed for the creation of 3D doped regions during the growth of GaAs as well as AlGaAs crystalline layers [34]. Despite the enormous potential of such a technique and the good quality of resultant structures, the Au-Si-Be dopant ion sources were incapable of charged particle beam fluxes sufficient for attaining an economically viable fabrication throughput. These initial setbacks largely halted the further development of scanning ion implantation using 100 – 200 kV acceleration columns.

More moderate $\sim$30 keV energy ions are stopped close to the material surface, as illustrated in Figure 1.9, and such shallow implantation is localized along all three dimensions. As an example, when a Si wafer surface is exposed to a small dose of Ga^+ ions, far below what would be required for pronounced milling, it becomes resistant to certain reactive ion plasma or wet chemical etching chemistries. Figure 1.12 provides an illustration of this effect in action.

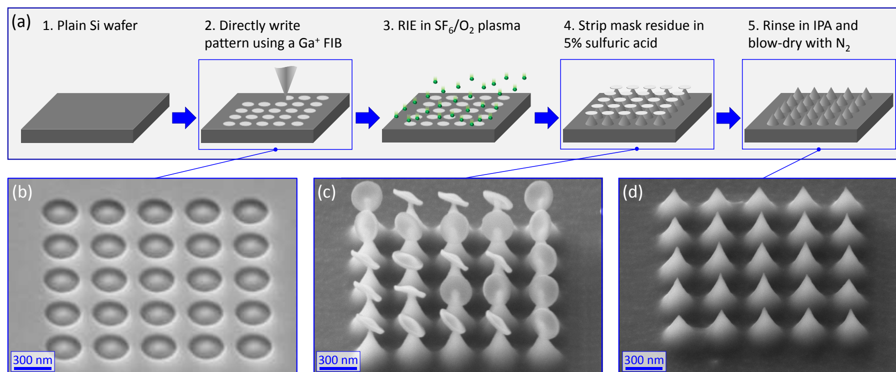

Figure 1.12: Lithographic fabrication of anti-reflective pattens by means of direct-write FIB definition of a negative tone mask on a Si substrate. (a) Sketch outlining the main fabrication steps, namely, Ga^+ ion beam scanning over a pre defined pattern, reactive ion etching in a SF_6/O_2 gas mixture plasma and chemical cleaning in dilute sulfuric acid to strip mask layer residues. Lower panels provide isometric SEM images illustrating the sequential step results after shallow Si wafer milling (b), after RIE etching (c), and the final cleaned structure (d).

Here, shallow FIB milling was performed to directly inscribe a lithographic mask pattern onto the crystalline silicon without any need to use resists or other substrate preparation steps. The modified nanoscale surface region was shown to be resistant to isotropic reactive ion etching in a SF_6/O_2 gas mixture plasma, used to perform pattern transfer and form submicron spikes suitable for anti-reflectance and bactericidal uses. The FIB modified material residues were subsequently stripped by sonication in a dilute sulfuric acid. In other words, this example follows the general lithography process outline provided in Section 1.1.3, only that here FIB was used to directly define a negative tone etching mask.

In addition to silicon, such resistless Ga^+ ion beam lithography was also demonstrated for chromium, diamond, and silica substrates. Furthermore, it was shown that etch resistance of the FIB patterned mask increases along with the exposure dose, however, its precise physical origin appears not to be settled quite yet [35]. Among feasible explanations of this phenomenon are implantation of Ga and Si surface amorphization, gallium oxide formation in ambient atmosphere, the formation of gallium fluorides during the etching process, or some combination thereof. Presently, this patterning method was shown to be capable of producing structures slightly smaller than 20 nm [35]. Still, the main advantage of such a lithography approach lies in its simplicity, however, has issues due to only moderate reproducibility during etching, hence, is unlikely to reach broader adoption apart from some niche research applications.

2 MICRO-RING PHOTONIC SENSORS

Optical sensors, with their broad range of photonic parameters such as absorbance, transmission, fluorescence, refractive index and polarization among others, represent a class of analytical tools capable of providing chemical information on analyte concentrations and reaction kinetics relevant in medical diagnosis, drug development, environmental monitoring and food quality control. A subset of such devices that rely on probing a defined local dielectric environment are known as refractive index (RI) sensors and encompass optical fibres, surface plasmon resonance setups, photonic crystals, interferometers and microcavity structures. Appropriate functionalization enables these devices to be used as label-free molecular sensors [36].

In particular, high quality factor resonant optical micro-cavity structures are becoming increasingly relevant due to their high sensitivity, resulting from the multiple-pass interactions between light and a respective analyte binding site, as well as miniaturization and integration potential afforded by wafer-scale semiconductor fabrication techniques. Specifically, waveguide-coupled single-mode micro-ring devices with subwavelength lateral dimensions are especially practicable in planar array geometries with large scale integration. While fabrication of micro-ring photonic structures has been demonstrated using a variety of materials such as glass [37], polymers [38], silicon nitride [39, 40] and plasmonic hybrid materials [41], silicon-on-insulator (SOI) has attracted significant attention, owing to its large refractive index value enabling resonators of an unprecedentedly small size, highly scalable and affordable manufacturing processes as well as compatibility with mature, hence, affordable telecommunications wavelength photonics technology [42, 43].

This chapter focuses on fabrication of novel micro-resonator designs in order to enhance the sensitivity and dynamic range of waveguide-coupled micro-ring resonator structures. The high resolution lithographic patterning capability of EBL enables rapid high precision prototyping of SOI resonators with control over feature sizes as small as 10 nm. It begins with a general overview of the operation principle of SOI-based telecommunications wavelength micro-ring resonator devices, which leads into the requirements and processes used for their fabrication. Lastly, two novel approaches for extending the performance label-free micro-ring chemical sensors, namely incorporation of gradient effective refractive index as well as dispersion engineering methods, are described using simulation and experimental findings.

2.1 Fundamentals of micro-cavity resonators

In general terms a ring resonator is comprised of a looped optical waveguide as well as a coupling mechanism to transfer optical energy into and out of the

loop. Ring resonators are a subset of a broader range of whispering gallery mode (WGM) microcavity devices, which confine optical energy in a higher refractive index dielectric material through internal reflection at a boundary with a lower refractive index medium. Provided that, after circumnavigating the edge of the microcavity, light is phase-matched to its point of optical insertion to interfere constructively a resonant mode is established. The resonance condition, therefore, can be expressed as a requirement that the optical path for any given mode must equal an integer number of wavelengths. For a circular cavity this condition can be stated as:

$$m\lambda_{\mathrm{r}} = 2\pi R n_{\mathrm{eff}}, \tag{2.1}$$

where m in an integer multiple of a resonant wavelength λ_r, R is the cavity radius and n_{eff} is the effective RI as sampled by the mode. Only light with wavelengths that match this constructive interference condition can be transferred into the cavity, typically from a tapered fiber or an adjacent waveguide, while all remaining non-resonant wavelengths bypass it altogether.

A resonant cavity only becomes useful as a device when it has the capability to collect and release energy, meaning that it is coupled to the surrounding environment. The most prevalent coupling mechanism uses codirectional evanescent coupling through a carefully matched submicrometer size gap between a resonator and an adjacent bus waveguide. This can be done either in horizontal side-by-side, as used in this work, or vertical arrangements.

In most cases WGM cavities made up of a continuous span of material, such as in the examples of spheres and disks, will support multiple radial order WGMs and therefore exhibit complicated multi-mode spectral characteristics. However, by adding an interior boundary and removing high-RI material from within the cavity where higher order modes would be localized, single mode operation can be obtained around the ring-like perimeter of the original structure. The single mode character of a micro-ring resonator comes at a cost of a decreased quality factor due to increased losses from surface scattering from the added interior boundary.

At the most fundamental level resonant cavity devices in general, and micro-ring resonators in particular, operate as temporary compressors of optical energy density and act as a spectral filter. As their planar nature is inherently compatible with monolithic lithographic fabrication technologies, waveguide-coupled micro-ring resonators show great promise as fundamental building blocks for a staggering variety photonic applications, such as spectral filters, optical switches and routers, delay lines, sensors, as well as lasers, among others. Furthermore, the intensity buildup in a micro-ring resonator gives rise to high power densities at modest overall power, this in turn lends itself as a convenient platform for the investigation of nonlinear optical effects, especially when Si photonic wires are used [44, 45].

2.1.1 Coupling and spectral characteristics

In its most basic form a micro-ring resonator device is composed of a closed waveguide loop coupled to a single adjacent input/output waveguide – the all-pass filter configuration sketched in Figure 2.1 (a). The spectral properties of an all-pass micro-ring can be calculated by assuming continuous wave operation and matched fields. In principle the calculation is conducted on a directional coupler section with one of the outputs connected back into its input thereby forming a feedback loop. The incident E_{in}, transmitted E_{out} as well as circulating fields E_3 and E_4 are related *via* the following unitary matrix [46]:

$$\begin{pmatrix} E_4(\omega) \\ E_{\text{out}}(\omega) \end{pmatrix} = \begin{pmatrix} r & ik \\ ik & r \end{pmatrix} \begin{pmatrix} E_3(\omega) \\ E_{\text{in}}(\omega) \end{pmatrix}, \tag{2.2}$$

where r and k respectively are the lumped self- and cross-coupling coefficients, considered to be frequency independent and to satisfy the condition $r^2 + k^2 = 1$, which effectively assumes that there are no losses in the coupling section (r^2 and k^2 are the power splitting ratios). The output from port 4 is connected back into the input port 3 *via* the $L = 2\pi R$ length feedback loop, hence, the relationship between the circulating fields is expressed as:

$$E_3 = e^{-\frac{\alpha}{2}L} e^{ikL} E_4 \equiv a e^{i\phi} E_4. \tag{2.3}$$

where α is the power attenuation coefficient incorporated into the single-pass amplitude transmission a, which includes both propagation loss during the round trip as well as loss in the coupling section. Similarly, the single-pass phase shift is denoted by ϕ and is related to the mode frequency as $\phi = \omega t_{\text{r}}$, where t_{r} is the round-trip transit time. Therefore, ϕ represents normalized frequency detuning.

As mentioned previously, ring resonators are capable of temporary storing optical energy within themselves. In practice this means that, provided a coherent pumping source is used, through constructive interference in the coupling section, the optical energy density circulating in the ring cavity can be built up to significantly exceed what was injected at the input port. On the other hand, if a perfectly incoherent excitation source is used and losses can be neglected, the intensity inside the resonator becomes equal to the incident intensity.

The ratio of the optical field E_3 circulating in the ring and the incident field E_{in} can be obtained by solving Equations 2.2 and 2.3:

$$\frac{E_3}{E_{\text{in}}} = \frac{ita e^{i\phi}}{1 - ra e^{i\phi}}. \tag{2.4}$$

By taking the squared modulus of this result the intensity ratio, otherwise known as the buildup factor B, can be calculated:

$$B = \frac{I_3}{I_{\text{in}}} = \left| \frac{E_3}{E_{\text{in}}} \right|^2 = \frac{(1 - r^2)a^2}{1 - 2ra\cos\phi + r^2 a^2} \xrightarrow[\phi = m2\pi, a=1]{} \frac{1+r}{1-r} \approx \frac{4}{k^2}, \tag{2.5}$$

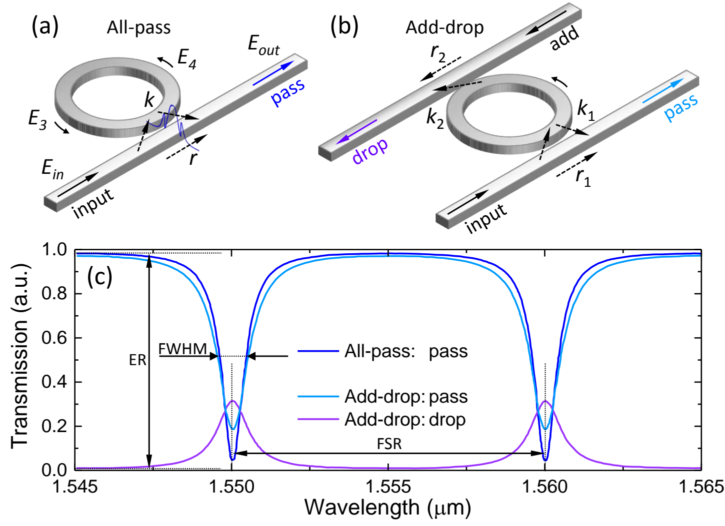

Figure 2.1: Schematic representation of micro-ring resonators in (a) all-pass and (b) add-drop coupling configurations. Solid arrows indicate traveling wave propagation directions whereas dashed-arrows illustrate radiation coupling. (c) A representative transmission spectrum of a single mode all-pass micro-ring, as well as of the two outputs of an add-drop device. The most important spectral parameters, such as the extinction ratio (ER), free-spectral range (FSR) and full-width at half-maximum (FWHM), are illustrated.

where the latter expression is valid when light is resonant with the ring and absorption losses can be disregarded. This result shows that light intensity in a ring resonator can be tens-of-times higher than what was injected in the input port, which is beneficial when nonlinear effects are desirable.

Similarly, Equations 2.2 and 2.3 can also be solved to obtain the ratio of incident and transmitted field in the bus waveguide:

$$\frac{E_{\text{out}}}{E_{\text{in}}} = e^{i(\pi+\phi)} \frac{a - re^{-i\phi}}{1 - rae^{i\phi}}, \tag{2.6}$$

as well as the intensity transmission given by the squared modulus:

$$T = \frac{I_{\text{out}}}{I_{\text{in}}} = \left|\frac{E_{\text{out}}}{E_{\text{in}}}\right|^2 = \frac{a^2 - 2ra\cos\phi + r^2}{1 - a^2 - 2ra\cos\phi + (ra)^2}. \tag{2.7}$$

As can be seen from equation 2.7, for negligible attenuation $a \approx 1$ the device allows complete transmission for all frequencies, therefore no change in amplitude would be observed in the output. However, the phase shift φ would vary drastically for frequencies close to the resonance condition, as given by

the equation [47]:

$$\varphi = \pi + \phi + \arctan\frac{r\sin\phi}{a - r\cos\phi} + \arctan\frac{ra\sin\phi}{1 - ra\cos\phi}. \tag{2.8}$$

In practical situations losses are always present, therefore, in particular near resonance, transmission dips appear. When power coupled into the resonator equals the power lost during one round trip ($1 - a^2 = k^2$ or $r = a$) the device is considered to be in critical coupling and the transmission at resonance drops to zero. The conventional mode of operation for a micro-ring resonator based sensing device is at slight overcoupling, but as close to critical coupling as is reasonably achievable.

When a ring resonator is coupled to two waveguides, as is shown in Figure 2.1 (b) it behaves like a narrow-band amplitude filter that can add or drop a frequency band from an incoming signal, which is where the name add-drop filter comes from. While transmission to the pass and drop ports could again be calculated by applying the same methods as in the previous all-pass ring case, as this micro-ring resonator coupling setup is mathematically equivalent to the classic Fabry-Perot interferometer the expressions are simply stated [46]:

$$T_{\text{pass}} = \frac{I_{\text{pass}}}{I_{in}} = \frac{r_2^2 a^2 - 2r_1 r_2 a\cos\phi + r_1^2}{1 - 2r_1 r_2 a\cos\phi + (r_1 r_2 a)^2}, \tag{2.9}$$

$$T_{\text{drop}} = \frac{I_{\text{drop}}}{I_{\text{in}}} = \frac{(1 - r_1^2)(1 - r_2^2)a}{1 - 2r_1 r_2 a\cos\phi + (r_1 r_2 a)^2}. \tag{2.10}$$

Unlike in the all-pass case, when attenuation is insignificant at $a \approx 1$, critical coupling is obtained if coupling is symmetrical $k_1 = k_2$. Conversely, for a lossy resonator critical coupling occurs when coupling is set to match the losses according to $r_2 a = r_1$ [47].

In a typical optical sensing setup employing an add-drop ring, one of the waveguides is used for pumping, and may also be probed at the pass port, whereas the second waveguide is viewed as a "tap" waveguide , constantly leaking energy from the micro-ring resonator, hence, can be considered equivalent to other sources of loss. It is preferable for an add-drop ring to operate at critical coupling. While the add-drop filter also exhibits similarly strong phase shifts at the two output ports, as is observed for an all-pass configuration, the dominant amplitude effects mean that it is rarely implemented for purely phase control purposes.

Another interesting aspect of an add-drop configuration is the way in which optical energy is accumulated inside the cavity. The buildup factor is in this case given by [46]:

$$B = \frac{I_3}{I_{\text{in}}} = \left|\frac{E_3}{E_{\text{in}}}\right|^2 = \frac{(1 - r_1^2) r_2^2 a^2}{1 - 2r_1 r_2 a\cos\phi + (r_1 r_2 a)^2} \xrightarrow[a=1, r_1=r_2=r]{\phi=m2\pi} \frac{r^2}{1 - r^2} \approx \frac{1}{k^2},$$

(2.11)

where the last result was obtained assuming negligible attenuation ($a = 1$), balanced critical coupling ($r_1 = r_2$), as well as resonant excitation ($\phi = m2\pi$). When comparing to the buildup factor expression obtained for the all-pass ring (last term in Equation 2.5) it becomes evident that the intensity buildup is 4 times lower in the add-drop configuration at the same coupling strength.

Fragments of typical throughput transmission spectra for both all-pass and add-drop configurations exhibiting the usual Lorentzian lineshape are illustrated in Figure 2.1 (c). Several parameters can be used to characterize the spectral behavior of a resonant cavity without any particular consideration of its structural of realization details.

Quality factor Q is the most often invoked parameter when describing resonators. It is used to characterize the rate of energy loss in a cavity and is typically expressed as a measure of the sharpness of a given resonance in relation to its central frequency. Its formal definition, within a factor of 2π, is the ratio between the total energy stored in the resonator and the energy lost in an optical cycle, which is shown to be roughly equivalent to a resonance frequency-to-bandwidth ratio:

$$Q = 2\pi \frac{\text{stored energy}}{\text{energy dissipated per cycle}} \approx \frac{\omega}{\Delta\omega} \approx \frac{\lambda}{\text{FWHM}}. \tag{2.12}$$

The rate of energy loss in waveguide-coupled resonators results from intrinsic light scattering, radiation loss and absorption, as described further on in Section 2.1.2, as well as extrinsic output coupling loss *via* adjacent waveguides. Therefore, the total Q factor is expressed as $Q^{-1} = Q_0^{-1} + Q_c^{-1}$, where the intrinsic Q_0 and coupling Q_c quality factors are evaluated as follows:

$$Q_0 = \frac{\omega_0 t_r}{\alpha L}; \quad Q_c = \frac{\omega_0 t_r}{k^2}. \tag{2.13}$$

The expression for Q_0 suggests that better quality factors can be obtained for long round trips and low cavity losses, but this relation is more complex than would appear at first glance, since both these terms share a dependence on cavity length L. However, in practice high-Q ring resonators tend to have longer cavities. For most sensing applications it is desirable to extend the number of optical cycles that light is able to interact with the analyte for maximum sensitivity. Therefore, high quality factor sensing devices are vigorously pursued.

Free-spectral range (FSR) is the spectral separation of successive resonances. If the resonance condition is expressed as $\omega t_r = m2\pi$, where t_r is the round-trip time and m is an integer, the FSR is given by:

$$FSR = \omega_2 - \omega_1 = \frac{2\pi}{t_\mathrm{r}} = \frac{2\pi c}{L n_\mathrm{g}} \equiv \lambda_2 - \lambda_1 = \frac{\lambda^2}{L n_\mathrm{g}}, \tag{2.14}$$

where n_g is the group index, which takes into account the dispersion of the waveguide and is defined as:

$$n_\mathrm{g} = n_\mathrm{eff} - \lambda \frac{\mathrm{d}n_\mathrm{eff}}{\mathrm{d}\lambda}. \tag{2.15}$$

In most RI sensing applications it is preferable to have a large FSR as it directly corresponds to the largest resonance lineshift that can be unambiguously determined. In most situations analyte concentrations vary widely both from one sample to the next and also among different analytes in the same sample. Therefore, large FSR devices would be useful for applications involving extreme RI shifts, such as those requiring sensing in both liquid and gas environments.

Finesse $\mathscr{F}$ is a convenient measure of the sharpness of the resonances in relation to their spacings. It is defined as the ratio of FSR and resonance width:

$$\mathscr{F} = \frac{\mathrm{FSR}}{\mathrm{FWHM}} = \frac{2\pi c}{L n_\mathrm{g}} \frac{1}{\frac{c\alpha}{n_\mathrm{g}}} = \frac{2\pi}{\alpha L}. \tag{2.16}$$

The physical meaning behind finesse can be elucidated by considering how many round-trips N it would take to reduce the energy to $1/e$ of its initial value [46]:

$$\exp(\alpha N L) = \frac{1}{e} \Rightarrow N = \frac{1}{\alpha L} \Rightarrow \mathscr{F} = 2\pi N. \tag{2.17}$$

Hence, finesse within a factor of 2π is equivalent to the number of round-trips light makes in the ring before being dissipated to $1/e$ of its intensity. Similarly, the definition of the quality factor can be given in the same form:

$$Q = \omega t_\mathrm{r} N, \tag{2.18}$$

which means that Q denotes the number of optical field oscillations it takes to deplete the energy in the cavity to $1/e$ of its initial value. Therefore, finesse $\mathscr{F}$ and quality factor Q respectively characterize the intensity buildup and the effective interaction time, as can be seen by their relation to the buildup factor for all-pass and add-drop coupling schemes:

$$\frac{\pi}{2} B_\mathrm{all-pass} = \mathscr{F} = \frac{Q}{m} \tag{2.19}$$

$$\pi B_\mathrm{add-drop} = \mathscr{F} = \frac{Q}{m}. \tag{2.20}$$

Light interacts with the coupling interface for a finesse number of times while interacting with the cavity interior for a Q number of cycles. Therefore, in order to devise an enhanced microresonator-based sensor operating on the

variation of a distributed optical property such as RI, it is preferable to make the cavity both high-Q and high-$\mathscr{F}$. Assuming combined propagation losses of 2.7 dB/cm, typical for a Si waveguide with air cladding fabricated by means of the Interuniversity Microelectronics Center (IMEC) process [48], the highest attainable Q-factor in the all-pass configuration would be $Q \approx 1.42 \cdot 10^5$ on a ring with $R \approx 1.6$ mm. An add-drop resonator could reach a slightly lower value of $Q \approx 1.36 \cdot 10^5$ at an increased ring radius of $R \approx 2$ mm [47]. However, a compromise needs to be made, since a longer round-trip length yields a lower finesse.

2.1.2 Silicon micro-ring loss mechanisms

Optical loss mechanisms in Si waveguide-coupled micro-resonators can broadly be classified into three groups: radiation loss (closely related to waveguide bend loss), propagation loss and losses in the coupling section [49]. Here a brief description of these mechanisms in the context of SOI micro-ring resonators is given.

Radiation loss poses the fundamental quality factor limit for any WGM cavity as it is dictated by the refractive index contrast associated with the choice of materials. Any curved open boundary WGM configuration will inherently leak energy from azimuthally guided modes into radially outward propagating radiation *via* tunnelling from a radial potential well (m/nr), where m denotes the number of effective wavelengths the field undergoes in space when completing one revolution around the cavity, that can also be expressed as an effective

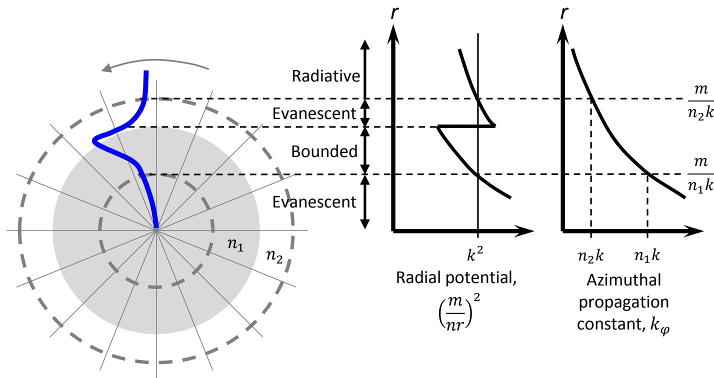

Figure 2.2: Schematic representation of the radial potential well which confines a WGM. The circulating power is confined between an inner caustic and the disk edge. At the outer radiation boundary the azimuthal phase velocity becomes is equal to the phase velocity in the surrounding medium. Beyond this radius, the fields cannot keep up and thus propagate into free space [46].

radial index n_r:

$$n_{\mathrm{r}} = \sqrt{n^2 - \frac{m^2}{k_0^2 r^2}}. \quad (2.21)$$

The mode is bounded on the inner caustic of the bend $R_1 = \frac{m}{n_1 k}$ below which the "optical inertia" is too large, and by an outer boundary $R_2 = \frac{m}{n_2 k}$ beyond which the azimuthal phase velocity would exceed the speed of light in vacuum. The radial potential well for a WGM is depicted in Figure 2.2 along with the regions where fields of the mode are bound, evanescent and outward propagating. Therefore, the radiation loss associated with WGM devices can be viewed as tunneling through a potential barrier defined by the resonator edge and radiation boundary, beyond which the evanescent tail of the field becomes propagating again.

Bend losses in waveguide sections occur due to the same tunneling phenomenon, albeit expressed by way of a more thorough mathematical treatment [50–52], in which the barrier width decreases with increasing curvature. This in effect, depending on the RI contrast, prescribes a minimum bend radius for either a waveguide section or a resonator loop. However, since most semiconductor waveguides have a refractive index $n > 3$, minimum bend radii < 1 µm can be used, although this leads to an enhanced influence of other loss mechanisms, such as scattering from sidewall roughness and leakage into the substrate, and in practice bending losses are rarely dominant.

Scattering or contradirectional coupling losses due to edge roughness is typically the leading cause of losses for most single-mode SOI waveguides. It becomes especially significant when reactive ion etching is used during fabrication. Also, compared to a microdisk cavity with a single outer wall, micro-ring resonators with both inner and outer sidewalls can be particularly severely affected. Sidewall roughness losses can manifest themselves as either backscattering that may give rise to counterpropagating modes and mode splitting, or light being scattered out of the device altogether [53]. Even the use of high resolution EBL based patterning techniques can give rise to semi-periodic surface roughness related to the step size of the scanning electron beam [54]. In addition to optimization of the resist exposure and dry etching fabrication processes, certain post-fabrication treatment methods, such as thermal reflow [55] as well as oxidation of a ~ 10 nm layer of Si with subsequent oxide removal [56] are known to decrease sidewall roughness and the associated propagation losses.

Scattering loss in the coupler gap spacing inevitably results from the perturbation and symmetry breaking introduced by the adjacent waveguide. This often leads to contradirectional coupling and mode splitting [57]. Furthermore, any fabrication imperfections or roughness may introduce additional scattering losses.

Leakage to the substrate can be quite significant for sub-micrometer SOI photonic structures due to the mode getting squeezed out of the core and

overlapping with the surrounding material, as can be seen in Figure 2.4. This leakage can be mitigated by undercutting the underlying SiO_2 by wet chemical etching in HF, as has been shown for undercut high quality factor $Q = 5 \cdot 10^6$ micro-disk resonators [58].

Absorption losses are another contribution to the overall dissipation of a propagating wave. It encompasses linear sub-band gap absorption at the surface states of device sidewalls, at defect states in the silicon bulk, as well as absorption by free carriers generated *via* the two previous absorption mechanisms. Furthermore, at telecom wavelengths nonlinear two photon absorption can become significant in the resonator cavity as energy is built up, due to its rate scaling quadratically with intensity. This, in turn, also generates free carriers which further contribute to absorption. In addition to propagation losses, free carrier absorption results in heating of the device and the associated deleterious drift in its parameters. Especially in micro-resonators the thermal effects can become dominant. Typical methods to curb absorption losses involve using high purity SOI substrates as well as various surface passivation methods.

2.1.3 Micro-ring resonators in sensing

As becomes evident when considering Equation 2.1, the resonance spectral position is determined by the optical round-trip length in the micro-ring, while the resonance lineshape is mostly affected by the total accumulated loss. As a result of the combined effects of intensity buildup and the multi-pass light-matter interaction that occur as electromagnetic energy circulates in the ring, the device is very sensitive to a multitude of environmental factors. This can be more clearly stated in relative terms as:

$$\frac{\Delta\lambda_r}{\lambda_r} = \frac{\Delta R}{R} + \frac{\Delta n_{\text{eff}}}{n_{\text{eff}}}. \tag{2.22}$$

where it is clear that any variation of the device geometrical parameters (represented by the ring radius R) and, more importantly, in the dielectric properties of volume regions sampled by the mode (accounted for by the effective refractive index n_{eff}) result in a relative shift of the resonance wavelength λ_r. Hence, the change in resonant wavelength and not the resonant wavelength value itself is the relevant parameter for sensing with waveguide-coupled micro-ring resonators.

Waveguide-coupled micro-ring resonator based sensing devices are label-free, meaning, that thy do not rely on labelling of the analytes to prime them for detection. However, to gain specificity vital for bio-sensing the surface of the device itself has to be functionalized with capture agents selective for certain molecules [36], with the general operational principle sketched in Figure 2.3. In this context it is instructive consider the changes in effective RI n_{eff} as encompassing contributions from a homogeneous surface molecular layer of mass $M = \rho St$ (where S is the sensing area, t is layer thickness and ρ is the

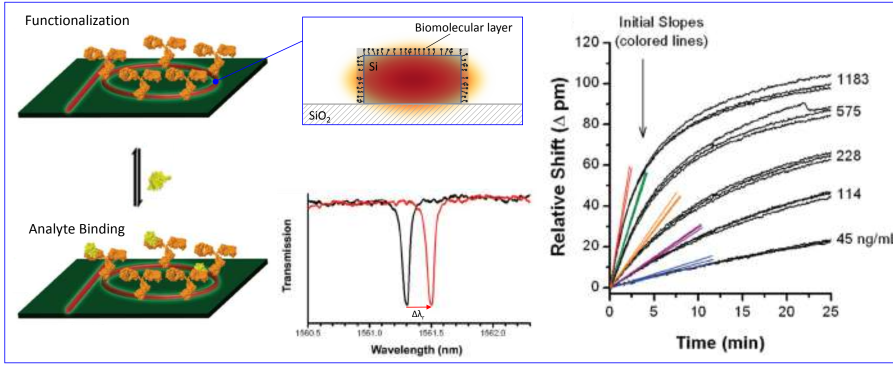

Figure 2.3: Label-free biosensing using micro-ring resonators [59]. Silicon waveguide surface is functionalized using biomolecules with affinity to specific analyte species. Inset shows how evanescent portions of the waveguided mode sample the immediate environment of the SOI structure. Any change in the RI of the surrounding environment results in a resonance peak shift, as illustrated in the lower-midle panel, which can be used to detect the concentration of analytes, as shown in the plot on the right.

mass density) and from the bulk RI changes in the surrounding medium, which respectively can be expressed as detection thresholds [42]:

$$\Delta M_{\text{min}} = \rho S \frac{m}{L} \left(\frac{\partial n_{\text{eff}}}{\partial n_{\text{bulk}}} \right)^{-1} \Delta \lambda_{\text{min}} \tag{2.23}$$

$$\Delta n_{\text{min}} = \frac{m}{L} \left(\frac{\partial n_{\text{eff}}}{\partial t} \right)^{-1} \Delta \lambda_{\text{min}}. \tag{2.24}$$

As can be deduced based on Equation 2.1, for a given wavelength band the ratio m/L is invariant due to the fact that mode order scales with the micro-ring round-trip length. Therefore, as is evident from Equation 2.24, device sensitivity to bulk RI changes does not depend on device size, however, according to Equation 2.23 the smallest detectable mass variation covering the surface does scale with area. Based on this there is strong incentive to pursue miniaturization of micro-resonator sensing devices, as it enables the detection of minuscule amounts of analyte molecules, with ΔM_{min} values ranging from 40 ag to 125 ag [60–62].

The aforementioned small detection thresholds rely on the ability to measure tiny shifts in the resonance wavelength, which is in turn is aided by spectrally narrow resonances. Therefore, high-Q microcavities are required not only to maximize sensitivity, but also to obtain low detection limits. However, in order to make the most use out of a high-Q microcavity resonance wavelength shifts

as low as $\Delta\lambda_{\text{min}} = 0.01$ pm may need to be measured. For this reason the ability to control or compensate for spectroscopic noise and thermal effects is often just as important as obtaining a high cavity Q factor.

When guided modes are used for probing their immediate dielectric environment, only the electromagnetic field fraction that is evanescent at the device surface, meaning that it extends into the surrounding medium whilst decaying exponentially with distance, contributes to the signal, as sketched in top-middle inset of Figure 2.3. The device response scales with the optical field intensity in the sensing region, therefore, with the fraction of modal power extending into said region [63]. The most straightforward way to force mode delocalization is to decrease the waveguide core dimensions, as can be seen in Figure 2.4, at the cost of increased losses and a decrease in surface specificity. As an example, slot waveguides, made up of two parallel thin SOI waveguide strips separated by a 90 nm gap, can increase the fraction of optical energy in the sensing volume up to 80 %, accompanied by a deleterious drop in the quality factor of such a resonator [64]. Furthermore, recently, novel designs of micro-rings with subwavelength perforations were shown to increase the light–matter interaction as well as the sensitivity [65].

Planar SOI waveguide structures exhibit a high refractive index contrast, which enables the localization of light within volumes of subwavelength dimensions as well as the production of exceedingly compact integrated optical devices. Silicon exhibits low attenuation for propagating electromagnetic radiation at $\lambda \simeq 1560$ nm, and highly miniaturized waveguide-coupled micro-rings with bend radii below 5 µm, thereby can be made with minimal radiation loss. Here, miniaturization has the benefit of both, extending the free spectral range as well as the finesse of the resonator, whilst not significantly compromising the attainable quality factors. Conversely, in the context of micro-ring sensing structures, their resonant modes can have a strong sensitivity to variations and refractive index changes in external environment, observed through wavelength shifts as described in the previous section, which scale with the decrease in surface area, meaning that fewer analyte molecules are needed to enact the same effect [42]. In addition, considering the auxiliary benefits of compatibility with prevalent telecommunications photonics as well as with CMOS wafer-scale manufacturing methods, planar waveguide-coupled micro-ring resonator devices offer high sensitivity on a large scale and at competitive cost.

The need to comply with a single mode waveguiding condition is an additional factor that forces miniaturization of components. To this end, settling on a desired mode intensity profile, by appropriately selecting the geometric parameters of the waveguide as well as by the refractive indices making up the core

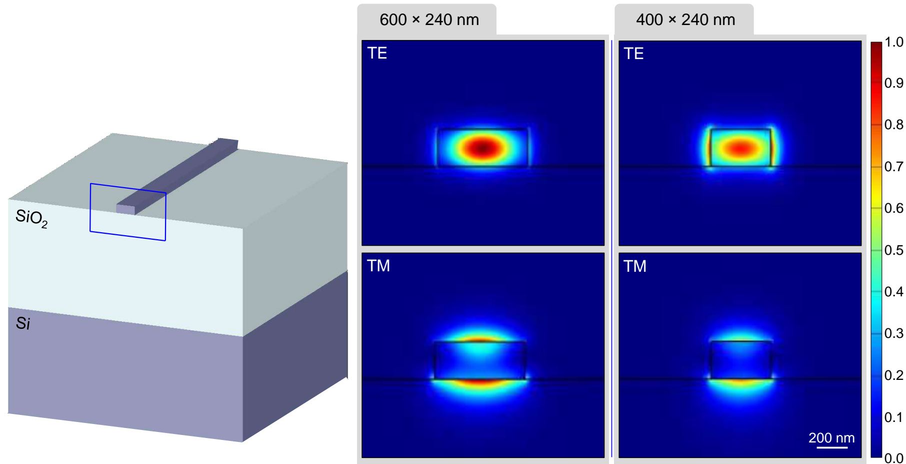

Figure 2.4: Visualization of a SOI strip waveguide that is the fundamental building block of most waveguide-coupled resonator devices considered in this work. Panels on the right depict the spatial intensity profiles of the fundamental TE and TM modes of waveguides with, respectively, 600×220 nm^2 and 400×220 nm^2 dimensions.

and cladding, is usually the first step in designing a confined radiation device. For the purposes of this work finite difference eigenmode (FDE) simulation methods were used to solve the Maxwell's equations on a 2D finite-difference algorithm-meshed cross-section of the waveguide to obtain the spatial profile and frequency dependence of modes. The solutions are obtained by first formulating the equations as a matrix eigenvalue problem and then solved using sparse matrix techniques [66]. This method also yields the values for effective refractive index as well as gives evaluations of the intrinsic and waveguide bend-related losses.

Typical FDE simulation results for the fundamental transverse electric (TE) and transverse magnetic (TM) modes of simple single mode SOI strip waveguides are displayed in Figure 2.4. From this example it is clear how the ground state TE mode ($n_{\text{eff}} \approx 2.19$) is significantly more strongly confined than the TM one ($n_{\text{eff}} \approx 1.63$). Since the TE mode is capable of sharper waveguide bends and is compatible with planar couplers, waveguide-coupled resonator devices considered in this work, like in most other cases reported in the literature, were designed to be driven by it. However, in some situations where losses need to be avoided the TM mode is used due to its negligible overlap with the often rough sidewalls and thereby minimizing scattering and backscattering effects [58].

Typically SOI micro-ring resonator structures require the waveguide dimensions to range between 300 nm and 600 nm in width and between 100 nm and 300 nm in height [47, 49]. It is also noteworthy that as the width of the strip is decreased the mode becomes more delocalized. This means stronger attenuation due to the aforementioned scattering from sidewalls, however, it has the advantage of stronger coupling to other waveguides as well as to the surrounding environment for sensing purposes. Here, as a compromise of such conflicting demands, the 400×220 nm^2 SOI strip waveguide was chosen to be used as the building block to construct the various functional components.

The notably submicron scale of even the most basic of components, however, reveals the downside of SOI photonics, where the substantial degree of optical energy localization in high refractive index Si requires the downsizing of functional components by a corresponding factor. Further sensing application-specific complications are introduced by the aforementioned mode delocalization derived increase in sensitivity to scattering from component surface roughness as well as any manufacturing imperfections down to $5-10$ nm in size. Therefore, only a select few high-resolution fabrication methods, namely deep ultraviolet (UV) optical projection or electron beam lithography, are capable of the nanoscale precision required for manufacturing high performance waveguide-coupled resonator structures for sensing, hence, are discussed and contrasted next.

2.2.1 Comparison of EBL and UV lithography

The default industrial approach for manufacturing integrated photonic circuits on the SOI platform is the complimentary metal-oxide-semiconductor (CMOS) projection lithography fabrication at deep UV wavelengths, which in the past decade have stepwise shifted from $\lambda = 248$ nm down to 193 nm, and the lowest achievable device critical dimensions (tied to the wavelength and the numerical aperture of the projection system according to the relationship $a_{min} = \lambda/NA$) have in turn decreased accordingly [48]. Due to SOI being compatible with CMOS in terms of materials and processing chemistry, most of such photonic structures can be made on industrial tools used in 130 and 90 nm CMOS microelectronics technology nodes. Consequently, large scale wafer-sized lithographic methods for the fabrication of planar photonic integrated circuits provide a multitude of benefits which previously led to the success of microelectronics, such as high compaction, increased reliability and a dramatic reduction in cost. Furthermore, integrated photonic circuits eliminate the need for subcomponent mechanical alignment steps, which tend to dominate the manufacturing costs of devices composed from discrete optoelectronic elements.

A good example of CMOS technology effectively used for the fabrication of SOI integrated photonic circuits is the IMEC process tailored to pattern SOI wafers with 220 nm-thick top Si layers. The process involves mask projection using $\lambda = 193$ nm deep UV radiation on a photoresist coated and soft-baked SOI wafer. Subsequently, following post-exposure bake and development steps, the exposed pattern is transferred onto the wafer using inductive coupled plasma RIE. Three etching stages, corresponding to $1/3$ and $2/3$ fractions as well as the full depth, can be defined, with overlay alignment accuracy below 20 nm. This process yields $400-500$ nm wide Si nanophotonic waveguides with exceptionally low propagation losses that fall under 2.7 dB/cm [67].

However, despite numerous advantages in terms of cost, reproducibility and waveguide quality, projection lithography approaches have significant shortcomings when it comes to fidelity. Figure 2.5 compares some select SOI photonic components fabricated using the IMEC deep UV process to similar structures created using EBL. Due to the spatial low-pass filter effect of the optical system and the associated loss of higher diffraction orders, blurring of the fine protrusions in Figure 2.5 (a), severe corner rounding for gradient refractive index micro-ring shown in Figure 2.5 (b), and the complete failure to define high aspect ratio features in Figure 2.5 (c) results. Furthermore, fabrication of dense photonic crystal structures poses significant challenges, such as limiting the hole diameters to ~ 160 nm and thus requiring completely separate design approaches, as well as necessitating complex design mask biasing to compensate for optical proximity effects, as can be seen in Figure 2.5 (d). Unlike CMOS components in microelectronics, which are layered structures

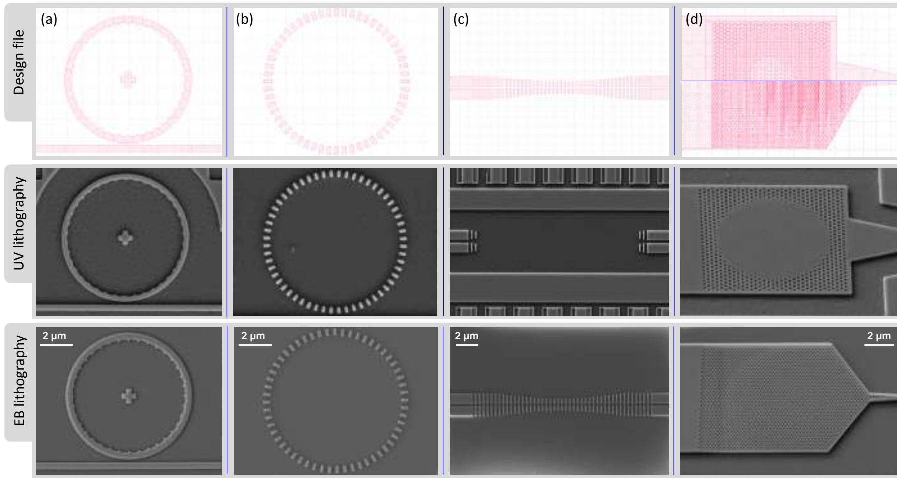

Figure 2.5: Comparison of select elements in SOI photonic circuits, with top row depicting the element as designed, middle row shows SEM images of these elements fabricated using the IMEC deep UV lithography process, and the bottom row shows identical features fabricated using EBL. (a) Optical vortex emitter based on a ring resonator patterned with a second order Bragg grating [68]. (b) Ring resonator with a radial effective refractive index gradient. (c) 1D photonic crystal cavity sensor [69]. (d) Photonic crystal coupler device.

and process conditions can be fine tuned for each layer separately, planar nanophotonic elements are all created on the same level and tight tolerances for alignment discourage the use of multiple lithography steps. Hence, fabricating disparate structures, such as photonic wires and photonic crystals, requires for a compromise between the optimal conditions for each to be made. Therefore, typical $\lambda = 193$ nm projection lithography methods are unable to guarantee fine control over sub-100 nm features [48, 67].

On the other hand, EBL is a fabrication technique with resolution in excess of 10 nm. While the relatively slow serial scanning of an electron beam severely limits the achievable throughput and, therefore, makes EBL impractical for use in commercial scale manufacturing as of now, the control over minute structural features afforded by its high accuracy, ability to independently tailor exposure conditions for different patterned components on a pixel-by-pixel basis and more flexibly compensate for proximity effects makes EBL the primary tool for research and rapid prototyping. As can be observed in Figure 2.5, EBL fabricated SOI photonic structures have been accurately defined, with ≤ 5 nm deviation from the design pattern. Furthermore, photonic crystal couplers, shown in the bottom panel of Figure 2.5 (d), composed of closely packed holes with controlled diameters down to 30 nm could be defined in the same patterning step as the rest of the waveguide-coupled resonator photonic

circuit. For the purposes of this work dealing with mode propagation control in ring resonator structures through the definition of $\sim \lambda/10$ size periodic modifications, EBL precision is of crucial importance in seeking experimental verification of predictions obtained by means of photonic simulations.

2.2.2 EBL patterning of photonic devices

Apart from distinct resolution advantages, while EBL is an overall quite a costly technique, the fact that it does not require the prior creation of a mask, which is a substantial investment necessary for deep UV lithography, makes this method the most expedient and accessible for the present work. Here the fabrication cost for initial device prototype creation was further decreased by using an affordable PMMA positive tone resist and by minimizing the EBL patterning duration by performing mask inversion.

The SIMOX, short for "separation by implantation of oxygen", type SOI wafers [70], used as the base into which the integrated photonic circuits according to a lithographic pattern are subsequently etched, were purchased form a commercial supplier. The total wafer thickness is around 500 µm, where the top device layer was 240 nm and the underlying insulating SiO_2 spacer was approximately 3 µm thick. So, the present task is to create a nanoscale resolution lithographic mask over what is set to become the integrated photonic circuit that is robust enough to withstand reactive ion etching during which all unmasked Si device layer regions are removed down to the underlying oxide.

The workflow of the EBL fabrication process used for initial prototyping is outlined in Figure 2.6 (a), and is in close accordance to the general principles outlined in Section 1.1.3. After sequential ultrasonic cleaning steps in organic solvents – acetone, isopropanol and methanol, a PMMA electron beam resist layer is spin-coated onto the SOI wafer at a thickness of ≈ 90 nm and a pre-exposure bake at 180°C for 2 min is performed to remove residual solvent molecules. Such a resist thickness is quite low, hence, it gets exposed uniformly, which helps to increase attainable patterning resolution. However, it would not be resilient enough to withstand direct pattern transfer during etching and a subsequent mask inversion process will become essential.

EBL exposure was conducted using the Raith EBPG5000plusES (Raith GmbH) tool at the Melbourne Centre for Nanofabrication. Three of the most important advantages provided by this tool are its 100 kV electron acceleration voltage, which allows for high resolution patterning, its field emission electron source, that is capable of generating large beam currents for an increased exposure rate, and the 1 mm^2 write-field – a significant improvement over the 50×50 µm^2 of conventional EBL tools – which minimizes the amount of stitching defects that scatter light, hence, decreases the propagation losses in photonic structures. As the electron beam is scanned along a pattern set by the design, the energetic particles induce scission of the PMMA polymer molecule chains (which on average have a molecular mass of $M \sim 950 \cdot 10^3$) thereby locally

increasing their solubility. In order to decrease patterning distortion due to charge accumulation during exposure, excess charge needs to be extracted away from the SOI substrate using copper or carbon conductive tapes. Following the electron beam patterning, the resist is developed in 1:3 Methyl isobutyl ketone (MIBK)/IPA mixture to remove PMMA from the electron exposed areas.

As mentioned previously, PMMA is a positive tone resist, meaning that resist areas which where exposed are cleared for subsequent processing steps upon development. The most straightforward approach to define waveguide-coupled resonator structures would then be to expose the areas surrounding the photonic circuit and to etch trenches around the desired waveguide pattern, much like the way the deep UV projection lithography structures were defined in Figure 2.5. However, this would significantly increase the overall area that needs to be exposed using a serial scanning electron beam, thereby increasing the exposure duration by up to a factor of ten. In this work an alternative

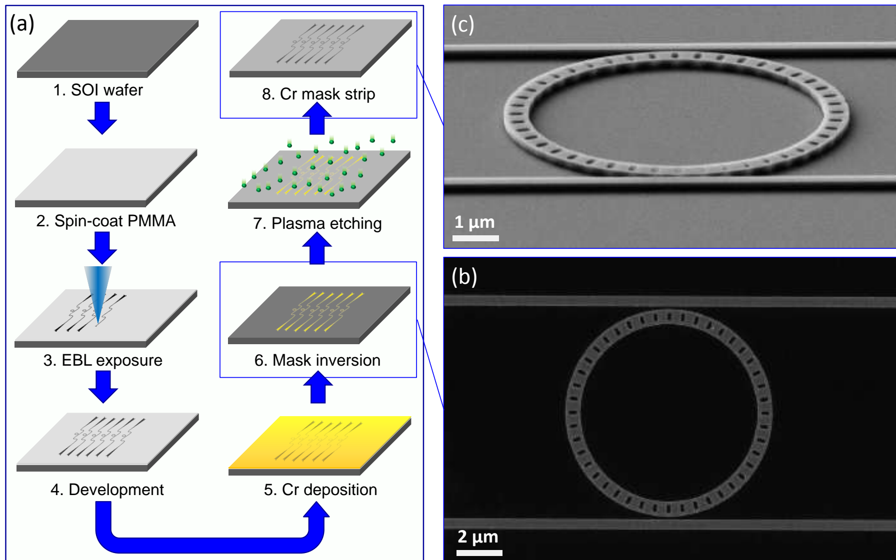

Figure 2.6: (a) Lift-off mask inversion EBL process used for initial fabrication of structures. SOI wafer is first sonicated in acetone, IPA and methanol for cleaning, then PMMA is spin-coated to 90 nm thickness and baked to remove residual solvent. EBL exposure is performed using 100 kV electron acceleration. Exposed resist is developed in a 1:3 MIBK/IPA solvent. A 12 nm thick Cr layer is deposited by means of thermal evaporation and then lift-off is performed in acetone resulting in mask inversion. ICP-RIE is conducted in a CF_4/O_2 plasma, and, lastly, residual Cr mask is stripped *via* wet chemical etching. (b) SEM image of the Cr mask after lift-off. (c) Isometric view of the fabricated waveguide-coupled micro-ring structure.

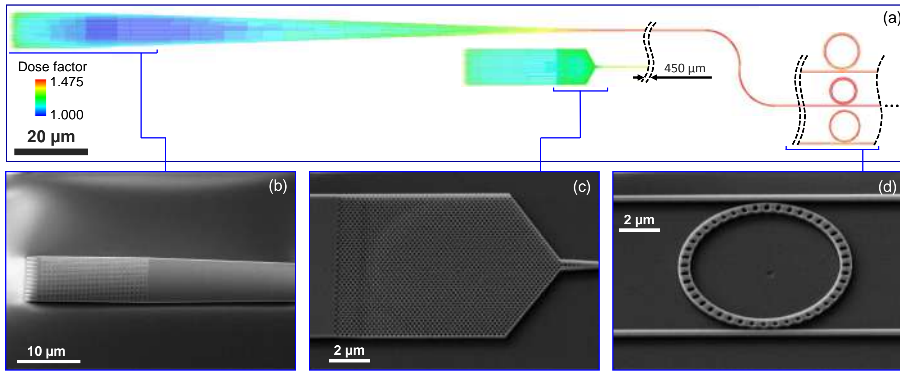

Figure 2.7: Proximity effect correction in EBL. (a) Fragments of a dose-corrected design file accounting for the proximity effect. Color scale represents the factor by which exposure dose is altered. (b), (c) and (d) respectively are SEM images of a gradient refractive index coupler, a photonic crystal coupler and a perforated micro-ring resonator, all fabricated during the same exposure process on a single SOI chip.

method which avoids this prolonged beam scanning was adopted. It involves exposure of the photonic structure pattern in PMMA, as if one was using a negative tone resist, and after development a mask inversion step is performed *via* metallization with subsequent lift-off.

The SOI substrate with developed PMMA waveguide-coupled resonator patterns is coated with a 12 nm Cr layer by way of electron beam heating-induced thermal evaporation using the AXXIS physical vapour deposition tool (Kurt J. Lesker). Typically, the deposited metal layer should be as thin as possible, while still remaining robust enough to withstand the etching procedure. After metallization the sacrificial PMMA resist layer is removed, which results in a Cr mask pattern covering only where the photonic circuit is supposed to be defined, as is illustrated by the SEM image in figure 2.6 (b). Subsequently the planar Cr mask pattern is transferred to form 3D waveguide photonic structures by means of inductively coupled plasma (ICP) RIE using a SAMCO RIE-101iPH tool by etching in a CF_4/O_2 plasma all the way through the 240 nm top Si layer to the underlying buried oxide. The final step involves stripping the residual Cr mask by using wet chemical etching in a nitric acid solution of ceric ammonium nitrate. A typical example of a resulting waveguide-coupled holey ring resonator structure is displayed in Figure 2.6 (c).

As mentioned before, the broad variation of components used in a typical photonic circuit, *i.e.* long thin and uniform waveguides, densely packed photonic crystal hole lattices and large area tapered couplers, each with different optimal process conditions for constituent structural features, present a considerable challenge for conventional parallel projection lithography techniques.

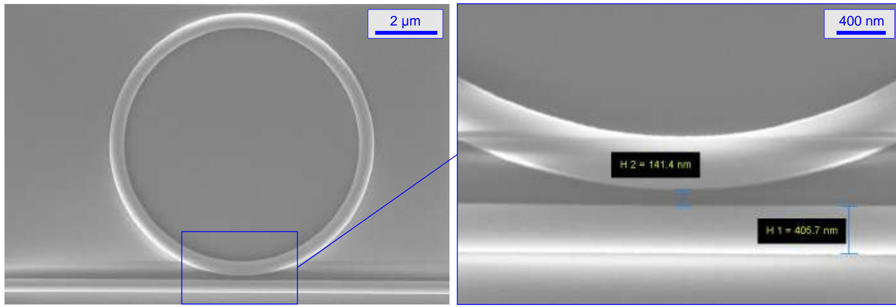

Figure 2.8: SEM image of a simple ring microcavity fabricated using EBL. Close-up view on the right shows how the critical parameters, such as waveguide-cavity coupling distance and waveguide width are defined at around 5 nm accuracy.

Serial scanning EBL is much more flexible in this respect, allowing to independently control the exposure conditions of each device segment. However, electron beam exposure is also susceptible to distortion through its own variation of the proximity effect introduced in Section 1.1.2. As is illustrated by the Monte Carlo simulation results displayed in the middle panel of Figure 1.5, even when focused down to a ≈ 5 nm spot energetic electrons experience scattering and cascading avalanche multiplication effects which spread a portion of the initial beam energy in a ≈ 25 μm radius. This in turn gives rise to superfluous exposure of surrounding resist regions, hence, causes a decrease of contrast which is especially detrimental for densely packed photonic structures like the ones depicted in Figure 2.7 (b) and (c).

However, the proximity effect in EBL can be mitigated by locally modifying the electron dose depending on the density of neighbouring pattern features and taking into consideration the background exposure evaluated by Monte Carlo simulations, like is shown in the photonic circuit segments displayed in figure 2.7 (a). Therein segments with large areas or concave boundaries are exposed at lower doses, whereas isolated small area features or sharply protruding corners are assigned a higher dose factor. During these initial PMMA resist-based fabrication runs the optimal base 100 kV electron exposure dose was found to be 650 $\mu\mathrm{Ccm}^{-2}$.

At optimized exposure conditions critical device parameters, such as the coupling distance between a waveguide and a ring resonator shown in Figure 2.8, can be controlled with a 5 nm accuracy. As a result, the fabrication fidelity is fully sufficient to adequately reproduce the photonic structures as set by the design file, so that they fulfill all the main functions as predicted by numerical simulations. However, the PMMA/Cr inverted mask based process results in the manufactured structures deviating from the ideal case in one major way – namely the up to ~ 10 nm average roughness of waveguide side walls that

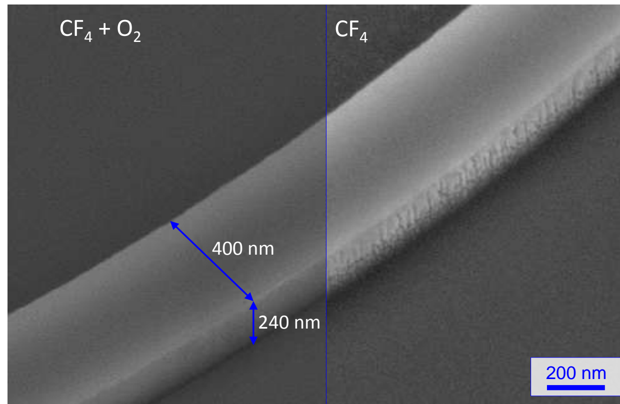

Figure 2.9: Isometric SEM view of a curved Si waveguide on a SiO_2 substrate, fabricated by RIE of a SOI wafer. Left-side image shows results attained using an optimized etching gas mixture. Minor sidewall roughness is still visible. Right-side depicts excess passivating fluoropolymer deposition on the sides of the waveguide during oxygen-free plasma etching.

gives rise to substantial propagation losses due to scattering. Therefore, to fully leverage the resolution advantage of EBL, more refined fabrication processes that can produce higher performance devices have to be sought.

2.2.3 Optimization for low propagation loss

As was mentioned previously in Section 2.1.2, the primary cause of propagation losses in Si micro-photonic waveguide structures is surface-roughness-induced scattering [49]. It is especially prominent for subwavelength-sized photonic elements, due to stronger evanescent optical field components at the boundaries of the structure. While light scattering at the top waveguide surface is typically small since the RMS roughness introduced by the wafer polishing process falls below ~ 0.1 nm, imperfections introduced during the RIE process can be much more severe [71]. Unevenness of the side walls, therefore, can be a product of either suboptimal etching conditions or defects of the lithographic mask itself.

One of the ways that faulty RIE process conditions can negatively affect quality of fabricated devices can be seen in Figure 2.9. The pronounced sidewall roughness on the right image side is due to excessive deposition of fluorocarbon-based polymers during the etching process. Some deposition of this material is necessary to attain anisotropic material removal by providing passivation of vertical side walls, whilst any such polymer overlaying horizontal surfaces is physically sputtered away by reactive ions accelerated towards the biased substrate, hence, exposing it to direct chemical attack. Here in a 40 sccm flow rate CF_4 gas plasma chemistry, however, passivation appears to be excessive

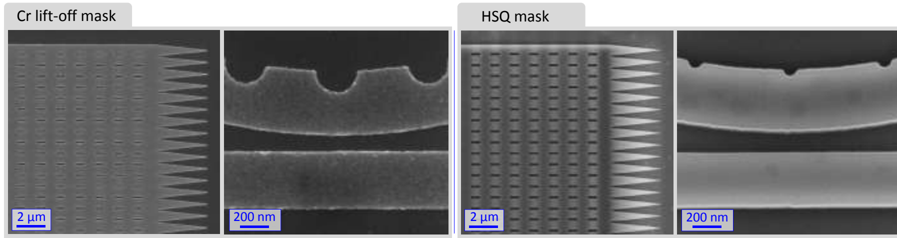

Figure 2.10: SEM image comparison between a 12 nm thickness Cr mask prepared by PMMA pattern lift-off, and a HSQ negative tone resist. Here planar coupler and annular grating-endowed ring resonator segments are shown as examples respectively on left and right sides of each panel. The metal films posess notable edge roughness due to their nanocrystalline structure.

and produces stochastic masking effects that generate nanoscale wedge-like sidewall protrusions that escalate with increasing etching depth. Still, such etching process related issues can be largely mitigated by appropriate recipe adjustments, as can be seen on the left side of Figure 2.9. The addition of a fairly small 5 sccm flow rate of O_2 tends to have two effects: (i) it plasma ashes away fluorocarbon polymers thus keeping the Si fluorination process in check, and (ii) it facilitates the dissociation of CF_4 molecules to produce particularly chemically active F^- ions that increases the overall etch rate [72]. However, care must be taken not to introduce too much oxygen, as it is liable to over-passivate surfaces by forming oxides, as well as to prematurely oxidize and destroy the metal mask.

While it is evident that etching process optimization can bring about considerable improvement in structure quality, waveguide sidewalls on the left of Figure 2.9 still exhibit appreciable unevenness. As these defects are most visible close to the top surface of the waveguide, *i.e.* closest to the Cr layer, it is reasonable to conclude that they are a caused due to etching mask material edge roughness. Indeed, the close-up SEM images of 12 nm thickness Cr mask patterns, prepared by way of PMMA lift-off, exhibit $\sim$ 10 nm scale grain sizes that can readily be transferred down into the waveguide structure during etching. Furthermore, in addition to scattering, residual surface contamination as well as diffusion into the underlying Si by the metal can also provide a source of absorbance losses detrimental to device performance. Hence, creation of micro-ring resonator devices suitable for purposes beyond merely establishing a point of concept prototype demonstration requires higher fidelity lithographic mask materials.

The high-performance negative tone resist chosen for this work was a 6% HSQ solution in MIBK, applied in a conceptually similar manner discussed in Section 2.2.2 for PMMA, and sketched in Figure 2.17, the key difference being that no metal deposition or mask inversion lift-off is required. Spin-coating

was performed at 4000 rpm and resulted in an approximately 200 nm resist thickness. In addition to its exorbitant cost, the primary drawback of HSQ is its low sensitivity, requiring a base dose of approximately 3500 μCcm^{-2}, and resulting in an exposure that is around five times longer than for the 650 μCcm^{-2} base dose PMMA. Following exposure, the HSQ resist was developed in a 25% aqueous tetramethylammonium hydroxide (TMAH) developer heated to a 55 °C temperature. Development of negative tone resists at elevated temperatures helps to increase the attainable contrast at the expense of sensitivity, as partly exposed and thus incompletely polymerized resist regions are dissolved more actively in warm solvents [73]. Conversely, positive tone resists, due to relying on the completely opposite process of chain scission, exhibit higher contrasts and lower exposure sensitivity when developed in cooled solvents.

The right panel of Figure 2.10 depicts the developed HSQ lithographic mask pattern defined on a SOI wafer prior to subsequent etching steps. When comparing with the previously described nanocrystalline Cr-based patterns, amorphous silica-like HSQ produces smooth features with ≤ 5 nm peripheral roughness. Furthermore, while both Cr and HSQ are effectively hard masks and exhibit a high etch selectivity, HSQ is not as vulnerable to the effects of O_2 plasmas as metals, hence, provide more flexibility when devising an optimal RIE etching process.

Reactive ion etching is a multivariate process with complex parameter interdependencies and nonlinear responses. In addition to the gas mixture, chamber pressure, power of the plasma generation source or substrate bias parameters mainly controlled in this work, the output result can be affected by factors as wide ranging as the process chamber geometry and usage history, substrate thermal insulation or etched wafer size. Consequently, RIE is best understood phenomenologically, and etch recipes are determined empirically by using those reported in the literature as starting points. Figure 2.11 summarizes the etch tests performed for the purpose of attaining maximum pattern transfer fidelity and minimum sidewall roughness. SEM images were taken at qualitatively different regions of the photonic circuit, so that structures as diverse as ring resonator coupling segments, sharp tapered features, a large area photonic crystal, and a solitary waveguide could be sampled and compared.

Without going into excessive detail, the first four rows of Figure 2.11 show etch tests performed in the CF_4 based chemistry using O_2 flow rates that were incrementally increased from 3 sccm to 15 sccm. The overall effect of oxygen in this case was subtle, but as described in the Cr mask case, at flow rates between 3-9 sccm O_2 increased the etch rate and decreased the amount of fluoropolymer deposition, particularly evident from the diminished amount of fence-like protrusions around the pattern periphery, which improved sidewall quality. Further increasing the amount of oxygen in the plasma started to decrease the etching rate without any noticeable benefit, hence, 6 sccm of O_2 was accepted as the optimal fraction for all further etch tests.

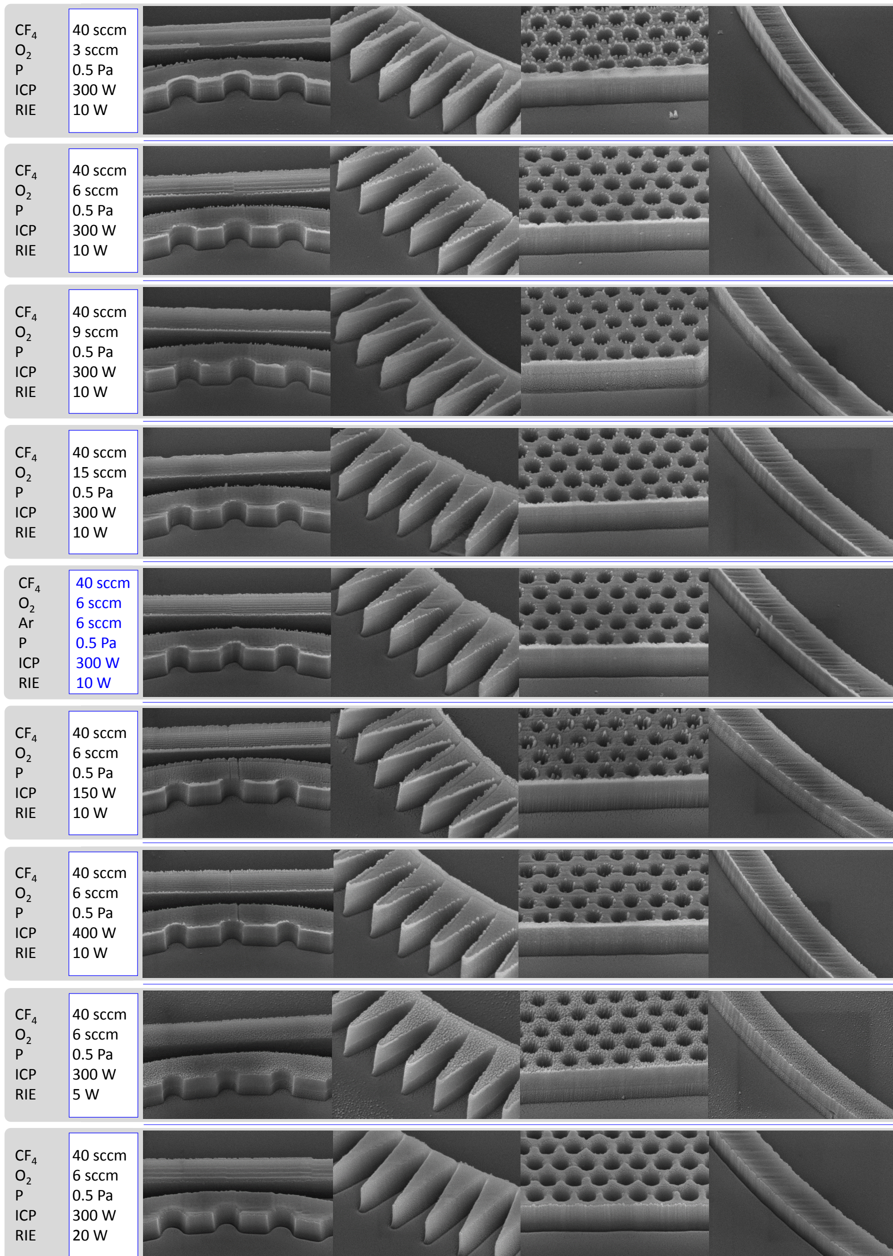

Figure 2.11: Optimization of reactive ion etch recipe for the creation of SOI waveguide integrated circuit devices when HSQ resist is used. Adjustable parameters include CF_4, O_2 and Ar gas flow rates, process pressure as well as ICP and RIE bias powers. Process duration was always 100 s. SEM images provide a comparison of sidewall smoothness at different representative regions. The optimal etch recipe is highlighted in blue. The top HSQ resist film is discernible in SEM images as a slightly brighter layer.

The fifth row introduces a 6 sccm flow of argon, which provides a purely physical sputtering component to the process and helps improve smoothness of all surfaces while facilitating faster mask erosion and preventing the buildup peripheral fence-like structures. Rows six and seven correspond to etches that were performed at different inductively coupled plasma source powers, 150 W and 400 W, which tends to directly correlate with the density of available reactive ions, hence, the etch rate, and somewhat less directly to substrate temperature as it increases during bombardment by more abundant charged particles. In this case, lowering the ICP power resulted in predictably lower etching rates as well as higher roughness of structures, whereas increasing it to 400 W allowed for faster Si removal but otherwise changed little. Lastly, the two final rows represent the effects of altering the RIE bias power, related to the acceleration and energy available to each ion incident on the substrate. Decreasing the bias power to 5 W also diminished the etching rate and caused instabilities during sputtering of both mask and Si material, producing more detrimental roughness. Conversely, a 20 W bias resulted in rapid sputtering of all materials. It would be expected to produce smother structures, however, here intense ion bombardment resulted in chipped mask fragments creating defects in fabricated photonic circuits and structures.

Ultimately, the best regime was found to be a 100 second duration etch in a $40/6/6$ sccm flow rate $CF_4/O_2/Ar$ gas plasma, at a $P = 0.5$ Pa pressure and using 300 W ICP and 10 W RIE bias powers, and the corresponding recipie is highlighted in Figure 2.11 by a blue font. The next section outlines select examples of waveguide-coupled micro-ring resonator devices, where the nanoscale precision of EBL was leveraged to exert both spatial as well as spectral subwavelength mode control.

Lithographically defined microscale cavity photonic sensors possess a multitude of desirable traits, such as a high degree of fabrication scalability, potential for complex integration and high sensitivity. As mentioned in prior sections, SOI micro/nano resonator optical biosensors, which constitute a novel and rapidly developing branch of optical sensor technology, are at the primary focus of this work. SOI waveguide structures exhibit low attenuation for propagating electromagnetic modes and their resonant structures can have high quality factors as well as strong sensitivity to variations of external environment. Furthermore, a resonant mode can be confined to extremely low volumes, meaning, that femtoliter amounts of bio-molecules can realistically be detected.

The problem with micro-resonator optical biosensors is that their sensitivity is significantly lower than that exhibited by surface plasmon resonant structures, in significant part diminished by the strong confinement of electromagnetic modes within the waveguides, primarily due to the high refractive index contrast between Si and most analytically relevant materials. Since the optical field is localized within the structure, it is unable to interact with bio-molecules present at or near the surface of the sensor. Furthermore, ring resonators support multiple resonances, and the distance between these resonances, the FSR, imposes a limit on the maximum range of measurable analyte concentrations. Both of these factors pose significant challenges for real-world sensing situations, where analyte concentrations can be both small and highly variable.

A promising route to further enhance the sensitivity as well as utility of waveguide-coupled micro-ring resonator sensors is to leverage the subwavelength resolution afforded by EBL to achieve advanced control over mode propagation inside a resonant cavity. For instance, by employing subwavelength

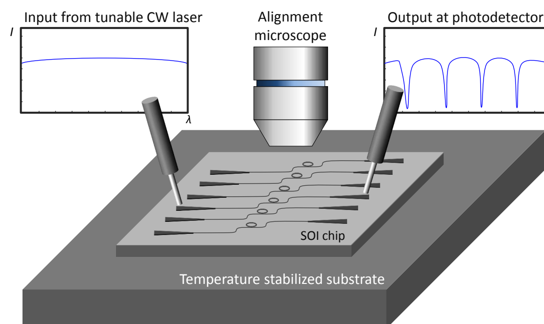

Figure 2.12: Schematic image of the characterization setup for transmittance spectral measurements. Light from a tunable telecom waveband laser is coupled into and out of the SOI chip *via* vertical fibers. Representations of typical input and output spectra are given as insets.

SOI structures, the optical field can be delocalized, its interaction strength with the local environment can be enhanced, and the sensitivity for potential biosensor applications can be increased. Conversely, by borrowing concepts from photonic crystals, periodic nanoscale perturbations can induce slow light effects and allow to control the dispersion of resonant modes and increase dynamic ranges of devices.

In this work EBL fabrication of advanced SOI micro-ring resonator devices was conducted at Melbourne Centre for Nanofabrication as well as at the Nanofabrication Facility at Swinburne University of Technology in Australia, whereas experimental characterization work was performed by colleagues at the Center for Physical Sciences and Technology.

The simplest realization of a micro-ring resonator molecular detection device, created as a planar integrated photonic circuit on the SOI platform, is comprised of two radiation coupler segments, for mediating the luminous energy transfer from free space into tightly confined propagation and *vice versa*, a waveguide for directing energy flow, and a resonant cavity for multipass storage and buildup of radiation energy for analyte probing. This general principle is represented in the schematic of a typical characterization setup in Figure 2.12, where waveguide-coupled micro-ring resonator structures are investigated by registering their transmission spectra down the optical line from the resonator. Light from a tunable Telecom C band ($\lambda = 1.53 - 1.57$ µm) continuous wave laser is coupled into the integrated SOI waveguide device through grating couplers with 150 µm-long tapered waveguide sections to minimize insertion losses and increase the tolerance for fiber misalignment [74]. Likewise, transmitted light is collected through a fiber *via* grating couplers at the output ports and passed on to a telecom wavelength InGaAs detector. Alignment of coupling fibers is controlled by means of a microscope and a precision positioning stage.

2.3.1 Gradient index micro-ring structures

The strong light confinement exhibited by high refractive index materials like Si allows for tight waveguide bends and therefore dense integration. However, strong localization of optical energy means that only a small fraction thereof will be evanescent and interact with the surrounding material. While the exceptionally rapid decay of the evanescent field around Si waveguide elements, estimated to decrease by a factor of $1/e$ at a distance of 63 nm [62], is useful for bio-sensing of water-borne analytes, as it allows for higher specificity due to the signal being dominated by contributions from the functionalized surface layer, strong confinement is detrimental when bulk sensitivity is required such as in gas sensing. In this field functionalization is often achieved by applying various cladding materials, such as spray-coating triphenylene-ketal receptor for TNT detection [75], drop-casting ZnO nanoparticles for ethanol sensing [76], dip-coating Pt-doped tungsten oxide in a sol-gel solution for H_2 detection *via*

catalytic combustion [77], deposited at thickness values ranging form 150 nm to multiple micrometers.

To make the most use of the available sensing volume it is therefore worthwhile to pursue methods of extracting light confined within the high refractive index resonator body into the surrounding medium. One way of partly delocalizing electromagnetic waves is by creating a resonator with subwavelength peripheral features [78], arranged periodically in such a way as to create a radially decreasing fill factor of the high-n material, hence, radially decreasing effective refractive index [79]. In addition to having stronger expected light-analyte interaction along the outer perimeter of the ring, a gradient effective refractive index resonator is also expected to significantly increase the typically nanometre-range error tolerance for the critical coupling distance to the adjacent waveguide.

A gradient effective refractive index ring resonator device was fabricated on a SOI platform using EBL according to the processes described in Section 2.2.2, and the resultant structure is depicted in figure 2.13. It is comprised of 101 triangle shapes aligned to form a 9.2 µm inner diameter circle in such a way that the most acute angles would radially protrude outwards, with each apex extending 800 nm from the inner boundary of the ring. The resonator is coupled to an adjacent strip waveguide in an all-pass configuration with a 130 nm gap. The key feature of this geometric arrangement is that constituent triangle shapes are sufficiently small to approach subwavelength scale, meaning that telecommunications wavelength $\sim$ 1550 nm radiation propagating even in high RI silicon are likely to perceive the resonator as a continuous medium. Furthermore, the structure becomes more sparse towards the ring periphery, where EBL enables triangle apex tip curvature radii to be as low as 30 nm, resulting in a progressively lower Si fill-factor. This, in turn, produces a radially decreasing effective refractive index, as sketched on the right side of Figure 2.13.

An experimentally measured transmission spectrum of the device is shown

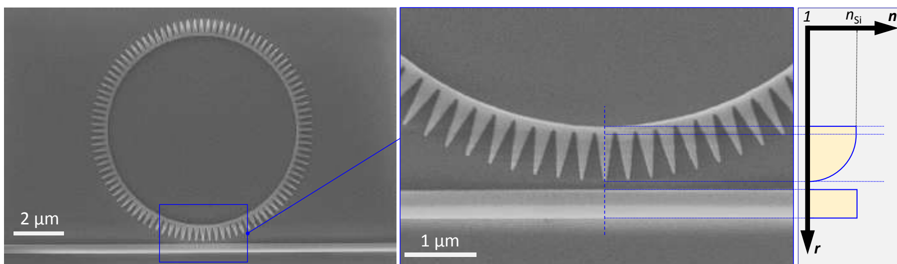

Figure 2.13: Top-down SEM image of an EBL fabricated SOI gradient effective refractive index resonator and an increased magnification view of the waveguide-resonator coupling gap. Inset on the right illustrates the effective refractive index profile along the marked line.

as the bottom plot of Figure 2.14, along with isometric views of a corresponding resonator. The transmittance exhibits a succession of equally spaced resonances, characteristic of a circular optical cavity, hence, directly shows that such a gradient effective refractive index structure is capable of guiding telecommunications wavelength radiation. Typical absorbance dips have an extinction ratio of -10 dB and a quality factor $Q \simeq 15000$, with a FSR of 18 nm. For comparison, a conventional micro-ring resonator, like the one displayed in Figure 2.8, made in the same fabrication run exhibits a quality factor of only $Q \simeq 5000$. Considering the threefold increased sidewall area of the gradient refractive index resonator over an equivalent simple micro-ring the large quality factor seems counterintuitive, as sidewall roughness is the leading cause of scattering losses. However, provided the pitch between neighboring spikes is maintained at least 4 times smaller than the resonant wavelength and said spikes also extend essentially perpendicularly to the direction of light propagation in the resonator, low loss is possible despite the numerous interfaces.

One peculiar trait of the transmittance dips in Figure 2.14 is that they tend to appear as doublets, with their separation decreasing for larger wavelength modes. Such a behavior would be considered detrimental for use of gradient effective refractive index micro-ring devices as sensors, since two closely-spaced resonances could create ambiguity during signal acquisition. In this particular case such spectral signatures can arise potentially due to either mode splitting caused by cross-coupling between the otherwise degenerate clockwise

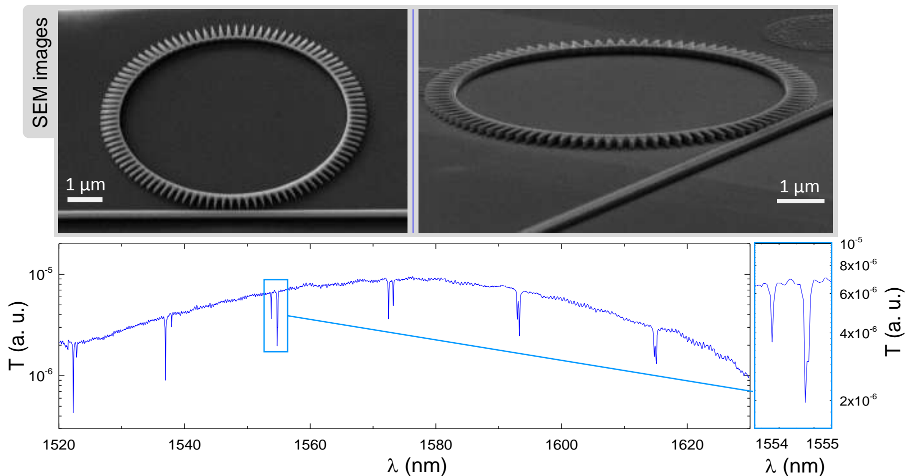

Figure 2.14: Top panels show perspective view SEM images of the gradient effective refractive index micro-ring. Plot at the bottom provides an experimentally measured near-infrared transmission spectrum of the SOI structure. Inset on the right displays an increased resolution plot of a resonant transmission doublet.

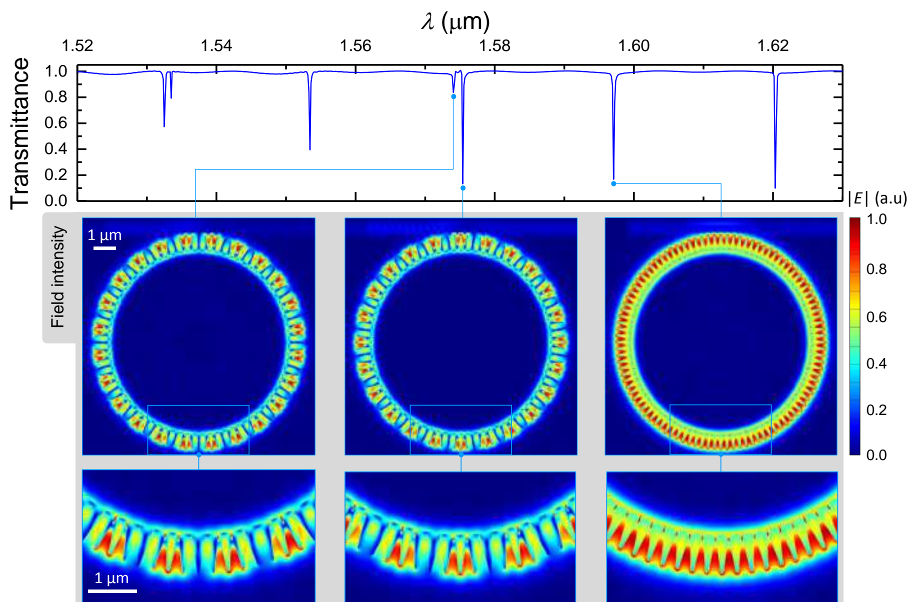

Figure 2.15: FDTD simulation results for a gradient effective refractive index waveguide-coupled micro-ring resonator structure. Plot at the top depicts the simulated transmittance spectrum. General overview and ring section close-up field intensity profiles for selected modes are given at the bottom. Mode splitting appears to correspond to orthogonal counterpropagating modes, established as a result of constructive interference of scattered radiation.

and counterclockwise WGMs, or due to the gradient refractive index resonator supporting two instead of the usual single mode.

The exact mechanism behind the appearance of doublets can be revealed by means of finite-difference time-domain FDTD simulations. This technique directly solves the 3D Maxwell's equations in a discrete spatial and temporal Cartesian grid of so called Yee cells [80, 81]. FDTD has the benefit of good accuracy, especially excelling when highly nonparaxial propagation due to high RI contrasts or ultrashort pulses is involved, the only major drawback is how computationally demanding it is. In this work, numerical experiments on waveguide-coupled resonator structures were conducted using the 2.5D variational FDTD method [82] supplied as part of the commercially available "MODE Solutions" solver software package (Lumerical Solutions Inc). This approach provides a more computationally efficient way to simulate planar integrated photonic devices in what in essence is a 2D calculation, whilst providing precision close to that of the full-vectorial 3D FDTD Maxwell's equation solution. As a result, full information of spectral and spatial distribution of radiation in a given waveguide-based device can be obtained using only a small

fraction of calculation power and time that would be needed in conventional FDTD, with the main limitation being that coupling between different modes should be kept small.

Figure 2.15 depicts the most relevant numerical simulation findings pertaining to gradient effective refractive index micro-ring resonator performance. Overall, the calculated transmittance spectrum, while not capable of fully reproducing the resonant peak positions, exhibits the general behavior observed in its experimental counterpart. Discrepancies between spectral positions are likely a result of slight departures from the design geometry due to RIE overetching that is likely to occur at sharp tips of the structure. This, in turn, gives rise to a sharper effective refractive index drop-off than intended by the patterned design. Furthermore, simulations reproduce the observed mode splitting, meaning that it is an inherent feature of the design, and not a product of manufacturing imperfections or sidewall roughness. Lastly, the lower degree of mode splitting for longer wavelength radiation is likewise present in the FDTD simulated transmittance, hence, can be attributed to the resonator geometry being a closer approximation of an effective medium farther towards the infrared.

More still can be learned by considering the field intensity distribution profiles for the different modes of a gradient effective refractive index micro-ring, shown in the lower part of Figure 2.15. Most notably, the intensity distributions of the two modes arising due to splitting are quite similar, exhibit the same number of nodes, yet appear with a phase offset that renders them orthogonal. This largely validates the hypothesis that mode splitting here represents clockwise and counterclockwise modes, established as a result of constructive interference of radiation back-scattered from the periodically arranged triangular sections. Lastly, higher wavelength modes do not appear to be prone to splitting, likely due to closer correspondence to the effective medium approximation. This, in turn, provides a clear path for mode splitting removal and device performance improvement by decreasing the period of individual triangular elements. Present EBL capabilities should allow to at least double the amount of radial spokes making up a single 10 μm diameter ring.

Regardless if a mode is split or not, however, FDTD simulation results show that gradient effective refractive index micro-ring resonators provide a way to achieve optical field delocalization for probing extended sensing volumes, whilst not compromising the quality factor. This is a significant improvement over the typical slot waveguide ring resonator structures used for enhanced coupling to surrounding material, which suffer from propagation loss due to scattering from the increased area of rough sidewall surface, further compounded by the strong optical fields in the slot, ultimately resulting in modest quality factors of $Q \simeq 330$ for SOI [83] and $Q \simeq 1800$ for Si_3N_4 [84] based devices. Also, the subwavelength (≤ 200 nm) slot can be difficult to fill, hence, may not be compatible with numerous functionalization methods such as nanoparticles. However, even if scattering-induced mode splitting is detrimental

for the performance of such gradient effective refractive index sensor devices, the ability to control radiation propagation through subwavelength structural modifications offers intriguing opportunities that are discussed next.

2.3.2 Dispersion-tuned resonators

Typically, the maximum range of analyte concentrations that can be measured using a multi-pass WGM device is limited by the FSR, that is to say spacing between neighboring modes, which in most cases for high-Q devices is narrower than 20 nm. However, if changes in the refractive index of the surrounding medium are large enough to cause resonance shifts that exceed the modest intermode spacing, the absolute line-shift can no longer be unambiguously determined. A natural route to alleviating this problem involves some type of modification of a cavity that exerts a disparate impact on previously indistinguishable modes. Conceptually, such functionality can be realized by endowing a micro-ring with a secondary resonant structure, particularly matched to one specific ring mode.

The azimuthal symmetry of a ring cavity can be broken by any number of perturbations, including scatterers, surface roughness or an inhomogeneity in its material. Such a structure can lift the inherent degeneracy of WGMs with the same spatial intensity distribution and energy, but opposite propagation direction [85], as was previously observed in Figure 2.15. When perturbations are periodically spaced in the second order $m = 2$ Bragg configuration, defined by the condition:

$$m\lambda_B = 2n_{eff}\Lambda, \tag{2.25}$$

where Λ is the period of scatterers and n_{eff} is the complex effective refractive index of a particular mode at Bragg resonance wavelength λ_B, micro-ring resonator dispersion can be engineered through repeated scattering and interference in such a way that modes which do not meet this condition are suppressed [86]. This type of filtering behavior can be advantageous as a way to circumvent the FSR limitations of high-Q resonant sensors expected to operate at vastly variable analyte concentrations that are commonplace for most practical bio-sensing challenges.

Effective mode filtering, however, has to proceed in a way that is not overly disruptive to the resonant mode that has to be preserved. Hence, any perturbations of a micro-ring resonator have to be small. Proof-of-concept for this principle is demonstrated by means of 2.5D variational FDTD simulations of annular grating modified SOI micro-rings [68] with 4 µm radii at center of the 400 nm width and 240 nm height waveguide. The bus strip waveguide has the same dimensions and is situated at a 130 nm coupling distance in an all-pass configuration. Crucially, a circular chain of equally spaced shallow hemicylindrical incisions, with radii ranging from 0 nm to 140 nm, is generated along the inner wall of the micro-ring. Lastly, the ring resonators were assumed

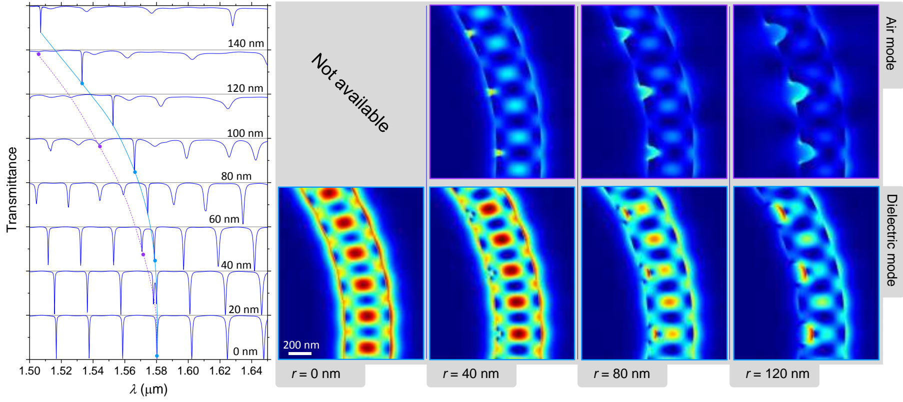

Figure 2.16: FDTD simulated near-IR mode propagation in annular grating modified micro-ring resonators with varying groove radii. Plot on the left depicts the simulated transmittance spectra of different micro-rings, showing how the split doublet mode drifts as the effective refractive index of the resonator becomes lower due to larger grooves along the inner wall leading to a decrease of Si fill factor. Panels on the right provide the field intensity plots of modes in an unmodified micro-ring, as well as for the Bragg grating split resonances.

to be operating in a dielectric environment with a refractive index $n_{\mathrm{env}} = 1$, corresponding to the ambient atmosphere.

The FDTD simulated transmission spectra on the right side of Figure 2.16 show how the unmodified ring device supports multiple equidistant resonator modes at which resonant transmission dips occur. On the other hand, when a small-to-moderate $r \geq 20$ nm grove size annular grating is patterned on the inner wall of the micro-ring, the resonant mode close to $\lambda = 1.58$ μm is split into two. This occurs due to a Bragg grating-induced band-gap and is related to the appearance of the no longer degenerate even and odd standing-wave modes as a symmetric and antisymmetric superposition of the counter-propagating traveling waves [87]. This is the expected consequence of power transfer between the deliberately excited mode propagating in the same direction as the light injected from the bus waveguide, and the counter-propagating mode sustained by Bragg reflections [47]. Therefore, from the forward propagating wave view point, the annular grating is a periodically phase-matched scatterer into the backward propagation direction, serving to transfer its electromagnetic energy into the counter-propagating mode thereby splitting the resonance, as was observed for micro-ring optical vortex generators [68].

As the annular grating groove radius is increased further, in the range from 60 nm to 100 nm both the extinction ratio as well as the quality factor of the lower energy split mode increases to exceed the values of the remaining micro-ring resonances. The mode splitting derived higher energy counter-propagating

excitation dip is suppressed exceptionally strongly. Hence, there is a range of angular grating parameters resulting in simultaneous quality factor enhancement and mode splitting removal for a Bragg-selected resonance. The underlying mechanism giving rise to the observed quality factor modifications is related to dispersion and slow light effects affecting modes split by the Bragg-induced photonic band-gap. It has been theoretically shown that highly dispersive media can be used to drastically increase micro-cavity lifetimes [88]. In the case of micro-ring resonators with annular gratings each of the mode-split doublet of lines is located on the opposite sides of the Bragg-induced photonic band gap. Therefore, the lower energy mode experiences normal dispersion, leading to a compression of the line-shape and an increase in the quality factor, whereas the higher energy counter-propagating wave undergoes anomalous dispersion, hence, a decrease in quality factor. Consequently, the device operates as a filter – only a single ring resonator mode, which matches the introduced second order Bragg condition [86, 89, 90] is preserved.

When the grating groove radii are increased further, all of the resonant modes except the Bragg selected one are gradually eliminated from the micro-ring. As the scattering losses become increasingly large, even the highest quality factor mode starts to become somewhat suppressed. However, the 2.5D variational FDTD technique does not account for out-of-plane scattering and, therefore, is liable to underestimate suppression of all modes. The overall trend of blueshifting resonant wavelength values with increased angular grating groove size is due to a decrease of the effective refractive index of the resonator as the Si fill factor in the micro-ring is lowered.

Further insight can be gleamed from the electric field intensity distributions in the annular grating modified structures at resonant wavelengths corresponding to even and odd split modes, shown for select transmittance spectra in left panels of Figure 2.16. For an unmodified micro-ring the mode at around $\lambda = 1.58$ μm is not split, hence, the vast majority of electromagnetic energy is confined in the Si strip waveguide. However, when grating incisions have modest radii of $r = 40$ nm, the two counter-propagating modes are no longer degenerate, and, as a result of the grating-induced asymmetry, exhibit highly disparate spatial intensity distributions. The Bragg-grating related photonic band gap ensures that forward-propagating radiation is confined almost exclusively within the semiconductor in a pattern that ensures minimum interaction with the periodic scatterers. Conversely, counter-propagating modes are situated mostly in air and strongly localized near incisions. Here they are particularly exposed to scattering effects and can be readily ejected out of the device plane in a helical phasefront, hence, upon interference form orbital angular momentum carrying beams [68]. When the incision radii are increased further to $r = 80$ nm and beyond, the grating starts to strongly affect the dielectric mode as well, leading to its suppression in the same way as for all other excitations.

For experimental investigation of the Bragg filtering effect the high reso-

lution patterning capabilities of EBL were essential to producing a series of SOI micro-ring resonators with finely controlled periodic groove-type features, fabricated within a 5 nm tolerance. The overall lithography process using a negative tone HSQ resist is schematically outlined in Figure 2.17 and was described in Section 2.2.3, although similar fully functional devices were created also using a Cr hard mask. As is evident from HSQ mask pattern SEM images in the lower panels of Figure 2.17, grating feature radii could be reproducibly varied from $r = 140$ nm to 50 nm in 10 nm increments, and values as low as $r = 20$ nm could be reliably achieved. Apart form the grating fill-factor related dimensions all other device parameters were set to remain the same.

Results of experimental transmittance measurements conducted on the EBL fabricated SOI devices that represent the most relevant $r = 50$ nm to 80 nm annular grating groove range, where divergence in mode behavior is especially apparent, is provided on the left of Figure 2.18. The evolution of the mode-split doublet closely mirrors the theoretical predictions summarized in Figure 2.16. Here also is the counter-propagating mode suppressed even at modest perturbation, effectively eliminating the detrimental mode splitting. Conversely, its counterpart is not only preserved, but even exhibits a higher quality factor than all other excitations supported by the micro-ring. The only substantial discrepancies between FDTD and experimental findings relate to the overestimation of mode extinction factor due to the aforementioned disregard for out-of-plane scattering in the 2.5D variational simulation scheme.

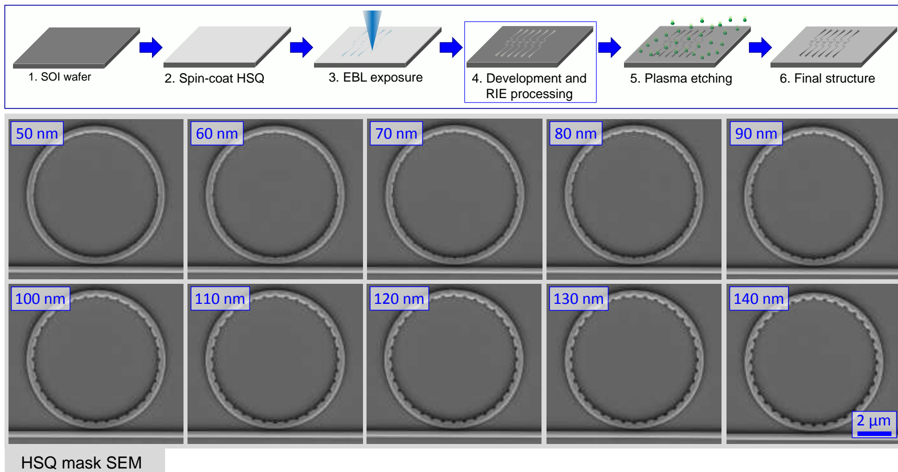

Figure 2.17: HSQ resist-based EBL fabrication of annular grating augmented micro-ring resonator structures. Sketch at the top illustrates the general lithography process workflow used in this work. SEM images at the bottom show developed HSQ mask patterns of resonators with hemicylindrical annular incisions of different radii.

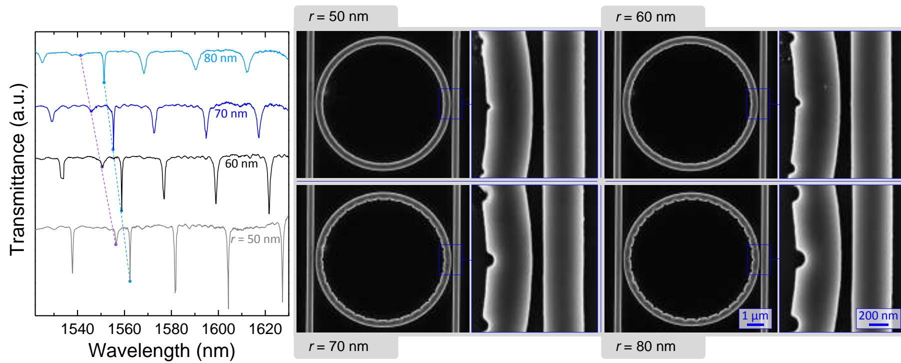

Figure 2.18: Experimental investigation of annular Bragg grating modified micro-ring resonators. Plot on the left provides experimentally measured transmission spectra for micro-rings with sidewall perforations of different radius. Dashed lines are guides for the eye and follow the two split modes. Panels on the right depict SEM images of EBL fabricated representative SOI resonator structures with corresponding geometries. Insets show close-up views of the waveguides in the coupling region.

As can be seen in the SEM images of the four different devices on the left panels of Figure 2.18, EBL can faithfully reproduce all but the smallest 5 nm scale patterns. The main issue hampering the performance of devices described here relates to the sidewall roughness introduced during pattern transfer. However, even this could be in large part minimized by using subsequent chemical polishing, although such a process proved not to be essential at this stage.

In summary, EBL fabrication, while not possessing the adequate throughput for industrial scale manufacturing, is an extraordinarily powerful technique for prototyping novel photonic devices and setting up nanoscale structures tailored to verifying hypotheses for advanced phenomena. Here it was used to create effective medium and photonic crystal-like features well below the λ/n_{Si} scale for near-IR radiation guided in single-mode Si waveguides. This allowed the creation of resonators that not only are constituted from subwavelength components to establish an effective refractive index medium, but also to control its value and mode confinement by setting up a desired gradient. Furthermore, work on micro-ring resonators patterned with annular gratings directly showed how the filtering behaviour of a Bragg-modified resonator is derived, and uncovered a mechanism for increasing the quality factor for a given resonant excitation and for elimination of mode splitting.

3 FOCUSED ION BEAM FABRICATION

Focused ion beam lithography provides a powerful complement to the distinct yet related EBL technique, as it is capable of engraving features directly into a substrate, thus reducing the number of process steps related to resist application and pattern transfer. Furthermore, by controlling the incident ion dose, FIB milling depth can be finely tuned to produce 3D structures with precision unparalleled by other direct-write patterning approaches. Lastly, the purely physical sputtering that underlies FIB milling is qualitatively indifferent to the type of substrate being processed. However, the serial scanned ablation mechanism, to which FIB owes its versatility, confines the technique to creating structures at the microscale or below.

As a result FIB processing is best reserved for applications where sufficiently pronounced physical effects can be realized through high precision localized removal of small volumes of a given substrate material. Fortunately, this is by no means a narrow domain, as broad disciplines such as visible wavelength photonics and plasmonics require structures with resolution and scale well within reach of FIB. Furthermore, the patterning fidelity of FIB is sufficient to extend diffractive functionality of surface patterns up to the X-ray spectral region [91]. Microfluidics is another field that can benefit from the 3D engraving capability of this lithographic approach, as it can be used to create efficient turbulent mixing [92]. Lastly, selective ion implantation into materials is employed in spin-based quantum information processing device fabrication [93].

This chapter describes several FIB lithography application examples, which both leverage its unique capabilities and take into considerations the relevant technological limitations. The first section deals with arguably the most simple device attainable by focused ion beam processing – a single $\sim$ 10 nm diameter pore in a nanoscale thickness Si_3N_4 membrane – which nevertheless can be used to perform complex detection of macromolecular compounds. Next, FIB processing on larger scale 2D patterns was employed to create subwavelength structures that can manipulate the propagation of light in advanced ways, such as how tailored metal grating patterns can produce desired light polarization behavior and provide a robust reference for advanced molecular spectroscopy techniques. Lastly, the large depth of focus of focused ion beams allows the nanoscale precision fabrication of complex diffractive metal patterns onto curved 3D refractive topologies, created by laser photopolymerization, which enable the realization of micro-optical elements with hybrid functionalities.

Direct material modification using sputtering by focused ion beams can be used to fashion a broad variety of complex photonic or electronic devices with nanoscale precision. However, even in the absence of any design complexity, FIB spot diameters can routinely be set to somewhat below 10 nm, *i.e.* approaching molecular lengthscales, which in and of itself is of tremendous utility. As a result, arguably the simplest conceivable FIB pattern – a single isolated hole in a membrane – can find use in a number of biochemical applications.

Owing inspiration to the biological example of protein translocation through channels in cellular membranes [94], nanopores show significant promise in highly sensitive single-molecule biosensing, such as the label-free real-time detection of anthrax toxin components [95], and DNA sequencing [96]. Artificial solid state nanopores represent a more robust, controllable and long-lasting alternative to their biological counterparts [97]. Such solid-state structures are typically generated in dielectric Si_3N_4 or SiO_2 membranes by locally piercing them using a variety of techniques, among which electron irradiation in a scanning high-voltage TEM [98] and focused ion beam milling [99], of primary interest here, are two of the more prevalent examples.

A membrane with a single nanopore can be used as a dividing wall in an

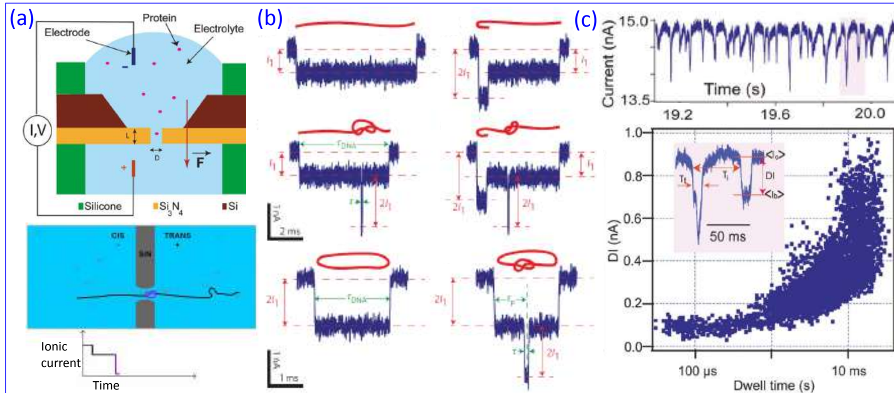

Figure 3.1: Operation principle of nanopore molecular detectors [100, 101]. (a) Solid-state membrane with a nanopore serves as a dividing wall in an electrolytic cell and single-macromolecule translocations can be detected *via* the modification of the ionic conduction. (b) Example events for different DNA confromations translocating through a 10 nm diameter solid-state nanopore [101]. (c) A typical protein translocation experiment. Top plot gives a current trace in the presence of protein molecules. Highlighted individual blockages are shown with increased temporal resolution in the event scatter plot of dwell time versus current blockade, shown below [100].

electrochemical cell, and molecular translocation events can be electrically detected through blockage-induced ionic current modifications as shown in Figure 3.1 (a). This enables extremely sensitive detection of single molecules and even the determination of their conformation states, as demonstrated in the example outlined in Figure 3.1 (b) through discrimination of folded and unfolded proteins [100] as well as observation of DNA knots [101]. The blockades that provide a detection signal are illustrated in the top panel of Figure 3.1 (c), where each dip in the ionic current corresponds to a single molecular translocation event. Conductance variations and dwell time observations can be visualized as scatter plots and subjected to statistic analysis to deduce certain geometric features of macromolecules present in the electrolyte. Furthermore, additional flexibility is afforded by various methods of either coating the membrane to change the electrostatic boundary conditions, or functionalizing it with organic compounds that possess specific affinities to certain molecules.

In this work, conducted in collaboration with the company "Nanopore Solutions Lda" based in Portugal, controlled FIB milling of sub-10 nm diameter solid-state nanopores in $10-30$ nm thickness Si_3N_4 membranes was performed [102]. Effects of the ion beam dose as well as its intensity distribution on the depth profile of the pore were investigated. Further shrinkage of the nanoscale perforations when exposed to electron beam raster scanning was demonstrated. Finally, examples of editing and sculpting of patterns milled in membranes *via* scanning electron exposure are presented.

3.1.1 Ion beam perforation of membranes

Solid-state nanometer-thickness membranes represent a unique platform that enables the exploration of nanoscale phenomena along one dimension whilst being simple to handle during fabrication and experimental characterization due to being macroscopic laterally. Their creation is quite simple and involves chemical vapor deposition (CVD) of a desired Si_3N_4 layer thickness on a Si wafer, followed by a subsequent self-limiting back-side wet chemical silicon etching to expose a nitride section of some predefined size that is ringed by a robust Si wafer frame [103]. Furthermore Si_3N_4 membranes are widely available commercially as TEM windows. The silicon nitride membranes used for this work ranged from 10 nm to 30 nm in thickness and were supplied by "Nanopore Solutions Lda".

Figure 3.2 provides a sketch of the membrane chip and illustrates the process for FIB generation of nanopores employed here. One of the key advantages of perforating Si_3N_4 membranes by FIB is the straightforward nature of the process. No resist coating or chemical processing steps are required, and metalization is only optional for easier subsequent imaging. Since single-dot holes can be induced rapidly within a few milliseconds, we can avoid pattern distortions due to charge buildup observed when milling more complex structures [31]. Hence, creation of solid-state membrane nanopores is one of the few cases where FIB

possesses a sufficiently high throughput for industrial scale fabrication.

However, the Raith ionLINE Plus FIB lithography system employed for the fabrication was only capable of using scanning ion microscopy for imaging, which (i) cannot penetrate the Si_3N_4 surface, hence, cannot distinguish between the thin membrane region and the surrounding frame, and (ii) is destructive and can easily compromise the integrity of a membrane. While this imaging issue could be resolved by equipping the FIB tool with an auxiliary electron column, here a much more affordable workaround, leveraging the high precision positioning stage of this system, was employed. To this end reference markers, depicted on the lower-left of Figure 3.2, were inscribed on the chip periphery using a 100 kHz operation frequency, $\lambda = 1030$ nm wavelength and 230 fs pulse duration PHAROS Yb:KGW laser (Light Conversion, Ltd.) at a known distance from the membrane window, as determined by optical imaging. These markers could then be safely imaged by FIB and used for stage alignment as well as substrate positioning so that the beam is directed into the membrane.

Generation of the smallest possible diameter nanopore necessitates the use of tightly focused beams, best achieved when using low ion currents on the order of a few picoamperes. The milling itself is brief even at such low currents, however, and proceeds as sketched in the top-left of Figure 3.3. The first stage of any lithographic fabrication process development, be it photon, electron

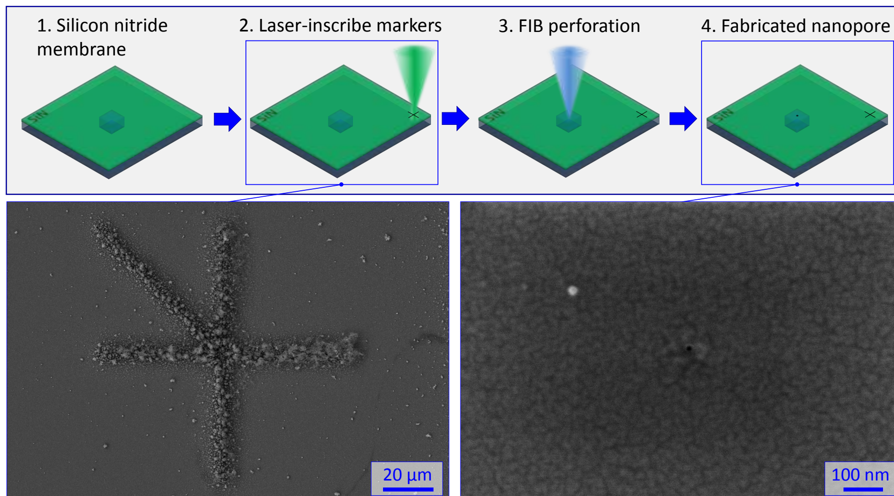

Figure 3.2: Solid-state nanopore creation in a 20×20 µm^2 area 10 nm to 30 nm thickness Si_3N_4 membrane using FIB. First, a marker is inscribed on the chip periphery for rapid reference of the membrane window. The thin Si_3N_4 layer is then perforated with a single-shot FIB exposure. Lower panels provide the SEM images of the laser-inscribed marker as well as of a typical solid-state nanopore.

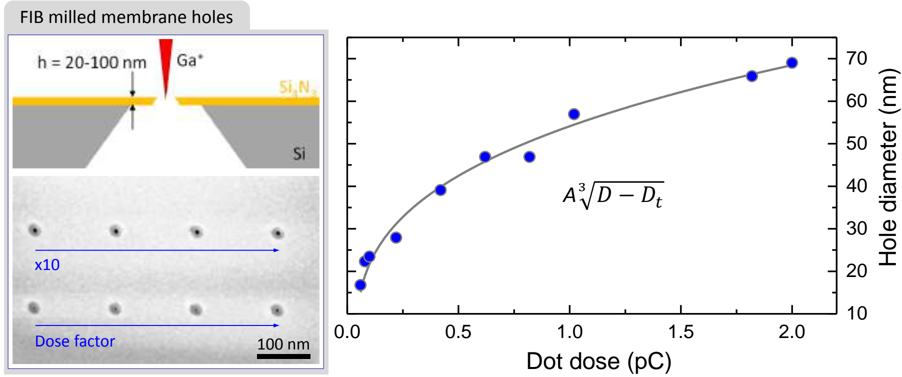

Figure 3.3: Ion irradiation dose influence on nanopore generation. Top of the left panel shows a simplified not to scale schematic sketch of FIB milling through a Si_3N_4 nano-membrane suspended on a Si frame. Lower-left provides an SEM image of pores FIB milled using incremental doses. The top row was created using one order of magnitude higher exposure doses than the bottom row. Graph on the right plots the nano-pore diameter dependence on ion dose for a 30 nm thick Si_3N_4 membrane.

or ion based, starts with deducing the optimal exposure doses to attain the requisite patterns. Here it was done by milling an array of single-pixel spots, each over an incrementally higher duration that linearly corresponds to the ion dose. A representative segment of an ion beam exposure dose matrix is given on the lower-left of Figure 3.3. Predictably, the threshold Ga^+ ion dose required to breach through the membrane is dependent on its thickness. For a 10 nm thickness membrane a pore was formed at a $\approx$0.01 pC dose, when the membrane was 20 nm thick a dose of $\approx$0.02 pC was needed, whereas for a 30 nm membrane a hole could be detected at a dose of $\approx$0.06 pC. As the dose is increased beyond the threshold value the resultant pore diameter progressively becomes larger in rough accordance to a $d \sim (D-D_t)^{1/3}$ dependence, as shown on the right side of Figure 3.3.

The dose dependence of nanopore diameter as well as their shape is governed by the radial intensity profile of the focused ion beam. The damage patterns observed around FIB-milled pores are consistent with an FIB current distribution that is comprised of two Gaussian central components, one much more acute than the other, and an exponential low intensity peripheral contribution [104, 105]. A schematic representation of a focused ion beam intensity is shown in Figure 3.4 (a), and both schematic and SEM examples of how this beam intensity profile is transferred into the membrane are given in Figure 3.4 (b). In this particular case, the high intensity central part of the ion beam has a FWHM of $\approx$9 nm and, at threshold dose, it produces a small pore, depicted in the first panel of Figure 3.4 (b). As the dose is increased

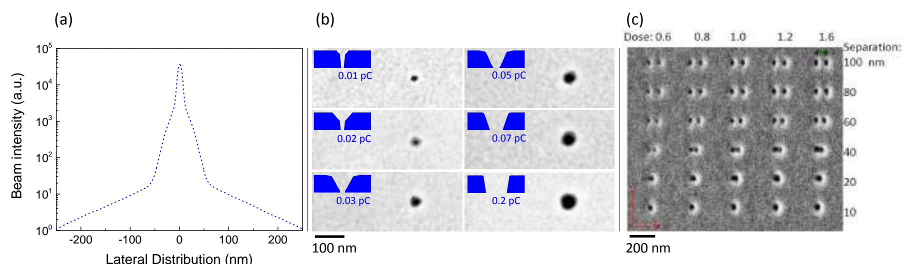

Figure 3.4: (a) Estimated FIB cross-sectional intensity distribution, comprised of two Gaussian contributions at the core and a much weaker exponentially diminishing peripheral sheath. (b) SEM images of nanopores milled using different beam doses, which show how the beam intensity profile becomes imprinted into the 20 nm thickness Si_3N_4 membrane. (c) Scanning FIB image of a dose and proximity test matrix for nanopore milling.

further the second Gaussian component with a ≈40 nm FWHM starts to remove material around the initial perforation, thereby widening the hole and giving it a funnel-like shape. If the ion beam exposure duration is increased further still, the central part of the second Gaussian component completely breaches through the membrane, and additional milling proceeds only around its low-intensity periphery, hence, at that stage pore diameter is only weakly dependent on dose. The exponential tail of the beam distribution has no appreciable effect on milling beyond slight re-sputtering of gold into particles, observable around the pores as a bright halo.

Figure 3.4 (c) provides a scanning FIB secondary electron image of the hole milling dose and proximity matrix, which can be used to deduce the maximum resolution of patterns milled into a membrane. As described previously, the resolution is mostly limited by the FWHM values of the two central Gaussian intensity components. Therefore milling of membranes provides an expedient way to evaluate the intensity distribution of a focused beam, as its small thickness gives a precise measurement scale and allows to probe the low intensity segments of the beam by avoiding distortions due to redeposition effects.

As is evident from the images in Figure 3.4, the resolution afforded by SEM is insufficient to discern the precise dimensions or shape of a 10 nm scale nanopore. Transmission electron microscopy is far more capable in this regard, as can be seen in the left panel of Figure 3.5, especially since the samples are already extraordinarily thin, *i.e.* 20 nm across, and highly translucent, nanoscale membranes particularly compatible with TEM. Here, the FIB milled nanopore is represented by the bright spot at the center, which is approximately 12.9 nm in diameter and is close to circular in shape – both desirable traits for single-molecule sensing. The TEM image shown in Figure 3.5 was acquired after a full compliment of macromolecule translocation experiments and was the same

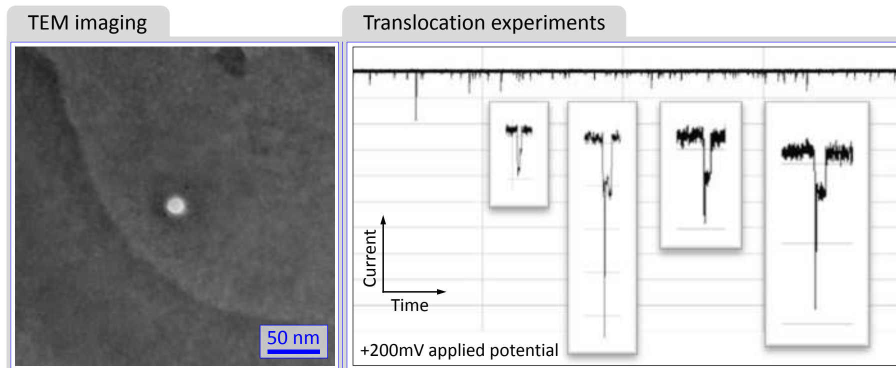

Figure 3.5: Experimental investigation of nanopore performance. Left panel shows a TEM image of a nanopore after extended translocation experiments. Its precise diameter was found to be 12.9 nm. Plot on the right side gives a general overview of 48.5kb phage lambda DNA translocation experiments in an electrochemical flow cell. Insets show close-up views of current blockage signatures; such events were on average 2 µs in duration. TEM and flow cell experiments were performed by specialists at Nanopore Solutions Lda.

in size as just after fabrication. This, in turn, highlights the key feature of solid state nanopores generated by FIB milling, *i.e.* their robustness, essential to attaining experimental reproducibility during routine analytical work.

Performance tests on the nanopore device were conducted by Nanopore Solutions Lda, and involved mounting the chips as a dividing wall in an electrochemical flow cell containing a 1 M KCl and a 10 mM 4-(2-hydroxyethyl)-1-piperazineethanesulfonic acid (HEPES) buffer mixture, tailored to maintain a pH 8.0, reasonably close to the typical physiological pH 7.4 in the human body. Signals were filtered up to a 20 kHz frequency and the digital sampling rate was 50 kHz. The nanopore membrane exhibited consistent ionic currents that responded linearly to applied potential. Molecular translocation experiments were performed by adding 48.5kb phage lambda DNA to the ground side of the flow cell, and by applying a positive +200 mV bias potential and pulling the negatively charged genome through the pore towards the working electrode. As mentioned previously, macromolecule translocation events cause K^+ and Cl^- ionic current blockages and appear as dips in the temporal current trace, as can be discerned in the plot on the right of Figure 3.5. Expanded current dips are shown as insets and were, on average, 2 µs in duration with notable consistency. Overall, conductivity and translocation experiments show that nanopores FIB milled through a 20 nm thickness Si_3N_4 membrane exhibit excellent stability and electrical behavior.

3.1.2 Electron beam sculpting

The initial nanopore perforations described here were approximately 13 nm in diameter. The FIB milling conditions for the prototype samples were set such that ion exposure dose was 25% above the estimated penetration dose, hence, attainable diameters could potentially be further decreased to somewhat below 10 nm, which is the ultimate limitation set by the sharpest Gaussian intensity distribution at the axis of a Ga^+ ion beam focused by a Raith ionLINE Plus system. However, for highest single-molecular sensitivities a pore should ideally be of macromolecular dimensions, *i.e.* anywhere between 1 nm and 10 nm in diameter.

For added process flexibility nanopore diameters can be further scaled down and fine-tuned by way of iterative scanning using a low energy 5 keV electron beam [99, 106], as shown in the left panel of Figure 3.6. Here, SEM images of a single nanopore, sequentially acquired one after another, are stacked from top to bottom and show the gradual closure of the opening. This shrinkage is typically understood as arising due to electron beam induced deposition of ambient hydrocarbons from the microscope chamber [106, 107]. The pore closure rate linearly depends on electron dose [107], and in practice means an inverse dependence on the area of scan, S [nm^2], scan repetition rate, v_s [loops/s] as well as direct scaling with beam current, which was kept constant over the

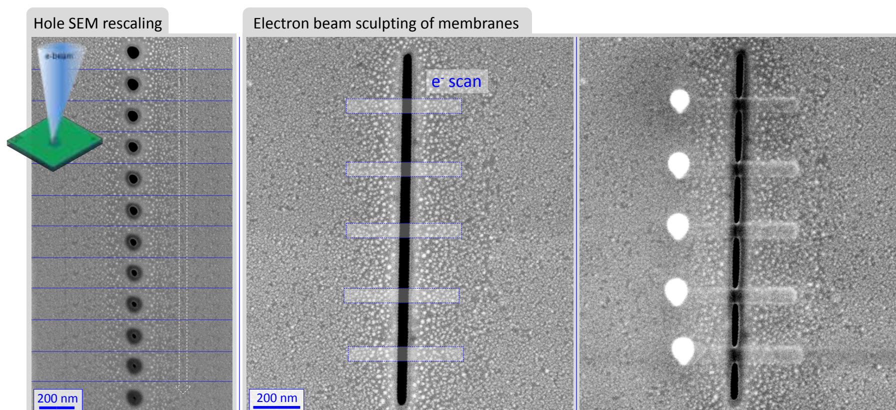

Figure 3.6: Nanopore shrinkage under electron beam irradiation. Left panel depicts sequential SEM images, arranged from top to bottom, showing the gradual closure of a nanopore during imaging, as shown in the inset. The two SEM images on the right depict a FIB incision in a 30 nm thickness Si_3N_4 membrane before and after 5 keV electron beam sculpting. Shaded regions mark areas over which electron beam scanning was to be conducted. Bright spots on the left side of the exposure regions arise due to charge accumulation in the position where the beam dwells between scans.

course of these experiments. Since nanopore closure and sample imaging occur simultaneously, the process can be conducted with a high degree of control over the ultimate result.

Electron beam induced alterations of membrane incisions are not limited in their applicability to isolated perforations and can be generalized into editing and stitching more complex membrane-milled patterns. A simple example of the concept is provided on the left side of Figure 3.6, where a line was first FIB milled into a 30 nm thickness Si_3N_4 membrane, then stitched back together using electron beam scanning. By adjusting the electron beam scanning direction with respect to a milled groove, bridges that span a nanoscale gap can be formed, as shown in the SEM image on the very right of the same Figure. As a further point of interest, this method can be used to create overlapping 3D patterns from initially planar FIB milled membrane patterns. On the other hand, a completely opposite effect of electron beam cutting through 20-30 nm-diameter polymerized free standing rods was carried out using SEM imaging as well [108].

Surface charging represents another important electron-related effect in FIB milling that, as mentioned in Section 1.2.2, tends to hamper fidelity and precision of nanoscale engraving or cutting by inducing pattern distortion or substrate drift. While the low beam currents and microsecond exposure durations offer little opportunity for notable charge accumulation during nanopore drilling in membranes, it can become substantial when more elaborate patterns have to be carved. During longer milling sessions substrate charging can be resolved by either coating it with a thin over-layer of metal, or by exploiting the photoelectric effect by way of deep-UV co-illumination [109]. These two approaches allow for real-time feedback during milling by detecting the emitted secondary electrons, which make it particularly evident when a membrane has been milled all the way through. Conversely, this signal gets drowned out if a more conventional electron flood gun charge compensation method is employed.

In summary, this work illustrates one of the few fields where FIB milling provides sufficient throughput for industrial fabrication – production of nanopore single-molecule sensing devices. Ion beams were shown to be capable of creating 10 nm diameter scale solid-state nanopores in $10-30$ nm thickness Si_3N_4 membranes. The axial focused ion beam current distribution is imprinted into the membrane during milling, and the central high intensity Gaussian portion of the beam determines the lowest achievable hole diameter. Molecular translocation experiments show that FIB milled nanopores possess excellent mechanical and electrical stability. Lastly, methods of editing and sculpting of patterns milled in membranes *via* scanning electron exposure are presented, however, such modified pores may be notably less stable.

When the nanoscale precision subtractive direct material modification, enabled by FIB milling systems, is combined with lithographic pattern generation capabilities, quite elaborate structures can be fashioned on a wide range of substrate materials. Furthermore, since pattern transfer is performed directly by focused ion beam induced sputtering, generally no resists or chemical treatment steps are required. This, in turn, makes it relatively straightforward to perform FIB lithography on even the most fragile of substrates. On the other hand, as was mentioned in Section 1.2.2, the serial scanning nature and low yield of FIB milling makes extensive reshaping of macroscopic surface areas technologically unfeasible.

In addition to the macromolecular scale solid-state nanopore perforation relevant to biophysics, which lies at the very limit of Ga^+ ion beam system resolution, nanophotonics provides a further avenue where the unique advantages of the FIB lithography technique are readily apparent. The 10 nm patterning resolution is more than sufficient to generate subwavelength structures that remain functional throughout the visible wavelength region and even beyond, as exemplified by the creation of confined mode devices such as photonic crystals [110, 111] as well as plasmonic patterns [112]. In addition to control over the localization of optical energy, deterministically aligned subwavelength structures can be employed to act as polarization-selective filters, the most prevalent of which are wire grid polarizers [113, 114]. The major advantages of these devices are their large spectral range, small footprint, and large acceptance angles. The high resolution afforded by FIB milling enables the creation of metal wire grid structures that remain subwavelength up to deep UV wavelengths [115], thus ensuring that only the zeroth diffraction order is allowed to propagate.

In this work, conducted in collaboration with the research group headed by Prof. Junko Morikawa at Tokyo Institute of Technology, FIB lithography was used to create 200 nm period 0.5 duty cycle Au gratings on an ultrathin 30 µm thickness sapphire wafer. These, in turn, were employed as reference samples to test a spatially resolved Fourier-transform IR microspectroscopy algorithm for the visualization of the degree of molecular orientation by way of absorbance images measured through a linear polarizer settled at four different angles [116]. Mid-IR absorbance mapping experiments were performed at the Australian Synchrotron Infrared Microspectroscopy Beamline, hence, in a spectral region where nanoscale FIB-milled gratings are exceedingly subwavelength. Veracity of the four polarization method was further validated by applying it to more complex molecular structures, such as poly-hydroxybutyrate (PHB) and poly-L-lactic acid (PLLA) spherulites, as well as silk fiber slices, all of which exhibit pronounced molecular alignment.

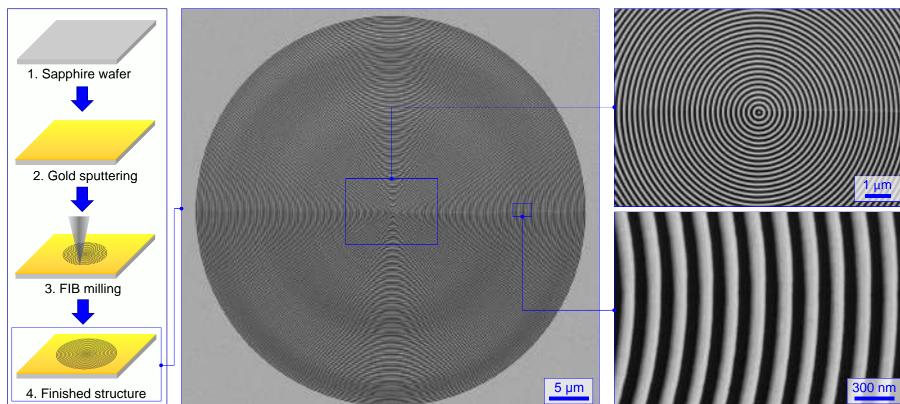

Figure 3.7: FIB lithography fabrication of 200 nm period 0.5 duty cycle Au concentric gratings on a 30 µm thickness sapphre wafer substrate. The proceedure is exceedingly simple, and involves only the sputter deposition of 100 nm thickness Au layer and subsequent Ga^{+} FIB pattering. SEM micrographs illustrate a 50 µm diameter concentric grating, and close-up images are provided on the right.

3.2.1 Fabrication of nanoscale-period concentric Au gratings

The principal features of a good quality wire grid polarizer device are a strong rejection of transverse electric (TE) modes and simultaneous high transmittance of transverse magnetic (TM) radiation. Furthermore, it is preferable for a polarizer to exhibit a consistent performance throughout a broad spectral region, especially when it is expected to be used in spectroscopy. Due to these considerations optical grade sapphire, with its $\lambda = 0.2$ to 5 µm optimal transmittance range, was chosen as the substrate material. The radiation fraction absorbed at the mid-IR edge of the transparency window was further limited by choosing the thinnest crystalline sapphire wafers available, which in the present case were 30 µm in thickness (Tecdia Ltd.).

As mentioned previously, FIB milling-based lithography processes in most cases are exceedingly straightforward, as illustrated in Figure 3.7, since they do not require resist films with special sensitivity to the method of irradiation, thus effectively combining exposure and pattern transfer steps. The ultrathin sapphire substrate was first magnetron sputtered with a 5 nm thickness Cr adhesion layer, followed by a 100 nm optically active Au film, in a AXXIS physical vapor deposition tool (Kurt J. Lesker). The 200 nm period and 0.5 duty cycle gratings, in both concentric and parallel configurations, were inscribed into the metal film using a a Raith ionLINE Plus Ga^{+} ion beam lithography system (Raith GmbH). Patterning was performed using a 70 pA beam current of ions accelerated using a 35 kV voltage and focused down to an approximately

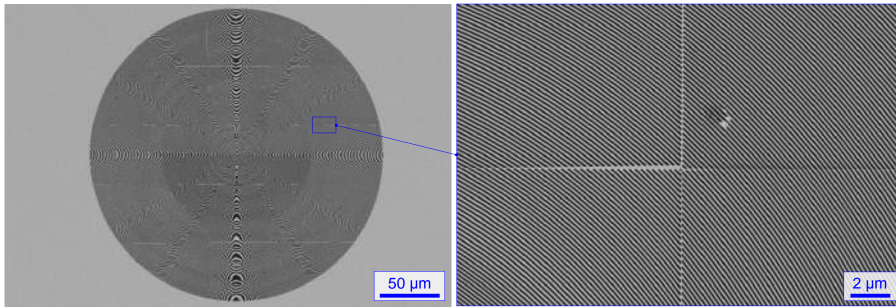

Figure 3.8: SEM image of a 250 μm diameter concentric 200 nm period grating, FIB patterned over 5 × 5 write-fields 50 μm across. Close-up image on the right shows the stitching defects that occur due to faults in write-field alignment.

45 nm diameter beam spot, as an adequate compromise between patterning rate and attainable resolution of structural features.

In addition to beam settings, pattern scanning parameters also profoundly affect the polarizer grating milling duration. The primary options are whether the grating slits are interpreted as raster-scanned polygons or beam paths. Wherever applicable path-type scanning is preferable, as it is subject to a lower computational processing overhead and is far easier to optimize dose conditions for. On the other hand, geometrical shapes with extended areas can be defined more naturally as polygons. Furthermore, milling can be conducted as a single pass, or over numerous repeated patterning loops. The main advantage of single-pass milling is, again, speed, however, the drawback is lower quality of resultant features as, in the present case, gold gets re-sputtered on the milled grooves, thereby lowering their overall optical transmittance. Like was mentioned in Section 1.2.2, the way of limiting redepositiong involves FIB milling over numerous repeated loops, but this can severely increase the process duration due additional beam blanking, which, in turn, results in more time for detrimental thermal or electrostatic drift to distort the fabricated structure. The Au gratings, one of which is depicted by the SEM images in Figure 3.7, were patterned by milling each groove as two explicitly defined beam path trajectories, which were nearly identical yet offset by $\sim$ 25 nm from each other to attain the full 100 nm incision width. By doing two passes of each feature individually, re-sputtering was significantly suppressed and drift-related distortion was prevented from affecting the pattern in its entirety.

The fabrication write-field in this work was limited to a 50×50 μm^2 square region, therefore, the concentric grating depicted in Figure 3.7 can be defined without any movement of the sample stage. However, considerably larger 100 μm and 250 μm diameter concentric grating structures were likewise prepared, where fracturing the pattern into multiple segments and performing write-field stitching becomes inevitable. This gives rise to one of the most

severe limitations of high resolution scanning particle beam lithography approaches, as such mechanical movements are sure to result in pattern defects, which manifest most strongly when long continuous features, such as waveguides or slits, need to be generated seamlessly. Write-field stitching defects are readily apparent in Figure 3.8, where a 250 μm diameter concentric grating was milled by sequentially processing each of the 5×5 squares 50 μm in width. The average processing duration for a single write-field is close to two hours, so any mechanical misalignment of the interferometrically controlled piezoelectric sample stage is further compounded by drift effects, resulting to stitching offsets as large as 100 nm, depicted in the close-up SEM image on the right side of the same figure.

While further fidelity improvements could potentially be attained through optimizing the process, say, by forcing a certain amount of overlap between adjacent write-fields, the present accuracy is completely adequate for uses in the mid-IR region of primary relevance here. Regardless, this example reveals most relevant features of basic FIB lithography fabrication, its advantages include straightforward direct material processing and a high resolution, with notable shortcomings being write-field stitching issues and a low throughput, where the milling duration of a 0.5 duty cycle 250 μm diameter concentric grating is close to 48 hours.

3.2.2 Mid-IR characterization of orientationally anisotropic systems

The purpose of FIB milled concentric gratings was to be reference samples for rigorously testing the validity of the four angle polarization procedure used to visualize the degree of in-plane molecular orientation by way of mid-IR Fourier-transform infrared spectroscopic imaging [117]. To this end, absorbance spectra have to be acquired at each pixel using two pairs of orthogonal incident radiation polarization states. In spectroscopy, absorbance A of polarized radiation is expressed as a scalar product:

$$A \propto (\mathbf{p} \cdot \mathbf{M})^2 = (pM \cos \mu)^2, \tag{3.1}$$

where μ is the angle between the transition moment vector $\mathbf{M}$ and the electric field vector of the incident polarized beam $\mathbf{p}$. In practice, the absorbance of polarized radiation corresponds to the aggregate absorbance for all molecular vibration transition moments within the measurement area, and for samples exhibiting some average anisotropy a sine-like orientational dependence is expected [116]. The four different $\pi/4$ offset polarization absorbance maps, required for this analysis, merely represent the minimum number of data points necessary to unambiguously determine this sinusoidal dependence by performing curve fitting.

Mid-IR hyperspectral imaging measurements described in this work were performed at the Australian Synchrotron Infrared Microspectroscopy Beamline, using a Hyperion 2000 infrared microscope, coupled to a Vertex V80v

Fourier-transform infrared spectrometer (Bruker Corp.). Far-field transmittance measurements were conducted using a $NA = 0.5$ Cassegranian lens with 36× magnification, a ZnSe wire grid linear polarizer (Speacac Ltd.) was employed to set the polarization of both the incident and transmitted radiation fields, whereas detection was realized using a nitrogen-cooled mercury cadmium telluride narrow-band detector. The microscopy setup was capable of focusing mid-IR radiation down to a 4.1 µm spot size, which sets the hyperspectral mapping resolution attainable by the system.

Top-left panel of Figure 3.9 depicts a transmittance mode optical microscopy image of different diameter concentric circular gratings, FIB milled into 100 nm thickness Au films on a 30 µm sapphire wafer. Reference orientational absorbance mapping was primarily conducted on the 50 µm concentric grating due to the higher overall quality of the structure as well as its more manageable area size. The four mapping plots shown on the right side of Figure 3.9 correspond to this particular circular grating, and represent mid-IR transmittance, expressed as absorbance $A = -\lg T$, at different wavelengths. Evidently,

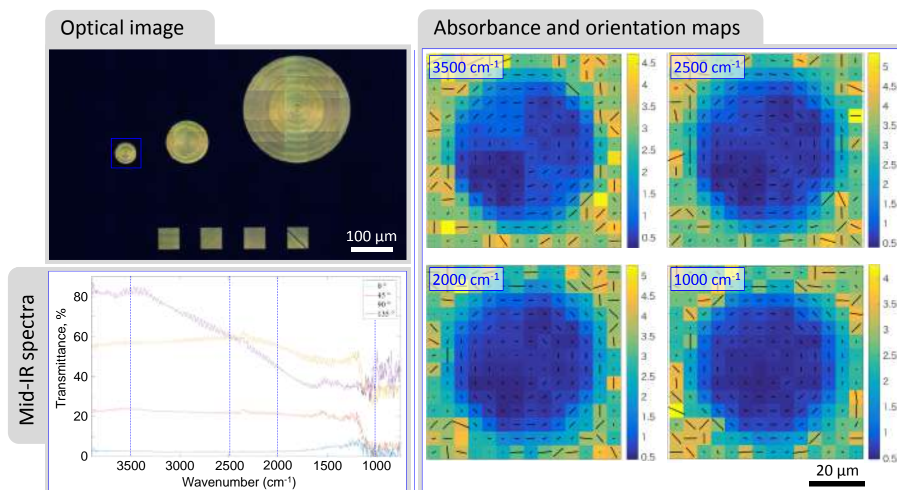

Figure 3.9: Mid-IR characterization of FIB milled reference grating patterns, used for calibration of the four polarization method-based absorbance and retardance hyperspectral maping algorithm. Image on the top-left provides a visible wavelength micrograph acquired in transmission mode. Plot bottom-left shows the transmittance spectra at a single point of the concentric grating for each of the four polarizations. Plots on the right depict average absorbance color maps, overlayed with a orientation vector distributions depicted by black bars, at different spectral positions. The four polarization analysis algorithm was developed and executed at Tokyo Institute of Technology by the research group under supervision of Prof. Junko Morikawa.

transmittance is at its highest in the FIB milled region, and corresponding single-pixel spectra for different polarizations of incident radiation are plotted lower-left. The circular grooves of the grating produce a local orientation-derived selectivity to polarization that gradually changes based on the spatial position. When the polarization of an incident electric field is colinear to the slit tangent the transmittance is negligible. Conversely, when the concentric grating tangent is at a right angle to the polarization of the incident radiation, transmittance can be as high as 80%, although for longer probe wavelengths some cut-off is observed due to the curvature of the slits acting as a spatial filter. Overall, FIB milled 200 nm period circular Au gratings exhibit an extinction ratio of $T_{\text{max}}/T_{\text{min}} \approx 150$.

The black bars overlaying the spatial absorbance plots in Figure 3.9 represent the orientation vector map of hypothetical incident radiation polarization states that would be most strongly rejected by the concentric wire grid. Their orientation angle θ at each pixel is determined based on the four polarization method according to the equation [116]:

$$\theta = \frac{1}{2}\arctan\left(\frac{A_{\phi_3} - A_{\phi_1}}{A_{\phi_4} - A_{\phi_2}}\right), \tag{3.2}$$

where absorbances $A_{\phi_{1,2,3,4}}$ correspond to values at the four $\pi/4$-spaced polarization azimuths. On the other hand, the length of the bar $Amp = A_{\text{max}} - A_{\text{min}}$ represents the difference between maximum and minimum polarization-dependent absorbance, and is defined as:

$$Amp = \sqrt{(A_{\phi_4} - A_{\phi_2})^2 + (A_{\phi_3} - A_{\phi_1})^2}. \tag{3.3}$$

The experimental orientation vector map of the concentric grating, determined using the four polarization method, is fully in line with its wire grid polarizer-like performance. Furthermore, the structure is highly broadband, and preserves its orientationally selective transmittance all the way to the cut-off at wavenumbers beyond 1000 cm^{-1}, induced by absorbance in the sapphire substrate.

However, while the rigorously patterned concentric polarizer grating example is instructive and provides a necessary point of reference, the primary purpose of the four polarization method is to investigate the alignment effects in complex molecular systems. Figure 3.10 provides examples of just such anisotropic polymer samples, namely poly-hydroxybutyrate (PHB) and poly-L-lactic acid (PLLA) spherulite structures, as well as a drawn fiber of natural silk. Spherulites are supermolecular structures that crystallize from a viscous molten linear polymer as highly ordered arrangements of molecular lamellae [118]. The top row of the figure represents PHB, which is a lower symmetry polymer were lamella crystallize with a radial twist, that optically manifests as a series of bright and dark bands in which the molecule is flat-on and edge-on with respect to incident light, respectively. Asymmetric CH_3 and CH_2 stretch vibration

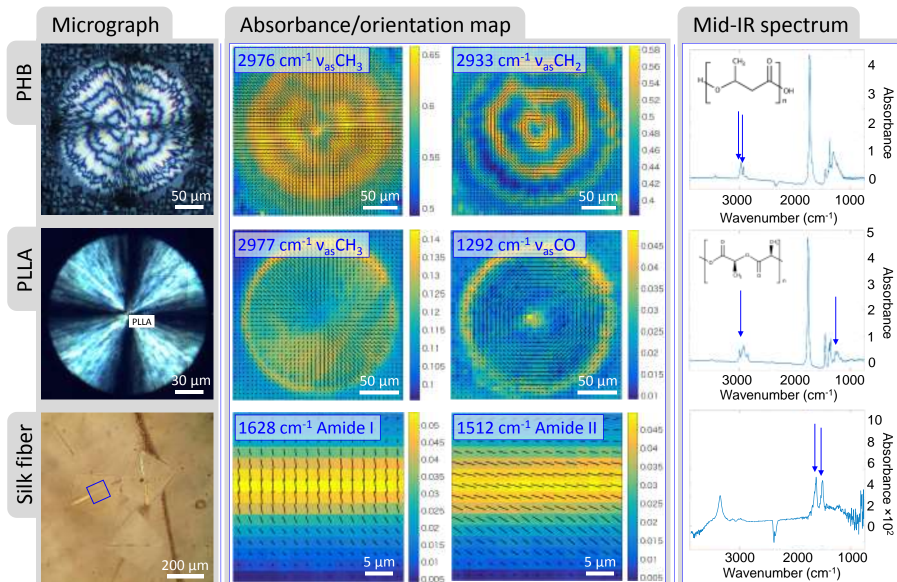

Figure 3.10: Examples of four polarization method application for determining the orientational absorption anisotropy in systems that exhibit molecular alignment. Leftmost column depicts the optical cross-polarised microscopy images of PHB and PLLA spherulites, as well as ultrathin slices of epoxy-embeded silk fibers. Spatial mapping plots in the middle display the average absorbance and orientation vector distributions for the respective systems at relevant mid-IR absorbance bands corresponding to orthogonal dipole transitions, marked by blue arrows in the spectra plotted on the right. The four polarization analysis algorithm was devised and executed at Tokyo Institute of Technology by the research group under supervision of Prof. Junko Morikawa.

modes at 2976 cm^{-1} and 2933 cm^{-1} represent orthogonal vibrations transverse and colinear to the polymer chain. The absorbance and orientation vector maps for PHB, depicted in Figure 3.10 for each of the two vibrations, reveal the average in-plane orientation of crystallized polymer chains.

Four polarization method-derived mid-IR orientation vector maps for a PLLA spherulite, depicted in the middle row of Figure 3.10, which, due to the higher symmetry of the macromolecule, fail to exhibit helical twists observed for PHB and therefore possesses a much more simple radial distribution of crystalline lamellas [119], also visible in the cross-polarized image on the left. Here, orthogonal molecular modes of choice are 2976 cm^{-1} wavenumber asymmetric CH_3 radical and 1292 cm^{-1} CO backbone vibrations, which represent radial and concentric orientational distributions respectively.

Lastly, the bottom row of Figure 3.10 depicts the mid-IR microspectroscopic molecular absorbance and alignment orientation maps for amide I and

amide II bands for a single silk fiber. Here, the silk embedded in epoxy and cut into 0.1 μm thickness slices using a cryo-microtome. Silk fibroin is a protein composite with multiple possible conformation states, such as random coils, α-helices and β-sheets, which in natural fibers form a complex network. However, amide I signatures are definitively assigned to C=O stretching with contributions from the out-of-phase C–N stretch, the C–C–N deformation and the N-H in-plane bending vibrations [120], and their orientation is primarily directed transversely to the stretched fiber and is likely indicative of the most prevalent direction along which hydrogen bonding proceeds. Conversely, amide II band arises due to out-of-phase combined N—H bending and C—N stretching vibrations [120], which are more strongly affected by the protein backbone and is largely indifferent to side chain conformation. Therefore, it is unsurprising that four polarization method-derived amide II orientation vectors are pointed along the direction in which the fiber was pulled.

Overall, FIB milling enabled the creation of 200 nm period 0.5 duty cycle Au polarizer gratings with nanoscale precision. Furthermore, no resists, hence, minimal preparation and chemical processing are required, which allows fabrication of complex structures on thin and fragile substrates. In this work concentric subwavelength gratings enabled the verification of the four polarization method for determining the molecular alignment in complex anisotropic materials. However, FIB milled metal patterns can also be used to perform different advanced optical functionalities, and are not necessarily confined to planar 2D surfaces, as described in the next section.

3.3 Curved micro-optical spiral zone plates

Among the key advantages of FIB milling-based lithography techniques is that their nanoscale resolution patterning capabilities extend not only laterally, but can also directly remove material to a specified depth, thus allowing for the creation of 3D topologies with great precision. Furthermore, this feature is bolstered by the large depth of focus of ion beams, which, in addition to helping maintain consistent milling rates, does not require the fabrication substrate surface to be strictly planar. Taken together, these properties of FIB-based fabrication approaches afford notable flexibility when creating devices with functionalities that rely on complex geometric arrangements.

One way that such capabilities can be leveraged involves the creation of miniaturized and hybridized optical systems that combine multiple optical functionalities within a single structure. An example of this trend is the lithographic fabrication of micro-lens arrays for multi-spot illumination or multi-aperture detectors, where photoresist reflow is employed to create micro-lenses and a subsequent laser writing step inscribes a diffractive phase correction element [121]. Such hybridization is pursued either to circumvent limitations in fabrication method, as in the aforementioned example, or when several independent optical functions have to be fulfilled by a single element. A noteworthy illustration of the latter concept is provided by the monolithic integration of dielectric axicons and spiral phase plates into helical axicons, fabricated by 3D laser photopolymerization, tailored for generating higher-order Bessel beams [122]. Not restricted to refractive elements, this concept was likewise employed for realization of multiplexed 2D metallic metasurface holograms [123, 124].

In creating complex optical devices the nanoscale precision of the generally substractive FIB milling is particularly well complimented by the additive laser photopolymerization method. While laser-based approaches are somewhat inferior to FIB in their resolution due to diffraction limitations, they exhibit orders of magnitude higher throughputs and are inherently capable of producing arbitrary refractive dielectric structures [125] that no 2D lithographic approach could replicate without considerable expense and difficulty. In contrast, subwavelength resolution FIB milling is not particularly efficient at removing bulk material, however, can readily generate delicate patterns in opaque nanometer thickness metal films and shells, which act as diffractive elements and metasurfaces [126].

In this work, conducted in collaboration with the team of researchers headed by Dr. Mangirdas Malinauskas at Vilnius University and the group supervised by Prof. Etienne Brasselet at University of Bordeaux, additive 3D structuring capability of laser photopolymerization and the subtractive subwavelength resolution patterning of focused ion beam lithography was combined to produce hybrid dielectric/metallic micro-optical elements for the purpose of topological shaping of light [127, 128]. The concept is illustrated by fabricating spiral zone

plate (SZP) binary transmittance diffractive patterns, which enable the generation of tightly focused orbital angular momentum (OAM) carrying beams, on photopolymerized substrates of different curvatures. The cooperative refractive interaction between the individual 2D metallic and 3D dielectric sub-parts is investigated by way of FDTD simulations, and the topological beam shaping performed by the structures is validated by experimental imaging of their transmittance. The devices are shown capable of generating tightly focused vortex beams with topological charges $\ell = 1, 2$ in a single step and the optical performance of 3D structures are compared to their corresponding planar counterparts both numerically and experimentally. Results suggest that additive manufacturing methods such as 3D direct laser writing, once combined with nanoscale FIB nanofabrication technologies, pave the way towards the realization of 3D hybrid metasurfaces of high topological complexity.

3.3.1 Beam shaping by spiral zone plates

New methods for attainment of compound optical functionality and enactment of miniaturization are particularly useful in fields related to light structuring, as this phenomenon inherently necessitates complex transformations of

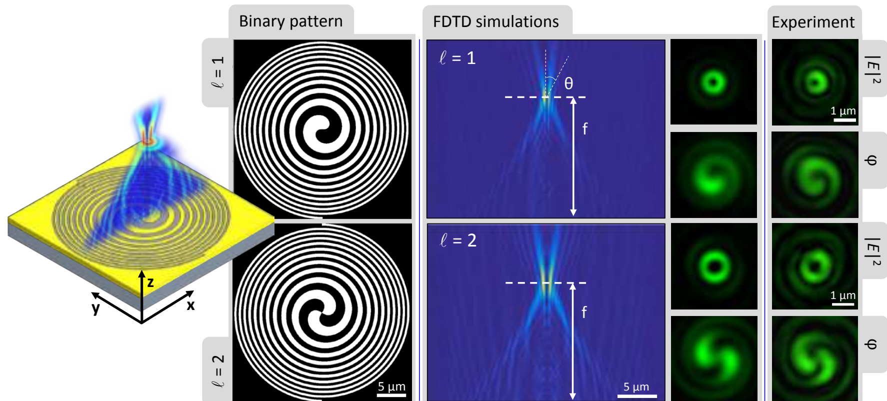

Figure 3.11: Beam shaping by a planar SZP binary pattern. Drawing illustrates the general principle of focused vortex beam formation by a SZP. Patterns for generating $\ell = 1$ and $\ell = 2$ topological charge vortices with focal distances of 18 µm for a $\lambda = 532$ nm wavelength are shown in the top and bottom middle-left panels respectively. Corresponding FDTD simulated field intensity distributions in the $x - z$ plane parallel to the propagation direction are shown in the middle. Two leftmost columns provide simulated and experimental close-up x-y intensity as well co-axial Gaussian beam interferrogram plots in the focal region, as highlited by the dashed line. Optical characterization was performed at University of Bordeaux by the research group under supervision of Prof. Etienne Brasselet.

the optical wavefront. The resulting optical fields possess non-trivial spatial distribution of one or several characteristics such as intensity, polarization and, of primary interest in this work, phase [129, 130]. Specifically, light endowed with optical phase singularities exhibits annular transverse intensity profiles and posses an azimuthal phase dependence of the local electric field amplitude given by $exp(i\ell\varphi)$, where ϕ is the azimuthal angle and ℓ the integer topological charge [131]. The most evident feature of such an optical field is that the phase becomes indeterminate at its center, thus, field intensity is forced to zero there to prevent the formation of a physical singularity, which is why it is frequently referred to as a vortex beam.

Optical vortices provide a new dimension for controlling light-matter interaction and confer substantial benefits to several important application areas. When employed for optical tweezing/spanning, phase structured beams can trap particles with higher both axial [132] and transverse [133] efficiency when compared to a Gaussian beam of equivalent intensity, which is of particular relevance in biological applications where reduction in the incident laser power diminishes the risk of sample damage [132]. In addition, vortex beams also provide enhanced optomechanical capabilities since their topological charge ℓ carries $\ell\hbar$ orbital angular momentum per photon [131] whereas the spin angular momentum contribution is limited to $\pm\hbar$ per photon. Thus they provide additional functionality by enabling orbital rotation on top of typical spinning motion as well as providing for stable trapping of absorbing particles [134]. A completely separate field of structured light application relates to astronomy, where optical vortex phase masking can be employed to identify faint objects close to bright coherent sources for producing coronagraphs and searching for exoplanets [135, 136]. Lastly, optical communications is another field where the theoretically unlimited range of topological charge ℓ eigenstates in OAM carrying beams exhibit notable multiplexing utility [137, 138].

Typical ways of generating vortex beams of either integral of fractional topological charge type involve the use of spatial light modulators, forked diffraction gratings, phase plates or mode converters [134, 139]. Recent efforts, however, have been focused on attaining optical trapping and manipulation at the microscale, hence, tend to forgo bulky tabletop options in favor of miniaturized and integrated implementations. Examples of such devices include topological nanoslits [140], photopolymerized structures [122], metasurfaces [126, 141], as well as spiral zone plates of both plasmonic [142] and diffractive [143] varieties, the latter of which was the method of choice here.

The diffractive binary spiral zone pattern used for wavefront shaping in this work is depicted on the left side of Figure 3.11. In essence, the spiral pattern represents a convolution of the radial Hilbert transform, that generates an azimuthal phase profile, and Fresnel zone plate pattern, that diffracts light towards the optical axis, which, when taken together, give rise to a focused vortex beam in transmission. The black and white pattern is defined by a 2D

binary transmittance function t of the form [144]:

$$t(r,\varphi) = \begin{cases} 0 & \text{if} \quad (2k-1)\pi \leq \ell\varphi - \frac{\pi r^2}{\lambda f} \leq 2k\pi \\ 1 & \text{if} \quad 2k\pi \leq \ell\varphi - \frac{\pi r^2}{\lambda f} \leq (2k+1)\pi \end{cases}, \tag{3.4}$$

where the polar coordinates in the SZP plane are denoted as (r,φ), λ is the wavelength of incident light, f is the corresponding focal length, whereas the index $k = 0, -1, -2...$ defines the spiral zone number. The overall diameter of the SZP was set to be $R = 30$ µm and contained a total of 10 zones. Similarly, the topological charge index $\ell = 1,2$ is reflected in the binary SZP patterns by the number of spiral arms the structure exhibits, and determines the order of the transmitted optical vortex.

Beam shaping effects of SZP binary masks can be readily revealed by way of FDTD simulations, conducted using a commercially available Maxwell's equation solver "FDTD solutions" (Lumerical Solutions Inc). The binary transmittance pattern was defined by applying a 200 nm thickness gold layer, assuming a $n_{\text{metal}} = 0.5106 + i2.2495$ refractive index, on top of a $n_{\text{dielectric}} = 1.504$ dielectric substrate, except for the surface region denoted by Equation 3.4. A general overview cartoon image of the simulation setup is provided by the sketch on the very left of Figure 3.11. The simulation volume $x \times y \times z$ was correspondingly $44 \times 44 \times 34$ µm^3, and was segmented by a mesh grid with sizes that varied from 10 nm in close proximity to the metal mask to 60 nm at remote far-field sites. Computational region was terminated using perfectly matched layer boundary conditions, which serve to minimize any spurious reflection effects. Each simulation is performed twice, by respectively using x-polarized and y-polarized $\lambda = 532$ nm wavelength plane waves impinging from the substrate side along the z axis at normal incidence. By doing so, the response to an arbitrarily polarized illumination can be deduced by employing the linear superposition principle.

Key FDTD simulation results, illustrating the operation of SZP structures with orders $\ell = 1,2$ under circularly polarized illumination, are provided in the middle panels of Figure 3.11. In both cases numerical findings, expressed as side-view field intensity plots, predict a tight focusing behavior, where the focal distance is quite close to the value of $f = 18$ µm set by Equation 3.4. The numerical aperture of such SZPs for a $\lambda = 532$ nm wavelength can be estimated at around $NA \approx 0.64$, based on the marginal ray of the structure as $NA = \sin\theta \approx 0.67$, where $\theta = \arctan(R/f)$ is the viewing angle of the pattern. Close-up electric field intensity plots at the SZP focal plane, depicted top-right of the respective FDTD simulation panels in Figure 3.11, reveal a near diffraction limited annular pattern with a dark hollow in the center that is characteristic for Laguerre-Gaussian-like beams. Also, this assignment is further bolstered by the evident increase of the radius of the doughnut shaped intensity pattern with $|\ell|$ as expected from the well-known $\sqrt{\ell}$-behavior of

optical vortices. Lastly, the spiraling interference patterns, depicted lower-right of respective panels and obtained as a coherent superposition of the SZP transmitted field with a co-axial Gaussian beam, are, again, associated with structured light that exhibits a spiral phase front.

All of the aforementioned FDTD simulation results are recovered experimentally for planar SZP structures fabricated by FIB milling of opaque Au films, as is shown on the very right of Figure 3.11. The process for creating such vortex beam generating devices on both flat substrates as well as on curved laser photopolymerized topologies is described next.

3.3.2 Fabrication of 3D SZP structures

The fabrication procedure for producing compound functionality SZP micro-optical vortex generator structures with nontrivial surface geometry combines laser photopolymerization, capable of creating transparent 3D microstructures for refractive phase front shaping, and FIB milling of an conformally magnetron sputtered metal mask pattern, well suited for generating binary diffractive elements. Similarly, the fully planar SZP test structures, briefly mentioned in Figure 3.11 of Section 3.3.1, are created by skipping the laser polymerization step, while keeping the FIB lithography process conditions largely the same.

Figure 3.12 outlines the hybrid curved SZP micro-optical element fabrication workflow, which is comprised of independent additive laser and subtractive FIB processing steps. A thin glass cover slip was used as a substrate onto which a hybrid organic-inorganic photopolymer SZ2080, doped with 2% by weight of Irgacure 369 photoinitiator [145], was drop cast. This material is particularly suitable for fashioning various micro-optical structures due to its high mechanical robustness and, more importantly, a refractive index of $n_{\mathrm{SZ2080}} = 1.504$, that is closely matched to the $n_{\mathrm{Glass}} = 1.52$ value of glass throughout the visible spectral region [146]. Following application onto the substrate the SZ2080 resist is pre-baked on a hotplate for 60 min at 90°C to remove any excess solvent.

3D photopolymerization by direct laser writing was conducted using a PHAROS Yb:KGW 300 fs optical pulse duration laser (Light Conversion Ltd.) operating at its second harmonic wavelength $\lambda = 515$ nm with a 200 kHz repetition rate. Resist exposure was conducted from the rear-side of the cover slip under tight focusing conditions, using a 63× magnification microscope objective (Carl Zeiss AG) with oil immersion for a total $NA = 1.4$ numerical aperture. Two types of 15 μm radius circular 3D dielectric structures were polymerized – elevated flat disk pedestals with a 3 μm height, and 165° full apex angle axicons. Flat disk pedestal structures, illustrated in the lower-right SEM image in Figure 3.12, were produced under 70 μW average laser irradiation power with a corresponding pulse energy of 0.35 nJ and a 0.988 TWcm^{-2} intensity per pulse at focus, using a 0.5 mms^{-1} scanning velocity along raster trajectories with 50 nm voxel overlap. Conversely, axicons, shown bottom-right

in Figure 3.13, were polymerized at a 27.5 μW laser power, where each pulse carried a 0.14 nJ energy and the irradiance at focus was 0.388 $TWcm^{-2}$. Here the same 50 nm voxel overlap was used, however, the scanning was conducted along spiral trajectories at a 0.1 mms^{-1} velocity. Following exposure the resist with laser imprinted latent structures was immersed in a pure MIBK developer, where all unirradiated resist regions were dissolved. Lastly, the silica cover slip substrates with photopolymerized pedestals and axicons were rinsed in IPA stopper and then dried.

In preparation of FIB milling of a binary SZP transmittance mask, the dielectric structures were coated with a 200 nm thickness layer of gold, that is totally opaque to visible light. Deposition was performed in an AXXIS physical vapor deposition system (Kurt J. Lesker) from a high purity Au target by way of Ar^{+} plasma magnetron sputtering. As evidenced by the SEM images

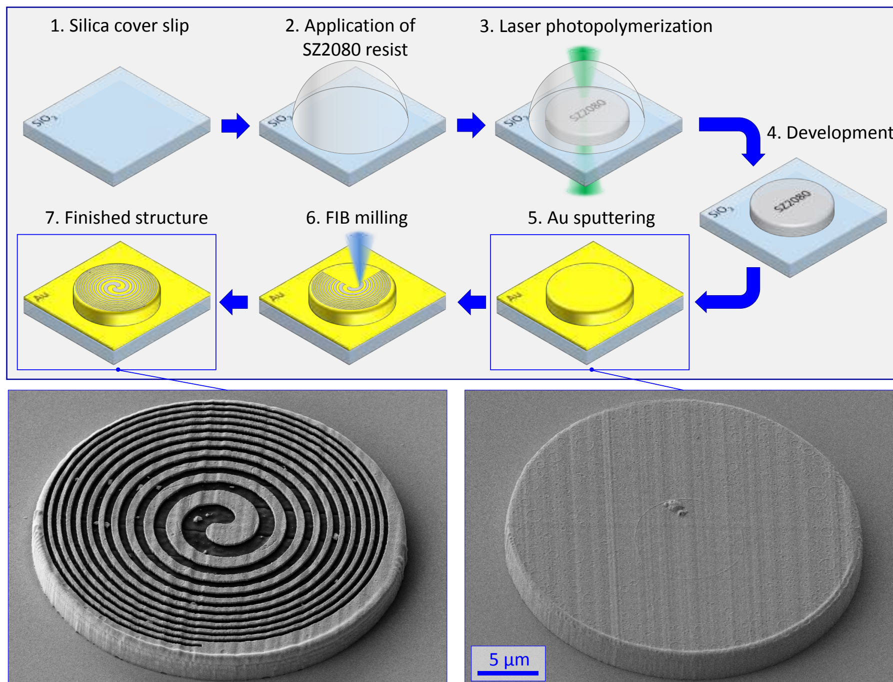

Figure 3.12: Laser photopolymerization and FIB milling based fabrication of curved SZP surfaces. The microscale dielectric pedestals were created using direct laser writing in a SZ2080 resist. The structures were sputter-coated with an opaque 200 nm conformal Au layer. Nanoscale SZP patterns were then inscribed using FIB lithography. SEM images show a planar Au coated pedestal before and after FIB processing. Laser photopolymerization was performed at Vilnius University by the research group under supervision of Dr. Mangirdas Malinauskas.

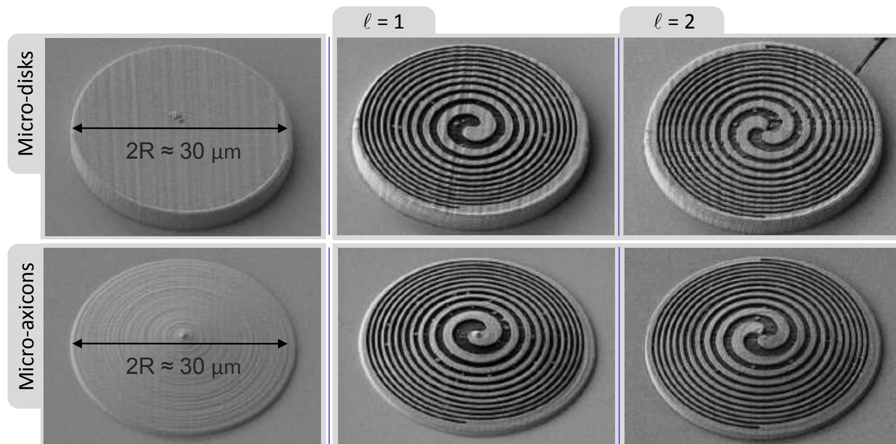

Figure 3.13: SEM images of laser photopolymerized flat disk pedestal and 165° full apex angle obtuse axicon structures, shown in top and bottom panels respectively, conformally sputter-coated with a 200 nm thickness Au film. Panels on the right provide SEM images of these structures after FIB milling vortex order $\ell = 1$ and $\ell = 2$ binary SZP patterns all the way through gold. Laser photopolymerization was performed at Vilnius University by the research group under supervision of Dr. Mangirdas Malinauskas.

in Figure 3.12, the resultant metal layer established a conformal shell around the 3D structure due to substantive scattering of Au atoms in the sputtering gas. Any residual roughness of the substrate surface is due to the finite-size polymerization voxels getting imprinted onto the resultant device as readily discernable laser scanning trajectories.

The final fabrication stage involved the milling of diffractive SZP patterns all the way through the gold film using high resolution FIB lithography, as shown in the bottom-left SEM image in Figure 3.12. Spiral zone pattern transfer was performed *via* direct removal of material using a Raith ionLINE Plus ion beam lithography system. An approximately 40 pA current of Ga^{+} ions were accelerated using a 35 kV voltage and focused down to a 25 nm diameter spot. The FIB imaging capability in conjunction with the interferometrically controlled piezoelectric stage allowed for the location and exact positioning of the pedestal structures at the very center of a 50 μm write-field, accessible to electronic deflection. Milling was performed without any further stage movement, by scanning the ion beam along the predefined spiral pattern until the 200 nm thickness Au film was completely removed. In order to avoid redeposition related effects FIB exposure was conducted over 10^4 sequential patterning loops, and the overall pattering duration for a single SZP was around 25 minutes. The strong secondary electron emission contrast between the Au shell and the underlying polymer allowed for real time feedback on the milling

process, making it reasonably clear when the metallic gold layer was fully breached.

Figure 3.13 provides representative SEM images of pedestal and obtuse axicon structures before and after FIB milling of spiral zone patterns with $\ell = 1$ and $\ell = 2$ orders. The binary transmission patterns were reproduced with high fidelity and closely follow the geometric parameters used in numerical FDTD simulations. Smallest features in the design were the spiral turns at the very periphery of the structure, which were roughly 200 nm wide, *i.e.* had a depth-to-width aspect ratio of 1. Yet, even for these challenging components, the FIB depth of focus was sufficiently high that no distortions occur even when 3 μm disparities in elevation are present. However, some residual gold islands can still be observed in the stripped sections, most likely resulting from impurities on the surface of the polymerized pedestal acting as crystallization sites for the sputtered Au, making it more resilient to ion bombardment then the rest of the structure.

Overall, FIB milling strongly complements 3D laser photopolymerization through its high patterning resolution and positioning precision. Here it is leveraged for high-fidelity sputtering of metal films, however, FIB milling can process nearly any material, hence, can be used to augment the performance of even fully dielectric structures generated by laser direct writing.

3.3.3 Characterization of focused topological beams

Optical investigation of the fabricated devices requires the experimental measurement of the propagation behavior of the transmitted light field and its comparison with numerical simulation results. Here this was accomplished by illuminating the SZP structures at normal incidence from the rear-side of the glass cover slip surface using a $\lambda = 532$ nm continuous wave laser. The incoming circularly polarized fundamental Gaussian probe beam was directed through a low numerical aperture lens, with its focal plane set to where the SZP structure was positioned. Since the Au layer thickness of 200 nm was large enough to ensure almost total opacity, the incident beam waist size w_0 was set to be double the radius R of the SZP pattern, which approximated the plane wave illumination assumed in FDTD simulations. In practice, the optical intensity profiles at a distance z from the plane of the structure were imaged using a CCD camera coupled to a 100× magnification and $NA = 0.8$ numerical aperture microscope objective. Conversely, information on beam phase profiles is obtained by recording interference patterns that result from the superposition of the transmitted optical field with a collinear Gaussian reference arm. These two types of experimental findings were previously shown in Figure 3.11, where performance of SZP structures without polymerized pedestals was first outlined.

The overall experimental transmittance behavior of micro-optical focused optical vortex beam generator structures is illustrated in Figure 3.14, where evolution of the lateral beam intensity distribution as it propagates along the z

direction away from the device plane is outlined. Evidently, intensity profiles obtained at $z = 0$ µm represent the optical images of the respective spiral zone structures. When imaging distance is increased and light propagation is allowed to proceed further, optical energy starts to concentrate along the device axis. At distances of $f \approx 20$ µm and $f \approx 15$ µm respectively for flat disk and obtuse axicon pedestals, corresponding to $NA \approx 0.6$ and $NA \approx 0.71$ marginal ray aperture values, intensity profiles converge into a well defined annular focus. As the probing distance z is increased further still the beam starts to diverge, and at distances of $z = 2f$ begins to reconstruct an inverted image of the SZP pattern.

The transmittance of the spiral zone structure has been evaluated based on numerical simulations. The total transmittance through the 30 µm diameter structures is $T \approx 22.5\%$ for flat pedestal structures and $T \approx 25\%$ for patterned cones. This is in part due to the 50% opacity of the metal pattern, the suppression of transmittance through subwavelength aspect ratio of 1 slits as well as the diffractive nature of the pattern itself. However, if the Poynting vector is integrated only in the $R \approx 2$ µm focal spot region, transmittance values become $T \approx 5.1\%$ for flat pedestal structures and $T \approx 5\%$ for patterned cones. The influence of the photopolymerized pedestals on the total losses is only marginal.

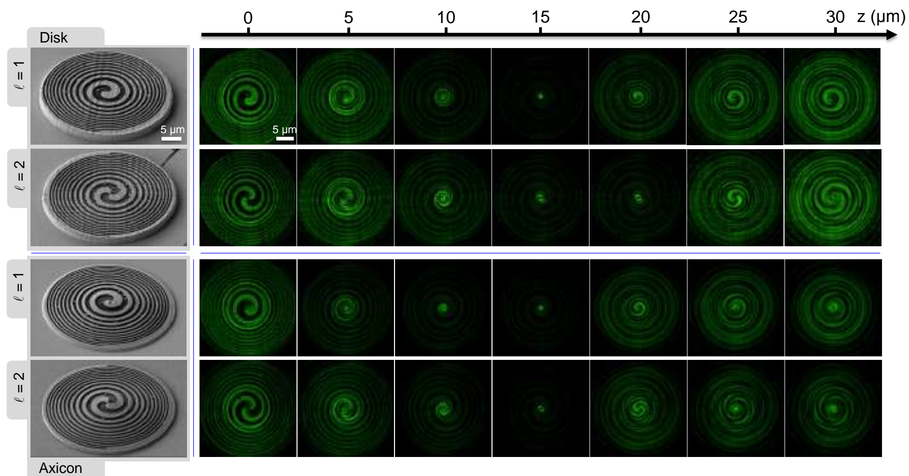

Figure 3.14: Experimental imaging of SZP transmitted optical field propagation behavior. Different rows correspond to flat pedestal and axicon structures with $\ell = 1$ and $\ell = 2$ topological charge SZP patterns FIB inscribed onto them. Optical microscopy images on the right show the evolution of transverse $\lambda = 532$ nm laser field intensity distributions as imaging focus is moved away from device plane at $z = 0$ µm in 5 µm increments up to a $z = 30$ µm distance. Optical characterization of the fabricated devices was performed at University of Bordeaux by the research group under supervision of Prof. Etienne Brasselet.

Experimentally derived SZP transmitted light propagation mirrors closely the results obtained by way of FDTD calculations, as outlined in the bottom section of Figure 3.15. Numerical data likewise predicts tight focusing, however, FDTD-derived focal distances are $f \approx 16.4$ μm and $f \approx 12.6$ μm for flat and axicon pedestals respectively, *i.e.* consistently around 20% lower then the experimentally retrieved values. Apart from this discrepancy, which can be attributed to either fabrication imperfections, residual form birefringence of patterned metal or, most likely, insufficient precision of the imaging microscope positioning stage, there is considerable overlap between numerical and experimental imaging findings. Furthermore, when the spiral zone pattern is generated on a flat 3 μm height 3D disk structure, light propagation behavior does not markedly change form the flat substrate case, shown previously in Figure 3.11. In general, the amount of bulk material in the pedestal does not affect the focusing performance of the device, as it only imparts some collective phase offset. Therefore, only the $\ell = 1$ case is plotted for a flat disk pedestal in Figure 3.15.

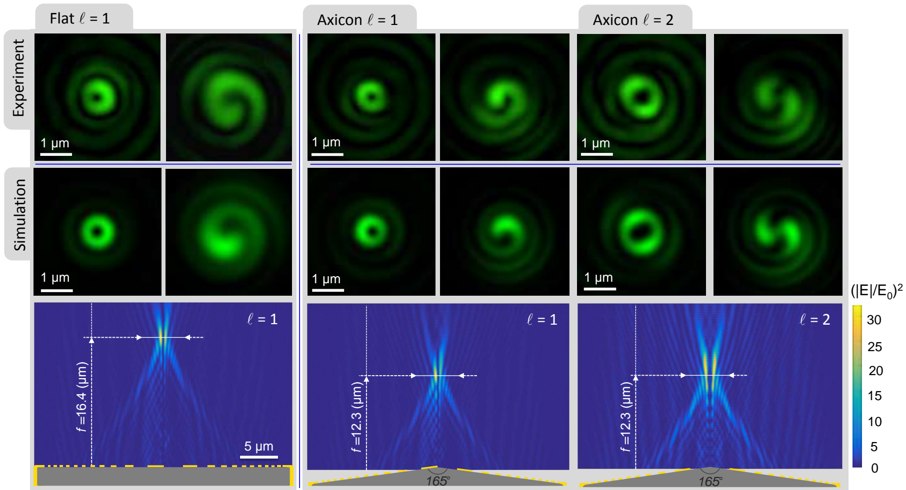

Figure 3.15: Beam shaping by a SZP structures milled on different photopolymerized surfaces. Bottom panels show FDTD simulated $x-z$ plane intensity distributions for $\lambda = 532$ nm light, diffracted through $\ell = 1$ SZP on a flat disk pedestal, along with both $\ell = 1$ and $\ell = 2$ patterns on cones with an obtuse full-apex angle of 165°. Top panels compare corresponding FDTD simulated and experimentally measured close-up x-y plane 3×3 μm^2 focal region total intensity plots and interference patterns resulting from coherent superposition with a co-axial Gaussian beam. Optical characterization was performed at University of Bordeaux by the research group under supervision of Prof. Etienne Brasselet.

Conversely, differences in optical path length due to the presence of a curved surface has a notable effect on light propagation. When a 165° full apex angle axicon pedestal is used there is a qualitative difference, wherein the refractive power of the underlying dielectric structure is added to that of the SZP. This manifests as an increase in the numerical aperture of the focused optical vortex generator structure from $NA \approx 0.64$ to $NA \approx 0.76$. While a similar adjustment can be achieved in a planar geometry by decreasing the SZP focal distance parameter f in Equation 3.4, as the focal distance is decreased the SZP pattern needs to be scaled down accordingly, along with corresponding increases to FIB patterning fidelity requirements. Therefore, a refractive subcomponent is especially useful in creating high-*NA* structures, where the hyperbolic dependence on focal distance f could create challenges for planar FIB fabrication.

The top row of Figure 3.15 depicts close-up experimentally imaged focal plane optical fields for SZP vortex generators FIB milled onto corresponding 3D pedestal structures. Intensity patterns, plotted leftmost of each panel in green, reveal tightly focused annular Laguerre-Gaussian-like beams that closely resemble their FDTD simulated counterparts. Similarly Gaussian reference arm interference patterns unambiguously reveal the phase singularities as well as $\ell = 1$ and $\ell = 2$ topological charge states exhibited by optical vortices generated using first and second order SZP binary transmittance patterns respectively. Even upon detailed experimental and FDTD inspection of the focal region of SZP structures FIB milled onto flat disk pedestals, no pronounced changes from a fully 2D case can be discerned. In both cases the doughnut beam diameters are ≈ 1.4 µm and ≈ 2.1 µm at FWHM respectively for the $\ell = 1$ and $\ell = 2$ SZP realizations.

Use of an axicon pedestal, due to the higher overall numerical aperture of the resulting micro-optical element, leads to a further decrease the focal spot size with ~ 1.3 µm and ~ 2.0 µm for vortices with topological charge of $\ell = 1$ and $\ell = 2$ respectively. Such slight shrinkage of annular intensity beams is hinted at by both optical imaging and FDTD simulation plots in Figure 3.15, therefore, is unlikely to be spurious. Observations suggest that the hybrid axicon/SZP structure is a way to create "perfect optical vortices" whose dark hollow radius does not depend on the topological charge [147] by appropriately selecting the full apex angle, hence the refractive power, of an axicon.

In summary, by leveraging the large depth of focus of FIB it becomes possible to directly mill various nanoscale structures onto complex 3D surface topologies. As a case in point demonstration, hybrid dielectric/metallic micro-optical elements, that, *via* cooperative refractive and diffractive capabilities, deliver a well-defined topological shaping of light, were fabricated. The proposed hybrid polymerization and FIB milling SZP design is useful for applications in microscopy and microfluidics where only an optical vortex beam should be generated, and all light that does not pass through the binary transmission mask is blocked. This facilitates dark-background imaging beneficial

in microscopy or for establishing well-defined tightly focused optical vortices in microfluidic channels for trapping and sorting applications. In addition to the aforementioned refractive modifications, flat pedestal design is appealing for easier integration into practical microfluidic chips for creating specific phase offsets.

4 LAYERED METAL FUNCTIONAL DEVICES

In physics a material is considered to be metallic if its Fermi level is situated in at least one band of energy states. This, in turn, means that there will be an abundance of both quasi-free charge carriers, as well as of unoccupied states to ensure their collective mobility in a lattice. Therein lies the origin of nondirectional bonding that produces the ductility and malleability of metals, the cause of their lustrous appearance, as well as of the high thermal and electrical conductivities. Similarly, magnetism, as a necessary yet insufficient condition, requires the presence of unpaired electron spins that are in abundance within the unfilled electronic orbitals of metals, which are likewise critical for enabling catalysis.

The unique properties of metals can be either altered or enhanced at the nanoscale, such as how gold can be turned from chemically inert to catalytic [148], or from highly reflective to strongly plasmonically absorptive of incident electromagnetic radiation, by fashioning it into nanoparticles of appropriate size. On the other hand, nanoscale multilayers of metals with disparate magnetic behaviors can produce materials with properties distinct from any of their constituents, such as the high perpendicular magnetic anisotropy thin-films harnessed for various data storage applications [149]. Benefits of miniaturization, of course, can be far more conventional, like the decreased footprint and lower energy consumption in microelectronics, or the increase in sensitivity observed when the junction volume in a Seebeck effect reliant thermocouple thermometer is made smaller [150].

This chapter focuses on fabrication of nanoscale devices that derive their properties, in whole or in part, from some inherent feature of certain metallic materials or their interfaces. It begins with the description of an EBL fabrication process by which a highly sensitive and responsive Au/Ni thermocouple thermometer was created by patterning these metals onto a 30 nm thickness membrane. The next section revolves around the hydrogen storage capability of Pd, and how its layering or alloying with Au affects the optical response of thin-films to H_2 exposure. Similarly, generating planar Pd patterns by way of optical lithography is explored as a way of realizing plasmonic hydrogen sensing at the mid-IR. This leads into the work on more elaborate metal–insulator–metal plasmonic absorber metasurfaces and an analysis of how their resonant response is affected by choice of materials. Lastly, high resolution patterning of submicron gratings in Co/Pd multilayer magnetic films, which were then used for the first reported trapping of ultracold ^{87}Rb atoms in a 700 nm period 2D lattice, is described.

4.1 Micro-thermocouple on a nano-membrane

Among all disparate metal junction-based devices the thermocouple, in essence merely two wires joined at one end, is definitely among the simplest. It relies on the differences of Seebeck effect electromotive forces induced in dissimilar metals to measure relative temperature between the ends of these conductors [151]. The considerable simplicity, ruggedness and low cost of thermocouple thermometry has ensured its wide adoption throughout wide swaths of consumer and industrial applications, although over past decades resistance temperature detectors, due to their higher accuracy and simple calibration, have subsumed much of the available market share in a trend that is unlikely to reverse.

However, the Seebeck thermoelectric effect driving electromotive forces is largely independent on the shape or size of the two constituent metals or by what means they are brought together. This, in turn, makes thermocouples uniquely well suited for miniaturization, where a small size directly results in a low thermal mass and, therefore, a high sensitivity, rapid response rate and low thermal distribution. As a result, they frequently form the basis of advanced nanoscale thermometric sensors, such as those employed in scanning thermal microscopy cantilevers [152]. Furthermore, since in their thin-film variety [153, 154] thermocouples can be fashioned to conform to unorthodox geometries, they have been demonstrated to provide *in situ* thermal feedback on processes as dissimilar as turbine engine component performance [155] or cellular thermal responses sampled by micropipette-based thermovoltage probes [156].

In this work, conducted in collaboration with the research group headed by Prof. Junko Morikawa at Tokyo Institute of Technology, a Au/Ni thin-film thermocouple comprised of a 2.5 μm width junction was EBL fabricated on a 30 nm thickness Si_3N_4 membrane [157]. Avoidance of the heat-sink effect associated with a bulk substrate made it possible for the device to be sensitive to minute both laser radiation and a focused electron beam induced heating. Furthermore, the low thermal capacity of the suspended structure ensured a rapid response, so that $\Delta T = 2$ K temperature changes could be detected at a 10 kHz modulation frequency.

4.1.1 Fabrication of thermocouples on membrane chips

Lithographic definition of planar thin-film thermocouple devices necessitates, at a minimum, two separate patterning, deposition, and lift-off steps to create the disparate metal junctions. This, however, demands an overlay exposure approach where overlapping structures have to be created with preferably submicron precision. Further complications are introduced by the 30 nm thickness Si_3N_4 membrane employed as a substrate, whose fragility precludes all but the most gentle chemical treatments and physical agitation during lift-off,

thereby considerably lowering the ease with which it can be achieved. Lastly, microscopic thermocouple devices have to interface with external measurement equipment, hence, require macroscopic metal contact pads that are too large to be practicable by most scanning lithography approaches.

The process steps involved in fabricating a nano-membrane suspended micro-thermocouple device are schematically outlined in Figure 4.1. Here, the 30 nm thickness and 250 × 250 μm^2 area Si_3N_4 membrane windows were suspended on a 5 mm width silicon frame, and where sourced form a commercial supplier (Norcada Ltd.). Similar fabrication was also performed on bulk silica substrates for reference, however, its realization corresponded to a simplified version of the process given in Figure 4.1, therefore, does not merit a separate description. The first step involved the creation of six macroscopic metal contact pads, two for the thermocouple and the remaining four for the respective Au and Ni reference resistances, that each stretch all the way from the membrane window periphery to the edges of the chip. This was achieved by means of

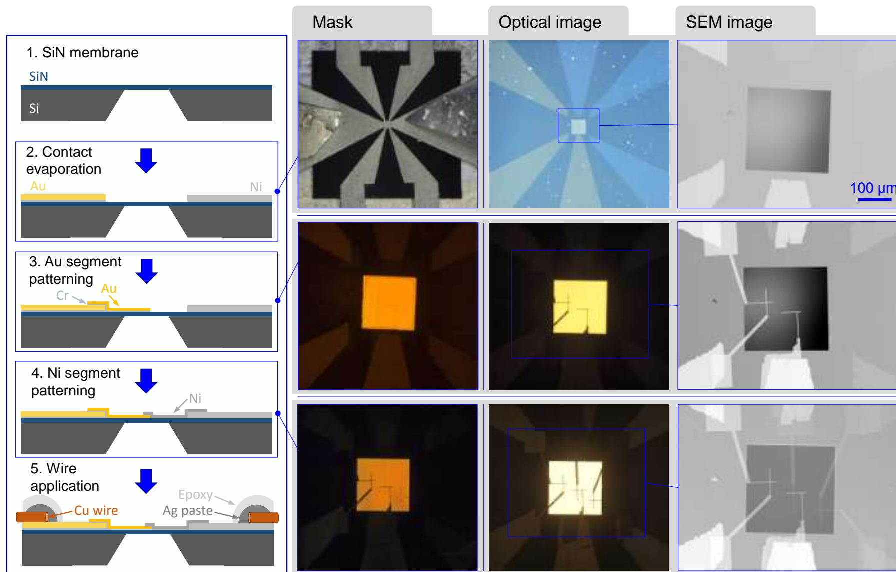

Figure 4.1: EBL fabrication of a Au/Ni micro-thermocouple on a 30 nm thickness Si_3N_4 membrane. Sketch in the panel on the left outlines the manufacturing process, whereas optical and SEM images of the mask pattern and the resulting metal structure are shown on the right. First of all, large area peripheral Au and Ni contact pads are thermally evaporated through a laser-cut stainless steel mask in two stages. Similarly thermocouple structures, along with reference resistance leads, are created using two overlay EBL exposure steps, each followed by respective metal deposition and lift-off. Images of the completed device are given bottom-right.

thermal evaporation of metals through a mask, that was carefully aligned under a microscope and pressed tightly against the substrate surface by a set of spring clamps, as shown in the top-left photograph in Figure 4.1. The evaporation mask itself was created by laser-cutting the requisite custom patterns out of a 100 µm thickness stainless steel foil. Metal PVD was performed in two stages, where separate contact pads for Au and Ni track connections were fashioned from the same corresponding metals by using thin aluminum foil sheets to block deposition on opposing substrate areas. Gold pads were generated by first depositing a 10 nm thickness Cr adhesion layer, followed by 90 nm of Au. Conversely, nickel exhibits strong adhesion to most materials and therefore was thermally evaporated directly as a 100 nm thickness film onto Si_3N_4. The dual metal contact pattern, shown in the top-right panel images in Figure 4.1, was chosen in order to extend the reference junction farther away from the membrane sensing region, where wires are to be bonded and the thicker Si frame chip can act as a stabilizing heat sink.

Next, the microscopic thermocouple junctions where defined by performing EBL using a rudimentary scanning electron microscope ACE-7000/EBU (Sanyu Electron Ltd.) equipped with a beam blanker-based pattern generator. The membrane chip was spin coated with a 300 nm thickness ZEP520A positive tone resist (ZEON Corporation) and heated on a 180 °C temperature hot-plate to evaporate any residual solvents. Substrate charging during EBL patterning was mitigated by an ultra thin layer of a water soluble ESpacer 300Z conductive polymer (Showa Denko K. K.) spin-coated onto the baked resist. Exposure was performed using a 500 pA current 25 kV accelerated electron beam that was scanned over a 500 µm width write-field. The patterning position was adjusted by using the pre-fabricated metal contact pads as alignment markers and moving the manually controlled micrometer stage to the center of the membrane window.

Following the first exposure step the latent electron irradiated ZEP520A resist pattern was developed in n-amyl acetate, rinsed in IPA, and the resultant mask pattern is shown in the micrograph middle-left in Figure 4.1. The first set of Au structures comprising the thermocouple and a reference resistance were then created by thermally evaporating a 5 nm Cr adhesion layer and a 50 nm thin-film of gold, and performing lift-off by stripping the resist in 60 °C dimethylacetamide by leaving the sample immersed overnight under gentle agitation. The process, starting with resist coating, is then repeated for the complementary 50 nm thickness Ni portion of the device, thus completing the junction as depicted in the lower-right row of images in Figure 4.1.

Finally, peripheral metal pads of the completed device were bonded to copper wires using silver paste and the point-of-contact was further reinforced by locally applying an epoxy resin droplet. The resolution afforded by the low performance SEM-based patterning setup enabled a reliable definition of 2.5 µm width metal tracks, that resulted in a 6.25 µm^2 Au/Ni cross-over

area. So, despite the lack of state of the art EBL capabilities, the process resulted in a thermocouple junction that is on par with the size of a typical CCD pixel. The Ohmic resistance of the thermocouple was found to be around 500 Ω, whereas the gold reference was predictably more conductive with a value of 90 Ω. The next section descries thermal response characterization of the nano-membrane suspended Au/Ni micro-thermocouple, directly related to its functional capabilities.

4.1.2 Micro-thermocouple response to beam-induced heating

Even bulky thermocouple devices have proven to be suitable for measuring minute transfer of thermal energy, emanating from a resistive heater, in an effort to measure the thermal diffusivity of polymer films [158, 159]. However, low thermal mass sensors can serve to enable more versatile and better spatially resolvable alternative methods of non-contact sample heating *via* laser irradiation [160]. Furthermore, even smaller temperature changes due to charged particle beam exposure can also be detected by such structures [150], although issues related to beam current induced electrical interference impose certain limitations on feasible measurement geometries. Therefore, the two latter beam irradiation heating methods were of particular focus in estimating performance of the prototype membrane-suspended micro-thermocouple device.

Thermovoltage response of the Au/Ni micro-junction device to laser induced heating is summarized in Figure 4.2. Top-left panel provides a microscope image of the thermocouple, irradiated by a $\lambda = 830$ nm continuous wave laser, incident at an approximately 45° angle and forming a somewhat elliptical $d = 10$ µm diameter spot on the membrane surface. The output of the light source was modulated to a specified frequency using a function generator, and the thermovoltage signal was acquired by means of a lock-in amplifier. Changes in temperature were deduced based on the relative Seebeck coefficient $S_{\mathrm{Au/Ni}} = 10.1\ \mu\mathrm{VK}^{-1}$ reported in the literature for a similar device [150], however, more robust absolute calibration could be performed by fabricating a nearby thin-film resistive heater element.

Plot in the top-right panel of Figure 4.2 provides the quasi-static thermal response of the thermocouple as well as that of an equivalent Au resistance when incident laser power was modulated at a low 30 Hz frequency. The membrane-suspended Au/Ni junction exhibited a high sensitivity to laser heating, which was approximately 34.5 higher than for the same metal pattern fabricated on bulk silica. However, while the low thermal capacity of the virtually free-standing device ensures an acute response to minute thermal shifts, the limited $250 \times 250\ \mu\mathrm{m}^2$ area of the Si_3N_4 window results in the onset of signal saturation due to the Si frame acting as a heat sink. Surprisingly, the gold reference structure also exhibited a mild level of voltage response to laser heating, which is likely attributable to the thermoelectric influence of an underlying Cr adhesion layer.

In addition to sensitivity, low thermal capacitance membrane-based thermocouple devices tend to exhibit a superior temporal response, characterized by the transients depicted at the bottom of Figure 4.2. Here, excitation was delivered by a 1.8 mW power laser, meander-modulated at f =2, 5 and 10 kHz frequencies. Furthermore, similar results for an equivalent Au/Ni structure, fabricated on a thick silica substrate, are given at $f = 2$ kHz frequency and 3.6 mW power $\lambda = 830$ nm wavelength laser heating. However, comparisons between the membrane-suspended and bulk reference devices cannot be very direct, since the 30 nm Si_3N_4 layer exhibits only a small fraction of the optical energy uptake that occurs in a ~ 1 mm thickness slide glass. Differences in absorbance together with disparities in cooling rate resulted in ΔT values on glass being an estimated 16 K, noticeably higher then the $\Delta T = 4.1$ K on a membrane, despite both surfaces reaching the same $T_s \approx 50$ °C stationary state temperature under illumination. Hence, membrane-suspended thermocouples remain considerably hotter due to the lack of thermal energy dissipation pathways. Nevertheless, this in itself is an advantage, as a membrane is not subjected

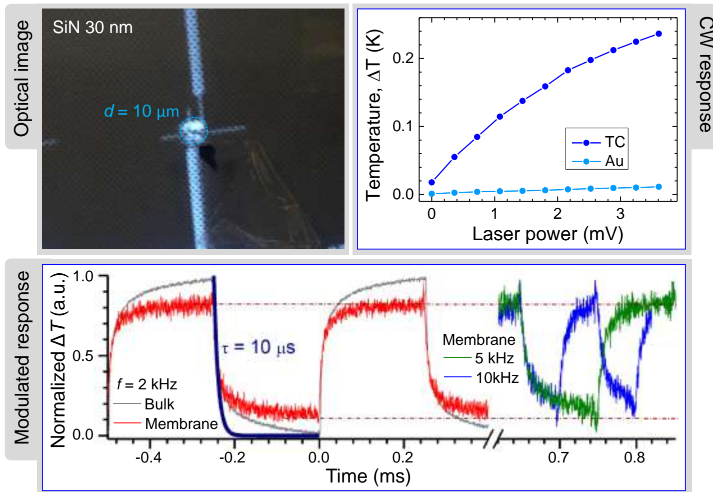

Figure 4.2: Micro-thermocouple response to near-IR laser induced heating [157]. Microscope image top-left shows the thermocouple junction under $d = 10$ µm spot size continious wave $\lambda = 860$ nm laser illumination. Plot top-right corresponds to a quasi-continious wave thermal response to increasing laser irratiation power for both the Au/Ni thermocouple and an equivalent Au resistor. Kinetics plotted in the bottom panel provide the temporal response of the 30 nm Si_3N_4 membrane-based micro-thermocouple to 1.8 mW laser irradiation modulated at different frequencies. Behavior of a similar device fabricated on bulk silica, excited at 3.6 mW laser power and 2 kHz modulation frequency, is given for comparison purposes.

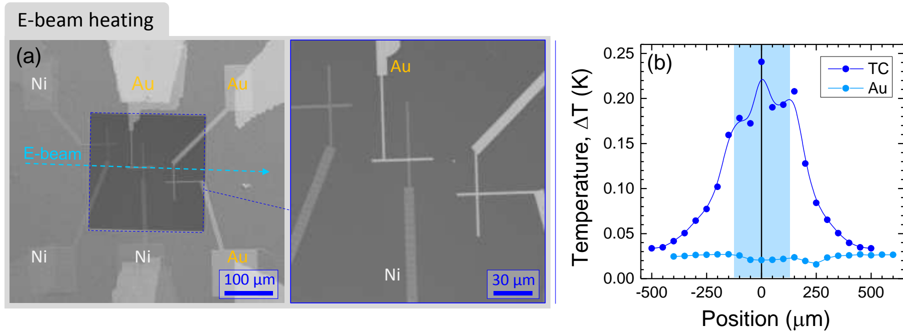

Figure 4.3: Micro-thermocouple response to scanning electron beam induced heating. (a) SEM images of the 250×250 µm^2 area 30 nm Si_3N_4 membrane with fabricated Au/Ni thermocouple and reference resistors. The dashed line corresponds to trajectory along which position-dependent response to 1.7 nA 25 keV electron beam induced heating is plotted in panel (b) for both thermocouple junction and an equivalent Au reference.

to heat redistribution in the transverse direction and, therefore is able to rapidly reach a stationary state, as evidenced by a much more rapid signal saturation for $f = 2$ kHz signal transients. While bulk substrate thermocouples struggle to reach a stationary state at 2 kHz, membrane devices were able to follow $f = 10$ kHz modulation frequencies, and the fastest signal rise and decay rate was $\tau = RC = 10$ µs. Therefore, membrane-suspended micro-thermocouple devices are able to trace $\Delta T \approx 2$ K temperature shifts that occur within the aforementioned 10 µs time-frame, thus making it possible to measure cooling or heating processes at up to 2×10^5 Ks^{-1} rates.

Thermal energy delivery by way of an electron beam affords better spatial control over heating due to precise SEM imaging feedback as well as a small focus spot, which in the rudimentary ACE-7000/EBU tool was around 500 nm in diameter. In this case using membrane substrates is particularly relevant, since the lack of a bulk substrate largely eliminates spurious electrical effects due to electron back-scattering. Thermocouple sensor tests were performed using a 1.7 nA current 25 keV energy electron beam modulated at 30 Hz by periodic blanking, and the output voltage signal was detected using a lock-in amplifier. SEM images of the metal-patterned 30 nm Si_3N_4 membrane are provided in Figure 4.3 (a), where the dashed light-blue line denotes the trajectory along which electron beam induced heating tests, plotted in Figure 4.3 (b), were conducted.

Electron beam heating was conducted by exposing single spots ~ 50 µm apart from each other whilst avoiding direct irradiation of metal components. The largest voltage response was observed in the immediate vicinity of the thermocouple and, on average, dropped only slightly when moving towards

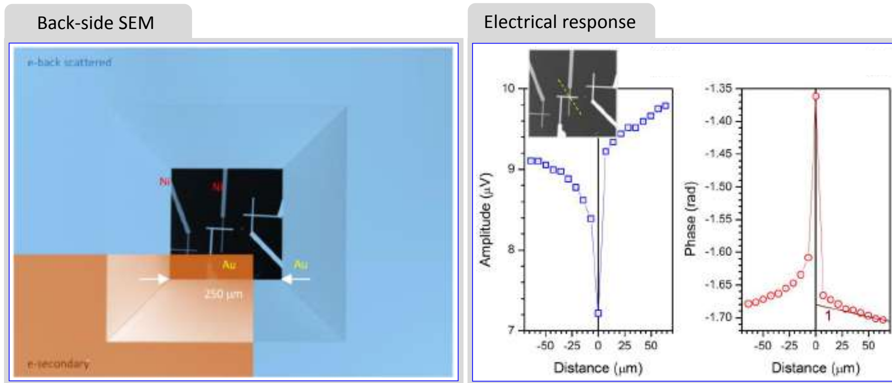

Figure 4.4: Micro-thermocouple response to scanning electron beam induced heating from the back-side of the membrane. Left panel gives SEM image fragments acquired using back-scattered (blue) and secondary (orange) electron detectors. Lock-in amplifier amplitude and phase signal output dependence on electron beam spot position in the vicinity of the thermocouple is plotted on the right. Dashed line in the inset illustrates the measurement trajectory. Slope 1 is the linear fit of phase that is used to determine the thermal diffusivity of a 30 nm Si_3N_4 membrane.

the membrane periphery, corresponding to boundaries of the shaded region in Figure 4.3 (b). The two notable dips, however, are attributable to the thermal conductivity of Au and Ni test resistances. As the probe beam is moved onto the bulky Si frame, which for this device fulfills the role of a heat sink, the voltage response signal starts to drop exponentially with distance until it becomes indistinguishable from either a Au resistor reference or background noise.

Higher resolution investigation of electron beam irradiation-induced heating was performed from the device back-side, depicted by the SEM image in Figure 4.4. Here, electron current transmitted through the membrane could be detected and used as a thermovoltage normalization signal for more stable measurements. Plots in the right panel of Figure 4.4 provide the lock-in amplifier output amplitude and phase ~ 7 µm step size spatial dependencies along a trajectory corresponding to the dashed line in the inset. The decrease in voltage signal amplitude that is observed when a beam directly irradiates the Au/Ni junction is attributable to a reduction of Seebeck coefficient as a result of electron injection that lowers the disparity between free electron densities in the two metals, responsible for the thermoelectric electromotive force. Lock-in amplifier phase, however, provides more relevant information, as its delay $\Delta\Theta$ with increasing electron beam spot distance d is directly related to the thermal diffusivity α of a material as $\Delta\Theta = \sqrt{\pi f/\alpha} d$, where f is the modulation frequency. Based on the linear fit shown in the corresponding plot, the thermal diffusivity

of the device membrane was determined to be $\alpha = 0.62 \times 10^{-4}$ m^{2}s^{-1}, which is 48 times larger than the value reported for a 600 nm thickness Si_3N_4 film [161], likely due to the thermal conductivity contributions of patterned metal contacts.

Overall, the versatility of EBL provides a straightforward way of generating complex patterns even on fragile nanoscale membranes for applications where influence of an underlying substrate is detrimental. Micro-thermocouples for detecting minute thermal changes represent just such a situation, as lowering the heat capacity of a device increases both its sensitivity as well as the response rate. Here a 6.25 μm^2 Au/Ni junction area thermocouple was created on a 30 nm thickness Si_3N_4 membrane. The ultra-thin sensor had a 34.5 times higher sensitivity than a bulk substrate-fabricated counterpart, which enabled detection of heating induced by both laser and electron beams. Lastly, further miniaturization using advanced EBL capabilities could enable derivatives of this device to probe heat transport at the nanoscale.

An intriguing property of most transition metals is their ability to establish chemical bonds with hydrogen, thus forming hydride complexes that can notably alter the structural, electric and magnetic properties of the host metal [162]. Palladium is uniquely effective in this regard for it possesses an enormously high H_2 absorption capacity at room temperature and atmospheric pressure, readily attaining a stoichiometric ratio of up to $PdH_{0.6}$ as octahedral interstices in the metal lattice become stochastically occupied with hydrogen [163]. Furthermore, as the process is mostly reversible, palladium has drawn longstanding interest for prospective applications as a hydrogen fuel storage medium.

Of similarly high concern is the ability to detect the presence of hydrogen gases in an ambient atmosphere, where it is both colorless and odorless whilst simultaneously becoming explosively volatile at only a 4% H_2 volume fraction in air [164]. As a result, any advances in harnessing hydrogen in lieu of fossil fuels will, necessarily, require solutions for managing the considerable risks posed by gas leaks. Here, again, the changes in material properties induced by formation of hydride complexes in Pd can be leveraged for H_2 sensing, and virtually every mode of detection, including magnetic [165], electric resistance [164] as well as optical [166], has been demonstrated, with the latter two being the most popular options.

However, the potential for electric discharge during electrical resistance

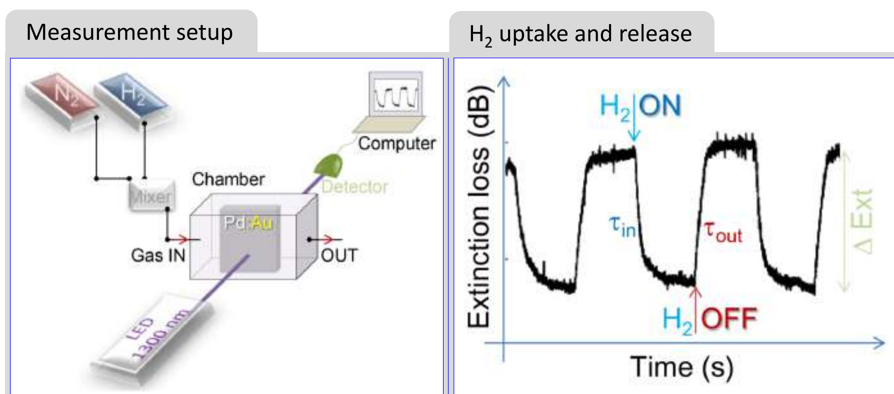

Figure 4.5: Measurements of H_2 uptake induced optical changes in thin metal films. Left panel shows a sketch of the setup used to conduct transmittance measurements in a controlled gas composition. Plot on the right displays a typical hydrogenation-induced change in extinction, defined as $\Delta\text{Ext} = -10\lg(I_t/I_0)$ where I_t and I_0 respectively are the transmitted and reference intensities. Hydrogen detection experiments were performed at Yokohama National University by the research group under supervision of Assoc. Prof. Yoshiaki Nishijima.

measurements can become a hazard in itself, hence, non-contact optical approaches are generally considered preferable for hydrogen sensing and monitoring. As illustrated in Figure 4.8 (a), when palladium becomes hydrogenated the imaginary part of its complex refractive index decreases, whereas the real part exhibits a more complex wavelength dependent behavior. This shift in Pd permittivity, resulting from lattice distortion during hydrogen accommodation, lies at the core of optical H_2 detection. Still, pursuit of optical sensing realizations with optimal sensitivity, specificity and low production costs involves tailoring the structural and morphological properties of the sensing medium, which for Pd generally entails creation of alloys with other metals as well as patterning structures that enable resonant photonic or plasmonic phenomena.

In this work, conducted in collaboration with the research group headed by Assoc. Prof. Yoshiaki Nishijima at Yokohama National University, methods of modifying palladium thin films to increase the sensitivity and response rate of their optical response to H_2 exposure were investigated [167]. First, various Pd thin-film composites with Au were prepared by magnetron sputtering, so that either multilayer or intermixed alloy layers were created. Changes in their transmittance in a hydrogen containing atmosphere were observed using the simple measurement setup displayed in the left panel of Figure 4.5, comprised of an isolated gas flow chamber and a $\lambda = 1.3$ nm LED light source based detection system. The resultant optical signal is depicted in the right plot of Figure 4.5, where hydrogenation gradually decreases the optical losses in a Pd-based film until a dynamic equilibrium state is achieved. Composition ratio of Au:Pd alloys and thermal treatment of films provided control over the optical extinction magnitudes as well as hydrogen uptake and release transient time constants. Furthermore, patterning of a Pd layer to create metal hole array (MHA) and nanodisk array (NDA) plasmonic structures was performed to enable detection of H_2 at mid-IR wavelengths by means of detecting resonant response spectral shifts [168].

4.2.1 Deposition of Pd/Au composite films

Alloying is the primary and the most longstanding method of tailoring the properties of metals towards specific purposes and applications, therefore, its undiminished relevance even in contemporary nanotechnology is largely unsurprising. For instance, creation of ternary alloys of the Au, Ag and Cu plasmonic metals allows for substantial control over their permittivity values and overall optical response [169]. More in line with the present topic, solid solutions of Rh and Ag mixed at the atomic level can store hydrogen much like Pd, a functionality virtually absent in either pure Rh or Ag [170]. Furthermore, alloying can have a strong effect on the catalytic properties of a metal, such as how incorporation of Pd into Ru results in a more efficient facilitation of carbon monoxide oxidation [171]. Similarly, combination of Pd and Au – the binary system under consideration here – is also known to increase the electrocatalytic

efficiency of nanoparticles [172]. These new functionalities tend to arise as a result of both changes in the lattice configuration and mismatch strain [173], as well as due to alterations in chemical activity due to different electron binding and charge distribution behaviors [174].

The Pd/Au composite samples investigated in this work were prepared by magnetron sputtering in a AXXIS PVD tool (Kurt J. Lesker) using two different modes of thin-film deposition: co-sputtering of Au:Pd alloys, and alternating deposition of Au/Pd multilayers. In all cases a 400 μm thickness silica cover glass (Matsunami Glass Ind. Ltd.) was used as an optically transparent substrate. Co-sputtering was performed by exposing the substrate, mounted on a coaxially spinning stage, to simultaneously active Pd and Au sputtering targets, as sketched in the inset of Figure 4.6. The Au:Pd alloy composition was controlled by changing the relative powers of the two direct current power supplies on the Ar^{+} plasma exposed sputtering targets and 2:1, 1:1, 2:3, 1:2 and 1:3 molar ratio mixtures were produced, each with 20, 30 and 40 nm layer thicknesses. Deposition rate calibration was performed by using a ContourGT optical interference microscope (Bruker Corp.) to determine isochronic sputter-coated layer thicknesses for each metal separately when different source powers are set. During co-sputtering the substrate was either kept at room temperature, or heated to 250 °C to aid in interdiffusion of the two metals to produce more homogeneous alloys. On the other hand, when alternating deposition is employed to generate multilayer thin-films the substrates are kept exclusively at RT. Systems composed of 2, 4, 10 and 20 deposition cycles, *i.e.* where one cycle corresponds to one Au/Pd layer pair, where thus created and each cycle in the respective films corresponds to 7.50, 3.75, 1.50 and 0.75 nm/cycle thickness. In all cases the film top surface was terminated by a Pd layer and prior to Au/Pd sputtering no adhesion-facilitating materials were deposited on the silica substrate.

Figure 4.6 depicts the X-ray diffractograms (XRD) of both the co-sputtered and alternating multilayer Au/Pd composite films in the left and right panels respectively. Since Au and Pd are known to be miscible in all ratios and exhibit only a 4% lattice mismatch [175], it is unsurprising that as the molar composition of Au:Pd alloys, sputtered onto a 250 °C pre-heated silica substrate, changes form 1:1 to 1:3, the $\langle 111 \rangle$ associated diffraction peaks are situated at angles intermediate to those of pure Au and Pd, and tend to shift towards the value of the prevalent metal. Furthermore, XRD peak widths provide information on the presence and degree of structural disorder, and, while in alloys the $\langle 111 \rangle$ diffraction band is marginally broader likely due to frustration in the lattice, it is nonetheless indicative of notably homogeneous alloying.

Conversely, cycling Au and Pd deposition gives rise to a far more complex XRD pattern, attributable to phase separation between the two constituents. When a low number of reasonably thick layers are used, as represented by the 2 and 4 deposition cycle cases where alternation half-periods are 7.5 and 3.75 nm

respectively, the XRD profiles of both Au and Pd still remain discernible. On the other hand, when 10 or 20 deposition cycles are used, the pure metal signatures vanish and only peaks associated with the presence of a superlattice remain. Angle-domain spacings between the different diffraction orders can therefore be used to deduce the deposition cycle thickness Λ according to the Bragg equation:

$$\Lambda = \frac{m-n}{\sin\theta_m - \sin\theta_n}\frac{\lambda_{\mathrm{K}_\alpha}}{2}, \tag{4.1}$$

where the indices m and n denote the X-ray diffraction orders of respective θ_n and θ_n peaks, and $\lambda_{\mathrm{K}_\alpha} = 0.15148$ nm is the Cu K_α line wavelength. The deposition cycle thickness values obtained by way of XRD were 20, 12, 6.4 and 3.4 nm for 2, 4, 10 and 20 cycles respectively. This indicates that multilayer films were overall thicker than expected based on sputtering calibration data, which is likely to result from delays in the shutter mechanism used to gate the Au and Pd targets.

Of further interest is that when Au:Pd co-sputtering is conducted at RT, the resultant XRD spectra become more in-line with those of a multilayer films

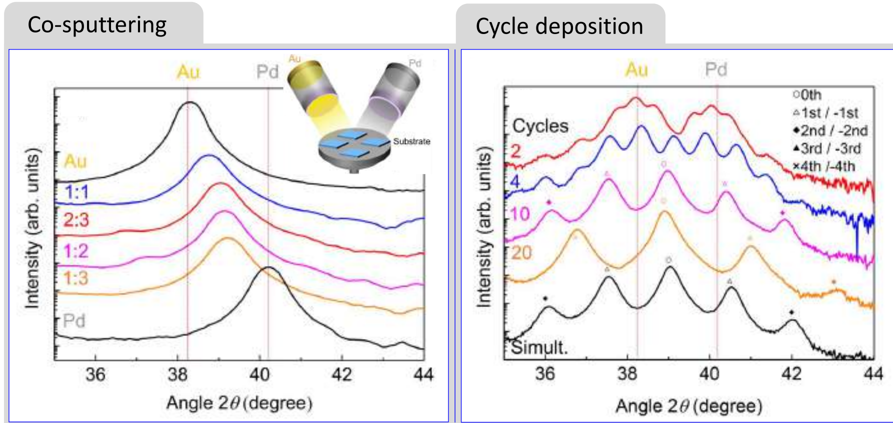

Figure 4.6: XRD investigation of Au:Pd composite films. Left plot shows XRD spectra of Pd and Au films simultaneously co-sputtered at different molar ratios onto a 250 °C pre-heated silica substrate, as sketched in the inset. Red lines denote the positions of ⟨111⟩ fcc peaks for pure Au and Pd films. Right plot gives the XRD of metal films, created by way of a different number of alternating Pd and Au deposition cycles at RT. Thickness of individual sub-layers for 2, 4, 10, and 20 cycle cases were 7.5, 3.75, 1.5, 0.75 nm respectively. Black curve at the bottom corresponds to a Pd:Au alloy co-sputtered at RT. XRD measurements were performed at Yokohama National University by the research group under supervision of Assoc. Prof. Yoshiaki Nishijima.

created over multiple deposition cycles than a homogeneous alloy, as evidenced by the bottom curve in the right plot of Figure 4.6. This can be explained *via* the deposition rate gradients that arise during sample stage rotation relative to the axes of the Au and Pd sources, which produce periodic oscillations in relative composition. These variations can be eliminated by diffusion-reliant alloy intermixing processes, largely described by the interdiffusion constant $\tilde{D}$, that scales exponentially with temperature. Extrapolating from data reported in literature [176] the Au/Pd interdiffusion constant at 250 °C is only around $\tilde{D} \sim 10^{-17}$ cm^{2}s^{-1}, however, at RT it is expected to be several further orders of magnitude lower, hence, unable to produce even a somewhat homogeneous film.

4.2.2 Optical transmittance response of thin-films to hydrogen

Hydrogenation induced optical property changes in thin Pd films provide a robust baseline to which the merits of all other Au/Pd composites can be compared and contrasted. Figure 4.7 depicts visible-to-near-IR normal incidence reflectance and transmittance spectra of pure 20, 30 and 40 nm thickness Pd films before and after exposure to a 4% H_2/N_2 mixture. Spectroscopic measurements were performed using a simple and compact optical fibre based setup that allowed simultaneous detection of reflected ant transmitted light [169], whilst being placed in a $50 \times 50 \times 15$ cm^3 sealed container that holds the volatile gas. Here, a fiber-coupled deuterium lamp L10290 (Hamamatsu Photonics Co. Ltd.) served as the UV-IR light source, whereas the signal was acquired using a CCD-based mini-spectrometer C10083CA-1050 (Hamamatsu Photonics Co. Ltd.).

As mentioned previously, accommodation of hydrogen renders palladium slightly more transparent to incident radiation, thereby increasing the attainable transmittance and lowering the observed reflectance. When this spectral information is available for two or more film thicknesses, the full complex refractive index $\tilde{n} = n + ik$ can be deduced, as shown in Figure 4.7 (b), according to equations:

$$T \simeq \frac{16 n_s (n^2 + k^2)}{[(n+n_s)^2 + k^2] \cdot [(1+n)^2 + k^2]} e^{-\frac{4\pi k d}{\lambda}}, \tag{4.2}$$

$$R \simeq \frac{(1-n)^2 + k^2}{(1+n)^2 + k^2}, \tag{4.3}$$

where n_s is the refractive index of the silica substrate, d is the Pd film thickness and λ is the wavelength of light. However, here the requisite calculations were performed by using the FEDataAnalysis permittivity analysis software (Otsuka Electronics Co. Ltd.).

The optical permittivity of metals is largely characterized by the abundance of electrons only weakly interacting with a bulk background of lattice ions, and is faithfully described by the Drude model for a quasi-free-electron gas [177]. When this model is fitted onto the Pd permittivity spectral data in Figure 4.7 (b), the free electron portion of the fit yields two key parameters – the plasma frequency ω_p that is effectively the ratio of electron density and their effective mass, and the damping time constant τ which incorporates the collective effects of various electron scattering mechanisms. When hydrogen infiltrates palladium it does so as either H^+ or H_2^+ [178], meaning that it donates an electron to the metal. Therefore it is unsurprising that hydrogenation of Pd results in an increase of the plasma frequency from $\omega_\mathrm{p}^{Air} = 1.5 \times 10^{16}$ Hz to $\omega_\mathrm{p}^{H_2} = 1.9 \times 10^{16}$ Hz, likely due to an enlargement in the density of free electrons. Conversely, there is a slight decrease in the relaxation time constant from $\tau^{Air} = 4.3 \times 10^{-16}$ s down to $\tau^{H_2} = 3 \times 10^{-16}$ s, which can be readily attributed to positively charged interstitial hydrogen ions acting as additional electron scatterers.

Next, the different Au/Pd thin-film composites – either co-sputtered at an elevated 250 °C temperature to produce homogeneous alloys, or prepared by cycle deposition or RT co-sputtering to give rise to an alternating gold-palladium multilayer – were tested for their hydrogen optical detection performance using the setup sketched on the left side of Figure 4.5. The real-time H_2 absorption optical response needs to be measured in a reasonably small chamber, so that

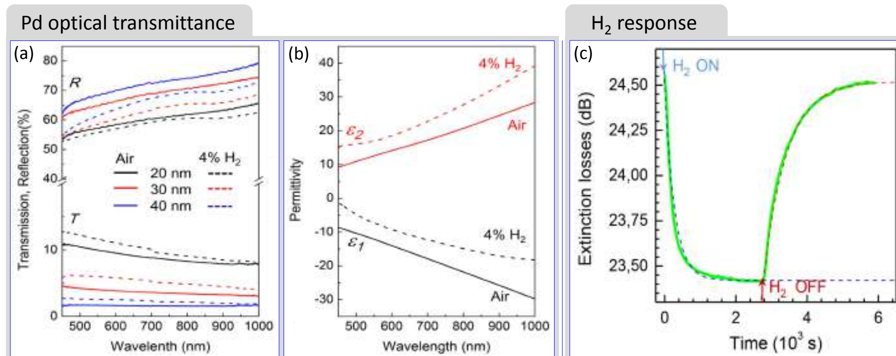

Figure 4.7: (a) Optical transmittance and reflectance spectra of Pd films 20, 30 and 40 nm in thickness, acquired in a pure N_2 atmosphere and after exposure to a 4% H_2/N_2 gas mixture. (b) Spectra of both real and imaginary components of Pd permittivity in the presence as well as absence of hydrogen. (c) Extinction transient of $\lambda = 1310$ nm radiation in a Au/Pd multilayer prepared over 4 deposition cycles, fitted assuming an exponential H_2 uptake and release. Hydrogen detection experiments were performed at Yokohama National University by the research group under supervision of Assoc. Prof. Yoshiaki Nishijima.

gas injection does not become the hydrogenation rate-limiting factor. Hence, the setup uses a 21.4 cm^3 volume sample container and is equipped with a gas mixing system that ensures a 500 mL/hour flow rate of a 4% H_2/N_2 mixture whilst maintaining a 0.1 MPa pressure. For rapid *in situ* metal film transmittance signal acquisition a monochromatic $\lambda = 1.31$ μm LED fiber optic source MPS-8012 (ILX Lightwave Corp.) and a Ge photodiode detector AQ2150A (Ando Electric Co., Ltd.) were employed. A $NA = 0.25$ fiber-optic collimator was used to focus the radiation to form a 2 mm spot at normal incidence onto the metal films placed within the chamber.

Figure 4.7 (c) depicts a typical hydrogen uptake and subsequent release transient of a Au/Pd multilayer prepared over 4 deposition cycles. Here, the extinction signal $Ext = -\lg(I_t/I_0)$ is defined as the ratio of transmitted I_t and reference $I_0 = 12.2$ μW radiation intensities. In all cases introduction of H_2 into the chamber results in Pd-containing films becoming more transmissive, whereas equivalent Au thin-films did not exhibit any optical response. Furthermore, temporal progression of both hydrogen absorption and release can be fitted using single exponential transients with corresponding τ_{in} and τ_{out} time constants, which is indicative that the rate of each process is limited by a single physical factor. Lastly, there is an evident asymmetry between the rates of H_2 accommodation in Pd and its release, with the former being approximately three times faster. This is related to the fundamental difference between hydrogen dissociation and association processes at Pd interfaces. In particular, Pd hydrogenation is reported to be an exothermic process [179], therefore its inverse will require some energy to proceed, and, furthermore, two hydrogen ions need to be brought together so that the diatomic molecule can be reconstituted.

Main parameters characterizing the temporal response of the different Au/Pd composite films to H_2 exposure are compared in Figure 4.8. In addition to the default pure Pd film, the samples fall into one of two general groups – multilayers prepared at RT, and intermixed alloys co-sputtered at a 250 °C temperature. Alternating Au/Pd films exhibit notably large changes in extinction ΔExt, as well as low rates of hydrogen uptake and release, denoted by τ_{in} and τ_{out}. Furthermore, all these parameters have a tendency to increase with the number of deposition cycles comprising a multilayer. Somewhat surprisingly, a RT co-sputtered 1:1 Au:Pd mixture exhibited the most pronounced H_2 exposure induced extinction changes among all prepared films, however, the relevant time constants were likewise markedly slower than in all other cases. Still, despite differences in their realization, all of the RT deposited Au/Pd films share similarities in their XRD spectra given on the right side of Figure 4.6, hence, appear to exhibit a layered structure. In this context the notably slow hydrogen response is likely the result of diffusion dynamics inside the multilayer stack.

When Au:Pd films are co-sputtered onto a 250 °C pre-heated silica substrate, the H_2 absorption related changes in optical extinction ΔExt were far more modest, falling below even that of pure Pd. Overall, extinction decrease signal

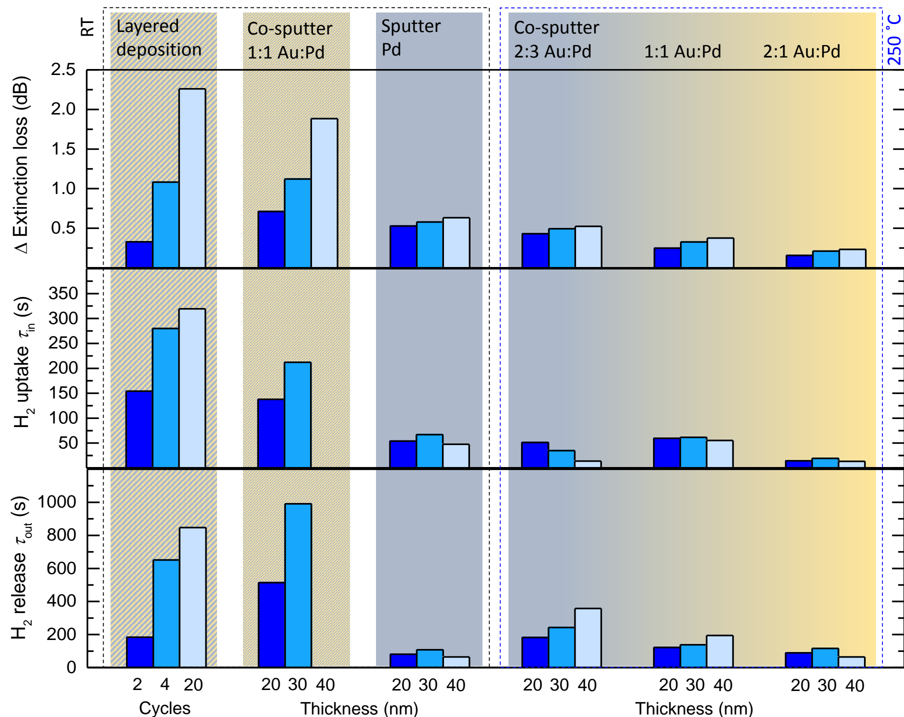

Figure 4.8: Comparison of key parameters characterizing the hydrogen related optical response of different Pd and Au/Pd composite films. From top to bottom, the ΔExt as well as both the H_2 uptake τ_{in} and release τ_{out} time constants are contrasted. Films are grouped based on the temperature of the silica substrate during sputtering as well as by the alloy composition fraction. The leftmost group represents Au/Pd multilayer films prepared by alternating sputtering over an increasing number of cycles. Hydrogen detection experiments were performed at Yokohama National University by the research group under supervision of Assoc. Prof. Yoshiaki Nishijima.

was found to scale with film thickness, in accordance with the Beer-Lambert law. Furthermore, ΔExt was larger for alloy films with a more substantive Pd fraction in their composition. On the other hand, the presence of Au results in a notable decrease hydrogen uptake and release time constants. The diffusion constant for hydrogen in Pd is on the order of $D \sim 10^{-5}$ cm^3 [180], meaning that the transport duration of H^+ in a homogeneous nanoscale film proceeds on a microsecond timescale, hence, is unlikely to be the rate limiting factor. Hydrogen adsorption and desorption provides a much more fitting explanation, as Au:Pd alloys, while readily dissociative of H_2 molecules, exhibit a decreased binding affinity to H adatoms due to the lower Fermi level placement [181, 182], therefore, possess a reduced activation energy for both hydrogen uptake and release.

In summary, straightforward all optical non-contact detection of gaseous hydrogen was demonstrated using pure palladium and Au/Pd composite thin-films. Cycle-sputtered alternating Au/Pd multilayers exhibited a higher optical extinction sensitivity to H_2 exposure, compared to pure Pd, at the cost of a low response rate. Conversely, homogeneous Au:Pd alloys co-sputtered at a 250 °C substrate temperature demonstrate shorter H_2 uptake and release times, however, a lower magnitude of optical response. In all cases hydrogenation was shown to be fully reversible, which is especially important for practical applicability in sensing devices. Similarly, alloying of palladium with gold results in a considerably more rapid response to hydrogen – a feature critical to safety-related monitoring purposes. Furthermore, as this is a structural property of the alloy, such materials can be incorporated in more elaborate signal transduction devices with resonant enhancement, such as the plasmonic structures described next.

4.2.3 Hydrogen sensing using Pd infrared wavelength plasmonics

While palladium is a prodigious material for hydrogen absorption, unlike noble metals it exhibits sub-optimal optical properties for hosting localized surface plasmon resonance (LSPR) excitations at visible wavelengths due to excessive damping of electron oscillations in this frequency range as a result of interband transitions. One way to side-step such a disadvantage is to use an indirect plasmonic detection scheme, where other metal nanoparticles with superior and tailored LSPR properties act as transducers that probe H_2 sensitive Pd structures *via* their optical near-fields [183]. On the other hand, in the infrared range many transition metals, such as Ni, Pt, and, of course Pd, are able to support plasmonic oscillations [184], and have likewise been used to perform direct spectroscopic detection of hydrogen [185, 186]. This latter method was chosen in this work for its simplicity, as it is not reliant on overlay exposure-based nanoscale fabrication techniques.

One of the benefits of employing longer wavelength radiation is that, due to the generally scalable nature of Maxwell's equations, size of structures sup-

porting resonant oscillations can also be made bigger. As a result, fabrication Pd plasmonic structures operating in the mid-IR range does not necessitate the use of costly EBL or FIB approaches, since the resolution of straightforward optical lithography is completely sufficient. Figure 4.9 (a) schematically illustrates the process used for fashioning palladium nanodisk array (NDA) and metal hole array (MHA) plasmonic structures by way of reduction projection photolithography with an *i*-line ($\lambda = 365$ nm) stepper NSR-2205i14E (Nikkon Corp.) tool, conducted by specialists at Tokyo Ohka Kogyo Co. Ltd. This is an advanced type of photolithography in which a mask, called a reticle, is projected onto a resist-coated substrate using an optical focusing system that demagnifies the pattern by up to 5 times. The technique gets its name from the sequential step-and-repeat manner that wafer-scale exposure is conducted. The particular system used here has a $NA = 0.63$ numerical aperture, employs a 22 mm square exposure field, and can attain a throughput of up to 103 $d = 200$ mm wafers per hour.

Silicon wafers are coated with either a positive tone TLOR-P003 HP, or a negative TLOR-N001 PM resist (Tokyo Ohka Kogyo Co. Ltd.), and subsequently UV exposed in a hexagonal lattice pattern of spots. Depending on the type of resist used, either a hole or disk array is established upon development for positive and negative tone cases respectively. Metal pattern generation was done by magnetron sputtering a 50 nm thickness film of Pd in an AXXIS PVD

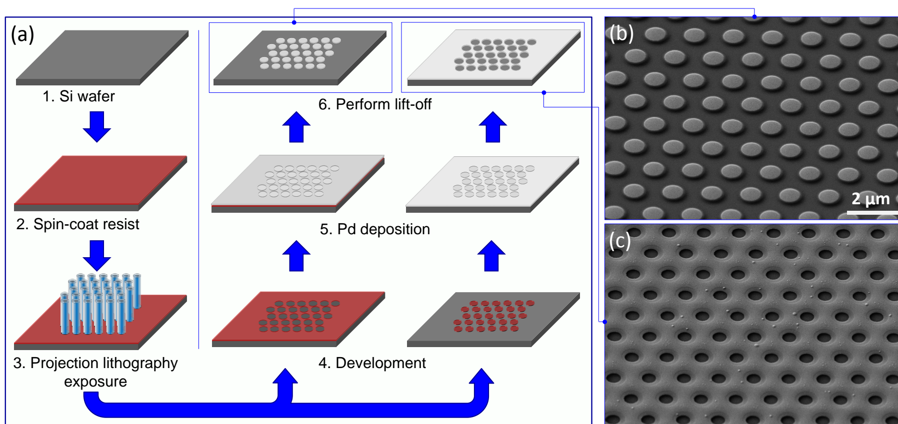

Figure 4.9: (a) Reduction projection photolithography based wafer-scale fabrication process of Pd mid-IR plasmonic structures. Si wafers are coated with photoresist and exposed in a hexagonally arranged disk pattern using an *i*-line stepper. Depending on whether the resist was positive or negative tone, after magnetron sputtering of 50 nm layer thickness of Pd and performing lift-off in acetone, either a (b) NDA or (c) MHA metal pattern is obtained, as shown in the respective SEM images on the right.

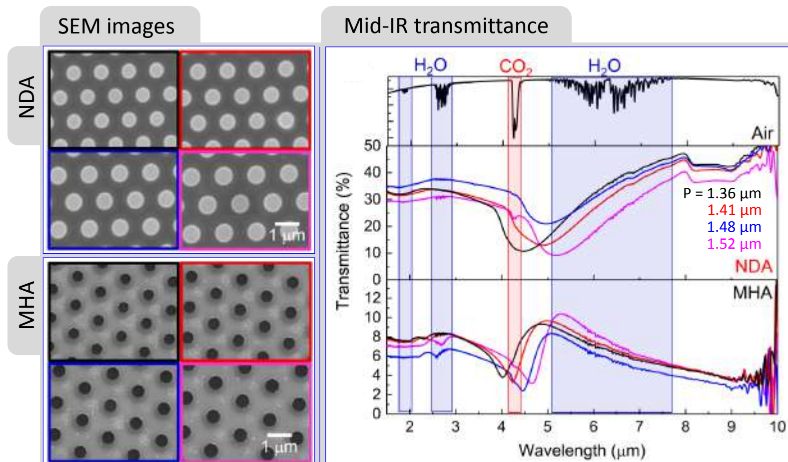

Figure 4.10: Mid-IR spectral response of different scale NDA and MHA Pd structures. SEM images on the left correspond to Pd NDAs and MHAs on a Si substrate patterned with incremantally increasing periods and disk or hole diameters, respectively. Spectra on the right show mid-IR transmittance of ambient air and of Pd plasmonic surfaces. Colored shading denotes the spectral regions with prevalent H_2O and CO_2 absorbance signatures. Infrared spectroscopy was performed at Yokohama National University by the research group under supervision of Assoc. Prof. Yoshiaki Nishijima.

tool (Kurt J. Lesker), and performing lift-off in acetone and MIBK. A hole pattern in a positive tone resist produces a Pd disk array pattern as illustrated by the SEM image in Figure 4.9 (b), whereas negative resists give rise to a hole pattern in a Pd film, shown in Figure 4.9 (c).

As shown in the left-side panels of Figure 4.10, the size-scale Pd film patterns can be controlled by altering the reduction performed by the optical system of the stepper lithography tool. Here, four sets of each structure were prepared, with periods ranging from $P = 1.36$ µm to 1.52 µm, where the exposure spot diameter-to-period ratio is maintained at 0.5, although a slight underexposure of negative resist resulted in only a 0.4 ratio for the MHA structure. The plasmonic behavior of nanodisks can be estimated by applying the Mie scattering theory for oblate spheroids, where the resonant wavelength of the structure scales with diameter and metal film thickness [187]. On the other hand, MHA resonant response is more closely related to their periodicity.

Mid-IR spectroscopy measurements for Pd NDA and MHA plasmonic structures, performed using a FT/IR-6200 spectrometer (JASCO Corp.) and plotted on the right of Figure 4.10, validate the aforementioned general predictions. The plasmonic absorbance related extinction features are quite broad and have FWHM values of up to ~ 1 µm, and as the scale of the pattern is increased

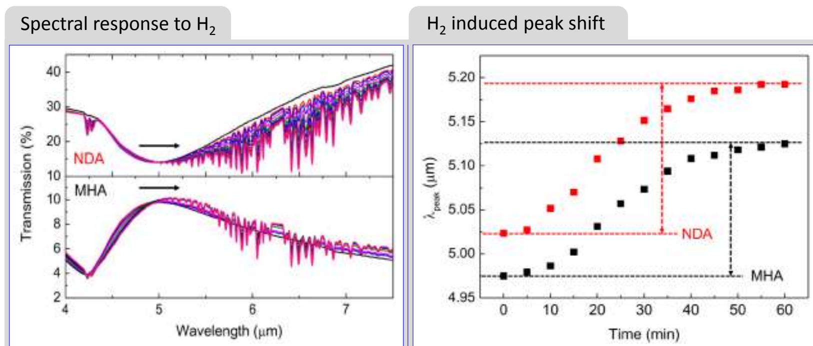

Figure 4.11: Hydrogen exposure induced variations in the mid-IR spectral response of Pd NDA and MHA structures. Plots on the left depict the transmittance spectra of $P = 1.36$ μm period NDA and MHA taken at 5 min intervals upon exposure to a 4% H_2 atmosphere. Right panel outlines hydrogen uptake related temporal shifts of the transmittance dips/peaks of respective strucures. Hydrogen uptake spectroscopic measurements were performed at Yokohama National University by the research group under supervision of Assoc. Prof. Yoshiaki Nishijima.

plasmonic extinction bands are shifted towards the longer wavelength region. Furthermore, the extinction-related transmittance dip in NDAs correspond to a peak at the same wavelengths for MHAs. Of further note is the abundance of mid-IR absorbance lines, associated with atmospheric CO_2 and H_2O, that were largely avoided by situating the plasmonic bands in the 3 μm to 5 μm wavelength transmittance window.

Hydrogen detection experiments were performed by mounting the Pd plasmonic samples in a $\sim$ 10000 cm^3 capacity evacuated chamber into which a 4% by volume H_2/N_2 gas mixture was injected at a 1000 sccm flow rate. Mid-IR transmittance spectra were subsequently acquired at 5 minute intervals, and the hydrogen absorption induced NDA and MHA extinction variations are shown in the left plot of Figure 4.11. As was mentioned previously in Section 4.2.2, hydrogenation results in Pd exhibiting more pronounced dielectric properties, leading to an increase in the refractive index n and a decrease in the extinction coefficient k. These alterations, in turn, manifest as a simultaneous redshift and broadening of the plasmonic extinction bands for both Pd NDA and MHA structures. Spectral changes reached saturation after approximately 40 minutes, producing a cumulative dip/peak broadening of 350 nm, and a substantive 160 nm wavelength position increase, illustrated by the transient plot on the right side of Figure 4.11. While the H_2 exposure induced extinction band shifts for mid-IR palladium plasmonic structures are much larger than those exhibited by equivalent near-IR counterparts, they appear to proceed at an up to 10 times

lower rate [186]. However, part of the reason for that can also be attributed to the excessive size of the gas container, where it takes up to 10 minutes after opening the hydrogen mixture injection valve for the spectral lineshift to start becoming observable, as evidenced by the slow onset of the transients. Therefore, more rigorous testing of the NDA and MHA Pd plasmonic structures is necessary for accurate estimation of temporal response-characteristic time constants.

In conclusion, hydrogen gas sensing was demonstrated in various palladium-based thin-film configurations, ranging from simple near-IR transmitted intensity measurements using different Au/Pd composites, to mid-IR plasmonic extinction band shift in lithographically patterned Pd layers. Alloying of Pd with Au resulted in an increase of the H_2 uptake and release rates, producing a notably faster response at the cost of total sensitivity. Conversely, generating nanoscale Au/Pd multilayers gave rise to an opposite result. Taken together these findings allow for tailoring of optical response to hydrogenation to fit a wide range of applications in H_2 sensing. Lastly, mid-IR plasmonic detection of hydrogen was demonstrated for the first time by using planar NDA and MHA palladium film patterns. Both of types of Pd structure exhibited a similarly strong and stable spectral response to hydrogen uptake, despite their different volume ratios and surface areas. The affordable and scalable reduction projection photolithography approach used here can also be employed to form more sensitive metal-dielectric-metal plasmonic absorber metasurface based signal transducers.

4.3 Plasmonic absorber metasurfaces at mid-IR

As a general principle, electromagnetic radiation incident on a subwavelength-scale metal object can induce its quasi-free charge carriers to collectively oscillate, thereby effectively turning it into a resonant cavity with a set of eigenmodes determined by material permittivity and boundary conditions [177]. These localized surface plasmon resonance (LSPR) excitations in a very basic sense where invoked in the previous Section 4.2.3 describing patterned Pd films. However, LSPRs are not fundamentally different from any other type of resonant cavity, which means that they can be made to couple and hybridize with each-other in a way that produces complex optical responses, best exemplified by plasmonic metamaterials and metasurfaces [188].

The key properties of metamaterials are dependent only in part on their elemental composition, and are predominately determined by the size, shape and arrangement of constituent resonator structures. This, in turn, makes it possible to engineer composites that exhibit unique performance features largely absent in the natural world, such as extraordinarily large [189] or even negative refractive indices [4], extremely low-frequency plasmonics [190], and chiral optical responses [191]. Still, electron scattering induced electromagnetic damping in plasmonic metal based resonant devices represents a principal limitation of what can be achieved, although ways of mitigating losses through either the use of heavily-doped semiconductors [192], or by offsetting the dispersed energy with optical gain [193], are vigorously pursued. Plasmonic absorbers, on the other hand, represent an application field for metamaterials where reflectance is suppressed through impedance matching and the dissipative nature of metals is leveraged to eliminate any transmittance, resulting in the almost total extinction of incident radiation at some resonant wavelength range [194]. Such plasmonic absorber metasurfaces can be tailored for specific spectral regions for uses as sensors [195], reflective filters [196] or thermal radiation absorbers and emitters [197].

In this work, conducted in collaboration with the research group headed by Assoc. Prof. Yoshiaki Nishijima at Yokohama National University, metal-insulator-metal nanodisk array plasmonic mid-IR radiation absorber metasurfaces are investigated both spectroscopically and numerically [198]. Particular focus is given to testing how the optical properties of several noble metals, namely Au, Ag, Cu, and Pd, as well as SiO_2, Si, ZnO insulators, used in all relevant configurations as illustrated in Figure 4.12, relate to the performance of the aggregate metasurfaces. The structures here, again, where fabricated by means of the wafer-scale reduction projection photolithography technique, as it was fully sufficient to attain features that were subwavelength at mid-IR wavelengths. In this spectral region the radiation properties of a plasmonic system are tied to its thermal conductivity, therefore, in all cases discussed here, ultrathin 10 nm insulator layers were preferred. Lastly, FDTD simulations pro-

vided a way to more finely investigate the effects that the dielectric properties of an insulating spacer, as well as systematic fabrication imperfections, exert on plasmonic absorbance of such layered nanodisk array devices.

4.3.1 Lithographic patterning of plasmonic metasurfaces

The plasmonic surface geometry employed in this work is sketched in the left panel of Figure 4.12, and is essentially comprised of a metal reflector base, a hexagonal 2D metal disk array, and an insulator layer interspersed between them. Here, the bottom layer was created by either using Au or Ag, whereas the constituent of capping disks was varied through almost the entire range of main plasmonic metals, including Au, Ag, Cu and Pd. Furthermore, nanodisk arrays comprised of Ti and Cr were also tested, however, despite exhibiting the strongly negative real part of permittivity required for hosting plasmonic oscillations at the mid-IR, no resonant plasmonic absorbance features were observed, hence these metals are omitted from further analysis. Lastly, the insulating spacer was made of either SiO_2, ZnO or undoped Si, with correspondingly increasing refractive indices $n_{SiO_2} \approx 1.4$, $n_{ZnO} \approx 2.0$ and $n_{Si} \approx 3.4$. As is evident from the SEM images on the right side of Figure 4.12 depicting plasmonic absorber metasurfaces comprised of a gold base layer, SiO_2 insulator, and different metal disks, choice of materials did not markedly affect the geometry of resultant structures.

The fabrication procedure used here relies on reduction projection lithography and largely mirrors the one outlined in Section 4.2.3, with the obvious exception being the differences in number and sequence of PVD steps. Workflow of the process is outlined in Figure 4.13, where it is performed by using a

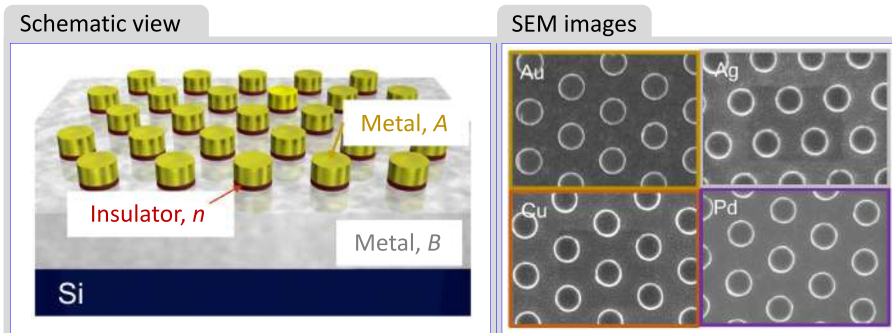

Figure 4.12: Overview of nanodisk array plasmonic absorber metasurfaces. Left panel depicts a conceptual sketch of the structure, comprised of a metal *B* base layer and metal *A* nanodisks, separated by an ultrathin *n* refractive index dielectric film. SEM images on the right depict plasmonic absorber metasurfaces, where the base metal is gold whereas capping disks are comprised of Au, Ag, Cu and Pd, as denoted in respective capions.

double-side polished Si wafer as a substrate. First, an optically opaque 200 nm thickness film of either Au or Ag is deposited by means of a thermal evaporation PVD process. Patterning of the NDA structures was done by specialists at Tokyo Ohka Kogyo Co. Ltd. by first spin-coating a positive tone TLOR-P003 HP photoresist (Tokyo Ohka Kogyo Co. Ltd.) and subsequently conducting UV exposure using an *i*-line stepper NSR-2205i14E (Nikkon Corp.). Following development of the latent nanohole array, Ar^{+} plasma magnetron sputtering PVD was performed using an AXXIS tool (Kurt J. Lesker) in order to create the arrangement of nanodisks, each situated on insulating films. Dielectric SiO_2, ZnO and Si layers, in all cases 10 nm in thickness, were transferred from the respective insulating targets by way of radio frequency sputtering. Similarly, 50 nm thick Au, Ag, Cu and Pd capping metal films were deposited using the simpler direct current bias source, as charge buildup is not an issue for conducting target materials. In order to ensure consistent adhesion between the different materials a 3 nm thickness Ti layer was sputtered before and after insulator film deposition. The final step of the procedure involves the resist lift-off in acetone, followed by a rinse in IPA and blow-drying using nitrogen gas.

In total, four sets of NDA absorber structures with 1.36 µm, 1.41 µm, 1.48 µm and 1.52 µm periods were prepared, where the disk diameter-to-period ratio was 0.5 in all cases. However, as the increase in pattern scale mainly resulted in a redshift of absorbance spectral peaks akin to what is depicted in Figure 4.10, as well as due to this work being directed at investigating the influence that different materials have on metasurface spectral characteristics, descriptions provided here limit themselves to the $P = 1.36$ µm case for brevity.

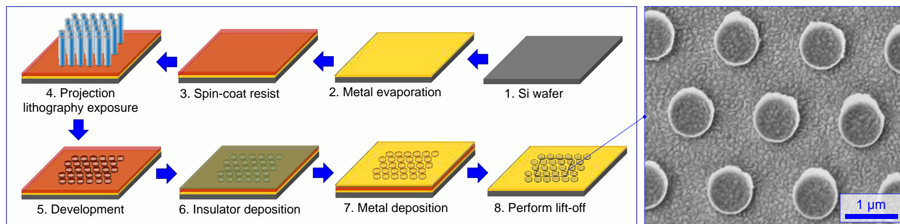

Figure 4.13: Reduction projection photolithography based wafer-scale fabrication process of different mid-IR plasmonic absorber metasurfaces. Si wafers are first coated with a 200 nm thickness base metal film using thermal evaporation. A positive tone photoresist is spin-coated and exposed to a hexagonally arranged spot illumination pattern using an *i*-line stepper. After development, 10 nm thickness insulator and 50 nm capping metal layers are sequentially deposited by way of magnetron sputtering. The nanodisk array pattern is obtained following a lift-off step in acetone. A SEM image of the resultant structure is shown on the right.

Still, all main findings and observations are equally applicable to the higher period plasmonic absorber surfaces [198].

The SEM image on the right side of Figure 4.13 depicts a representative segment of a Au/SiO_2/Au NDA plasmonic absorber metasurface and illustrates the main morphological features shared between all realizations regardless of the materials comprising them. In all cases the metasurfaces retained pattern consistency over the entire 1×1 cm^2 fabrication area. However, individual nanodisks did exhibit certain flaws, such as chipping as well as slight bowing around their periphery. This is due to the high degree of coating conformality associated with magnetron sputtering deposition, which results in substantial amount of material covering the resist side-walls. In general, sputtering is not advisable for lift-off lithography, with high-vacuum thermal evaporation being far more preferable, however, here its use was necessary to ensure the correct stoichiometry of deposited SiO_2 and ZnO dielectrics. Another fabrication imperfection was due to the ~ 50 nm root mean square roughness of thick base metal films, which translate into unevenness of the deposited nanodisks. Still, despite these issues, NDA patterns were defined with sufficient fidelity to exhibit most of the predicted mid-IR plasmonic properties.

4.3.2 Spectroscopic characterization of mid-IR absorbance

Performance of the reduction projection lithography fabricated metal-insulator-metal NDA plasmonic absorbers was expermentaly investigated by means of mid-IR reflectance microspectroscopy. The apparatus used for that purpose was a FT/IR-4200 Fourier-transform IR spectrometer equipped with a IRT-1000 in-compartment microscope unit attachment (JASCO Corp.). The optical system was comprised of a $NA = 0.5$ Cassegrain reflector objective lens, and a liquid nitrogen cooled mercury cadmium telluride detector was employed for signal acquisition. While the 500×500 µm^2 sub-fields, corresponding to different NDA period structures, were large enough to perform measurements without any need for microscopy, the increased resolution was useful in investigating the spatial uniformity of plasmonic absorbance. Calibration of the absolute reflectance was performed using a gold mirror with a tabulated reflectivity that averages around $\sim 98\%$ throughout the mid-IR wavelength range.

Figure 4.14 outlines the mid-IR reflectance spectra of various NDA plasmonic absorber metasurfaces prepared on an Au metal base layer. In all cases, dips in reflectivity appeared in roughly the same $\lambda \approx 3$ to 5 µm spectral region, hinting at the resonance being mainly set by the structure geometry. All tested structures exhibited a high degree of spatial uniformity in their spectral response, which is indicative that consistent fabrication fidelity was maintained throughout the large area samples. Furthermore, the hexagonal NDA lattice ensured a reasonably isotropic response to linearly polarized excitation, as it maintains equidistant spacings between neighboring disks along three directions. Lastly, the sharp reflectance dip at around $\lambda \approx 4.2$ µm is due to CO_2

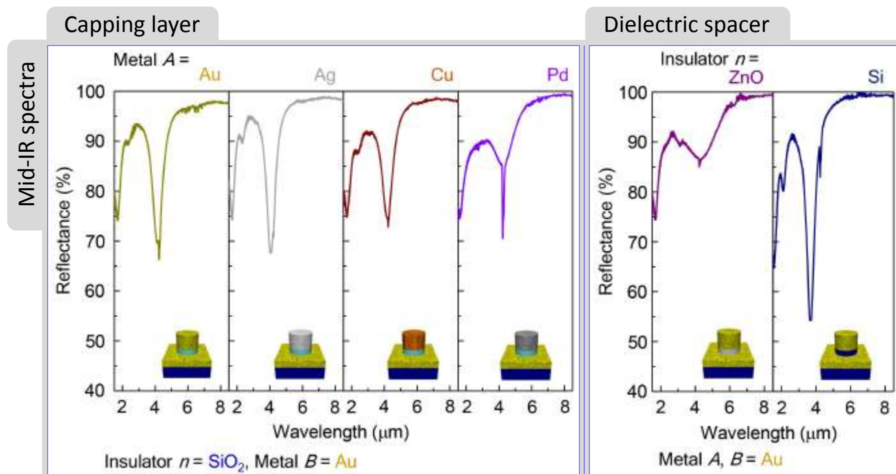

Figure 4.14: Experimental mid-IR reflectance of 1.34 μm period plasmonic absorber metasurfaces with an Au base layer. Plots in the left panel depict reflectance spectra that correspond to capping disks made from different Au, Ag, Cu, and Pd metals, where in all cases the dielectric spacer is comprised of SiO_2. Right panel plots show corresponding spectral characteristics for gold plasmonic structures with ZnO and Si insulator spacers. Infrared spectroscopy experiments were performed at Yokohama National University by the research group under supervision of Assoc. Prof. Yoshiaki Nishijima.

absorbance, hence, is not intrinsic to the structures.

Plots in the left panel of Figure 4.14 contrast the reflectances of Au metal base and SiO_2 insulator layer plasmonic absorbers, where the 50 nm thickness capping disks are comprised of Au, Ag, Cu and Pd. The minimum reflectance values were around 70%, 65%, 75%, and 85% for each of the respective metals. Also, while the resonant wavelength dependence on the type of capping metal is fairly minor, there still is a noticeable redshift trend that is smallest for Ag, increases when Au as well as Cu is used, and is largest for Pd. This dependence mirrors the slight differences in permittivity between the metals at mid-IR, which result in minor shifts of the nanodisk resonance condition. Conversely, disparities between FWHM and extinction ratio values are readily apparent, and become especially severe for Cu and Pd cases. Here, again, differences in material properties provide the underlying cause, since Cu and Pd exhibit much stronger electron scattering than Ag or Au, thus resulting in more rapid dissipation of energy and plasmonic resonances that have a lower quality factor Q, as was previously defined by Equation 2.12 in Section 2.1.1.

The effect of using different insulator spacers interspersed between Au metal reflectors and nanodisks is illustrated by the reflectance plots on the right of Figure 4.14. It is clear that ZnO gives rise to a much broader and

less pronounced absorbance peak. While part of this effect can be attributed to its larger $n_{\text{ZnO}} \approx 2.0$ refractive index, a much more likely explanation is that ZnO itself possesses an electronic conductivity in the 10^{-3} to 10^{8} Scm^{-1} range, and exhibits piezoelectricity as well as polarizability even in the absence of doping [199, 200]. Much more surprising is the performance of the Si dielectric spacer-based metasurface, which, contrary to expectations, surpasses the extinction observed for the SiO_2 case by roughly 15%. Furthermore, the resonance dip is quite narrow, and possesses all the expected higher order counterparts at approximately $\lambda = 3$ µm and $\lambda = 2$ µm wavelengths.

Of additional note is that a magnetron sputtered intrinsic Si insulator proved to be superior as far as resonant reflectance suppression was concerned in conjunction with most metal combinations, as shown in the Figure 4.15 (a) plots for Au, Ag, Cu and Pd nanodisks, applied onto Au and Ag base layers. Hence, the effect appears consistent between numerous samples and fabrication batches. Neither increases in refractive index nor the presence of conductivity in the insulating layer are able to account for this, as such factors would be

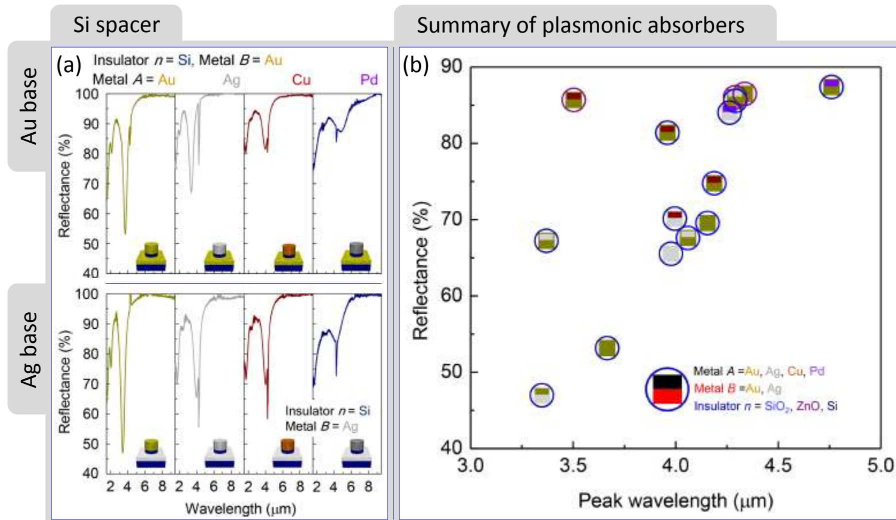

Figure 4.15: (a) Experimental mid-IR reflectance of 1.34 µm period plasmonic absorber metasurfaces with a Si insulating spacer layer. Plots at the top and bottom of the panel respectively show Au and Ag base metal layer reliant surfaces with Au, Ag, Cu, and Pd capping disks. (b) Summary of defining spectral signatures for each investigated plasmonic absorber metasurface, where minimum reflectance is plotted against the wavelength at which the dip is observed. Infrared spectroscopy experiments were performed at Yokohama National University by the research group under supervision of Assoc. Prof. Yoshiaki Nishijima.

expected to produce an opposite effect, more in line what was observed for ZnO. Likely partial explanations for such findings include oxidation of the ultrathin 10 nm insulator post fabrication to create a SiO_x layer, or by invoking the inherent porosity of the magnetron sputtered amorphous film, which would both result in the refractive index of the layer becoming considerably smaller than the $n_{Si} \approx 3.4$ values for bulk crystalline Si.

All experimental mid-IR spectroscopy results pertaining to different composition NDA plasmonic absorber metasurfaces are summarized in Figure 4.15 (b), where the spectral position and reflectance associated with the dominant extinction band for each case is provided as a scatter plot. Overall, fundamental resonant absorption dips appeared in the 3.2-to-4.8 µm wavelength range, whereas reflectance reached values between 45% and 90%. When silver is used as the reflector layer an approximately 5%–10% across-the-board improvement in extinction at resonance is observed. This is largely unsurprising, as Ag exhibits lower damping related losses, hence, tends to outperform Au by yielding sharper plasmonic resonances. On the other hand, the propensity for silver to oxidize considerably diminishes its utility, particularly when used at elevated temperatures in an ambient atmosphere. Such oxidation is the likely cause for gold performing just as well or better than silver as a 50 nm thickness capping disk layer, followed by copper and, lastly, by palladium. The dielectric spacer related extinction signature variations are far more counter-intuitive, with ZnO being the least well suited, SiO_2 offering intermediate performance, and Si exhibiting both strongest absorbance and the most blueshifted reflectance dips, despite the opposite being the expected result based solely on Maxwell's equations, as is described next.

4.3.3 FDTD simulation of insulator and morphology effects

The operation of NDA metasurfaces relies on the interaction between the two coupled functional metal layers, where the two-dimensional disk array and planar mirror layers under electromagnetic excitation support antiparallel currents [195]. In other words, plasmonic oscillations in one of the metal layers give rise to complementary excitations in the other. At resonance, electromagnetic energy gets tightly confined within the dielectric spacer layer and exhibits a strong local field enhancement. Hence, the insulator layer interspersed between a metal base and the disk structure fulfills the role equivalent to a capacitive element in an equivalent circuit model [201]. This trapped radiation is gradually dissipated in the metal components, therefore, a narrowband dip is observed in the reflectance spectra for a wavelength at which impedance matching is ensured.

While the classical equivalent circuit model can account for some aspects of NDA plasmonic absorber performance, particularly those relating to geometric parameters of the metal components, it nevertheless gives predictions regarding dielectric spacer choice that are contrary to experimental observa-

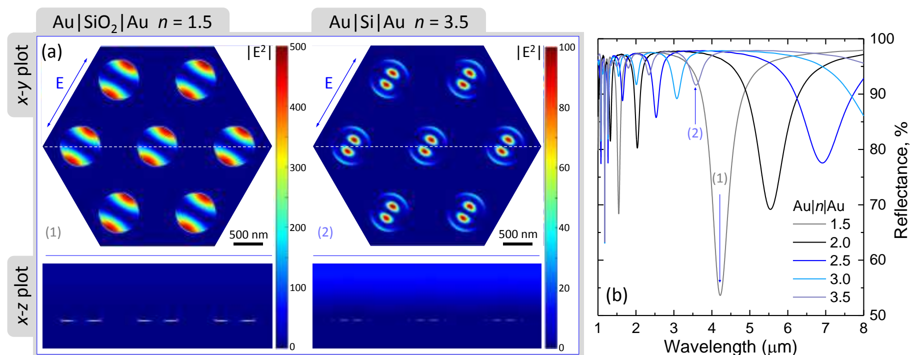

Figure 4.16: FDTD simulation results for gold-based NDA plasmonic absorber metasurfaces. (a) Plasmon resonance electric field intensity distributions at the dielectric spacer for insulator refractive indices $n = 1.5$ and $n = 3.5$, approximately representative of SiO_2 and Si, respectively. The bottom-row plots show corresponding field intensity distributions in the x-z plane, marked in the x-y representation as a white dashed line. (b) FDTD simulated mid-IR reflectance spectra for plasmonic absorbers with different refractive index n insulator layers. Arrows mark the two resonance peaks for which field intensity profiles were provided.

tions. Therefore, full vectorial solutions of Maxwell's equations by way of the FDTD method are employed here using the commercially available "FDTD Solutions" (Lumerical Solutions Inc.) solver software package. The numerical investigation was performed on large 3D renderings of NDA plasmonic metasurfaces, spanning three periods of the structure. Feature dimensions were set based on SEM imaging results, with the brunt of calculations performed on the $P = 1.34$ μm period and $d = 0.67$ μm nanodisk diameter variants represented in Section 4.3.2. The simulation region was terminated using periodic boundary conditions in x and y surface-perpendicular directions, whereas perfectly matched layer boundaries were applied across the z axis radiation incidence direction. A normally incident pulsed plane wave source, spanning the $\lambda = 1$–8 μm wavelength range, was used for excitation, and metasurface spectral response was registered in a reflectance configuration. The complex mid-IR permittivity values for the different metals and dielectrics making up the layered NDA devices were obtained from the literature [202]. Due to the computationally demanding nature of the work, which requires nanoscale mesh precision to define ultrathin material layers over microscale volumes pertinent to mid-IR wavelengths, calculations were done on the swinSTAR supercomputer at Swinburne University of Technology.

A summary of FDTD simulation results for idealized geometry Au-based plasmonic absorber metasurfaces, realized with different refractive index insu-

lating spacer layers, is provided in Figure 4.16. More specifically, panel (a) on the left depicts electromagnetic field intensity distributions at resonance within the 10 nm thickness insulator layer as both x–y and x–z cross-sections at the top and bottom respectively. It is readily apparent that virtually the entirety of the plasmonic mode is confined within the dielectric, resulting in substantial local field intensity enhancements. When the two different refractive index cases are compared, $n = 1.5$ being close to values associated with SiO_2 whereas $n = 3.5$ is more in line with Si, it becomes clear that different order modes are operative at around $\lambda \sim 4$ µm wavelengths for the two spacer materials. NDA structures possessing the lower refractive index SiO_2 dielectric support what appears to be the fundamental dipolar excitation, whereas for Si an additional node is present in the field distribution, meaning that this is a second order mode.

Further information on the insulator refractive index influence on plasmonic absorber performance can be gleamed from the simulated reflectance spectra plotted in Figure 4.16 (b). As expected based on the analytical equivalent circuit model, increasing the refractive index n of the insulator induces a redshift as well as a broadening and diminishment of the resonant plasmonic band. The fundamental dipolar mode associated peak moves from $\lambda \approx 4.2$ µm to $\lambda \approx 7$ µm when the refractive index increases substantially from $n = 1.5$ to $n = 2.5$, and further still for the $n = 3.5$ case that makes the second order mode the dominant spectral feature in the simulated IR band. However, simulation data matches only the experimental spectroscopy results for SiO_2 spacer NDA structures, and strongly deviates for both ZnO and Si. While in the former case electronic conductivity can be invoked to account for much of the discrepancy, the reasons behind silicon insulator behavior appearing entirely opposite to simulation predictions is far less clear.

Of course, as was stated in Section 4.3.1, experimentally fabricated NDA plasmonic absorber metasurfaces do not quite exhibit the idealized planar reflector or flat capping disk geometries assumed in the aforementioned FDTD simulations. Indeed, the close-up SEM image of a single nanodisk, depicted in the top-left panel of Figure 4.17, illustrates the extent of nanoscale geometry distortion that can be expected. However, by harnessing the extensive computational resources at the disposal of the swinSTAR supercomputer, far more realistic geometric configurations, which include the fabrication process limitation-induced deviations from initial design, can be investigated. Two flaws where given particular attention – namely the bowl-like shape that develops during lift-off due to sputter-deposition onto resist side-walls, and the nanoscale surface roughness that gets transferred from the metal base layer. The middle panels in Figure 4.17 depict the side-view refractive index distribution profiles representing the idealized flat and bowl-like shape cases, as well as the rough surface depicted in the 3D rendering bottom-left that is most reminiscent of the experimental SEM image.

The simulated reflectance spectra of the three respective metasurface mor-

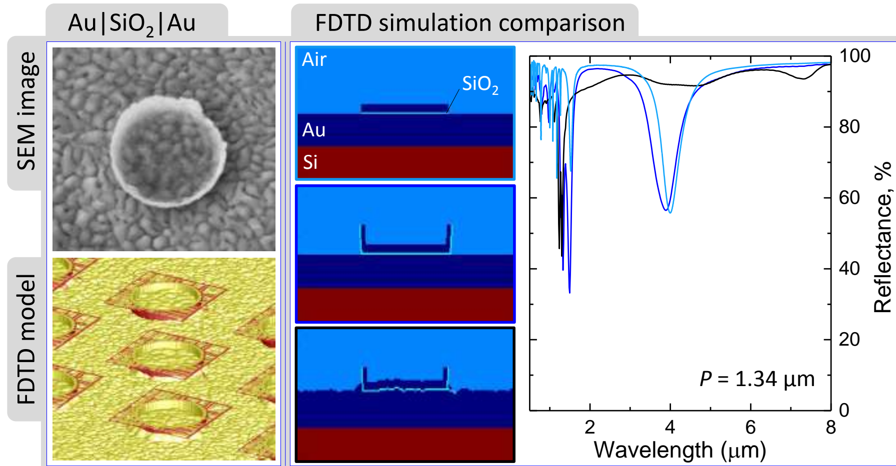

Figure 4.17: NDA plasmonic absorber performance dependence on fabrication imperfections as revealed by a FDTD simulated mid-IR reflectance response. SEM image top-left gives a close-up view of a nanodisk exhibiting surface roughness as well as a bowl-like periphery. A realistic rendering used of FDTD simulations is shown bottom-left. Cross-section plots in the middle depict the refractive index distributions in three different FDTD simulated geometries with an increasing degree of distortion. Reflectance plots on the right show the plasmonic resonances for each of the NDA geometry cases.

phology cases are plotted in the right panel of Figure 4.17. Compared to a planar arrangement, the bowl-like patterns did not exhibit a particularly strong departure from the idealized spectral response, and merely had slightly blueshifted resonances and a somewhat increased linewidth, likely due to a higher contribution of scattering losses. Apart from this the overall extinction remains approximately the same, which means that such minor deviations in shape are not substantially detrimental. Conversely, roughness of the absorber surface can have a very negative effect on fundamental plasmonic absorbance mode spectral signatures, rendering them exceedingly broad and indistinct, although the more strongly localized higher order excitations appear to be less affected. Hence, it can be understood that experimentally fabricated structures possess a higher degree of fabrication fidelity than was assumed for these rough surface simulations, however, their higher extinction could potentially be the result of stochastic averaging over a large number of nanodisks.

Overall, metal-insulator-metal nanodisk array based plasmonic absorber metasurfaces have been shown as viable for potential applications as photothermal radiation energy harvesting or sensing devices at the mid-IR. The present realization uses the highly scalable and cost-effective reduction projection photolithography technique, capable of rapid wafer-scale throughput, to

attain plasmonic resonances with around 50% extinction at a predefined narrow-band wavelength range. As an extension of the present work, EBL patterning was also used to attain absorbance values in excess of 90% when inter-disk gaps were shrunk down to 30 nm [198]. Unsurprisingly, Au and Ag noble metals were shown to exhibit the highest degree of reflectance suppression, however, contrary to expectation and for reasons as of yet undetermined, Si insulator spacers proved to be far superior to SiO_2 when the layer thickness was set to 10 nm. High fidelity FDTD simulations revealed how deviations from idealized metasurface geometry are expected to affect performance, demonstrating that stochastic surface roughness can have substantially more dissipative effects than bowing around the periphery due to lift-off imperfections. Lastly, simulated electromagnetic field intensity distribution plots were used to visualize the tight radiation energy confinement in the ultrathin insulator spacers which, apart from increasing thermal conductivity of the device, could be harnessed in advanced molecular sensing applications that by a wide margin surpass the microscale diffraction limitations at mid-IR.

Disparate metals exhibit different magnetic properties that can range anywhere from being diamagnetic for heavy elements like Pb as well as Ag, antiferromagnetic like Cr, paramagnetic as exemplified by Al and Ti, or outright ferromagnetic in the manner of Co, Fe and Ni. Furthermore, macroscopic properties, such as the static susceptibility and magnetization, can be significantly altered by preparing different multilayer superlattice systems, where interfacial interactions and collective effects can even lead to the aggregate structure behaving opposite to its constituent building block materials [203]. One major field of practical application for magnetic multilayer films involves their usage as magnetic recording media [204], however, more recently they have been employed as a trapping substrate for cold atoms and degenerate quantum gases [205].

Ultracold atom gases represent an intriguing and powerful model system for simulating complex condensed matter or many-body quantum phenomena [210]. To this end, optical lattices produced by interfering laser beams are the most popular choice of method for creating periodic trapping potentials, applied as high precision atomic clocks [211], quantum gates for information processing [212], and quantum gas microscopes [213]. Fundamental insights regarding the metal to insulator cross-over [214], the 1D Ising spin model [215], Anderson localization in disordered systems [216] and the quantum Hall effect [217] have also been obtained from ultracold atom trapping experiments using such optical lattices. However, permanent magnetic lattices, comprised of periodic microtrap arrays created by patterning magnetic films, provide an alternative approach that operates under relaxed laser power, stability and alignment requirements, can be used to generate virtually arbitrary 2D geometries, and exhibits substantial integration potential for on-chip quantum functionality.

Figure 4.18 gives a general overview of the main features and prerequisites of magnetic lattice microtrap operation. Panel (a) depicts an atom chip, essentially comprised of a magnetic lattice supporting wafer and an underlying machined foil substrate with various current-carrying conductive tracks. Said wires can be Z-shaped or U-shaped [218], and their magnetic fields are used to deliver and load the atom gas, already pre-cooled down to the micro-Kelvin temperature range by laser-based techniques such as Doppler, polarization gradient, or magneto-optical trap cooling [219], onto the magnetic lattice. This trapping structure is generally made from a perpendicularly magnetized multilayer film, patterned to form a wide range of configurations, although the 1D linear grating, shown in the inset of Figure 4.18 (a), is likely the simplest [206]. The intrinsic magnetic field distribution of a lattice is further reshaped using external bias fields B_x and B_y to produce adjustable depth periodic magnetic potential traps. By lowering the trapping barrier height it becomes possible to force further evaporative cooling of the captured atoms, as shown in Figure 4.18 (c) where

2 μK ^{87}Rb clouds initially comprised of an estimated 5350 atoms were brought down to 380 nK with 200 particles remaining, which resulted in Bose-Einstein condensation [209]. Lastly, ultracold atom clouds can be visualized by way of laser absorbance imaging, as sketched in Figure 4.18 (b), which results in direct observation of various trapping configurations [207]. Notable examples include the 10 μm period 2D triangular and square symmetry gratings [208], visualized in Figure 4.18 (d), however, at such distances clouds of trapped atoms are effectively isolated from each other, hence, observation of advanced phenomena such as quantum tunneling is not possible.

In this work, conducted in collaboration with the group headed by Prof. Peter Hannaford at Swinburne University of Technology and researchers at University of Augsburg under the supervision of Prof. Manfred Albrecht, 700 nm

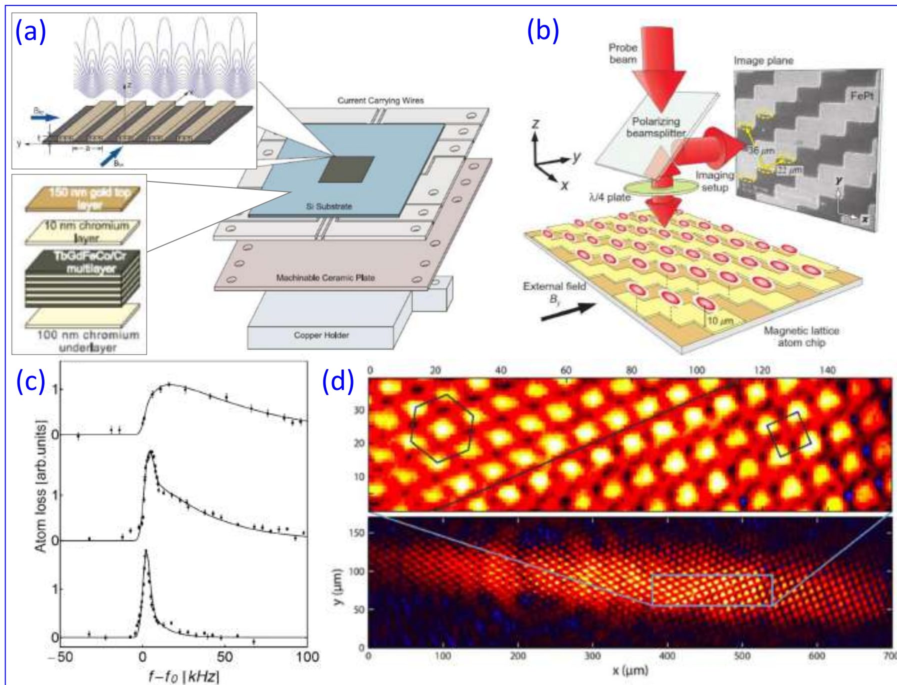

Figure 4.18: Overview of ultracold atom trapping in magnetic lattices [205]. (a) Construction of a magnetic lattice atom chip, comprised of the 1D multilayer grating depicted in insets, and an underlying foil with different conductor wire traps for atom loading [206]. (b) Schematic illustration of the absorption imaging scheme used to visualize atom clouds trapped in a 10 μm period 2D lattice [207], in a way that is similar to square and triangular symmetry cases shown in (d) panel [208]. (c) Radio frequency spectra of ^{87}Rb atom clouds in a 1D lattice, exhibiting the onset of Bose-Einstein condensation with progressive evaporative cooling [209].

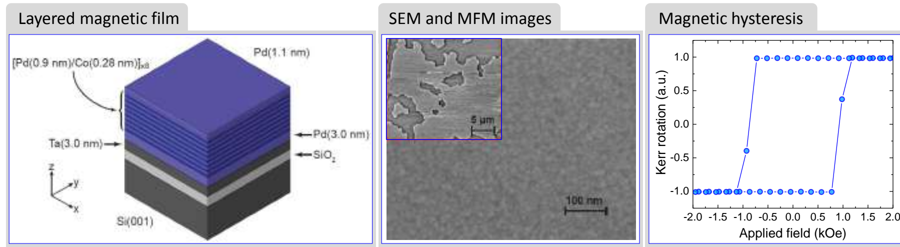

Figure 4.19: Magnetic film used for fabricating submicron atom trapping lattices [221]. Left panel shows the schematic multilayer stack composition of 0.28 nm thickness magnetic Co and 0.9 nm non-magnetic Pd. Middle panel shows an SEM image of the film surface that exhibits 10 nm average grain size. The MFM image in the inset reveals the presence of large magnetic domains. Rightmost plot shows the Co/Pd multilayer magnetic hysteresis measured by way of Kerr rotation. Magnetic film preparation and characterization was performed at University of Augsburg by the research group under supervision of Prof. Manfred Albrecht.

period 2D magnetic lattices were patterned into a magnetic multilayer film using EBL and employed to demonstrate the first reported loading of ultracold ^{87}Rb atoms into submicron spacing magnetic traps [220]. The requisite structures were fabricated with ~ 5 nm pattern fidelity over large 1×1 mm^2 areas by using state of the art EBL capabilities at the Melbourne Centre for Nanofabrication. Performance of one specific design, namely the 700 nm period 2D triangular symmetry lattice, is described in some detail and underlying causes of trap lifetime limitations are discussed.

4.4.1 EBL fabrication of submicron magnetic lattices

A high quality permanent magnetic material is a basic prerequisite for the realization any functional magnetic trap lattice. It has to exhibit a strong perpendicular magnetic anisotropy to ensure a high degree of magnetic domain alignment, hence, high magnetic homogeneity, as well as a high saturation magnetization to produce tight trapping potentials and large gradients. Furthermore, a magnetic material should have a large coercivity so as not to demagnetize when bias fields are applied, and its Curie temperature should be above 300 °C to withstand a vacuum bake-out step. An additional requirement imposed by lithographic patterning is that magnetic layers should exhibit small grain sizes so as not to limit the attainable resolution.

Here, a metallic multilayer composed of 8 alternating films of ferromagnetic transition metal Co, and a noble metal Pd, which combines both a large perpendicular magnetic anisotropy and a small grain size primarily geared towards high-density magnetic recording media [221, 222]. The left panel of

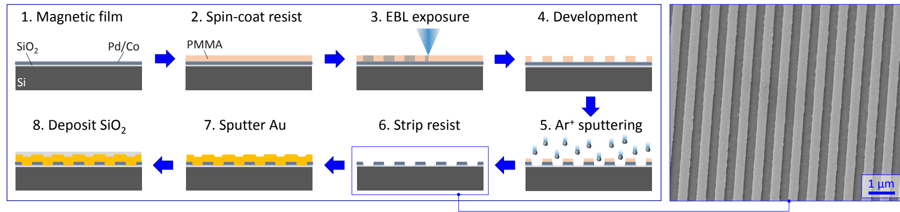

Figure 4.20: EBL fabrication of submicron magnetic ultracold atom trapping lattices. The Si wafer with a sputtered metal multilayer is spin-coated with a 300 nm PMMA resist film and exposed using a high performance EBL tool. The latent pattern is developed in MIBK and its transfer through Co/Pd is pefromed by way of anisotropic Ar^{+} ion physical sputtering. Resist residue is stripped away with anisole. Lastly the resulting lattices are sputtered with a 50 nm thickness of Au to increase surface reflectance and 25 nm of silica to prevent ^{87}Rb atom sticking. SEM image on the left depicts an etched 700 nm period 1D grating.

Figure 4.19 shows a sketch of the magnetic film layer structure, magnetron sputtered on a 500 µm thickness (100) surface plane native oxide coated Si substrate. First, seed layers of 3 nm-thick Ta and Pd are deposited in sequence to provide a uniform (111) crystallographic base. Next, the eight bi-layers of 0.28 nm Co, equivalent to approximately 2 atomic layers, and 0.9 nm of Pd are sputtered at room temperature. The Co/Pd multilayer exhibits a roughly $\sim 20\%$ increased magnetization relative to bulk cobalt due to polarization of the Pd atoms by interspersed Co layers. Lastly, the magnetic film is terminated by a 1.1 nm Pd capping layer to safeguard the structure against oxidation.

As can be observed in the SEM image in the middle panel of Figure 4.19, the resultant metallic multilayer is notably smooth, with grain sizes generally falling below approximately 6 nm [223], hence, is unlikely to impede the high resolution fabrication of structures. The inset shows a magnetic force microscopy (MFM) image of the AC-demagnetized Co/Pd film, where the binary map is indicative of the magnetic domain structure, and represents the magnetization pointing either up or down at a right angle to the film plane as a result of a strong perpendicular magnetic anisotropy. Right side of Figure 4.19 shows the hysteresis loop for the Co/Pd multilayer film as measured by Kerr rotation. The hysteresis response has a near-ideal square shape, where the measured film coercivity is $H_c = 1$ kOe, and the saturation magnetization is quite high at 5.9 kG, which provides a fitting medium for creation of advanced atom trapping lattice designs.

Various magnetic lattice structures were fabricated by means of EBL according to the process visually summarized in Figure 4.20. Prior to resist coating, the Co/Pd film sputtered Si wafer was cleaned over several sonication steps

in organic solvents: first in acetone, then isopropanol and finally in methanol. After organic solvent processing the wafer was blow-dried using N_2 gas and any residual solvent molecules were removed by heating on a 180 °C temperature hot-plate for 3 minutes. Next step involved the the spin coating of a 300 nm thickness PMMA 495k positive tone electron beam resist (MicroChem Corp.) film. This thickness was selected as a compromise between a higher resolution afforded by thinner films, and higher etch resistance provided by thicker ones. The resist was then soft-baked for 30 seconds at 180 °C to evaporate away any anisol PMMA solvent remnants. EBL exposure was performed using a Raith EBPG5000plusES tool operating at 100 kV electron acceleration voltage. The 1 mm^2 write-field span provided by this machine allowed to expose the entire 2D magnetic lattice without any stage movement related stitching errors. A 5 nm FWHM electron spot was focused and scanned along the designated pattern at a 50 MHz rate afforded by the 12 bit pattern generator. Complexity of the lattice design, which required pattern fracturing into an unusually large number of elementary geometric shapes to preserve fidelity, resulted in memory buffer overload of the controlling software, which was the main factor limiting the patterning rate. For this reason exposure durations ranged from 30 min for simple 1D gratings depicted in a SEM image on the right side of Figure 4.20, to 2 hours for the complex square and triangular 2D lattices.

As mentioned previously in Section 1.1.2, when EBL exposure is performed over large areas or when it aims to define tightly-packed structure arrays, it becomes important to account for proximity effects that arise due to additional resist irradiation by electrons back-scattered from deep within the substrate. This is particularly evident from the Monte Carlo simulated spatial optimal exposure dose distributions, displayed in the left panels of Figure 4.21. Here, the central parts of the patterned array are subject to more unintentional exposure contributions from electrons back-scattered during exposure of neighboring regions, whereas the ~ 25 μm width peripheral regions and especially the corners are much less affected. SEM images of fabricated 200×200 μm^2 area triangular 2D lattices for atom trapping reveal the influence of unaccounted for proximity effect, which results in overexposed central regions, even if doses for high quality definition of isolated features are correct around the corners.

However, the serial scanning nature of EBL allows to account for proximity effects by modifying the dose of each feature separately. Hence, after conducting Monte Carlo simulations to evaluate how the electron beam is scattered and obtaining the point spread function, the design file can be updated to compensate any unwanted exposure and obtain a good lattice uniformity, as shown in lower-right SEM images in Figure 4.21. In general terms, when a 1 mm^2 area structure is exposed the process is not much different from the 200×200 μm^2 case given here as an example – the central part is scanned using the base dose of around 670 $\mu C cm^{-2}$, whereas in the corner and periphery regions it is increased by up to a factor of $\times 1.5$ – as the ~ 25 μm width frame is set

solely by the scattering behavior of the incident beam that remains completely unchanged.

After resist exposure the latent pattern was developed for 80 seconds in 1:3 mixture of MIBK and IPA. Subsequently the wafer was immersed in pure IPA, which acts as a stopper, and blow-dried with N_2. The next step involved resist pattern transfer down to the Co/Pd multilayer film in a Samco RIE-101iPH ICP-RIE tool (SAMCO Inc.) by way physical sputtering *via* argon ion bombardment for 12 seconds. During this process the remaining unexposed PMMA resist areas act as a protective mask against the incident energetic ions. Hence, exposed areas are stripped of Co/Pd film down to the underlying Si wafer, whereas the coated metal multilayer regions remain unaffected. After the plasma treatment step all of the remaining resist was removed by sonicating the wafer in 60 °C anisole, acetone and, lastly IPA solvents. The elevated temperature was necessary in order to strip the parts of resist mask that were

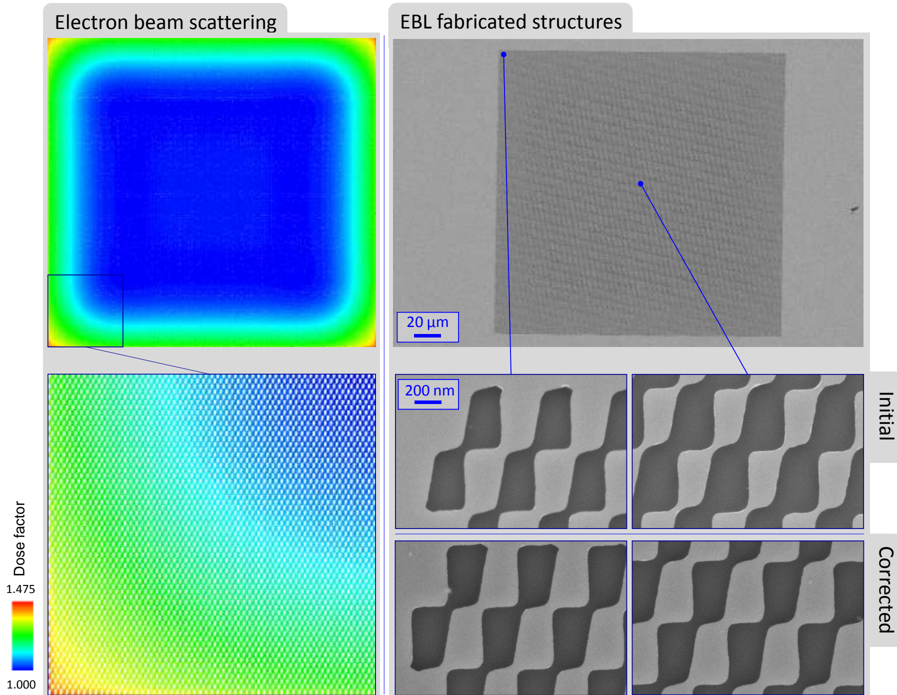

Figure 4.21: Influence of the proximity effect during EBL patterning of densely packed $200 \times 200\ \mu m^2$ lattice arrays. Left panel shows wide view and close-up illustrations of a dose-corrected design pattern as determined by Monte Carlo simulations. Right panel gives an overview SEM image of the lattice, and provides comparisons of structural elements obtained in its peripheral and central regions, fabricated with and without proximity effect correction.

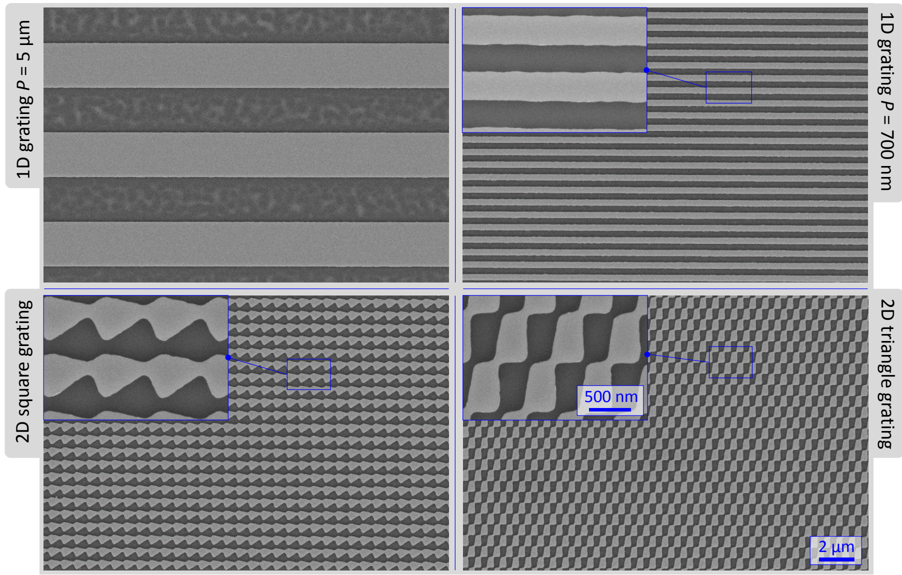

Figure 4.22: SEM images of different magnetic lattice structures, acquired after reactive ion etching and befroe deposition of reflective Au and protective SiO_x films. Top panels show 1D gratings with $P = 5$ µm and 700 nm periods. Bottom panels illustrate $P = 700$ nm 2D lattices with square and triangular translational symmetry in left and right panels respectively. Dark gray areas correspond regions where the magnetic film was sputtered away.

cross-linked and hardened during Ar^+ bombardment.

Examples of etched 1D grating and 2D lattice magnetic film patterns prepared using the present EBL-based fabrication process are given in Figure 4.22. In all cases very high pattern fidelity was achieved and only minor unevenness of the pattern edges due to 10 nm scale metal grain size proved to be the ultimate limitation to resolution. In preparation for ultracold atom trapping experiments the etched Co/Pd multilayer film patterns were coated with a reflective 50 nm thickness layer of gold, necessary for realization of a mirror magneto-optical trap [224], by way of magnetron sputtering in an AXXIS physical vapor deposition system (Kurt J. Lesker). An additional final 25 nm-thick layer of protective silica SiO_x was also deposited in the same tool using electron beam-induced thermal evaporation to prevent rubidium atoms from sticking to the metallic surface where they can create disruptive inhomogeneous electric fields [225].

The final fabrication step involved cutting the wafer down to the required 35×40 mm^2 size, whilst keeping the four grating structures situated at the center. This was done by using a $\lambda = 1030$ nm wavelength PHAROS femtosecond laser (Light Conversion, Ltd.) and by moving the wafer along the cutting trajectory on a high precision air-bearing x-y positioning stage (Aerotech Inc.).

After cutting the wafer was again washed in acetone and IPA to remove any debris, followed by a final N_2 blow drying step. Next, the performance of EBL fabricated magnetic lattices is illustrated by taking the ultracold atom trapping behavior of a 2D triangular symmetry subwavelength period structure, depicted bottom-right of Figure 4.22, as a representative example.

4.4.2 Atom trapping in a submicron-period 2D lattice

The complicated curvy continuous shapes that generally comprise 2D magnetic atom trapping lattices, depicted in the bottom row of Figure 4.22, were arrived at numerically by using a linear programming algorithm that aims to avoid the occurrence of magnetic field zeros, which lead to Majorana spin flips and loss of atoms [226]. Magnetization of the submicron 2D triangular lattice symmetry realization, described in further detail here, can be understood as supporting a virtual current that circulates around the edges of the EBL patterned structure, as indicated by the arrows in Figure 4.23 (a). Predictably, the magnetic field potentials produced by such imaginary currents can be controlled by applying orthogonal bias fields, where B_x can be used to suppress fields generated by the vertical portion of the current contour marked red, and B_y works to cancel the short horizontal black segment. Thus, a periodic arrangement of magnetic traps, stretching along the respective grating intervals as shown in the simulated contour plots of the magnetic lattice potential given in Figure 4.23 (b), can be created.

Decreasing the period of a magnetic atom trapping lattice invariably results in the trapping potential getting pushed closer to the chip surface. For $a =$ 700 nm periods described here the baseline trap distance $z = z_{\mathrm{min}} = a/2$ is approximately $z \approx 350$ nm, and can be lowered further through the application of appropriate bias fields. This, in turn, leads to a qualitative change in lattice behavior, as the trapping is no longer set solely by the magnetic lattice potential $V_{\mathrm{M}}(z)$, but also heavily affected by interactions with the chip surface placed at distance d from the trap center, expressed as the combined Casimir-Polder and van der Waals potential $V_{\mathrm{CP}}(d)$ [227, 228].

Figure 4.23 (c) outlines the calculated trapping potentials in a micro-Kelvin temperature scale, each established using increasingly higher bias fields B_x, where the yellow line indicates the top silica surface of the atom chip. In general, a larger bias tends to produce tighter and deeper lattice traps that are situated ever closer to the magnetic film. Here, by changing B_x from 7 G to 52 G, the trap center shifts from $z = 339$ nm to 139 nm. However, at chip surface distances roughly below ~ 200 nm, the attractive Casimir-Polder interaction starts to deform the magnetic potential, causing it to become increasingly shallow, as evident in the $B_x = 52$ G case in Figure 4.23 (c), and rendering the atom trapping short-lived.

Experimental demonstration of triangular symmetry submicron period 2D magnetic lattice atom trapping was done using ^{87}Rb atoms that, due to their

closed optical loop energy level structure, can be laser cooled down to extremely low temperatures over the course of a vast number of photon recoil events that occur as a result of absorption-spontaneous emission cycles. Without going into much detail [220], a cloud of $\sim 5\times10^5$ ^{87}Rb atoms is cooled down to a ~ 1 μK temperature using a standard four-beam mirror magneto-optical trap, pumped to the low-field seeking $|F=1, m_\mathrm{F}=-1\rangle$ ground state. In preparation for lattice loading, atoms are transferred to a position roughly ~ 670 μm below the atom chip *via* U-wire and Z-wire magnetic traps realized in the Cu foil substrate onto which the Si wafer is fastened. The various current-carrying conductive tracks are depicted in the top-left image of Figure 4.24 as white lines. Atom cloud visualization was conducted by way of reflection absorption imaging sketched just below, wherein a laser beam comes in at a 2° glancing incidence to the mirror-like Au surface of the atom chip, which results in CCD acquisition of both the real and virtual image, as shown in the left panel of Figure 4.24.

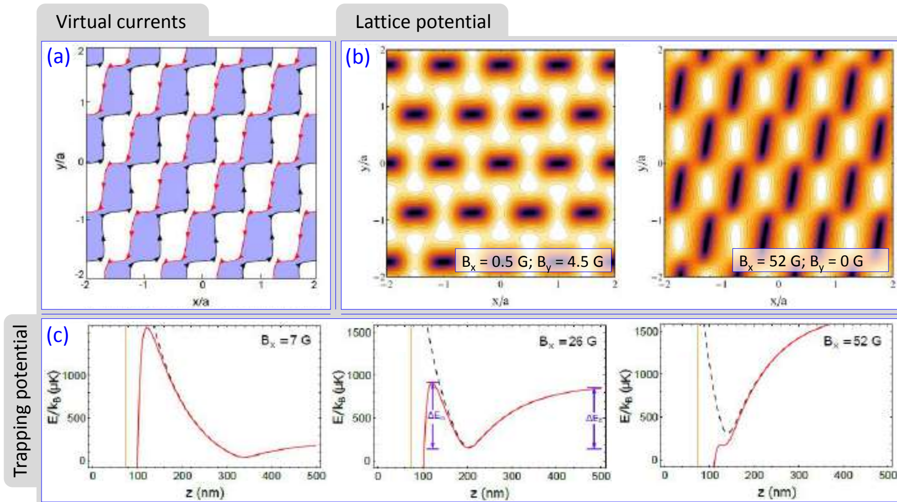

Figure 4.23: Simulated triangular magnetic lattice trapping potentials and their dependence on bias fields [220]. (a) Schematic depiction of the triangular magnetic lattice with arrows showing the virtual currents circulating around the metal pattern. (b) Magnetic lattice potential contour plots under the predominant effects of B_x and B_y bias fields, where darker regions correspond to trap minima located at $z_\mathrm{min} = 350$ nm and 139 nm above the metal film in left and right plots respectively. (c) Calculated trapping potential for ^{87}Rb atoms in a 700 nm period triangular magnetic lattice subject to different B_x bias fields. Black dashed curves represent the lattice potential and the solid red curves also account for atom interaction with the surface, marked by the yellow line. Lattice potential simulations were done at Swinburne University of Technology by the research group under supervision of Prof. Peter Hannaford.

Atom loading is performed by smoothly merging the potential wells of the the Z-wire trap, used as a ^{87}Rb reservoir, and the EBL fabricated magnetic lattice. The process is illustrated by the sequence of atom cloud images at the bottom of the left panel of Figure 4.24. Here, the ^{87}Rb atom cloud is pushed close towards the magnetic lattice chip by reducing the Z-wire trap current I_Z, and then rapidly ramping it back up again to force retraction. Top-right plot in the same panel provides a representative close-up reflection absorption image, which shows the direct and mirror images of the Z-wire atom reservoir, as well as a smaller ^{87}Rb cloud very close to the chip surface, which is attributable to atoms trapped by the submicron magnetic multilayer 2D lattice. However, imaging resolution is insufficient to directly observe the individual trap sites or to distinguish the ~ 200 nm gap from the chip surface. Still, lattice trapping is maintained even when the Z-wire trap is inactive, and is estimated to hold approximately $\sim 2 \times 10^4$ atoms, which gives an average of 4 per lattice site.

The lattice-trapping lifetime can be measured by observing the atom popula-

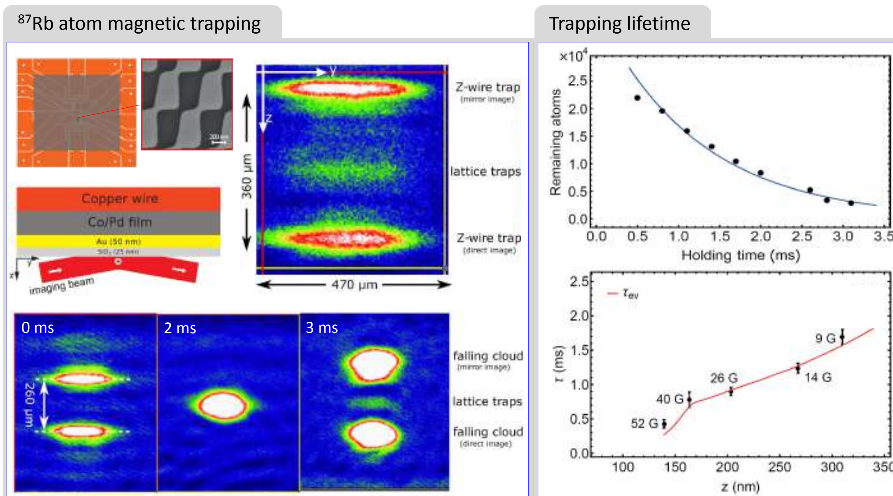

Figure 4.24: Traping of ultracold ^{87}Rb atoms in a 700 nm period triangular magnetic lattice [220]. Sketch and inset top left show the chip and the underlying copper plate with wire traps for transporting and loading atom couds onto the trapping lattices. Schematic below gives the reflection absorption imaging geometry, used for acquiring the atom cloud image on the right. Lower panels give the temporal evolution of a cloud as it is brought in contact with the lattice. Panels on the left show plots of traped atom decay over time, and trapping lifetime dependance on trap distance from the magnetic film surface set by the B_x bias field magnitude. Atom trapping experiments were conducted at Swinburne University of Technology by the research group under supervision of Prof. Peter Hannaford.

tion decay over time, as shown in the top-right plot of Figure 4.24. Furthermore, by changing the applied bias fields B_x, atom trapping lifetime dependence on proximity to the magnetic film, depicted lower-right of the same figure, can likewise be deduced. In general, the decay curves are single-exponential, with characteristic lifetimes ranging from approximately 1.69 ms for $B_x = 9$ G, to 0.43 ms at the largest $B_x = 52$ G bias. The three main loss mechanisms for lattice-trapped atoms are spin flips as a result of Johnson magnetic noise in the conducting Au, three-body recombination, or one-dimensional thermal evaporation following transfer of the thermal atom cloud, with the latter method providing the best fit of the observed lifetime dependence on distance to chip surface [220].

In conclusion, high resolution EBL fabrication allowed the patterning of submicron period 2D ultracold atom trapping lattices in a Co/Pd magnetic multilayer film. This, in turn, facilitated the first reported experiments of ^{87}Rb atom trapping at this small scale and distance to the chip. While the current device realization allows to probe interesting fundamental effects relating to ultracold atom interaction with surfaces, the presently attained trapping lifetimes of ~ 1.69 ms are insufficient for observing appreciable quantum tunneling effects. However, while improvements to the fabrication process are possible, it appears that trap lifetimes are mainly limited due to atom loading method imperfections rather than more fundamental surface interaction, Johnson noise, three body recombination, or spin flip effects, hence, are likely to be considerably augmented in the near future.

CONCLUSIONS

This work is centered around nanoscale high-precision fabrication of various structures and components exhibiting a range of functionalities relating to radiation interaction with mater, including integrated photonic waveguide resonators, micro-optical elements for shaping custom wavefronts, and plasmonic metasurfaces for absorbance enhancement. In addition, miniaturization here is leveraged to provide novel capabilities for thermometric detection, molecular sensing and even in the quantum science of ultracold atom trapping. The principal findings of this thesis are summarized as follows.

- The high resolution serial patterning capability of EBL enables precise fabrication of photonic devices, with flexibility far beyond that provided by conventional photolithographic mask replication methods. While not cost-effective for industrial scale fabrication, EBL allows for immediate translation from design concept to testable prototype, hence, is the method of choice for experimental verification of new devices, particularly those that rely on subwavelength scale components for their operation. This principle is leveraged here to investigate advanced approaches to enhance the sensitivity and broaden the utility of SOI waveguide-coupled micro-ring resonator label-free molecular sensor structures.
    1. The 10 nm patterning fidelity of EBL is fully sufficient to establish effective medium and photonic crystal-like features well below the required λ/n_{Si} scale for near-IR radiation guided in single-mode Si waveguides.
    2. Micro-ring resonator augmentation with annular second-order Bragg gratings results in suppression of all modes that are at odds with the diffraction condition, elimination of mode splitting, and simultaneously exhibits dispersion-derived Q-factor enhancement for a specific resonant excitation.
    3. Gradient effective refractive index micro-ring resonators achieve optical field delocalization for probing extended sensing volumes and, despite having an increased surface area, these devices exhibit a $Q \simeq 15000$ quality factor, which represents a threefold improvement over a conventional micro-ring of equivalent diameter.
- Direct nanoscale material modification and engraving, as realized by FIB milling, does not require resists or complicated pattern transfer steps. While the throughput of this technique is considerably lower than that of the already exceedingly slow EBL, focused ion beams allow for even more flexibility in component fabrication, as substrates with either a fragile constitution, uneven surface, or unorthodox material composition

can be patterned in a similarly straightforward fashion. Although the amount of material that can be practicably removed is limited to the single-micrometer depth range, FIB patterning can produce structures with a broad variety of substantive effects on a wavelength or macromolecular scale.

4. Gallium ion beams are capable of creating 10 nm diameter scale solid-state nanopores in $10-30$ nm thickness Si_3N_4 membranes, applicable as high mechanical and electrical stability single-molecule translocation sensing devices.

5. FIB milling allows for the creation of 200 nm period 0.5 duty cycle Au polarizer gratings with an extinction ratio upwards of $T_{\max}/T_{\min} \approx 150$ throughout the entire mid-IR spectral region.

6. The large depth of focus of FIB lithography systems can directly mill various nanoscale structures onto complex non-planar topology surfaces, as exemplified through the creation of 3D hybrid dielectric/metallic micro-optical elements, comprised of FIB milled diffractive spiral zone plates and underlying laser photopolymerized refractive axicon pedestals, that generate spatially confined $NA \approx 0.7$ numerical aperture optical vortices at a $f \approx 12.3$ µm focal distance.

- In addition to the 2D patterning facilitated by lithography, layered physical vapor deposition of disparate metal films provides a way to exert control over the third fabrication dimension as well. To this end PVD can be leveraged to establish discrete stacks of media with specific bulk properties, to induce novel behaviors through the creation of junctions as well as nanoscale multilayer or superlattice stacks, or to modify and tailor a given material through alloying. In particular, metals, due to their rich variety of electron mobility-derived properties which include plasmonic, magnetic, catalytic and electric among others, provide a wide range of possibilities for creating advanced subwavelength scale devices.

7. A 6.25 μm^2 Au/Ni junction area thermocouple EBL patterned on a 30 nm thickness Si_3N_4 membrane, due to its exceedingly small heat capacity, exhibits a 34.5 times higher sensitivity than a bulk substrate-fabricated counterpart and is capable of detecting heating induced by both laser and electron beams that corresponds to estimated 2×10^5 Ks^{-1} temperature changes and a 10 kHz response rate.

8. Optical transmittance-reliant sensing of hydrogen can be realized using various palladium-based thin-film configurations, where alloying of Pd with Au results in an increase of the H_2 uptake rate at the cost of total sensitivity, generation of nanoscale Au/Pd mul-

tilayers gives rise to increases the observable change in optical extinction for a given level of hydrogenation that proceed much slower, and NDA and MHA structuring of Pd films can support H_2 incorporation dependent plasmonic resonances readily detected at mid-IR.

9. Reduction projection photolithography-patterned metal-insulator-metal nanodisk array based plasmonic mid-IR wavelength range absorber metasurfaces support narrowband resonances with around 50% extinction, and highest quality plasmonic modes are attained when using Au and Ag noble metals in conjunction with Si or SiO_2 10 nm thickness dielectric spacers.
10. Large 1 mm^2 area high resolution EBL patterned 700 nm period ultracold atom trapping 2D lattices in a Co/Pd magnetic multilayer film enable the capture ^{87}Rb atoms at a 100 nm distance to the chip with an up to $\sim$ 1.69 ms lifetime.

These conclusion statements are validated and further elaborated on in the peer-reviewed papers published as part of this PhD project, all of which are summarized in the Appendix "Publications during this PhD project".

ABSTRACT

The purpose and goal that directs the broad field of lithographic fabrication is to establish and provide reliable methods of producing structures with maximally strictly defined geometries. In general terms, the dimensions of functional component features or their arrangements dictate which physical phenomena they will be capable of affecting or interfacing with, as well as the duration of various transport processes. Therefore, on one end miniaturization can result in increased device efficiency, or, conversely, be absolutely essential for enabling a certain functionality. However, among all of the available approaches only a select few possess patterning resolution capability in the nanoscale, necessary, in particular, for realization and fine control over numerous photonic phenomena.

This work is geared towards leveraging the nanoscale resolution patterning capabilities of electron and ion beam lithography approaches, as well as the auxiliary pattern transfer techniques such as physical vapor deposition or reactive ion etching, to fashion structures and devices that for their operation rely on subwavelength scale features along at least one of their dimensions. It is divided into three parts, based on which fabrication technique was more critical in attaining the requisite properties, and deals with electron beam lithography for silicon-on-insulator photonics, focused ion beam milling of micro-optical components, as well as metal junction or multilayer based devices.

Planar silicon-on-insulator waveguide structures exhibit a high refractive index which enables highly miniaturized and, due to compatibility with large scale complementary metal-oxide-semiconductor fabrication methods, cost effective label-free sensors to be created. On the other hand, the tight confinement of electromagnetic energy in Si represents a considerable challenge for generating structures that are capable of advanced control over spatial and spectral distribution of propagating or resonant modes. Here, after overviewing the key concepts pertaining to waveguide-coupled micro-ring resonator sensors, we focus on the ways 10 nm resolution of electron beam lithography can be harnessed for the creation of custom subwavelength structural features that serve to incorporate effective refractive index and dispersion engineering concepts to enhance the sensitivity and broaden the utility of resonant multi-pass label-free sensors. Micro-ring resonators equipped with annular second-order Bragg gratings gave rise to suppression of all modes at odds with the diffraction condition and simultaneously exhibited dispersion-derived Q-factor enhancement for a specific resonant excitation. A different approach relies on fine control over pattern geometry to ensure a desired gradient effective refractive index, which, when applied onto micro-ring resonators, achieves optical field delocalization for probing extended sensing volumes, thereby side-stepping the limitations associated with strong mode confinement in Si structures.

One of the difficulties associated with electron beam lithography is that the small charged particle mass renders their energy transfer to atoms largely inefficient. Hence, patterning has to proceed by first inducing chemical changes in a resist film and then performing pattern transfer, which may not be convenient for substrates of certain chemistry or constitution. Focused ion beam milling, on the other hand, relies on massive ions that are capable of direct surface atom sputtering. Although the amount of material that can be practicably removed is limited to the single-micrometer depth range, processing layers with some type of a strong contrast in material properties can nevertheless yield substantive effects. A case-in-point example of this principle relates to generation of 10 nm diameter pores in nanoscale Si_3N_4 membranes, which, despite being arguably the simplest conceivable lithographically patterned device type, can operate as single-molecule sensors by detecting their individual translocation events. From a photonic perspective, directly milling complex patterns in high opacity metal films can be employed for the creation subwavelength feature size diffractive components as well as polarizer structures. Furthermore, the large depth of focus possessed by focused ion beam systems allows for patterning of complex curved surface geometries, which, in conjunction with complimentary laser photopolymerization additive fabrication methods, can be harnessed for the creation of hybrid diffractive/refractive micro-optical elements.

Nanofabrication is not constrained to the planar dimension accessible to lithographic exposure, since pattern transfer methods such as etching or physical vapor deposition can generate different structures to exert control over the third out-of-plane fabrication dimension as well. Materials can be layered as discrete stacks of media with bulk properties, as disparate component junctions as well as nanoscale multilayer or superlattice stacks with novel behaviors, or tailored in their composition and characteristics by way of alloying. In particular, metals, due to their rich variety of electron mobility-derived properties, including plasmonic, magnetic, catalytic and electric among others, provide a wide range of possibilities for development of advanced subwavelength scale devices. Here, the principles of creating layered metal functional components, patterned mostly but not exclusively by way of lithography, are illustrated by examples of membrane-suspended micro-thermocouples, palladium-based alloy composites for hydrogen sensing, metal-insulator-metal plasmonic absorber metasurfaces, as well as magnetic ultracold atom trapping lattices. Miniaturization of such structures confers a multitude of different benefits, ranging from the fairly mundane decrease in heat capacity of a thermocouple that results in higher sensitivity and a higher response rate, or how nanoscale thickness of metal films makes it possible to register their permittivity changes by monitoring optical transmittance, all the way to advanced instances where downscaling atom trapping lattices may provide opportunities to study quantum tunneling phenomena, or how creating subwavelength plasmonic structures allows to control and tailor their resonant response.

REFERENCES

[1] J.E. Green, J.W. Choi, A. Boukai, Y. Bunimovich, E. Johnston-Halperin, E. DeIonno, Y. Luo, B.A. Sheriff, K. Xu, Y.S. Shin, H.-R. Tseng, J. F. Stoddart, and J. R. Heath. A 160-kilobit molecular electronic memory patterned at 1011 bits per square centimetre. *Nature*, 445(7126):414–417, 2007.

[2] B. Hoefflinger. *ITRS 2028 international roadmap of semiconductors. In Chips 2020*, volume 2. Springer, 2016.

[3] R. M. De La Rue and C. Seassal. Photonic crystal devices: some basics and selected topics. *Laser Photon. Rev.*, 6(4):564–597, 2012.

[4] D.R. Smith, J.B. Pendry, and M. C. K. Wiltshire. Metamaterials and negative refractive index. *Science*, 305(5685):788–792, 2004.

[5] S.-J. Jeong, J. Y. Kim, B. H. Kim, H.-S. Moon, and S. O. Kim. Directed self-assembly of block copolymers for next generation nanolithography. *Mater. Today*, 16(12):468–476, 2013.

[6] R. P. Seisyan. Nanolithography in microelectronics: A review. *Tech. Phys.*, 56(8):1061–1073, 2011.

[7] N. Kooy, K. Mohamed, L. T. Pin, and O. S. Guan. A review of roll-to-roll nanoimprint lithography. *Nanoscale Res. Lett.*, 9(1):320, 2014.

[8] M. Malinauskas, A. Žukauskas, S. Hasegawa, Y. Hayasaki, V. Mizeikis, R. Buividas, and S. Juodkazis. Ultrafast laser processing of materials: from science to industry. *Light Sci. Appl.*, 5:e16133, 2016.

[9] R. Garcia, A. W. Knoll, and E. Riedo. Advanced scanning probe lithography. *Nat. Nanotechnol.*, 9:577–587, 2014.

[10] Y. Chen. Nanofabrication by electron beam lithography and its applications: A review. *Microelectron. Eng.*, 135:57–72, 2015.

[11] A. Joshi-Imre and S. Bauerdick. Direct-write ion beam lithography. *J. Nanotechnol.*, 2014:170415, 2014.

[12] K. J. Kuhn. Considerations for ultimate CMOS scaling. *IEEE Trans. Electron Devices*, 59(7):1813–1828, 2012.

[13] Z. Cui. *Nanofabrication: Principles, Capabilities and Limits*. Springer, New York, NY, USA, 2008.

[14] I. Haller, M. Hazakis, and R. Srinivasan. High resolution positive resists for electron beam exposure. *IBM J. Res. Dev.*, 12:251–256, 1968.

[15] A.F. Mayadas and R.B. Laibowitz. One-dimensional superconductors. *Phys. Rev. Lett.*, 28:156, 1972.

[16] R. F. Pease, L. Han, G. I. Winograd, W. D. Meisburger, D. Pickard, and M. A. McCord. Prospects for charged particle lithography as a manufacturing technology. *Microelectron. Eng.*, 53:55–60, 2000.

[17] N. Yao. *Introduction to the focused ion beam system. In. Nanofabrication: Principles, Capabilities and Limits*. Cambridge University Press, New York, NY, USA, 2007.

[18] C. Constancias, S. Landis, L. Manakli, S. Martin, L. Pain, and D. Rio. *Electron beam lithography. In Lithography*. John Wiley & Sons, Hoboken, NJ, USA, 2013.

[19] J. Morikawa, M. Ryu, K. Maximova, A. Balčytis, G. Seniutinas, L. Fan, V. Mizeikis, J. Li, X. Wang, M. Zamengo, X. Wang, and S. Juodkazis. Silk fibroin as a water-soluble bio-resist and its thermal properties. *RSC Adv.*, 6(14):11863–11869, 2016.

[20] S. Kim, B. Marelli, M. A. Brenckle, A. N. Mitropoulos, E.-S. Gil, K. Tsioris, H. Tao, D. L. Kaplan, and F. G. Omenetto. All-water-based electron-beam lithography using silk as a resist. *Nat. Nanotechnol.*, 9: 306–310, 2014.

[21] R. Shimizu and D. Ze-Jun. Monte carlo modelling of electron-solid interactions. *Rep. Prog. Phys.*, 55:487, 1992.

[22] S. Cabrini and A. Risbud. *Electron beam lithography. In Nanofabrication handbook. Eds. S. Cabrini, S. Kawata*. Taylor & Francis Group, Boca Raton, FL, USA, 2012.

[23] V. E. Krohn and G. R. Ringo. Ion source of high brightness using liquid metal. *Applied Physics Letters*, 27:479, 1975.

[24] R. G. Forbes. *The Theory of Bright Field Electron and Field Ion Emission Sources. In Nanofabrication Using Focused Ion and Electron Beams. Eds. I. Utke and S. Moshkalev and P. Russell*. Oxford University Press, New York, NY, USA, 2012.

[25] C. Boit, R. Schlangen, U. Kerst, and T. Lundquist. Physical techniques for chip-backside IC debug in nanotechnologies. *IEEE Des. Test. Comput.*, 25:250–257, 2008.

[26] T. Koshikawa, A. Nagai, Y. Yokoyama, and T. Hoshino. A new write

head trimmed at wafer level by focused ion beam. *IEEE Trans. Magn.*, 34:1471–1473, 1998.

[27] O. Scholder, K. Jefimovs, I. Shorubalko, C. Hafner, U. Sennhauser, and G.-L. Bona. Helium focused ion beam fabricated plasmonic antennas with sub-5 nm gaps. *Nanotechnology*, 24:395301, 2013.

[28] R.L. Kubena, J. W. Ward, F. P Stratton, R. J. Joyce, and G. M. Atkinson. A low magnification focused ion beam system with 8 nm spot size. *J. Vac. Sci. Technol. B*, B9:3079, 1991.

[29] H.-B. Kim and G. Hobler. *Simulation of Focused Ion Beam Milling. In Nanofabrication Using Focused Ion and Electron Beams. Eds. I. Utke and S. Moshkalev and P. Russell*. Oxford University Press, New York, NY, USA, 2012.

[30] J. Gierak, R. Jede, and P. Hawkes. *Nanofabrication with focused ion beams. In Nanofabrication handbook. Eds. S. Cabrini, S. Kawata*. Taylor & Francis Group, Boca Raton, FL, USA, 2012.

[31] G. Gervinskas, G. Seniutinas, and S. Juodkazis. Control of surface charge for high-fidelity nanostructuring of materials. *Laser Photon. Rev.*, 7:1049–1053, 2013.

[32] T. Kosugi, T. Yamashiro, R. Aihara, K. Gamo, and S. Namba. The characteristics of ion-beam-induced spontaneous etching of gaas by low-energy focused ion beam irradiation. *Jpn. J. Appl. Phys.*, 30:3242, 1991.

[33] T. Bret and P. Hffmann. *How to Select Compounds for Focused Charged Particle Beam Assisted Etching and Deposition. In Nanofabrication Using Focused Ion and Electron Beams. Eds. I. Utke and S. Moshkalev and P. Russell*. Oxford University Press, New York, NY, USA, 2012.

[34] E. Miyauchi and H. Hashimoto. Application of focused ion beam technology to maskless ion implantation in a molecular beam epitaxy grown GaAs or AlGaAs epitaxial layer for three-dimensional pattern doping crystal growth. *J. Vac. Sci. Technol. A*, 4:933–938, 1986.

[35] M. Rommel, M. Rumler, A. Haas, A. J. Bauer, and L. Frey. Processing of silicon nanostructures by ga^{+} resistless lithography and reactive ion etching. *Microelectron. Eng.*, 110:177–182, 2013.

[36] M. S. Luchansky and R. C. Bailey. High-Q optical sensors for chemical and biological analysis. *Anal. Chem.*, 82(12):793–821, 2012.

[37] A. Ramachandran, S. Wang, J. Clarke, S. J. Ja, D. Goad, L. Wald, E. M. Flood, E. Knobbe, J. V. Hryniewicz, S. T. Chu, D. Gill, W. Chen, O. King,

and B. E. Little. A universal biosensing platform based on optical microring resonators. *Biosens. Bioelectron.*, 23(7):939–944, 2008.

[38] G.-D. Kim, G.-S. Son, H.-S. Lee, K.-D. Kim, and S.-S. Lee. Integrated photonic glucose biosensor using a vertically coupled microring resonator in polymers. *Opt. Commun.*, 281(18):4644—-4647, 2008.

[39] C. A. Barrios, K. B. Gylfason, B. Sánchez, A. Griol, H. Sohlström, M. Holgado, and R. Casquel. Slot-waveguide biochemical sensor. *Opt. Lett.*, 32(21):3080–3082, 2007.

[40] C. A. Barrios, M. J. Ba nuls, V. González-Pedro, K. B. Gylfason, B. Sánchez, A. Griol, A. Maquieira, H. Sohlström, M. Holgado, and R. Casquel. Label-free optical biosensing with slot-waveguides. *Opt. Lett.*, 33(7):708–710, 2008.

[41] L. Zhou, X. Sun, X. Li, and J. Chen. Miniature microring resonator sensor based on a hybrid plasmonic waveguide. *Sensors*, 11(7):6856–6867, 2011.

[42] K. De Vos, I. Bartolozzi, E. Schacht, P. Bienstman, and R. Baets. Silicon-on-Insulator microring resonator for sensitive and label-free biosensing. *Opt. Express*, 15(12):7610–7615, 2007.

[43] D.-X. Xu, A. Densmore, A. Delâge, P. Waldron, S. Janz R. McKinnon, J. Lapointe, G. Lopinski, T. Mischki, E. Post, P. Cheben, and J. H. Schmid. Folded cavity soi microring sensors for high sensitivity and real time measurement of biomolecular binding. *Opt. Express*, 16(19): 15137–15148, 2008.

[44] H. K. Tsang and Y. Liu. Nonlinear optical properties of silicon waveguides. *Semicond. Sci. Tech.*, 23(6):064007, 2008.

[45] M. Dinu, F. Quochi, and H. Garcia. Third-order nonlinearities in silicon at telecom wavelengths. *Semicond. Sci. Tech.*, 82(18):2954–2956, 2003.

[46] J. Heebner, R. Grover, and T. Ibrahim. *Optical Microresonators: Theory, Fabrication and Applications*. Springer Series in Optical Sciences. Springer, London, UK, 2008.

[47] W. Bogaerts, P. De Heyn, T. Van Vaerenbergh, K. De Vos, S. K. Selvaraja, T. Claes, P. Dumon, P. Bienstman, D. Van Thourhout, and R. Baets. Silicon microring resonators. *Laser Photon. Rev.*, 6(1):47–73, 2012.

[48] W. Bogaerts, R. Baets, P. Dumon, V. Wiaux, S. Beckx, D. Taillaert, B. Luyssaert, J. Van Campenhout, P. Bienstman, and D. Van Thourhout. Nanophotonic waveguides in silicon-on-insulator fabricated with CMOS

technology. *J. Light. Technol.*, 23(1):401–412, 2005.

[49] S. Feng, T. Lei, H. Chen, H. Cai, X. Luo, and A. W. Poon. Silicon photonics: from a microresonator perspective. *Laser Photon. Rev.*, 6(2): 145–177, 2012.

[50] M. Heiblum and J. Harris. Analysis of curved optical waveguides by conformal transformation. *IEEE J. Quantum Electron.*, 11(2):75–83, 1975.

[51] F. Ladouceur and E. Labeye. A new general approach to optical waveguide path design. *J. Light. Technol.*, 13(3):481–492, 1995.

[52] R. T. Schermer and J. H. Cole. Improved bend loss formula verified for optical fiber by simulation and experiment. *IEEE J. Quantum Electron.*, 43(10):899–909, 2007.

[53] B. E. Little, J. P. Laine, and S. T. Chu. Surface-roughness-induced contradirectional coupling in ring and disk resonators. *Opt. Lett.*, 22(1): 4–6, 1997.

[54] T. Wang, Z. Zhang, F. Liu, Y. Tong, J. Wang, Y. Tian, M. Qiu, and Y. Su. Modeling of quasi-grating sidewall corrugation in SOI microring add-drop filters. *Opt. Commun.*, 282(17):3464–3467, 2009.

[55] C.-Y. Chao and L. J. Guo. Thermal-flow technique for reducing surface roughness and controlling gap size in polymer microring resonators. *Appl. Phys. Lett.*, 84(14):2479–2481, 2004.

[56] K. K. Lee, D. R. Lim, L. C. Kimerling, J. Shin, and F. Cerrina. Fabrication of ultralow-loss si/sio$_2$ waveguides by roughness reduction. *Opt. Lett.*, 26(23):1888–1890, 2001.

[57] M. A. Popović, C. Manolatou, and M. R. Watts. Coupling-induced resonance frequency shifts in coupled dielectric multi-cavity filters. *Opt. Express*, 14(3):1208–1222, 2006.

[58] M. Borselli, T. J. Johnson, and O. Painter. Beyond the rayleigh scattering limit in high-Q silicon microdisks: theory and experiment. *Opt. Express*, 13(5):1515–1530, 2005.

[59] A. L. Washburn, L. C. Gunn, and R. C. Bailey. Label-free quantitation of a cancer biomarker in complex media using silicon photonic microring resonators. *Anal. Chem.*, 81(22):9499–9506, 2009.

[60] K. De Vos, J. Girones, T. Claes, Y. De Koninck, S. Popelka, E. Schacht, R. Baets, and P. Bienstman. Multiplexed antibody detection with an array of silicon-on-insulator microring resonators. *IEEE Photon. J.*, 1

(4):225–235, 2009.

[61] D. X. Xu, M. Vachon, A. Densmore, R. Ma, A. Delage, S. Janz, J. Lapointe, Y. Li, G. Lopinski, D. Zhang, Q. Y. Lu, P. Cheben, and J. H. Schmid. Label-free biosensor array based on silicon-on-insulator ring resonators addressed using a WDM approach. *Opt. Lett.*, 35(16):2771–2773, 2010.

[62] M. S. Luchansky, A. L. Washburn, T. A. Martin, M. Iqbal, L. C. Gunn, and R. C. Bailey. Characterization of the evanescent field profile and bound mass sensitivity of a label-free silicon photonic microring resonator biosensing platform. *Biosens. Bioelectron.*, 26(4):1283–1291, 2010.

[63] K. Tiefenthaler and W. Lukosz. Sensitivity of grating couplers as integrated-optical chemical sensors. *J. Opt. Soc. Am. B*, 6(2):209–220, 1989.

[64] S. Xiao, M. H. Khan, H. Shen, and M. Qi. Compact silicon microring resonators with ultra-low propagation loss in the C band. *Opt. Express*, 15(22):14467–14475, 2007.

[65] M. Gabalis, D. Urbonas, and R. Petruskevicius. A perforated microring resonator for optical sensing applications. *J. Opt.*, 16(10):105003, 2014.

[66] Z. Zhu and T. G. Brown. Full-vectorial finite-difference analysis of microstructured optical fibers. *Opt. Express*, 10(17):853—864, 2002.

[67] W. Bogaerts, S. K. Selvaraja, P. Dumon, J. Brouckaert, K. De Vos, D. Van Thourhout, and R. Baets. Silicon-on-insulator spectral filters fabricated with CMOS technology. *IEEE J. Sel. Top. Quantum Electron.*, 16(1):33–44, 2010.

[68] X. Cai, J. Wang, M. J. Strain, B. Johnson-Morris, J. Zhu, M. Sorel, J. L. O'Brien, M. G. Thompson, and S. Yu. Integrated compact optical vortex veam emitters. *Science*, 338(6105):363–366, 2012.

[69] P. Xu, K. Yao, J. Zheng, X. Guan, and Y. Shi. Slotted photonic crystal nanobeam cavity with parabolic modulated width stack for refractive index sensing. *Opt. Express*, 21(22):26908–26913, 2013.

[70] S. Nakashima and K. Izumi. Analysis of buried oxide layer formation and mechanism of threading dislocation generation in the substoichiometric oxygen dose region. *J. Mater. Res.*, 8(3):523–534, 1993.

[71] K. K. Lee, D. R. Lim, H.-C. Luan, A. Agarwal, J. Foresi, and L. C. Kimerling. Effect of size and roughness on light transmission in a

Si/SiO_2 waveguide: Experiments and model. *Appl. Phys. Lett.*, 77(11): 1617–1619, 2000.

[72] G. S. Oehrlein, S. W. Robey, and J. L. Lindström. Surface processes in CF_4/O_2 reactive etching of silicon. *Appl. Phys. Lett.*, 52(14):1170–1172, 1988.

[73] A. S. Gangnaik, Y. M. Georgiev, and J. D. Holmes. New generation electron beam resists: A review. *Chem. Mater.*, 29(5):1898–1917, 2017.

[74] X. Xu, H. Subbaraman, J. Covey, D. Kwong, A. Hosseini, and R. T. Chen. Complementary metal–oxide–semiconductor compatible high efficiency subwavelength grating couplers for silicon integrated photonics. *Appl. Phys. Lett.*, 101(3):031109, 2012.

[75] R. Orghici, P. Lützow, J. Burgmeier, J. Koch, H. Heidrich, W. Schade, N. Welschoff, and S. Waldvogel. A microring mesonator sensor for sensitive detection of 1,3,5-trinitrotoluene (TNT). *Sensors*, 10(7):6788–6795, 2010.

[76] N. A. Yebo, P. Lommens, Z. Hens, and R. Baets. An integrated optic ethanol vapor sensor based on a silicon-on-insulator microring resonator coated with a porous ZnO film. *Opt. Express*, 18(11):11859–11866, 2010.

[77] N. A. Yebo, D. Taillaert, J. Roels, D. Lahem, M. Debliquy, D. Van Thourhout, and R. Baets. Silicon-on-insulator (SOI) ring resonator-based integrated optical hydrogen sensor. *IEEE Photon. Technol. Lett.*, 21(14):960–962, 2009.

[78] Z. Wang, X. Xu, D. Fan, Y. Wang, and R. T. Chen. High quality factor subwavelength grating waveguide micro-ring resonator based on trapezoidal silicon pillars. *Opt. Lett.*, 41(14):3375–3378, 2016.

[79] T. Stoeferle. Electromagnetic wave resonator with effective refractive index gradient. *International patent WO 2012/123835 A1*, issued 20 Sept. 2012.

[80] K. Yee. Numerical solution of initial boundary value problems involving Maxwell's equations in isotropic media. *IEEE Trans. Antennas Propag.*, 14(3):302–307, 1966.

[81] A. Taflove and S. C. Hagness. *Computational Electromagnetics: The Finite-Difference Time-Domain Method.* Artech House, Boston, Mass. USA, 2005.

[82] M. Hammer and O. V. Ivanova. Effective index approximations of

photonic crystal slabs: a 2-to-1-D assessment. *Opt. Quant. Electron.*, 41 (4):267–283, 2009.

[83] T. Claes, J. G. Molera, K. De Vos, E. Schacht, R. Baets, and P. Bienstman. Label-free biosensing with a slot-waveguide-based ring resonator in silicon on insulator. *IEEE Photon. J.*, 1(3):197–204, 2009.

[84] C. A. Barrios, K. B. Gylfason, B. Sánchez, A. Griol, H. Sohlström, M. Holgado, and R. Casquel. Slot-waveguide biochemical sensor. *Opt. Letters*, 32(21):3080–3082, 2007.

[85] J. Zhu, S. K. Ozdemir, Y.-F. Xiao, L. Li, L. He, D.-R. Chen, and L. Yang. On-chip single nanoparticle detection and sizing by mode splitting in an ultrahigh-Q microresonator. *Nat. Photon.*, 4:46–49, 2010.

[86] D. Urbonas, A. Balčytis, M. Gabalis, K. Vaškevičius, G. Naujokaitė, S. Juodkazis, and R. Petruškevičius. Ultra-wide free spectral range, enhanced sensitivity, and removed mode splitting SOI optical ring resonator with dispersive metal nanodisks. *Opt. Lett.*, 40(13):2977–2980, 2015.

[87] S. Werquin, S. Verstuyft, and P. Bienstman. Integrated interferometric approach to solve microring resonance splitting in biosensor applications. *Opt. Express*, 21(14):16955–16963, 2013.

[88] M. Soljačić, E. Lidorikis, L. V. Hau, and J. D. Joannopoulos. Enhancement of microcavity lifetimes using highly dispersive materials. *Phys. Rev. E*, 71(2):026602, 2005.

[89] S. V. Boriskina, T. M. Benson, P. Sewell, and A. I. Nosich. Directional emission, increased free spectral range and mode Q-factors in 2-D wavelengthscale optical microcavity structures. *IEEE J. Sel. Topics Quantum Electron.*, 12(6):1175–1182, 2006.

[90] S. Qiu, J. Cai, Y. Li, and Z. Han. Mode frequency shifts and Q-factor changes in 2D microflower cavity and its deformed cavity. *Opt. Commun.*, 277(2):406—-410, 2010.

[91] K. Keskinbora, C. Grévent, M. Bechtel, M. Weigand, E. Goering, A. Nadzeyka, L. Peto, S. Rehbein, G. Schneider, R. Follath, J. Vila-Comamala, H. Yan, and G. Schütz. Ion beam lithography for fresnel zone plates in X-ray microscopy. *Opt. Express*, 21(10):11747–11756, 2013.

[92] E. Palacios, L. E. Ocola, A. Joshi-Imre, S. Bauerdick, M. Berse, and L. Peto. Three-dimensional microfluidic mixers using ion beam lithography and micromachining. *J. Vac. Sci. Technol. B*, 28(6):C6I1–C6I6, 2010.

[93] J. Wang, X. Zhang, Y. Zhou, K. Li, Z. Wang, P. Peddibhotla, F. Liu, S. Bauerdick, A. Rudzinski, Z. Liu, and W. Gao. Scalable fabrication of single silicon vacancy defect arrays in silicon carbide using focused ion beam. *ACS Photonics*, 4(5):1054–1059, 2017.

[94] T. A. Rapoport. Protein translocation across the eukaryotic endoplasmic reticulum and bacterial plasma membranes. *Nature*, 450:663–669, 2007.

[95] L. Wang, Y. Han, S. Zhou, G. Wang, and X. Guan. Nanopore biosensor for label-free and real-time detection of anthrax lethal factor. *ACS Appl. Mater. Interfaces*, 6(10):7334–7339, 2014.

[96] F. Haque, J. Li, H.-C. Wu, X.-J. Liang, and P. Guo. Solid-state and biological nanopore for real-time sensing of single chemical and sequencing of DNA. *Nano Today*, 8(1):56–74, 2013.

[97] C. Dekker. Solid-state nanopores. *Nat. Nanotechnol.*, 2:209–215, 2007.

[98] M. J. Kim, M. Wanunu, D. C. Bell, and A. Meller. Rapid fabrication of uniformly sized nanopores and nanopore arrays for parallel DNA analysis. *Adv. Mater.*, 18(23):3149–3153, 2006.

[99] C. J. Lo, T. Aref, and A. Bezryadin. Fabrication of symmetric sub-5 nm nanopores using focused ion and electron beams. *Nanotechnology*, 17 (13):3264–3267, 2006.

[100] A. Oukhaled, B. Cressiot, L. Bacri, M. Pastoriza-Gallego, J.-M. Betton, E. Bourhis, R. Jede, J. Gierak, L. Auvray, and J. Pelta. Dynamics of completely unfolded and native proteins through solid-state nanopores as a function of electric driving force. *ACS Nano*, 5(5):3628–3638, 2011.

[101] C. Plesa, D. Verschueren, S. Pud, J. van der Torre, J. W. Ruitenberg, M. J. Witteveen, M. P. Jonsson, A. Y. Grosberg, and Y. Rabin C. Dekker. Direct observation of DNA knots using a solid-state nanopore. *Nat. Nanotechnol.*, 11:1093–1097, 2016.

[102] A. Balčytis, C. Briosne-Fréjaville, A. Mau, X. Li, and S. Juodkazis. Rescalable solid-state nanopores. In *AIP Conf. Proc.*, volume 1874, page 030002, 2016.

[103] A. W. Grant, Q.-H. Hu, and B. Kasemo. Transmission electron microscopy 'windows' for nanofabricated structures. *Nanotechnology*, 15 (9):1175–1181, 2004.

[104] S. Tan, R. Livengood, Y. Greenzweig, Y. Drezner, and D. Shima. Probe current distribution characterization technique for focused ion beam. *J. Vac. Sci. Technol. B*, 30(6):06F606, 2012.

[105] G. Seniutinas, G. Gervinskas, J. Anguita, D. Hakobyan, E. Brasselet, and S. Juodkazis. Nano-proximity direct ion beam writing. *Nanofabrication*, 2(1):54–62, 2016.

[106] S. Liu, T. D. Yuzvinsky, and H. Schmidt. Effect of fabrication-dependent shape and composition of solid-state nanopores on single nanoparticle detection. *ACS Nano*, 7(6):5621–5627, 2013.

[107] R. Kox, C. Chen, G. Maes, L. Lagae, and G. Borghs. Shrinking solid-state nanopores using electron-beam-induced deposition. *Nanotechnology*, 20 (11):115302, 2009.

[108] S. Juodkazis, V. Mizeikis, K. K. Seet, M. Miwa, and H. Misawa. Two-photon lithography of nanorods in SU-8 photoresist. *Nanotechnology*, 16(6):846–849, 2005.

[109] G. Seniutinas, A. Balčytis, and S. Juodkazis. Ultraviolet-photoelectric effect for augmented contrast and resolution in electron microscopy. *APL Photonics*, 1(2):021301, 2016.

[110] C. Grillet, C. Smith, D. Freeman, S. Madden, B. Luther-Davies, E. C. Magi, D. J. Moss, and B. J. Eggleton. Efficient coupling to chalcogenide glass photonic crystal waveguides via silica optical fiber nanowires. *Opt. Express*, 14(3):1070–1078, 2006.

[111] J. Riedrich-Möller, L. Kipfstuhl, C. Hepp, E. Neu, C. Pauly, F. Mücklich, A. Baur, M. Wandt, S. Wolff, M. Fischer, S. Gsell, M. Schreck, and C. Becher. One- and two-dimensional photonic crystal microcavities in single crystal diamond. *Nat. Nanotechnol.*, 7:69–74, 2012.

[112] J. Lin, J. P. B. Mueller, Q. Wang, G. Yuan, N. Antoniou, X.-C. Yuan, and F. Capasso. Polarization-controlled tunable directional coupling of surface plasmon polaritons. *Science*, 340(6130):331–334, 2013.

[113] G. R. Bird and M. Parrish. Impact of the slit geometry on the performance of wire-grid polarisers. *J. Opt. Soc. Am.*, 50(9):886–891, 1960.

[114] T. Weber, T. Käsebier, E.-B. Kley, and A. Tünnermann. Broadband iridium wire grid polarizer for UV applications. *Opt. Lett.*, 36(4):44–447, 2011.

[115] G. Mélen, W. Rosenfeld, and H. Weinfurter. Impact of the slit geometry on the performance of wire-grid polarisers. *Opt. Express*, 23(25):32171–32178, 2015.

[116] M. Ryu, A. Balčytis, X. Wang, J. Vongsvivut, Y. Hikima, J. Li, M. J. Tobin, S. Juodkazis, and J. Morikawa. Orientational mapping augmented

sub-wavelength hyper-spectral imaging of silk. *Sci. Rep.*, 7:7419, 2017.

[117] Y. Hikima, J. Morikawa, and T. Hashimoto. FT-IR image processing algorithms for in-plane orientation function and azimuth angle of uniaxially drawn polyethylene composite film. *Macromolecules*, 44(10): 3950–3957, 2011.

[118] B. Crist and J. M. Schultz. Polymer spherulites: A critical review. *Prog. Polym. Sci.*, 56:1–63, 2016.

[119] M. Gazzano, M. L. Focarete, C. Riekel, and M. Scandola. Structural study of poly(L-lactic acid) spherulites. *Biomacromolecules*, 5(2):553–558, 2004.

[120] A. Barth. Infrared spectroscopy of proteins. *Biochim. Biophys. Acta, Bioenerg.*, 1767(9):1073–1101, 2007.

[121] P. Dannberg, F. Wippermann, A. Brückner, A. Matthes, P. Schreiber, and A. Bräuer. Wafer-level hybrid integration of complex micro-optical modules. *Micromachines*, 5(2):325–340, 2014.

[122] A. Žukauskas, M. Malinauskas, and E. Brasselet. Monolithic generators of pseudo-nondiffracting optical vortex beams at the microscale. *Appl. Phys. Lett.*, 103(18):181122, 2013.

[123] D. Wen, F. Yue, G. Li, G. Zheng, K. Chan, S. Chen, M. Chen, K. F. Li, P. W. H. Wong, K. W. Cheah, E. Y. B. Pun, S. Zhang, and X. Chen. Helicity multiplexed broadband metasurface holograms. *Nat. Commun.*, 6:8241, 2015.

[124] L. Huang, H. Mühlenbernd, X. Li, X. Song, B. Bai, Y. Wang, and T. Zentgraf. Broadband hybrid holographic multiplexing with geometric metasurfaces. *Adv. Mater.*, 27(41):6444–6449, 2015.

[125] M. Malinauskas, A. Žukauskas, V. Purlys, K. Belazaras, A. Momot, D. Paipulas, R. Gadonas, A. Piskarskas, H. Gilbergs, A. Gaidukevičiūtė, I. Sakellari, M. Farsari, and S. Juodkazis. Femtosecond laser polymerization of hybrid/integrated micro-optical elements and their characterization. *J. Opt.*, 12(12):124010, 2010.

[126] N. Yu and F. Capasso. Flat optics with designer metasurfaces. *Nat. Mater.*, 13:139–150, 2014.

[127] A. Balčytis, D. Hakobyan, M. Gabalis, A. Žukauskas, D. Urbonas, M. Malinauskas, R. Petruškevičius, E. Brasselet, and S. Juodkazis. 3D micro-optical elements for generation of tightly focused vortex beams. In *MATEC Web Conf.*, volume 32, page 03002, 2015.

[128] A. Balčytis, D. Hakobyan, M. Gabalis, A. Žukauskas, D. Urbonas, M. Malinauskas, R. Petruškevičius, E. Brasselet, and S. Juodkazis. Hybrid curved nano-structured micro-optical elements. *Opt. Express*, 24 (15):16988–16998, 2016.

[129] D. L. Andrews. *Structured Light and Its Applications: An Introduction to Phase-Structured Beams and Nanoscale Optical Forces*. Academic Press-Elsevier, Burlington, MA, USA, 2008.

[130] A. M. Yao and M. J. Padgett. Orbital angular momentum: origins, behavior and applications. *Adv. Opt. Photon.*, 3(2):161–204, 2011.

[131] L. Allen, M. W. Beijersbergen, R. J. C. Spreeuw, and J. P. Woerdman. Orbital angular momentum of light and the transformation of Laguerre-Gaussianlaser modes. *Phys. Rev. A*, 45(11):8185–8189, 1992.

[132] N. B. Simpson, D. McGloin, K. Dholakia, L. Allen, and M. J. Padgett. Optical tweezers with increased axial trapping efficiency. *J. Mod. Opt.*, 45(9):1943–1949, 1998.

[133] M. A. Taylor, M. Waleed, A. B. Stilgoe, H. Rubinsztein-Dunlop, and W. P. Bowen. Enhanced optical trapping via structured scattering. *Nat. Photon.*, 9:669–673, 2015.

[134] M. Padgett and R. Bowman. Tweezers with a twist. *Nat. Photon.*, 5: 343–348, 2011.

[135] G. A. Swartzlander. Peering into darkness with a vortex spatial filter. *Opt. Lett.*, 26(8):497–499, 2001.

[136] G. Foo, D. M. Palacios, and G. A. Swartzlander. Optical vortex coronagraph. *Opt. Lett.*, 30(24):3308–3310, 2005.

[137] J. Wang, J.-Y. Yang, I. M. Fazal, N. Ahmed, Y. Yan, H. Huang, Y. Ren, Y. Yue, S. Dolinar, M. Tur, and A. E. Willner. Terabit free-space data transmission employing orbital angular momentum multiplexing. *Nat. Photon.*, 6:488–496, 2012.

[138] N. Bozinovic, Y. Yue, Y. Ren, M. Tur, P. Kristensen, H. Huang, A. E. Willner, and S. Ramachandran. Terabit-scale orbital angular momentum mode division multiplexing in fibers. *Science*, 340(6140):1545–1548, 2013.

[139] G. F. Brand. Phase singularities in beams. *Am. J. Phys.*, 67(1):55–60, 1999.

[140] E. Brasselet, G. Gervinskas, G. Seniutinas, and S. Juodkazis. Topological shaping of light by closed-path nanoslits. *Phys. Rev. Lett.*, 111(19):

193901, 2013.

[141] M. I. Shalaev, J. Sun, A. Tsukernik, A. Pandey, K. Nikolskiy, and N. M. Litchinitser. High-efficiency all-dielectric metasurfaces for ultracompact beam manipulation in transmission mode. *Nano Lett.*, 15(9):6261–6266, 2015.

[142] Y. Gorodetski, A. Drezet, C. Genet, and T. W. Ebbesen. Generating far-field orbital angular momenta from near-field optical chirality. *Phys. Rev. Lett.*, 110(20):203906, 2013.

[143] H. Liu, M. Q. Mehmood, K. Huang, L. Ke, H. Ye, P. Genevet, M. Zhang, A. Danner, S. P. Yeo, C.-W. Qiu, and J. Teng. Twisted focusing of optical vortices with broadband flat spiral zone plates. *Adv. Opt. Mater.*, 2(2): 1193–1198, 2014.

[144] L. Wei, Y. Gao, X. Wen, Z. Zhao, L. Cao, and Y. Gu. Fractional spiral zone plates. *J. Opt. Soc. Am. A*, 30(2):233–237, 2013.

[145] A. Žukauskas, G. Batavičiūtė, M. Ščiuka, T. Jukna, A. Melninkaitis, and M. Malinauskas. Characterization of photopolymers used in laser 3d micro/nanolithography by means of laser-induced damage threshold (LIDT). *Opt. Mater. Express*, 4(8):1601–1616, 2014.

[146] A. Ovsianikov, J. Viertl, B. Chichkov, M. Oubaha, B. MacCraith, I. Sakellari, A. Giakoumaki, D. Gray, M. Vamvakaki, M. Farsari, and C. Fotakis. Ultra-low shrinkage hybrid photosensitive material for two-photon polymerization microfabrication. *ACS Nano*, 2(11):2257–2262, 2008.

[147] A. S. Ostrovsky, C. Rickenstorff-Parrao, and V. Arrizón. Generation of the "perfect" optical vortex using a liquid-crystal spatial light modulator. *Opt. Lett.*, 38(4):534–536, 2013.

[148] M. Haruta, T. Kobayashi, H. Sano, and N. Yamada. Novel gold catalysts for the oxidation of carbon monoxide at a temperature far below 0 °C. *Chem. Lett.*, 16(2):405–408, 1987.

[149] B. Tudu and A. Tiwari. Recent developments in perpendicular magnetic anisotropy thin films for data storage applications. *Vacuum*, 146:329–341, 2017.

[150] D. Chu, D. T. Bilir, R. F. W. Pease, and K. E. Goodson. Submicron thermocouple measurements of electron-beam resist heating. *J. Vac. Sci. Technol. B*, 20(6):3044–3046, 2002.

[151] T. W. Kerlin and M. Johnson. *Practical Thermocouple Thermometry*. International Society of Automation, Research Triangle Park, NC, USA,

2nd edition edition, 2012.

[152] S. Gomès, A. Assy, and P.-O. Chapuis. Scanning thermal microscopy: A review. *Phys. Status Solidi A*, 212(3):477–494, 2015.

[153] R. M. Sandfort and E. J. Charlson. Calibration curves for gold-nickel and silver-nickel thin film thermocouples. *Solid State Electron.*, 11(6): 635–637, 1968.

[154] F. Yang, G. Li, J. Yang, Z. Wang, D. Han, F. Zheng, and S. Xu. Measurement of local temperature increments induced by cultured HepG2 cells with micro-thermocouples in a thermally stabilized system. *Sci. Rep.*, 7: 1721, 2017.

[155] J.-F. Lei and H. A. Will. Thin-film thermocouples and strain-gauge technologies for engine applications. *Sens. Actuator A-Phys.*, 65(2-3): 187–193, 1998.

[156] M. S. Watanabe, N. Kakuta, K. Mabuchi, and Y. Yamada. Micro-thermocouple probe for measurement of cellular thermal responses. In *Proc. of the 2005 IEEE Engineering in Medicine and Biology 27th Annual Conference*, volume 5, pages 4858–4861, 2005.

[157] A. Balčytis, M. Ryu, S. Juodkazis, and J. Morikawa. Micro-thermocouple on nanomembrane: thermometer for nanoscale measurements. *Sci. Rep.*, 8:6324, 2018.

[158] J. Morikawa, A. Orie, T. Hashimoto, and S. Juodkazis. Thermal diffusivity in femtosecond-laser-structured micro-volumes of polymers. *Appl. Phys. A*, 98(3):551–556, 2010.

[159] J. Morikawa, A. Orie, T. Hashimoto, and S. Juodkazis. Thermal and optical properties of femtosecond-laser-structured PMMA. *Appl. Phys. A*, 101(1):27–31, 2010.

[160] J. Morikawa, E. Hayakawa, T. Hashimoto, R. Buividas, and S. Juodkazis. Thermal imaging of a heat transport in regions structured by femtosecond laser. *Opt. Express*, 19(21):20542–20550, 2011.

[161] X. Zhang and C. P. Grigoropoulos. Thermal conductivity and diffusivity of free-standing silicon nitride thin films. *Rev. Sci. Instrum.*, 66(2): 1115–1120, 1995.

[162] H. D. Kaesz and R. B. Saillant. Hydride complexes of the transition metals. *Chem. Rev.*, 72(3):231–281, 1972.

[163] B. D. Adams and A. Chen. The role of palladium in a hydrogen economy. *Mater. Today*, 14(6):282–289, 2011.

[164] C. H. Moon, N. V. Myung, and E. D. Haberer. Chemiresistive hydrogen gas sensors from gold-palladium nanopeapods. *Appl. Phys. Lett.*, 105 (22):223102, 2014.

[165] C. S. Chang, M. Kostylev, and E. Ivanov. Metallic spintronic thin film as a hydrogen sensor. *Appl. Phys. Lett.*, 102(14):142405, 2013.

[166] J. I. Avila, R. J. Matelon, R. Trabol, M. Favre, D. Lederman U. G. Volkmann, and A. L. Cabrera. Optical properties of Pd thin films exposed to hydrogen studied by transmittance and reflectance spectroscopy. *J. Appl. Phys.*, 107(2):023504, 2010.

[167] Y. Nishijima, S. Shimizu, K. Kurihara, Y. Hashimoto, H. Takahashi, A. Balčytis, G. Seniutinas, S. Okazaki, J. Juodkazytė, T. Iwasa, T. Taketsugu, Y. Tominaga, and S. Juodkazis. Optical readout of hydrogen storage in films of Au and Pd. *Opt. Express*, 25(20):24081–24092, 2017.

[168] Y. Nishijima, A. Balčytis, G. Seniutinas, S. Juodkazis, T. Arakawa, S. Okazaki, and R. Petruškevičius. Plasmonic hydrogen sensor at infrared wavelengths. *Sens. Mater.*, 29(9):1269–1274, 2017.

[169] Y. Hashimoto, G. Seniutinas, A. Balčytis, S. Juodkazis, and Y. Nishijima. Au-Ag-Cu nano-alloys: tailoring of permittivity. *Sci. Rep.*, 6:25010, 2016.

[170] K. Kusada, M. Yamauchi, H. Kobayashi, H. Kitagawa, and Y. Kubota. Hydrogen-storage properties of solid-solution alloys of immiscible neighboring elements with Pd. *J. Am. Chem. Soc.*, 132(45):15896–15898, 2010.

[171] K. Kusada, H. Kobayashi, R. Ikeda, Y. Kubota, M. Takata, S. Toh, T. Yamamoto, S. Matsumura, N. Sumi, K. Sato, K. Nagaoka, and H. Kitagawa. Solid solution alloy nanoparticles of immiscible Pd and Ru elements neighboring on Rh: Changeover of the thermodynamic behavior for hydrogen storage and enhanced CO-oxidizing ability. *J. Am. Chem. Soc.*, 136(5):1864–1871, 2014.

[172] M. Hirano, K. Enokida, K. Okazaki, S. Kuwabata, H. Yoshida, and T. Torimoto. Composition-dependent electrocatalytic activity of AuPd alloy nanoparticles prepared *via* simultaneous sputter deposition into an ionic liquid. *Phys. Chem. Chem. Phys.*, 15(19):7286–7294, 2013.

[173] M. F. Juárez, G. Soldano, H. Guesmi, F. Tielens, and E. Santos. Catalytic properties of Au electrodes modified by an underlayer of Pd. *Surf. Sci.*, 631:235–247, 2015.

[174] H. Kobayashi, K. Kusada, and H. Kitagawa. Creation of novel solid-

solution alloy nanoparticles on the basis of density-of-states engineering by interelement fusion. *Acc. Chem. Res.*, 48(6):1551–1559, 2015.

[175] C.-W. Yi, K. Luo, T. Wei, and D. W. Goodman. The composition and structure of Pd-Au surfaces. *J. Phys. Chem. B*, 109(39):18535–18540, 2005.

[176] M. Murakami, D. deFontaine, and J. Fodor. X-ray diffraction study of interdiffusion in bimetallic Au/Pd thin films. *J. Appl. Phys.*, 47(7): 2850–2856, 1976.

[177] L. Novtony and B. Hecht. *Principles of nano-optics*. Cambridge University Press, Cambridge, UK, 2st edition, 2012.

[178] K. Juodkazis, J. Juodkazytė, A. Grigucevičienė, and S. Juodkazis. Hydrogen species within the metals: Role of molecular hydrogen ion H_2^+. *Appl. Surf. Sci.*, 258(2):743–747, 2011.

[179] D. M. Nace and J. G. Aston. Palladium hydride. i. the thermodynamic properties of pd_2h between 273 and 345°k. *J. Am. Chem. Soc.*, 79(14): 3619–3623, 1957.

[180] G. L. Holleck. Diffusion and solubility of hydrogen in palladium and palladium-silver alloys. *J. Phys. Chem.*, 74(3):503–511, 1970.

[181] W.-Y. Yu, G. M. Mullen, and C. B. Mullins. Hydrogen adsorption and absorption with Pd-Au bimetallic surfaces. *J. Phys. Chem. C*, 117(38): 19535–19543, 2013.

[182] P. M. Quaino, R. Nazmutdinov, L. F. Peiretti, and E. Santos. Unravelling the hydrogen absorption process in Pd overlayers on a Au(111) surface. *Phys. Chem. Chem. Phys.*, 18(5):3659–3668, 2016.

[183] N. Liu, M. L. Tang, M. Hentschel, H. Giessen, and A. P. Alivisatos. Nanoantenna-enhanced gas sensing in a single tailored nanofocus. *Nat. Mater.*, 10:631–636, 2011.

[184] Y. Fuzi, G. W. Bradberry, and J. R. Sambles. Infrared surface plasmon-polaritons on Ni, Pd and Pt. *J. Mod. Opt.*, 36(11):1405–1410, 1989.

[185] C. Langhammer, I. Zorič, B. Kasemo, and B. M. Clemens. Hydrogen storage in Pd nanodisks characterized with a novel nanoplasmonic sensing scheme. *Nano Lett.*, 7(10):3122–3127, 2007.

[186] C. Wadell, S. Syrenova, and C. Langhammer. Plasmonic hydrogen sensing with nanostructured metal hydrides. *ACS Nano*, 8(12):11925–11940, 2014.

[187] C. Langhammer, Z. Yuan, I. Zoriċ, and B. Kasemo. Plasmonic properties of supported Pt and Pd nanostructures. *Nano Lett.*, 6(4):833–838, 2006.

[188] N. Meinzer, W. L. Barnes, and I. R. Hooper. Plasmonic meta-atoms and metasurfaces. *Nat. Photon.*, 8:889–898, 2014.

[189] M. Choi, S. H. Lee, Y. Kim, S. B. Kang, J. Shin, M. H. Kwak, K.-Y. Kang, Y.-H. Lee, N. Park, and B. Min. A terahertz metamaterial with unnaturally high refractive index. *Nature*, 470:369–373, 2011.

[190] J. B. Pendry, A. J. Holden, W. J. Stewart, and I. Youngs. Extremely low frequency plasmons in metallic mesostructures. *Phys. Rev. Lett.*, 76(25): 4773–4776, 2017.

[191] J. K. Gansel, M. Thiel, M. S. Rill, M. Decker, K. Bade, V. Saile, G. von Freymann, S. Linden, and M. Wegener. Gold helix photonic metamaterial as broadband circular polarizer. *Science*, 325(5947):1513–1515, 2004.

[192] A. Boltasseva and H. A. Atwater. Low-loss plasmonic metamaterials. *Science*, 331(6015):290–291, 2011.

[193] O. Hess, J. B. Pendry, S. A. Maier, R. F. Oulton, J. M. Hamm, and K. L. Tsakmakidis. Active nanoplasmonic metamaterials. *Nat. Mater.*, 11: 573–584, 2012.

[194] N. I. Landy, S. Sajuyigbe, J. J. Mock, D. R. Smith, and W. J. Padilla. Perfect metamaterial absorber. *Phys. Rev. Lett.*, 100(20):207402, 2008.

[195] N. Liu, M. Mesch, T. Weiss, M. Hentschel, and H. Giessen. Infrared perfect absorber and its application as plasmonic sensor. *Nano Lett.*, 10 (7):2342–2348, 2010.

[196] H. Zhang, H. Volkan Demir, , and A. O. Govorov. Plasmonic metamaterials and nanocomposites with the narrow transparency window effect in broad extinction spectra. *ACS Photonics*, 1(9):822–832, 2014.

[197] C. Wu, B. Neuner III, J. John, A. Milder, B. Zollars, S. Savoy, and G. Shvets. Metamaterial-based integrated plasmonic absorber/emitter for solar thermo-photovoltaic systems. *J. Opt.*, 14(2):024005, 2012.

[198] Y. Nishijima, A. Balčytis, S. Naganuma, G. Seniutinas, and S. Juodkazis. Tailoring metal and insulator contributions in plasmonic perfect absorber metasurfaces. *ACS Appl. Nano Mater.*, 1(7):3557–3564, 2018.

[199] T. Minami, H. Nanto, and S. Takata. Highly conductive and transparent zinc oxide films prepared by rf magnetron sputtering under an applied external magnetic field. *Appl. Phys. Lett.*, 41(10):958–960, 1982.

[200] G. Xiong, J. Wilkinson, B. Mischuck, S. Tüzemen, K. B. Ucer, and R. T. Williams. Control of *p*- and *n*-type conductivity in sputter deposition of undoped ZnO. *Appl. Phys. Lett.*, 80(7):1195–1197, 2002.

[201] M. S. Eggleston, K. Messer, L. Zhang, E. Yablonovitch, and M. C. Wu. Optical antenna enhanced spontaneous emission. *Proc. Nat. Acad. Sci.*, 112(6):1704–1709, 2015.

[202] E. Palik, editor. *Handbook of Optical Constants of Solids*, volume I-III. Academic Press, Burlington, Mass., USA, 1997.

[203] R. E. Camley and R. L. Stamps. Magnetic multilayers: spin configurations, excitations and giant magnetoresistance. *J. Phys.: Condens. Matter*, 5(23):3727–3786, 1993.

[204] M. K. Grobis, O. Hellwig, T. Hauet, E. Dobisz, and T. R. Albrecht. High-density bit patterned media: Magnetic design and recording performance. *IEEE Trans. Magn.*, 47(1):6–10, 2011.

[205] Y. Wang, P. Surendran, S. Jose, T. Tran, I. Herrera, S. Whitlock, R. McLean, A. Sidorov, and P. Hannaford. Magnetic lattices for ultracold atoms and degenerate quantum gases. *Sci. Bull.*, 61(14):1097–1106, 2016.

[206] M. Singh, M. Volk, A. Akulshin, A. Sidorov, R. McLean, and P. Hannaford. One-dimensional lattice of permanent magnetic microtraps for ultracold atoms on an atom chip. *J. Phys. B*, 41(6):065301, 2008.

[207] S. Whitlock, R. Gerritsma, T. Fernholz, and R. J. C. Spreeuw. Two-dimensional array of microtraps with atomic shift register on a chip. *New J. Phys.*, 11:023021, 2009.

[208] V. Y. F. Leung, D. R. M. Pijn, H. Schlatter, L. Torralbo-Campo, A. L. La Rooij, G. B. Mulder, J. Naber, M. L. Soudijn, A. Tauschinsky, C. Abarbanel, B. Hadad, E. Golan, R. Folman, and R. J. C. Spreeuw. Magnetic-film atom chip with 10 μm period lattices of microtraps for quantum information science with Rydberg atoms. *Rev. Sci. Instrum.*, 85(5): 053102, 2014.

[209] P. Surendran, S. Jose, Y. Wang, I. Herrera, H. Hu, X. Liu, S. Whitlock, R. McLean, A. Sidorov, and P. Hannaford. Radio-frequency spectroscopy of a linear array of Bose-Einstein condensates in a magnetic lattice. *Phys. Rev. A*, 91(2):023605, 2015.

[210] I. Bloch, J. Dalibard, and W. Zwerger. Many-body physics with ultracold gases. *Rev. Mod. Phys.*, 80(3):885–964, 2008.

[211] M. Takamoto, F.-L. Hong, R. Higashi, and H. Katori. An optical lattice clock. *Nature*, 435:321–324, 2005.

[212] C. Monroe. Quantum information processing with atoms and photons. *Nature*, 416:238–246, 2002.

[213] W. S. Bakr, J. I. Gillen, A. Peng, S. Fölling, and M. Greiner. A quantum gas microscope for detecting single atoms in a Hubbard-regime optical lattice. *Nature*, 462:74–77, 2009.

[214] T. Uehlinger, G. Jotzu, M. Messer, D. Greif, W. Hofstetter, U. Bissbort, and T. Esslinger. Artificial graphene with tunable interactions. *Phys. Rev. Lett.*, 111(18):185307, 2013.

[215] J. Simon, W. S. Bakr, R. Ma, M. E. Tai, P. M. Preiss, and M. Greiner. Quantum simulation of antiferromagnetic spin chains in an optical lattice. *Nature*, 472:307–312, 2011.

[216] J. Billy, V. Josse, Z. Zuo, A. Bernard, B. Hambrecht, P. Lugan, D. Clément, L. Sanchez-Palencia, P. Bouyer, and A. Aspect. Direct observation of Anderson localization of matter waves in a controlled disorder. *Nature*, 453:891–894, 2008.

[217] M. Mancini, G. Pagano, G. Cappellini, L. Livi, M. Rider, J. Catani, C. Sias, P. Zoller, M. Inguscio, M. Dalmonte, and L. Fallani. Observation of chiral edge states with neutral fermions in synthetic Hall ribbons. *Science*, 349(6255):1510–1513, 2015.

[218] J. Reichel. Microchip traps and Bose-Einstein condensation. *Appl. Phys. B*, 74(6):469–487, 2002.

[219] W. D. Phillips. Nobel lecture: Laser cooling and trapping of neutral atoms. *Rev. Mod. Phys.*, 70(3):721–741, 1998.

[220] Y. Wang, T. Tran, P. Surendran, I. Herrera, A. Balčytis, D. Nissen, M. Albrecht, A. Sidorov, and P. Hannaford. Trapping ultracold atoms in a sub-micron-period triangular magnetic lattice. *Phys. Rev. A*, 96(1): 013630, 1995.

[221] I. Herrera, Y. Wang, P. Michaux, D. Nissen, , P. Surendran, S. Juodkazis, S. Whitlock, R. J. McLean, A. Sidorov, M. Albrecht, and P. Hannaford. Sub-micron period lattice structures of magnetic microtraps for ultracold atoms on an atom chip. *J. Phys. D*, 48(11):115002, 2015.

[222] P. F. Carcia, A. D. Meinhaldt, and A. Suna. Perpendicular magnetic anisotropy in Pd/Co thin film layered structures. *Appl. Phys. Lett.*, 47(2): 178–180, 1985.

[223] A. G. Roy, D. E. Laughlin, T. J. Klemmer, K. Howard, S. Khizroev, and D. Litvinov. Seed-layer effect on the microstructure and magnetic properties of Co/Pd multilayers. *J. Appl. Phys.*, 89(11):7531–7533, 2001.

[224] M. A. Clifford, G. P. T. Lancaster, R. H. Mitchell, F. Akerboom, and K. Dholakia. Realization of a mirror magneto-optical trap. *J. Mod. Opt.*, 48(6):1123–1128, 2001.

[225] J. A. Sedlacek, E. Kim, S. T. Rittenhouse, P. F. Weck, H. R. Sadeghpour, and J. P. Shaffer. Electric field cancellation on quartz by Rb adsorbate-induced negative electron affinity. *Phys. Rev. Lett.*, 116(13):133201, 2016.

[226] R. Schmied, D. Leibfried, R. J. C. Spreeuw, and S. Whitlock. Optimized magnetic lattices for ultracold atomic ensembles. *New J. Phys.*, 12: 103029, 2010.

[227] E. A. Power. Casimir-Polder potential from first principles. *Eur. J. Phys.*, 22(4):453–461, 2001.

[228] Y.-J. Lin, I. Teper, C. Chin, and V. Vuletić. Impact of the Casimir-Polder potential and Johnson noise on Bose-Einstein condensate stability near surfaces. *Phys. Rev. Lett.*, 92(5):050404, 2004.

ACKNOWLEDGMENT

This work was made possible only thanks to the guidance, assistance and opportunities granted to me by many different people. I owe a great deal of thanks to my supervisor Dr. Raimondas Petruškevičius for his continued assistance and patience throughout my extended four year placement far abroad. During this time, the overwhelming majority of the research initiatives described among these pages were initiated, facilitated or at the very least enabled by my supervisor Prof. Saulius Juodkazis at Swinburne University of Technology, Australia, where most of the fabrication work was undertaken, all of which I sincerely appreciate.

I am very grateful to Dr. Gediminas Račiukaitis for his extremely valuable help and support in navigating and clearing any hurdles which inevitably arose due to my remote placement. My good friend Dr. Gediminas Seniutinas is due my warmest thanks for teaching me almost everything I now consider important when it comes to nanofabrication. I am also deeply thankful to Assoc. Prof. Yoshiaki Nishijima for being an invaluable source of inspiration, and for giving me numerous beneficial opportunities to contribute to his work. Furthermore, I wish to express my gratitude to Prof. Junko Morikawa for the many fruitful collaborative research efforts and for being a wonderful host during my visit to Tokyo Institute of Technology. My appreciation also goes to Meguya Ryu, for always being a most capable and reliable partner through numerous challenging experiments, as well as to Darius Urbonas, for many thought-provoking and informative discussions.

Over the course of my studies I was allowed the opportunity to join a multitude of intriguing projects headed by, in no particular order, Prof. Etienne Brasselet, Prof. Peter Hannaford, Dr. Mangirdas Malinauskas, Prof. Elena Ivanova, Prof. Yasuyuki Tsuboi, Assoc. Prof. Koji Hatanaka, and Dr. Sivashankar Krishnamoorthy, to all of whom I am ever grateful.

I thank Pierrette Michaux for showing me the ropes of, and the discipline needed for, working in a cleanroom environment. Also, an important portion of this research was performed on the Infrared Microspectroscopy beamline at the Australian Synchrotron, part of ANSTO. Special thanks go out to beamline scientists Dr. Pimm Vongsvivut and Dr. Mark Tobin for going above and beyond the call of duty in their help and guidance over the course of several hectic experiments. Similarly, parts of this work, particularly pertaining to EBL fabrication, were conducted at the Melbourne Centre for Nanofabrication (MCN) in the Victorian Node of the Australian National Fabrication Facility (ANFF). Important monetary support to cover fabrication costs was provided by the European Social Fund (ESF) Agency in Lithuania, as part of the VP1-3.1-SMM-10-V-02-026 project.

Lastly, I thank my love, Aurina, for following me all the way to Australia and for letting me be the benefactor of her invaluable help, support, understanding and sense of humor. Most of all I owe an immeasurable debt of gratitude to my mother, Nijolė, not only for the great care and effort spent in raising me, but also for bravely weathering any and all hardships that came up over the course of my long time away.

LIST OF PUBLICATIONS

Publications pertaining to the thesis

1. D. Urbonas, A. Balčytis, M. Gabalis, K. Vaškevičius, G. Naujokaitė, S. Juodkazis, and R. Petruškevičius. Ultra-wide free spectral range, enhanced sensitivity, and removed mode splitting SOI optical ring resonator with dispersive metal nanodisks. *Opt. Lett.*, 40(13):2977–2980, 2015.
2. D. Urbonas, A. Balčytis, K. Vaškevičius, M. Gabalis, and R. Petruškevičius. Air and dielectric bands photonic crystal microringresonator for refractive index sensing. *Opt. Lett.*, 41(15):3655–3658, 2016.
3. A. Balčytis, D. Hakobyan, M. Gabalis, A. Žukauskas, D. Urbonas, M. Malinauskas, R. Petruškevičius, E. Brasselet, and S. Juodkazis. Hybrid curved nano-structured micro-optical elements. *Opt. Express*, 24(15): 16988–16998, 2016.
4. Y. Hashimoto, G. Seniutinas, A. Balčytis, S. Juodkazis, and Y. Nishijima. Au-Ag-Cu nano-alloys: tailoring of permittivity. *Sci. Rep.*, 6:25010, 2016.
5. G. Seniutinas, A. Balčytis, and S. Juodkazis. Ultraviolet-photoelectric effect for augmented contrast and resolution in electron microscopy. *APL Photonics*, 1(2):021301, 2016.
6. Y. Wang, T. Tran, P. Surendran, I. Herrera, A. Balčytis, D. Nissen, M. Albrecht, A. Sidorov, and P. Hannaford. Trapping ultracold atoms in a sub-micron-period triangular magnetic lattice. *Phys. Rev. A*, 96(1): 013630, 2017.
7. K. Vaškevičius, M. Gabalis, D. Urbonas, A. Balčytis, R. Petruškevičius, and S. Juodkazis. Enhanced sensitivity and measurement range SOI microring resonator with integrated one-dimensional photonic crystal. *J. Opt. Soc. Am. B*, 34(4):750–755, 2017.
8. Y. Nishijima, Y. Hashimoto, A. Balčytis, G. Seniutinas, and S. Juodkazis. Alloy materials for plasmonic refractive index sensing. *Sens. Mater.*, 29 (9):1233–1239, 2017.
9. Y. Nishijima, S. Suda, G. Seniutinas, A. Balčytis, and S. Juodkazis. Plasmonic sensor: towards parts-per-billion level sensitivity. *Sens. Mater.*, 29(9):1253–1258, 2017.
10. Y. Nishijima, A. Balčytis, G. Seniutinas, S. Juodkazis, T. Arakawa, S. Okazaki, and R. Petruškevičius. Plasmonic hydrogen sensor at infrared wavelengths. *Sens. Mater.*, 29(9):1269–1274, 2017.

11. Y. Nishijima, S. Shimizu, K. Kurihara, Y. Hashimoto, H. Takahashi, A. Balčytis, G. Seniutinas, S. Okazaki, J. Juodkazytė, T. Iwasa, T. Taketsugu, Y. Tominaga, and S. Juodkazis. Optical readout of hydrogen storage in films of Au and Pd. *Opt. Express*, 25(20):24081–24092, 2017.
12. A. Balčytis, M. Ryu, S. Juodkazis, and J. Morikawa. Micro-thermocouple on nano-membrane: thermometer for nanoscale measurements. *Sci. Rep.*, 8:6324, 2018.
13. Y. Nishijima, A. Balčytis, S. Naganuma, G. Seniutinas, and S. Juodkazis. Tailoring metal and insulator contributions in plasmonic perfect absorber metasurfaces. *ACS Appl. Nano Mater.*, 1(7):3557–3564, 2018.

Other publications

14. R. Komatsu, A. Balčytis, G. Seniutinas T. Yamamura, Y. Nishijima, and S. Juodkazis. Plasmonic photo-thermoelectric energy converter with black-Si absorber. *Sol. Energ. Mater. Sol. Cells*, 143:72–77, 2015.
15. Y. Nishijima, R. Komatsu, T. Yamamura, A. Balčytis, G. Seniutinas, and S. Juodkazis. Design concept of a hybrid photo-voltaic/thermal conversion cell for mid-infrared light energy harvester. *Opt. Mater. Express*, 7(11):3484–3493, 2015.
16. A. Balčytis, M. Ryu, G. Seniutinas, Y. Nishijima, Y. Hikima, M. Zamengo, R. Petruškevičius, J. Morikawa, and S. Juodkazis. Si-based infrared optical filters. *Opt. Eng.*, 54(12):127103, 2015.
17. A. Balčytis, M. Ryu, G. Seniutinas, J. Juodkazytė, B. C. C. Cowie, P. R. Stoddart, M. Zamengo, J. Morikawa, and S. Juodkazis. Black-CuO: surface-enhanced Raman scattering and infrared properties. *Nanoscale*, 7:18299–18304, 2015.
18. S. Dinda, V. Suresh, P. Thoniyot, A. Balčytis, S. Juodkazis, and S. Krishnamoorthy. Engineering 3D nanoplasmonic assemblies for high performance spectroscopic sensing. *ACS Appl. Mater. Interfaces*, 7(50): 27661–27666, 2015.
19. F. C. P. Masim, H.-L. Liu, M. Porta, T. Yonezawa, A.Balčytis, S. Juodkazis, W.-H. Hsu, and K. Hatanaka. Enhanced photoacoustics from gold nano-colloidal suspensions under femtosecond laser excitation. *Opt. Express*, 24(13):14781–14792, 2016.
20. F. C. P. Masim, W.-H. Hsu, C.-H. Tsai, H.-L. Liu, M. Porta, M. T. Nguyen, T. Yonezawa, A. Balčytis, X. Wang, S. Juodkazis, and K. Hatanaka. Enhanced photoacoustics from gold nano-colloidal suspensions under femtosecond laser excitation. *Opt. Express*, 24(15):17050–17059, 2016.
21. W.-H. Hsu, F. C. P. Masim, M. Porta, M. T. Nguyen, T. Yonezawa, A. Balčytis, X. Wang, L. Rosa, S. Juodkazis, and K. Hatanaka. Femtosec-

ond laser-induced hard X-ray generation in air from a solution flow of Au nano-sphere suspension using an automatic positioning system. *Opt. Express*, 24(18):19994–20001, 2016.

22. A. Balčytis, T. Tolenis, X. Wang, G. Seniutinas, R. Drazdys, P. R. Stoddart, and S. Juodkazis. Percolation threshold gold films on columnar coatings: characterisation for SERS applications. *Asian J. Phys.*, 25(7): 871–878, 2016.
23. G. Seniutinas, A. Balčytis, Y. Nishijima, A. Nadzeyka, S. Bauerdick, and S. Juodkazis. Ion beam lithography with gold and silicon ions. *Appl. Phys. A*, 122:383, 2016.
24. J. Morikawa, M. Ryu, G. Seniutinas, A. Balčytis, K. Maximova, X. Wang, M. Zamengo, E. P. Ivanova, and S. Juodkazis. Nanostructured antireflective and thermoisolative cicada wings. *Langmuir*, 32(18):4698–4703, 2016.
25. J. Morikawa, M. Ryu, K. Maximova, A. Balčytis, G. Seniutinas, L. Fan, V. Mizeikis, J. Li, X. Wang, M. Zamengo, X. Wang, and S. Juodkazis. Silk fibroin as a water-soluble bio-resist and its thermal properties. *RSC Adv.*, 6(14):11863–11869, 2016.
26. K. Maximova, X. Wang, A. Balčytis, L. Fan, J. Li, and S. Juodkazis. Silk patterns made by direct femtosecond laser writing. *Biomicrofluidics*, 10 (5):054101, 2016.
27. B. Sanchez-Padilla, A. Žukauskas, A. Aleksanyan, A. Balčytis, M. Malinauskas, S. Juodkazis, and E. Brasselet. Wrinkled axicons: shaping light from cusps. *Opt. Express*, 24(21):24075–24082, 2016.
28. X. Wang, G. Seniutinas, A. Balčytis, I. Kašalynas, V. Jakštas, V. Janonis, R. Venckevičius, R. Buividas, D. Appadoo, G. Valušis, and S. Juodkazis. Laser structuring for control of coupling between THz light and phonon modes. *J. Laser Micro Nanoeng.*, 11(3):377–380, 2016.
29. Y. Nishijima, R. Komatsu, S. Ota, G. Seniutinas, A. Balčytis, and S. Juodkazis. Anti-reflective surfaces: Cascading nano/microstructuring. *APL Photonics*, 1(7):076104, 2016.
30. T. Shoji, A. Mototsuji, A. Balčytis, D. Linklater, S. Juodkazis, and Y. Tsuboi. Optical tweezing and binding at high irradiation powers on black-Si. *Sci. Rep.*, 7:12298, 2017.
31. A. Balčytis, M. Ryu, G. Seniutinas, P. R. Stoddart, M. A. Al Mamun, J. Morikawa, and S. Juodkazis. Nano-rescaling of gold films on polystyrene: thermal management for SERS. *Nanoscale*, 9(2):690–695, 2017.
32. G. Seniutinas, A. Balčytis, I. Reklaitis, F. Chen, J. Davis, C. David, and

S. Juodkazis. Tipping solutions: emerging 3D nano-fabrication/-imaging technologies. *Nanophotonics*, 6(5):923–941, 2017.

33. F. C. P. Masim, W.-H. Hsu, H.-L. Liu, T. Yonezawa, A. Balčytis, S. Juodkazis, and K. Hatanaka. Photoacoustic signal enhancements from gold nano-colloidal suspensions excited by a pair of time-delayed femtosecond pulses. *Opt. Express*, 25(16):19497–19507, 2017.
34. W.-H. Hsu, F. C. P. Masim, A. Balčytis, S. Juodkazis, and K. Hatanaka. Dynamic position shifts of X-ray emission from a water film induced by a pair of time-delayed femtosecond laser pulses. *Opt. Express*, 25(20): 24109–24118, 2017.
35. A. Balčytis, M. Ryu, X. Wang, F. Novelli, G. Seniutinas, S. Du, X. Wang, J. Li, J. Davis, D. Appadoo, J. Morikawa, and S. Juodkazis. Silk: Optical properties over 12.6 octaves THz-IR-Visible-UV range. *Materials*, 10 (4):356, 2017.
36. M. Ryu, A. Balčytis, X. Wang, J. Vongsvivut, Y. Hikima, J. Li, M. J. Tobin, S. Juodkazis, and J. Morikawa. Orientational mapping augmented sub-wavelength hyper-spectral imaging of silk. *Sci. Rep.*, 7:7419, 2017.
37. M. Ryu, H. Kobayashi, A. Balčytis, X. Wang, J. Vongsvivut, J. Li, N. Urayama, V. Mizeikis, M. Tobin, S. Juodkazis, and J. Morikawa. Nanoscale chemical mapping of laser-solubilized silk. *Mater. Res. Express*, 4(11):115028, 2017.
38. M. Ryu, D. Linklater, W. Hart, A. Balčytis, E. Skliutas, M. Malinauskas, D. Appadoo, Y.-R. E. Tan, E. P. Ivanova, J. Morikawa, and S. Juodkazis. 3D printed polarizing grids for IR-THz synchrotron radiation. *J. Opt.*, 20 (3):035101, 2018.
39. D. H. K. Nguyen, V. T. H. Pham, V. Khanh Truong, I. Sbarski, J. Wang, A. Balčytis, S. Juodkazis, D. E. Mainwaring, R. J. Crawford, and E. P. Ivanova. Role of topological scale in the differential fouling of *Pseudomonas aeruginosa* and *Staphylococcus aureus* bacterial cells on wrinkled gold-coated polystyrene surfaces. *Nanoscale*, 10(11):5089–5096, 2018.
40. C. M. Bhadra, M. Werner, V. A. Baulin, V. K. Truong, M. Al Kobaisi, S. H. Nguyen, A. Balčytis, S. Juodkazis, J. Y. Wang, D. E. Mainwaring, R. J. Crawford, and E. P. Ivanova. Subtle variations in surface properties of black silicon surfaces influence the degree of bactericidal efficiency. *Nano-Micro Lett.*, 10(2):36, 2018.
41. Z. Wei, M. Janczarek, M. Endo, K. Wang, A. Balčytis, A. Nitta, M. G. Méndez-Medrano, C. Colbeau-Justin, S. Juodkazis, B. Ohtani, E. Kowalska. Noble metal-modified faceted anatase titania photocatalysts: Octahedron versus decahedron. *Appl. Catal. B*, 237574–587, 2018.

42. E. Mitsai, A. Kuchmizhak, E. Pustovalov, A. Sergeev, A. Mironenko, S. Bratskaya, D. P. Linklater, A. Balčytis, E. Ivanova, S. Juodkazis. Chemically non-perturbing SERS detection of a catalytic reaction with black silicon. *Nanoscale*, 10:(20):9780–9787, 2018.
43. A. Balčytis, Y. Nishijima, S. Krishnamoorthy, A. Kuchmizhak, P. R. Stoddart, R. Petruškevičius, S. Juodkazis. From fundamental toward applied SERS: Shared principles and divergent approaches. *Adv. Opt. Mater.*, 6:(16):1800292, 2018.

Conferences and proceeding papers pertaining to the thesis

1. R. Petruškevičius, D. Urbonas, M. Gabalis, K. Vaškevičius and A. Balčytis. Plasmonic and silicon-on-insulator nanostructures for optical biosensing. In *IEEE Proc. 2014 16th International Conference on Transparent Optical Networks (ICTON)*, 6-10 July, Graz, Austria, pages 1–4, 2014.
2. A. Balčytis, G. Seniutinas, D. Urbonas, M. Gabalis, K. Vaškevičius, R. Petruškevičius, G. Molis, G. Valušis, S. Juodkazis. High precision fabrication of antennas and sensors. In *Proc. SPIE 9446, Ninth International Symposium on Precision Engineering Measurement and Instrumentation*, 8-10 August, Changsha, China, page 94461G, 2015.
3. G. Seniutinas, G. Gervinskas, A. Balčytis, F. Clark, Y. Nishijima, A. Krotkus, G. Molis, G. Valusis, S. Juodkazis. Nanoscale precision in ion milling for optical and terahertz antennas. In *Proc. SPIE 9374, Advanced Fabrication Technologies for Micro/Nano Optics and Photonics VIII*, 8-11 February, San Francisco, CA, USA, page 93740P, 2015.
4. Y. Nishijima, Y. Hashimoto, S. Gediminas, A. Balčytis and S. Juodkazis. Alloy plasmonic materials. In *Lasers and Electro-Optics Pacific Rim (CLEO-PR), 2015 11th Conference on, Vol. 1*, 24-28 August, Busan, South Korea, pages 1-2, 2015.
5. A. Balčytis, D. Hakobyan, M. Gabalis, A. Žukauskas, D. Urbonas, M. Malinauskas, R. Petruškevičius, E. Brasselet, S. Juodkazis. 3D micro-optical elements for generation of tightly focused vortex beams. In *MATEC Web of Conferences 32, International Symposium of Optomechatronics Technology (ISOT 2015)*, 14-16 October, Neuchatel, Switzerland, page 03002, 2015.
6. A. Balčytis, D. Urbonas, M. Gabalis, S. Juodkazis, R. Petruškevičius. Mode control in SOI microring resonators through sub-wavelength modifications. In *Applied Nanotechnology and Nanoscience International Conference (ANNIC 2016)*, 9-11 November, Barcelona, Spain, 2016.
7. C. Briosne-Fréjaville, A. Mau, A. Balčytis, X. Li, S. Juodkazis. Resizable nanopores. In *Applied Nanotechnology and Nanoscience International*

Conference (ANNIC 2016), 9-11 November, Barcelona, Spain, 2016.

8. A. Balčytis, D. Urbonas, M. Gabalis, S. Juodkazis, R. Petruškevičius. Sub-wavelength modifications in silicon-on-insulator microring resonators for enhanced sensing. In *IONS Conference on Optics, Atoms and Laser Applications 2016 (KOALA 2016)*, 27 November - 2 December, Melbourne, VIC, Australia, 2016.
9. A. Balčytis, C. Briosne-Fréjaville, A. Mau, X. Li, S. Juodkazis. Rescalable solid-state nanopores. In *AIP Conference Proceedings 1874, International Conference on Metamaterials and Nanophotonics (METANANO-2017)*, 18-22 September, Vladivostok, Russia, page 030002, 2016.

Other conferences and proceeding papers

10. Y. Nishijima, R. Komatsu, T. Yamamura, G. Seniutinas, A. Balčytis, S. Juodkazis. Photo-Thermoelectric Energy Converter with Black-Si Absorber. In *IEEE Proc. 2014 Conference on Optoelectronic and Microelectronic Materials and Devices (COMMAD)*, 14-17 December, Perth, Australia, pages 109–112, 2014.
11. G. Seniutinas, A. Balčytis, R. Tomašiūnas, R. Petruškevičius, S. Urnikaitė and V. Getautis. Photo-Switching dynamics of azo-phenylcarbazoles in polycarbonate around β transition temperature. In *IEEE Proc. 2014 16th International Conference on Transparent Optical Networks (ICTON)*, 6-10 July, Graz, Austria, pages 1–4, 2014.
12. Y. Nishijima, A. Balčytis, R. Komatsu, T. Yamamura, G. Seniutinas, B. T. Wong, S. Juodkazis. Thermal to electrical energy converter based on black Si. In *Proc. SPIE 9374, Advanced Fabrication Technologies for Micro/Nano Optics and Photonics VIII*, 8-11 February, San Francisco, CA, USA, page 93740J, 2015.
13. A. Balčytis, G. Seniutinas, J. Juodkazytė, B. C. C. Cowie, F. Lapierre, S. Juodkazis. Nanotextured CuO: sensing and light harvesting platform. In *Proc. SPIE 9374, Advanced Fabrication Technologies for Micro/Nano Optics and Photonics VIII*, 8-11 February, San Francisco, CA, USA, page 93740K, 2015.
14. R. Komatsu, A. Balčytis, G. Seniutinas, Y. Nishijima, S. Juodkazis. Energy harvesting with black Si/plasmonics composite material. In *Lasers and Electro-Optics Pacific Rim (CLEO-PR), 2015 11th Conference on, Vol. 2*, 24-28 August, Busan, South Korea, pages 1-2, 2015.
15. J. Getautis, A. Balčytis, R. Tomašiūnas, R. Petruškevičius, S. Urnikaitė and V. Getautis. All-optical poling kinetics of azophenylcarbazoles influenced by attached anchor. In *2015 17th International Conference on Transparent Optical Networks (ICTON)*, 5-9 July, Budapest, Hungary,

pages 1-4, 2015.

16. A. Balčytis, J. Juodkazytė, G. Seniutinas, X. Li, G. Niaura, S. Juodkazis. Nanotextured surfaces for surface enhanced Raman spectroscopy and sensors. In *Proc. SPIE 9736, Laser-based Micro- and Nanoprocessing X*, 16-18 February, San Francisco, CA, USA, page 97360G, 2016.
17. K. Maximova, X. Wang, A. Balčytis, J. Li, S. Juodkazis. Writing of bio-compatible silk patterns: 3D laser nano-printing. In *Conference on Lasers and Electro-Optics, OSA Technical Digest*, 5–10 June, San Jose, CA, USA, page AF1J.2, 2016.

NOTES

NOTES

Vilniaus universiteto leidykla
Universiteto g. 1, LT-01513 Vilnius
El. p. info@leidykla.vu.lt,
www.leidykla.vu.lt
Tiražas 20 egz.